

UNIVERSITÉ DE MONTRÉAL

CHARACTERIZATION AND MODELLING OF SCATTERED WIRELESS CHANNEL AT 60
GHZ IN AN UNDERGROUND MINE GALLERY

SHAH AHSANUZZAMAN MD TARIQ
DÉPARTEMENT DE GÉNIE ÉLECTRIQUE
ÉCOLE POLYTECHNIQUE DE MONTRÉAL

THÈSE PRÉSENTÉE EN VUE DE L'OBTENTION
DU DIPLÔME DE PHILOSOPHIE DOCTOR
(GÉNIE ÉLECTRIQUE)
AOÛT 2016

UNIVERSITÉ DE MONTRÉAL

ÉCOLE POLYTECHNIQUE DE MONTRÉAL

Cette thèse intitulée :

CHARACTERIZATION AND MODELLING OF SCATTERED WIRELESS CHANNEL AT 60
GHZ IN AN UNDERGROUND MINE GALLERY

présentée par : TARIQ Shah Ahsanuzzaman Md
en vue de l'obtention du diplôme de : Philosophie Doctor
a été dûment acceptée par le jury d'examen constitué de :

M. CARDINAL Christian, Ph. D., président
M. NERGUIZIAN Chahé, Ph. D., membre et directeur de recherche
M. DESPINS Charles, Ph. D., membre et codirecteur de recherche
M. AFFES Sofiène, Ph. D., membre et codirecteur de recherche
M. AKYEL Cevdet, Ph. D., membre
M. TALBI Larbi, Ph. D., membre externe

DEDICATION

To my mother and father.

To all my family members and friends.

ACKNOWLEDGEMENTS

To fulfill the research objective, it would not be successful without the supervisions of my research director and co-directors, and the help of my colleagues, friends, and family.

I would like to thank PhD director Professor Chahé Nerguizian, for his excellent guidance, care, encouragements, availability and suggestions during my Ph.D. program. He always encourages me to overcome the research problems and provides moral help in a friendly manner. Also, I would like to express my special thanks to my co-directors Professor Charles Despins (ETS) and Professor Sofiène Affes (INRS) their support in my research project. I would like to thank them for their guidance and help.

I would like to thank Mohamad El Khaled and Birahima Ndiaye for their contributions during measurement campaign in Underground mine. Also I would like to thank Professor Mourad Nedil (UQAT), Professor Nahi Kandil (UQAT), Professor Nadir Hakem and Mr. Mohamed Aïlas for their valuable assistance to do measurements and campaigns with the setup and the administrative process in the Canadian Center for Minerals and Energy Technology (CANMET) underground mine located in Val-d'Or, Quebec. I would like to also thank for the help of Dr. Yacouba Coulibaly and Mr. Bilel Mnasri as well.

I would like to acknowledge Ron Casselman, Chris Richards, Chris Nizman, Gary Boudreau, Virgil Cimpu and Farshad Sarabchi, members of Wi-Fi group as well as colleagues involved in the LTE-U project at Ericsson, Ottawa for their help and technical support during my internship period.

Moreover, I would like to thank to Mr. Gauthier and Mr. Maxime for their assistance in handling the system setup and antenna issues at Poly-Grames Research Center of Polytechnique Montréal.

The financial support of the LRTCS (Laboratoire de recherche Télébec en communications souterraines) and PERSWADE (Pervasive and Smart Wireless Applications for the Digital Economy) – NSERC (Natural Sciences and Engineering Research Council of Canada) for this research and the internship work are acknowledged. This is obviously necessary to say thanks that all of my colleagues at Poly-Grames Research center for their valuable support to upgrade technical and personal development skills during all these years. Special thanks to my mother for her continuous support and inspiration.

RÉSUMÉ

Depuis plus d'une décennie, les applications du système de communication sans fil sont exigeantes et augmentent rapidement pour fournir des services multimédias au public. De nos jours, la recherche se concentre sur la conception de communication sans fil à haute vitesse (i.e., 1 Gbps) en particulier dans des zones denses telles que des salles de conférence, des centres commerciaux, des stades et des lieux d'événements publics ouverts. Des réseaux locaux sans fil (WLAN) et des réseaux cellulaires utilisent des hauts potentiels pour réussir les haut débit de données en utilisant différentes technologies de pointe telles que la coexistence entre l'évaluation à long terme non autorisé (LTE-U) et les canaux Wi-Fi. En outre, la faisabilité d'utiliser le spectre à haute fréquence (i.e., > 6 GHz), une couche physique à 60 GHz pour les réseaux denses sont mis en évidence lorsque des liens de communication à courte distance (par exemple, <10 m) sont nécessaires aussi bien dans WLAN (i.e., WiGig) et le réseau cellulaire (i.e., 5G petite cellule). Cependant, les applications à 60 GHz se dirigent vers la communication sans fil souterraine pour une meilleure géolocalisation, les applications haute définition (HD) de streaming vidéo dans une galerie plus grande longueur (i.e., > 100 m) en raison de sa capacité de formation de faisceau et de plus grande capacité. Pour aider le concepteur du système, il est nécessaire de connaître les informations de propagation du canal sans fil diffusé puisque le plancher de la galerie, le plafond et le mur ont différentes rugosités (i.e., > 5 mm). Cette thèse présente les résultats de la caractérisation du canal sans fil et la modélisation statistique à 60 GHz d'une mine souterraine à CANMET ayant des galeries dont la profondeur varie entre 40 m et 70 m. Depuis plus d'une décennie, les applications du système de communication sans fil sont exigeantes et augmentent rapidement pour fournir des services multimédias au public. Les résultats montrent que l'écart angulaire de la propagation par trajets multiples est inversement proportionnel à la distance entre l'émetteur et le récepteur. Un phénomène de dispersion solide est également observé dans le canal en observant l'angle de propagation des différents trajets. Des polarisations horizontales (H) et verticales (V) ont été utilisées puisque les diagrammes de rayonnement sont différents et peuvent fournir des comportements de dispersion temporelle différents. Les résultats montrent que l'antenne à polarisation verticale fournit un plus grand nombre de trajets multiples par rapport à polarisation horizontale et une valeur plus élevée de moyenne quadratique (RMS) par rapport à une horizontale. Par ailleurs, les mesures du coefficient de réflexion ont été effectuées pour étudier l'effet de dispersion de la surface rugueuse. Étant donné qu'aucun effet de regroupement sur le canal multitrajets n'a été observé, une approche de modélisation statistique a été considérée en tenant compte des différents trajets parcourus et leur amplitude. Par insertion des paramètres de hauteur de la surface de mesure, les modèles de diffusion connus ont également été analysés pour permettre la mise en œuvre d'une approche de modélisation du canal dispersif.

ABSTRACT

More than a decade, there is a surge in demand and development of wireless communication system applications to deliver multimedia services. Nowadays the research is focused on the design of high speed (i.e., 1 Gbps) wireless system particularly in dense areas such as conference room, shopping mall, stadium and open public events. Wireless local area network (WLAN) and cellular network are making high potential approaches to fulfill high data rate by using different advanced technologies such as coexistence between Long Term Evaluation Unlicensed (LTE-U) and Wi-Fi wireless channels. Moreover, the feasibility to use high-frequency spectrum (i.e., > 6 GHz), a physical layer research at 60 GHz for dense networks are highlighted where short-distance communication links (i.e., < 10 m) are required both in WLAN (i.e., WiGig) and cellular network (i.e., 5G small cell). However, the applications of 60 GHz bands is driven into underground wireless communication for higher precision geolocation, a High Definition (HD) video streaming applications in a larger gallery length (i.e., > 100 m) due to its beamforming capability and higher capacity. To assist the system designer, it is necessary to know the scattered wireless channel propagation information since the gallery floor, ceiling and walls consist of the different magnitude of the roughness (i.e., > 5 mm). This thesis presents the results of wireless channel characterization and statistical modeling at 60 GHz where the measurements were carried out in CANMET underground mine (40 m and 70 m gallery depths). Several measurements were conducted with different antenna configurations and polarizations. Results show that angular and temporal dispersion are proportional to the mine gallery dimensions. Results also show that the angular spread of the multipath is inversely proportional to the transmitter receiver separation distance. A strong scattering phenomenon is also observed in the channel by observing multipath angle of arrivals. The use of Horizontal (H) and vertical (V) polarizations were performed due to its different radiation pattern can provide a different temporal dispersion behavior. The results show that a vertically polarized antenna provides a lower value of path loss exponent and a higher value of root mean square (RMS) delay spread compared to a horizontal one. Since no clustering effect was observed, a statistical modeling approach with the multipath arrivals and amplitudes was considered. In addition, the reflection coefficient measurements were conducted to investigate the scattering effect from the rough surface. By inserting measured surface height parameters, the known scattering models were also analyzed to have an idea to implement a modeling approach of the scattered channel.

TABLE OF CONTENTS

DEDICATION	iii
ACKNOWLEDGEMENTS	iv
RÉSUMÉ	v
ABSTRACT	vi
TABLE OF CONTENTS	vii
LIST OF TABLES	xi
LIST OF FIGURES	xii
LIST OF ABBREVIATIONS	xviii
LIST OF APPENDICES	xxi
CHAPTER 1 INTRODUCTION	1
1.1 Basic overview	1
1.1.1 Research problem	1
1.1.2 Objective of the research	2
1.1.2.1 Specific objectives	3
1.1.2.2 Scientific hypotheses	3
1.1.3 Research methodology	3
1.1.3.1 Channel measurements-PHASE I	3
1.1.3.2 Channel characterization and modeling-PHASE II	4
1.1.3.3 Polarization and scattering analysis-PHASE III	4
1.1.4 Contribution based on state of the art	5
1.2 Short summary of results	6
1.3 Structure of the thesis	7
CHAPTER 2 STATE OF THE ART	8
2.1 Technological advantages at 60 GHz frequency	10
2.1.1 Ease to reuse frequencies due to the high signal attenuation	10
2.1.2 Minimize the electronic circuits package size	10

2.1.3	High data rates	10
2.2	60 GHz standards	11
2.3	60 GHz applications in indoor and outdoor	13
2.4	60 GHz applications in Underground Mine	13
2.5	Wireless propagation phenomena	15
2.6	State of the art of wireless channel characterization and model	16
2.6.1	Background study	17
2.6.2	Related underground mine measurements	18
2.6.3	Related 60 GHz indoor measurements with and without use of different antenna polarizations	19
2.6.4	Related antenna polarization measurements in underground mine	21
2.7	State of the art of scattering analysis	21
2.8	State of the art of scattering analysis based on reflection coefficients	22
2.9	State of the art of angular spread analysis	23
2.10	State of the art of channel modeling	23
2.11	Measurement approaches	24
2.11.1	Large scale ($< 10\text{ m}$ at 60 GHz) measurement approach	24
2.11.2	Small scale (1 cm^3) measurement approach	25
2.11.3	Scattering measurement approach	25
2.11.4	Angular dispersion measurement approach	25
2.11.5	Antenna polarization measurement approach	26
2.12	Difference between other CANMET 60 GHz experimental works	26
2.13	Summary and benefits of the thesis	27
CHAPTER 3	MEASUREMENT SETUP AND PROTOCOLS	28
3.1	Underground mine galleries and environment	28
3.2	Measurement setup and campaigns	30
3.3	Velmex 3D experimental table	33
3.4	mmWave measurement prerequisites for underground mine	33
3.5	Measurement protocols	35
3.5.1	Large scale	35
3.5.2	Small scale	35
3.5.3	Scattering	36
3.5.4	Angle of Arrivals (AoA)	36
3.6	PDP post processing procedure	36
CHAPTER 4	SCATTERING ANALYSIS	38

4.1	Scattering analysis based on Kirchhoff approximation (KA)	38
4.1.1	Kirchhoff scattering theory	38
4.1.2	Surface height characteristics	40
4.1.3	Height measurement	40
4.1.4	Roughness characterization	40
4.1.4.1	Height distribution	40
4.1.4.2	Height correlation	41
4.1.5	Scattered power measurement setup and procedure	43
4.1.6	Implementation and discussion	44
4.2	Scattering analysis based on reflection coefficients	46
4.2.1	Reflection models	47
4.2.1.1	Fresnel model	47
4.2.1.2	Gaussian rough surface scattering model	48
4.2.1.3	Modified Gaussian rough surface scattering model	48
4.2.2	Experimental setup and procedure	48
4.2.2.1	Procedure	49
4.2.3	Measurement results	49
CHAPTER 5 CHANNEL CHARACTERIZATION WITH DIFFERENT ANTENNA POLARIZATIONS		56
5.1	Large scale characterization with different antenna polarizations.	56
5.1.1	Post processing	57
5.1.2	Path loss	58
5.1.3	Interference fading	60
5.1.4	Delay spread	61
5.2	Small scale characterization	62
5.2.1	Channel parameters	63
5.2.2	Small scale fading and delay-spread statistics	63
5.2.2.1	Fading	63
5.2.2.2	Delay spread	65
5.3	Antenna polarizations effect	68
5.3.1	Comparison with other results	70
5.3.2	Impact of antenna polarizations on the scattered channel	71
5.3.2.1	Experimental explanations	73
5.3.2.2	Conceptual explanations	74
5.3.2.3	Geometrical explanations	75

5.4	Wireless InSite Simulation results	77
5.5	Rician K-factor and Co-polarization ratio results	80
5.5.1	K-factor	82
5.5.2	Co-polarization ratio	85
CHAPTER 6	ANGLE OF ARRIVAL ANALYSIS	88
6.1	Measurement setup and experimental protocol	88
6.1.1	Post processing	89
6.2	Angular dispersion characteristics	90
6.2.1	Angular spread	90
6.2.2	Angular constriction	91
6.2.3	Maximum fading angle	91
6.2.4	Maximum AoA direction	91
6.3	Results and discussions	91
6.3.1	70 m gallery results	92
6.3.2	40 m gallery results	95
6.3.3	Comparison with other experiments	98
CHAPTER 7	STATISTICAL MODELING	100
7.1	Modeling process	100
7.1.1	Path arrival modeling	102
7.1.2	Path amplitude modeling	102
7.1.3	Simulation of impulse responses	107
CHAPTER 8	CONCLUSION AND FUTURE WORK	109
8.1	Summary of measurement results	109
8.2	General conclusion	110
8.3	Future work	111
8.3.1	High frequency (e.g., 60 GHz) channel sharing	111
REFERENCES	114
APPENDICES	128

LIST OF TABLES

Table 2.1	IEEE 802.15.3c RF channel assignment.	12
Table 2.2	CANMET underground mine experimental results in Line of Sight (LOS). .	20
Table 2.3	Difference between other CANMET 60 GHz experimental works with this work	26
Table 3.1	Approximate dimensions of mine galleries.	30
Table 3.2	Parameters of 60 GHz channel measurements	32
Table 4.1	Comparison of reflection coefficients of Wall and Floor.	52
Table 4.2	Pathloss difference values of Wall and Floor in dB.	53
Table 5.1	Large scale measurement configurations	56
Table 5.2	Large scale measurement results.	59
Table 5.3	Small scale measurement configurations	62
Table 5.4	Small scale measurement results	66
Table 5.5	Comparison of CANMET underground mine experimental results.	71
Table 5.6	Channel simulation parameters	80
Table 5.7	Simulation results	81
Table 5.8	Rician distribution fitting of K-factor values (with Omni - Horn configura- tion at 40 m gallery)	85
Table 6.1	AoA statistical parameters of 70 m gallery according to transmitter receiver separation distances. Λ and γ are dimensionless, θ_{max} , max AoA and Lobe angles are in degree, Peak Avg. values are in dB.	93
Table 6.2	AoA statistical parameters of 40 m gallery according to transmitter recei- ver separation distance. Λ and γ are dimensionless, θ , max AoA and Lobe angles are in degree, Peak Avg. values are in dB.	96
Table 6.3	A comparison with different angle of arrival experimental results.	98
Table 7.1	Measurement configurations.	100
Table 7.2	Path amplitude model parameters for all configurations.	105
Table 7.3	Performance results compared to experimental RMS delay spread.	108
Table A.1	AoA statistical parameters of 70 m gallery according to transmitter recei- ver separation distance. Λ and γ are dimensionless, θ_{max} and Max AoA in degrees ($^{\circ}$).	128
Table D.1	LTE-U setup parameters and performance results at LTE-U	154
Table D.2	Setup parameters and performance results with Wi-Fi (5 GHz) channel . .	154

LIST OF FIGURES

Figure 1.1	Flow chart of the research problem.	2
Figure 1.2	General objective of the research.	3
Figure 1.3	Specific objective of the research.	4
Figure 2.1	An example of cmWave and mmWave networks.	9
Figure 2.2	Signal attenuation caused by oxygen and water vapour ($T=20^{\circ}\text{C}$. water content = $7.5 \text{ g}/\text{m}^3$)	11
Figure 2.3	Reflection, diffraction and scattering.	15
Figure 2.4	Block diagram of a channel model.	18
Figure 3.1	Measurement zone at 40 m level.	28
Figure 3.2	Measurement zone at 70 m level.	29
Figure 3.3	(a) 40 m and (b) 70 m galleries.	30
Figure 3.4	Measurement setup.	31
Figure 3.5	Illustration of the Velmex 3D table.	33
Figure 3.6	Large scale measurement procedure.	35
Figure 3.7	3D small scale measurement procedure.	36
Figure 4.1	Rough surface scattering geometry.	39
Figure 4.2	Rough surface scattering behaviour according to the value of roughness factor g	39
Figure 4.3	Wall surface height measurement at 40 m mine gallery.	41
Figure 4.4	Height measurement procedure.	41
Figure 4.5	3D color map of measured surface height distribution.	42
Figure 4.6	(a) CDF of measured surface heights (b) Auto correlation function of the heights $C(\tau)$	42
Figure 4.7	(a) Digital photograph for scattering measurement at 70 m mine gallery (b) Illustration of the measurement procedure.	43
Figure 4.8	3D kirchhoff scattering model for mine.	45
Figure 4.9	(a) Simulated angular dependent scattered received power (b) Measured and simulated scattered received power.	46
Figure 4.10	Rough surface reflection geometry.	47
Figure 4.11	Reflection measurement campaign of the floor.	50
Figure 4.12	Reflection measurement campaign of the wall.	50
Figure 4.13	Illustration of the Line of Sight signal measurement procedure.	50
Figure 4.14	Illustration of the reflected signal measurement procedure.	51

Figure 4.15	Channel impulse response of LOS signal for the wall surface.	51
Figure 4.16	Channel impulse response of REF signal for the wall surface.	51
Figure 4.17	Measured reflection coefficients for the wall surface.	53
Figure 4.18	Measured reflection coefficients for the floor surface.	53
Figure 4.19	Predicted reflection coefficients for the wall surface.	54
Figure 4.20	Predicted reflection coefficients for the wall surface with the special case of Kirchhoff model.	54
Figure 5.1	An example of a PDP.	57
Figure 5.2	Scatter plot of path loss as a function of Tx - Rx separation distance with different antenna and polarization configurations. (a) and (b) are the Horn-Horn configurations at 40 m and 70 m, (c) and (d) are the Omni-Horn at 40 m and Horn-Omni at 70 m gallery, respectively.	60
Figure 5.3	An example of shadow fading CDF fitted with the normal distribution at 70 m (Horn-Horn).	61
Figure 5.4	An example of correlation function of the frequency deviation at 70 m (Horn-Omni).	64
Figure 5.5	An example of a spatial distribution of total multipath power with $x \times y$ and $z = \lambda$ (which is aligned) for different antenna configurations. (a) 40 m (the upper plot is $D - D_{VV}$ and the lower plot is $D - O_{HH}$) and (b) 70 m (the upper plot is $D - D_{VV}$ and the lower plot is $D - O_{VV}$).	64
Figure 5.6	An example of a spatial distribution of total multipath power with $x \times y \times z$. (a) 40 m $D - D_{VV}$ and (b) 70 m $D - D_{VV}$	65
Figure 5.7	An example of small scale fading distribution with $D - O_{VV}$ configuration at 70 m.	66
Figure 5.8	(a) RMS delay spread values with different antenna configurations. Note : the measurements at 3 m Tx Rx separation distance consisting of 125 (5×5) points and (b) CDF of RMS delay spread values.	67
Figure 5.9	Scatter plot of time dispersion characteristics with different antenna and polarization configurations. (a) the number of multipath, (b) the RMS delay spread, with respect to Tx Rx separation distance.	69
Figure 5.10	CDF of RMS delay spread and coherence bandwidth (i.e. $B_{c0.9}$) in both galleries. (a) the RMS delay spread, (b) the coherence bandwidth.	70
Figure 5.11	The spherical coordinates of the transmitter and receiver antennas.	72
Figure 5.12	3D simulated Horn antenna radiation pattern with different polarizations with an approximation of the 70 m gallery dimensions. a) Vertical and b) Horizontal orientation, respectively.	73

Figure 5.13	An illustration of the LOS path and the scattered paths with Horn and Omnidirectional antenna configurations by considering a rough surface, where σ_h and ρ are the standard deviation of the surface heights and scattering coefficient, respectively. The θ_i and θ_r are the incident and reflected angles, respectively. The $\hat{\eta}$ is the tangent plane of the surface.	73
Figure 5.14	Measured 2D antenna radiation patterns with different polarizations. a) Horn and b) Omnidirectional (horizontal polarization - elevation direction). Note : in the vertical polarization (azimuth direction) of the Omnidirectional antenna consists between 0 dB and -3 dB.	75
Figure 5.15	Mine model (70 m gallery).	77
Figure 5.16	3D vertical Horn antenna radiation pattern.	78
Figure 5.17	3D horizontal Horn antenna radiation pattern.	78
Figure 5.18	3D antenna radiation pattern with different antenna configurations.	79
Figure 5.19	Illustration of the simulation results with different setups listed in Table 5.7	81
Figure 5.20	Number of the multipath components (with Omni - Horn configuration at 40 m gallery).	83
Figure 5.21	Kolmogorov-Smirnov test (KST) scores with different distributions of the number of multipath components for (a) the VV and (b) the HH configurations (with Omni - Horn configuration at 40 m gallery).	83
Figure 5.22	K-factor values (in dB) versus the transmitter receiver separation distance (with Omni - Horn configuration at 40 m gallery).	84
Figure 5.23	Rician distribution fitting of K-factor results (with Omni - Horn configuration at 40 m gallery) for (a) VV and (b) HH configurations.	84
Figure 5.24	CPR versus the transmitter-receiver separation distance.	86
Figure 5.25	Kolmogorov-Smirnov test for the measured CPR values.	86
Figure 6.1	AoA measurement procedure with Omnidirectional antenna at the Tx and directional horn antenna at the Rx.	88
Figure 6.2	Normalized PAPs according to transmitter receiver separation distance between 3.2 m and 4.4 m with a step of 40λ at 70 m gallery.	92
Figure 6.3	Normalized measured and simulated PAPs at 70 m level gallery. a) and (b) based on rough surface (with around 6 cm on magnitude) and zero roughness, respectively.	93
Figure 6.4	AoA simulation results with Omnidirectional antennas both at the Tx and the Rx at 70 m gallery.	94

Figure 6.5	Distribution fitting of relative path arrivals with respect to the angles at 70 m gallery. Superimposed by the best fitted Gaussian distribution ($\sigma_\theta = 14.33^\circ$) is illustrated in (a), (b) illustrates the Gaussian distribution fitting of 7 PAPs of different distances and (c) is the standard deviation of AoA according to Tx Rx separation distances.	96
Figure 6.6	Normalized PAPs according to the transmitter receiver separation distance of 3 m and 4 m at 40 m gallery.	97
Figure 6.7	Gaussian distribution fitting, $\sigma_\theta = 34.75^\circ$ at 3 m and $\sigma_\theta = 12.63^\circ$ at 4 m.	97
Figure 6.8	Measured normalized PAPs according to transmitter receiver separation distances of 3.2 m along the z directions with a step of $\lambda/2$ at 70 m gallery.	99
Figure 6.9	Measured PAPs at $z = 0$ for all Tx Rx separation distances.	99
Figure 7.1	An example of a PDP post processing. (a) the recorded signal, (b) peaks and inflection detection, (c) final detected dominant path and multipath, and (d) shifted power delay profile.	100
Figure 7.2	Flowchart of the statistical modeling.	101
Figure 7.3	Probability of path occupancy as a function of path index with different antenna polarization configurations. (a) and (b) are the 40 $m_{O-D_{HH}}$ and 40 $m_{O-D_{VV}}$ configurations, respectively.	103
Figure 7.4	An example of path arrival distribution of 40 $m_{O-D_{HH}}$ configuration, where N in the total number of cosidered path indexes without considering the first path occurance at first path index.	103
Figure 7.5	An example of path arrival distribution of 40 $m_{O-D_{VV}}$ configuration, where N in the total number of cosidered path indexes without considering the first path occurance at first path index.	104
Figure 7.6	An example of the MMSE of three distributions compare to measurement results of 40 $m_{O-D_{HH}}$	104
Figure 7.7	An example of the MMSE of three distributions compare to measurement results of 40 $m_{O-D_{VV}}$	104
Figure 7.8	An example of Kolmogorov-Smirnov (KS) test and corresponding K values with different antenna polarization configurations at 40 m. (a) and (b) are the HH and VV polarization of first path index according to the amplitude of 40 m_{O-D} configuration, respectively.	106
Figure 7.9	An example of normalized mean and standard deviation of amplitude with different polarization configurations of 40 m gallery. (a) and (b) are the mean and standard deviation of 40 $m_{O-D_{HH}}$, (c) and (d) are the mean and standard deviation of 40 $m_{O-D_{VV}}$, respectively.	106

Figure 7.10	An example of kolmogorov-Smirnov (KS) test and corresponding k values between measured and simulated RMS delay spread of 40 m _{O-D_{VV}} configuration.	107
Figure 8.1	LTE-U wired setup with Pico 6402 small cell product.	112
Figure 8.2	An example of a high frequency (i.e., 60 GHz) channel sharing scenario in an underground mine gallery.	113
Figure A.1	Normalized PAPs according to transmitter receiver separation distance at 3.4 m with different distances in z directions with a step of $\lambda/2$ at 70 m gallery.	129
Figure A.2	Normalized PAPs according to transmitter receiver separation distance at 3.6 m with different distances in z directions with a step of $\lambda/2$ at 70 m gallery.	129
Figure A.3	Normalized PAPs according to transmitter receiver separation distance at 3.8 m with different distances in z directions with a step of $\lambda/2$ at 70 m gallery.	129
Figure A.4	Normalized PAPs according to transmitter receiver separation distance at 4 m with different distances in z directions with a step of $\lambda/2$ at 70 m gallery.	130
Figure A.5	Normalized PAPs according to transmitter receiver separation distance at 4.2 m with different distances in z directions with a step of $\lambda/2$ at 70 m gallery.	130
Figure A.6	Normalized PAPs according to transmitter receiver separation distance at 4.4 m with different distances in z directions with a step of $\lambda/2$ at 70 m gallery.	130
Figure C.1	Simulation geometry (2D gallery height with Ceiling and Floor) with VV configuration based on the 70 m gallery dimension by using Vertical cross section between the antenna radiation pattern and the gallery height.	132
Figure C.2	Simulation geometry (2D gallery width Left Wall and Right Wall)) with VV configuration based on the 70 m gallery dimension by using Vertical cross section between the antenna radiation pattern and the gallery width.	132
Figure C.3	Geometry of scattered ray tracing simulation.	134
Figure D.1	Radio Dot System	138
Figure D.2	Pico RBS 6402	139
Figure D.3	BelAir 20E	140
Figure D.4	Ericsson AP 6321	140
Figure D.5	(a) Same frequency band allocation, (b) Different frequency band allocation.	142

Figure D.6	(a) Intra band (contiguous) (b) Intra band (non-contiguous) (c) Inter band (non-contiguous).	143
Figure D.7	LTE, LTE-U and Wi-Fi networks	144
Figure D.8	Receiver energy levels.	146
Figure D.9	An example of the duty cycle	147
Figure D.10	Primary explanation of CSAT.	147
Figure D.11	LTE-U setup with RDS.	150
Figure D.12	Real time QXDM output.	151
Figure D.13	Fair sharing output (Bandwidth monitor).	152
Figure D.14	Performance results. (a) and (b) are the fair sharing with TCP traffic and fair sharing output with UDP (post processed), respectively.	153
Figure D.15	Channel sharing with different percentage of duty cycle values.	155

LIST OF ABBREVIATIONS

dB _i	Decibel-isotropic
dB _m	Decibel-milliwatt
LOS	Line Of Sight
NLOS	Non Line Of Sight
AOA	Angle Of Arrival
LRTCS	Le laboratoire de Recherche Télébec en Communications Souterraines
CANMET	Canada centre for Mineral and Energy Technology
RMS	Root Mean Square
CPR	Co-Polarization Ratio
RF	Radio Frequency
SNR	Signal to Noise Ratio
mW	MilliWatt
Mbps	Mega bit per second
Gbps	Giga bit per second
MB	Mega Byte
WLAN	Wireless Local Area Network
MIMO	Multiple Input Multiple Output
eNB	Evolved NodeB
3GPP	3rd Generation Partnership Project
5GPPP	5G Infrastructure Public Private Partnership
TG3	Task Group 3
CQI	Channel Quality Indicator
CA	Carrier Aggregation
HARQ	Hybrid Automatic Repeat Request
PHY	Physical
MAC	Medium Access Control
LTE-U	Long Term Evolution - Unlicensed
LTE-A	Long Term Evolution - Advanced
LBT	Listen Before Talk
HetNet	Heterogeneous Network
UE	User Equipment
UNII	Unlicensed National Information Infrastructure
HDTV	High Definition TV

WiGig	Wireless Gigabit Alliance
HDMI	High-Definition Multimedia Interface
PAL	Phase Alternating Line
PPDU	PLCP Protocol Data Unit
PLCP	Physical Layer Convergence Protocol
TxOP	Transmission Opportunity
3D	Three Dimension
OFDM	Orthogonal Frequency Division Multiplexing
Tgad	Task Group ad
BW	Bandwidth
GO	Geometrical Optics
UTD	Uniform Theory of Diffraction
TOA	Time Of Arrival
VNA	Vector Network Analyzer
SOLT	Short-Open-Load-Thru
PL	Path Loss
LP	Linear Polarization
CP	Circular Polarization
VV	Vertical Vertical
HH	Horizontal Horizontal
VP	Vertical Polarization
HP	Horizontal Polarization
HPBW	Half Power Beam Width
EM	ElectroMagnetic
IFBW	Intermediate Frequency Band Width
PDP	Power Delay Profile
IFFT	Inverse Fast Fourier Transform
KA	Kirchhoff Approximation
KST	Kolmogorov Smirnov Test
ACF	Auto Correlation Function
CDF	Cumulative Density Function
RCS	Radar Cross Section
REF	REflected Signal
UWB	Ultra Wide Band
SISO	Single Input Single Output
PDF	Probability Density Function

PAP	Power Angular Profile
RAT	Radio Access Technology
DC	Duty Cycle
CSAT	Carrier Sensing Adaptive Transmission
RTT	Round Trip Time
PoE	Power over Ethernet
BF	Beam Forming
RAN	Radio Access Network
CC	Component Carrier
FDD	Frequency Division Duplex
ED	Energy Detection
RBS	Radio Base Station
CS	Carrier Sense
RB	Resource Block
RSSI	Received Signal Strength Indicator
AP	Access Point
QXDM	Qualcomm eXtensible Diagnostic Monitor
QCAT	QualComm log Analysis Tool
RDS	Radio Dot System
DU	Digital Unit
IRU	Indoor Radio Unit
STA	STAtion
UDP	User Datagram Protocol
TCP	Transmission Control Protocol
RE	Resource Element
VoIP	Voice over Internet Protocol

LIST OF APPENDICES

Appendix A	ANGULAR DISPERSION RESULTS	128
Appendix B	DYNAMIC THRESHOLD	131
Appendix C	SCATTERING SIMULATION PROCEDURE	132
Appendix D	LTE-U SMALL CELL AND WIFI CHANNEL SHARING EXPERIMEN- TAL INFORMATION	135
Appendix E	LIST OF PUBLICATIONS	156

CHAPTER 1 INTRODUCTION

1.1 Basic overview

Wireless communication systems at 60 GHz are new wireless gigabit transmission phenomena for short range multimedia communication [1]. Due to the low data rate and the interference problems, the lower frequency bands do not allow the degree of freedom to design a high-speed wireless communication system for short-range distances. In the underground mine environment, the use of 60 GHz band is important due to its 5 mm wavelength, large bandwidth, possibility of frequency reuse and large scale path loss [2]. A wireless communication system designed for this wavelength is extremely dependent on the propagation channel, environment and angle of arrival of the multipath. The roughness of the underground mine surface that produces scattering is a dominant factor in the system design perspective. The objective of the thesis is to study the characteristics of the scattered propagation channel at 60 GHz in an underground mine and in order to provide channel modeling tools for propagation prediction.

1.1.1 Research problem

Wireless channel measurements and modeling at 60 GHz are of interest for communication researchers, particularly in an underground mine environment. During the last few years, 60 GHz radio frequency (RF) modules are being developed in industries and research centers, but not yet been commercialized so far for all environments application perspectives. The challenges involved for the channel characterization in the experimental mine (i.e., CANMET) are summarized below :

Measurement campaigns

Measurement campaign procedure at 5 mm wavelength at 40 m and 70 m mine gallery due to the existence of a some roughness of the gallery floor.

Investigation of scattering effect

Measurement campaign and investigation of the scattering phenomenon and establishing a scattered channel modeling approach.

Investigation of polarization effect with different antennas

Investigation of the effect of a wireless multipath channel with different antennas (such as directional and omnidirectional) and different polarizations.

Investigation of multipath angle of arrivals

Investigation of angular dispersion measurements, and the characterisation of the multipath arrivals and the analysis of the scattering existence.

Statistical modeling of the channel

Investigation of the statistical modeling complexities due to the differential results of the number of multipath, multipath arrivals and amplitudes (due to the use of antenna polarizations and lower number of multipath).

The challenges are to study the scattering and polarization effects on the scattered channel which could provide different radio propagation behavior as compared to the smooth surface due to the different dimensions of the galleries and different roughness magnitudes of the wall, floor and ceiling of the surface. The scattered wave (coherent and incoherent field components), both in specular and non-specular direction, results in the extreme time variations and unpredictability. Therefore, the scattering and polarization investigations could provide a new research aspect of the feasibility to use dual or single polarized antennas. In general, 60 GHz dual antenna polarized antenna may offer an advantage in this particular environment since the polarization may change due to roughness. Hence, wireless propagation phenomena such as reflection, diffraction, and scattering make major contributions at this small wavelength in which the phase shifts by 180 degrees for every 2.5 mm in the propagation direction. Therefore, in an underground mine, for communication system design perspective at 5 mm wavelength, the physical phenomena of scattering, angular dependencies of the multipath profile and wireless channel behavior with different antennas and with different polarizations are required to be investigate in order to find a scattered channel modeling approach. As a summary, the flow chart of the research problem is illustrated in Fig. 1.1.

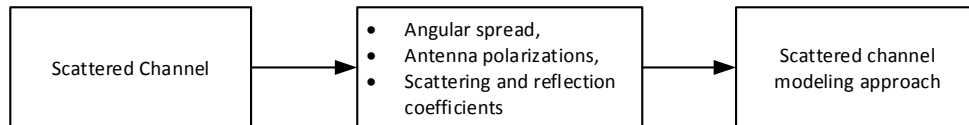


Figure 1.1 Flow chart of the research problem.

1.1.2 Objective of the research

Scattered wireless channel characterization and modeling at 60 GHz provide a contribution on wireless communication system design in underground mine environment in which system designer will be informed particularly the channel information with different antennas and polarizations. Fig. 1.2 shows the generalized flowchart of the research objective.

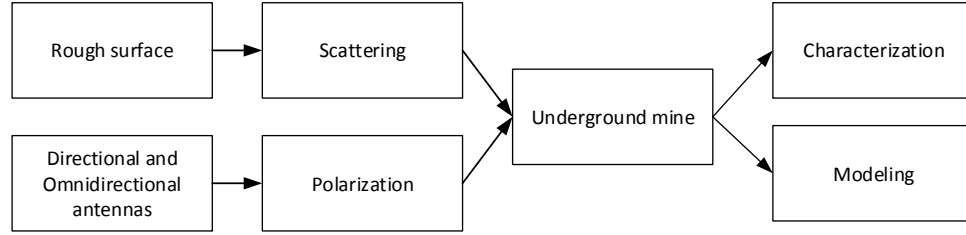


Figure 1.2 General objective of the research.

1.1.2.1 Specific objectives

To characterize and model the scattered channel, the following specific objectives are given below :

- Perform 60 GHz channel measurements in an underground mine.
- Characterize 60 GHz channel with different antennas and polarizations.
- Estimate the angular spreads and characterize the multipath angular dependencies.
- Estimate the reflection coefficients of the mine surface and include it into the scattering modeling approach.
- Develop a statistical channel model.
- Analyze the experimental results and make a conclusion and propagate new research issues.

In contrast, the flowchart of the research objectives is illustrated in Fig. 1.3.

1.1.2.2 Scientific hypotheses

- Hypothesis 1 : Different antenna polarizations will provide the feasibility to use of dual or single polarized antenna and polarization diversity. The use of different antennas, such as directional and omnidirectional, will provide the feasibility of beamforming in underground mine.
- Hypothesis 2 : Statistical channel model will provide a concept of channel modeling approach in underground mine.
- Hypothesis 3 : Scattering and reflection coefficients measurement results will provide an estimated scattered wireless channel information.

1.1.3 Research methodology

1.1.3.1 Channel measurements-PHASE I

- Setup : A Vector Network Analyzer (VNA) for wideband measurements in underground mine was used to perform the measurements. A 3D movable table was used in the mine gallery to have accurate measurements with 5 mm wavelength for the antenna rotation and grid movement for

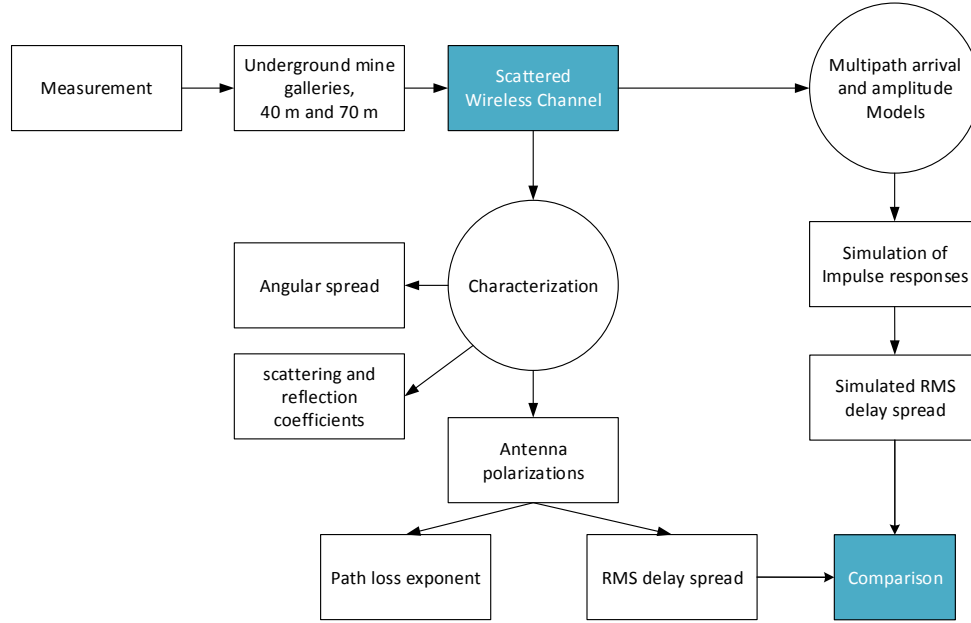


Figure 1.3 Specific objective of the research.

the large scale and small scale measurements.

- Procedure : The objective of the measurements is to have the Power Delay Profile (PDP) according to different transmitter receiver separation distances.
- Validation : The channel parameters were extracted from the measurement results and compared with previous works.

1.1.3.2 Channel characterization and modeling-PHASE II

- Characterization : The fundamental idea in this approach was to extract scattered channel statistical parameters such as path loss exponent, delay spread, angular spread and reflection coefficients.
- Modeling : Considered statistical modeling approach in order to generate impulse responses of the channel is based on scattered path arrival and amplitudes. Reflection and scattering coefficient results could perform an integration into a deterministic modelling approach.

1.1.3.3 Polarization and scattering analysis-PHASE III

- Polarization issue : Polarization is a property of EM waves that describes the orientation of electric field E and magnetic intensity H in space and time. In order to find the polarization impact on the scattered channel, channel information with different antenna polarizations are required.

The reflection coefficients are different since E field component is parallel and perpendicular to the plane of incidence for vertical and horizontal polarization of the antennas, respectively.

- Scattering issues : The scattering from the rough surfaces on a specular and non specular reflections were considered as the impact of scattering on the channel. Scattering coefficients were estimated by known scattering models based on the reflection coefficient measurement results. Particularly, Kirchhoff scattering approach were considered with a single ray concept for the floor and the wall of the gallery.

1.1.4 Contribution based on state of the art

Concerning the public demand at present and future, 60 GHz wireless communication promises potential contribution for home and particularly confined environments such as underground mine where the high-speed data transfer over the wireless channel is about the main concern. Among other major applications of the 60 GHz, HD video streaming and remotely controlling of heavy vehicles are highly elevated. These applications can contribute to wireless communication system design for the underground mining industry. This is to note that the difference between home and underground mine is the rough surface and narrower passages of the gallery.

The core contribution of the thesis is to characterize (such as power distance relationship and multipath delay spread) the 60 GHz channel based on the measurements of different underground mine gallery depth levels in large (less than 10 m) and 3D small scale (10 mm^3) cases. Polarization effect due to the use of different antenna polarizations is highlighted as the first-degree contribution of this thesis. Scattering effect based on reflection coefficient measurements and angular discrepancies of multipath arrivals is considered as the second-degree contribution of the thesis. Simulation of impulse responses of the channel based on the statistical parameters of the measurement results and comparison between different amplitude distributions by curve fitting techniques are considered as a third-degree contribution of the thesis.

Therefore, the contributions compared with other works are given below :

- Use of different CANMET mine galleries.
- Use of directional and omnidirectional antennas.
- Use of 3D small scale (10 mm^3) measurements.
- Use of vertical and horizontal antenna polarizations.
- Scattering and reflection coefficients measurements.
- Angle of arrival measurements.
- Statistical channel model with vertical and horizontal antenna polarizations.

Thesis keywords : 60 GHz wireless channel measurements, angle of arrivals, antenna polariza-

tions, scattering and reflection coefficients and statistical modeling.

1.2 Short summary of results

Measurements have been carried out in CANMET underground mine at both 40 m and 70 m gallery depths.

The summary of the large scale measurement results : The results of the two levels show that the larger gallery dimension provides higher root mean square (RMS) delay spread values. Waveguide effect is mostly dominant with vertically polarized antennas in both galleries. Directional antenna with vertical polarization provides higher number of multipath than horizontal polarizations. For statistical model, multipath arrivals and amplitudes of each time index are best fitted for modified Poisson and lognormal distributions, respectively.

The summary of the small scale measurement results : 3D (5 m×5 m×5 m) Measurement results show that the small scale fading ranges from 1 to 2 dB and 3 to 5 dB for Horn - Horn and Horn - Omni antenna configurations, respectively. Results of the Horn - Horn configuration yield lower values of RMS delay spread than those of the Horn - Omni or Omni - Horn antenna configurations. 70 m gallery is more time disperse than 40 m gallery. Rician distribution is fitted with small scale fading.

The summary of the scattering measurement results : Surface roughness measurements show that the maximum, mean and standard deviation of the wall heights are 37.5 cm, 20.5 cm, and 6.0658 cm, respectively. The correlation length of the heights is found to be 84 cm. The scattered power loss is not insignificant and originated around the specular direction from wall and floor surface. Based on these results a channel modeling approach is initiated with known Kirchhoff scattering Approximation.

The summary of the polarization measurement results : In the considered mine environment, the surface walls, floor, and ceiling have different values of roughness. The results show that the use of different antenna polarizations has a direct impact on the radio propagation channel due to antenna radiation pattern. Moreover, the VV (transmitter as vertical and receiver as vertical) antenna polarization configuration offers a larger number of multipath components than the HH (transmitter as horizontal and receiver as horizontal) one. A correlation coefficient between VV and HH is found to be about 0.86, and an average co-polarization ratio (CPR) of about 6 dB. The average value of the Rician K-factor shows little difference between the HH and VV polarizations but higher standard deviation is observed with VV than HH.

The summary of the angle of arrival measurement results : The angle of arrival measurement results are in the azimuth directions and show that a higher gallery dimension provides a higher

value of angular spread. The angular spread value lies around 14.3° (3.2 m - 4 m) at 70 m and 34.75° (3 m), and 12° (4 m) at 40 m gallery. Estimated multipath shape factor values do not severely change within a short distance (3.2 m to 4.4 m). A simulation scenario (with smooth surface) of 70 m gallery is compared with measurements (rough surface). Based on multipath angular dispersion the comparison results show that the scattering exists with 5 mm wavelength.

1.3 Structure of the thesis

The Thesis is organized as follows : Chapter 2 presents the state of the art of the thesis. Chapter 3 describes measurement setup and protocols. Chapter 4 provides the reflection and scattering coefficients measurement results, analysis, and modeling approaches. Chapter 5 provides the channel characterization with different antenna polarizations. Chapter 6 discusses angular dispersion measurement results. Chapter 7 provides statistical modeling of the channel. Finally, chapter 8 consists of the conclusion of the thesis, the future work and an analysis of the extension of a possible future work based on LTE-U and Wi-Fi channel coexistence measurement results.

CHAPTER 2 STATE OF THE ART

Wireless Local Area Network (WLAN) standards IEEE 802.11a and 802.11b provide the connectivity in indoor and outdoor environments. The speed of the wireless system is relatively low about 54 Mbps at 5 GHz and 11 Mbps at 2.4 GHz for 802.11a and 802.11b, respectively and does not satisfy the current public demand. IEEE 802.11g is introduced with the maximum data rate of 54 Mbps. Later in 2009, with maximum single channel data rate of 100 Mbps, the 802.11n standard with MIMO technology is introduced to carry with 4 physically separated transmitter and receiver antennas.

In recent decades, wireless systems at 60 GHz was planned to be used in a wide variety of applications including the establishment of access networks. In the spectrum of millimeter wave, however, the band around 60 GHz has major advantages, especially regarding unlicensed regulations and allocation of frequencies. In Europe, European Radiocommunications Board (ERO) proposes to reserve the band 59-62 GHz for WLAN applications. In the US, the 59-64 GHz band can be used for mobile applications without having a license. In Japan, a band from 59 GHz to 66 GHz is available for general wireless applications with or without a license. The first prototype of WLAN at 60 GHz was conducted in Japan in 2000 with a gross rate of 51.84 Mbps [3].

Since last decade, millimeter wave communication systems appear as a promising solution for new types WLAN and cellular networks. A significant amount of theoretical and experimental studies in millimeter wave frequency band have been conducted on wireless channel characteristics and modeling in confined environments such as underground mines and tunnels. An outdoor propagation measurement campaign at 28 GHz has been conducted in New York City to find a channel model as reported in [4]. Proposed statistical model for the large scale parameters between 28 GHz and 73 GHz are compared in [5]. Frequency spectrum, such as 28 GHz, 38 GHz, 60 GHz, 70 GHz, 80 GHz and 90 GHz are providing tremendous research opportunities for future cellular and WLAN communications.

There is a possibility to use cmWave and mmWave combined with cellular, WLAN, Internet of things (IoT) network as illustrated in Fig. 2.1. Transferring those frequency bands into confined environments such as railway tunnels and underground mines is creating a new research domain, particularly in wireless channel propagation.

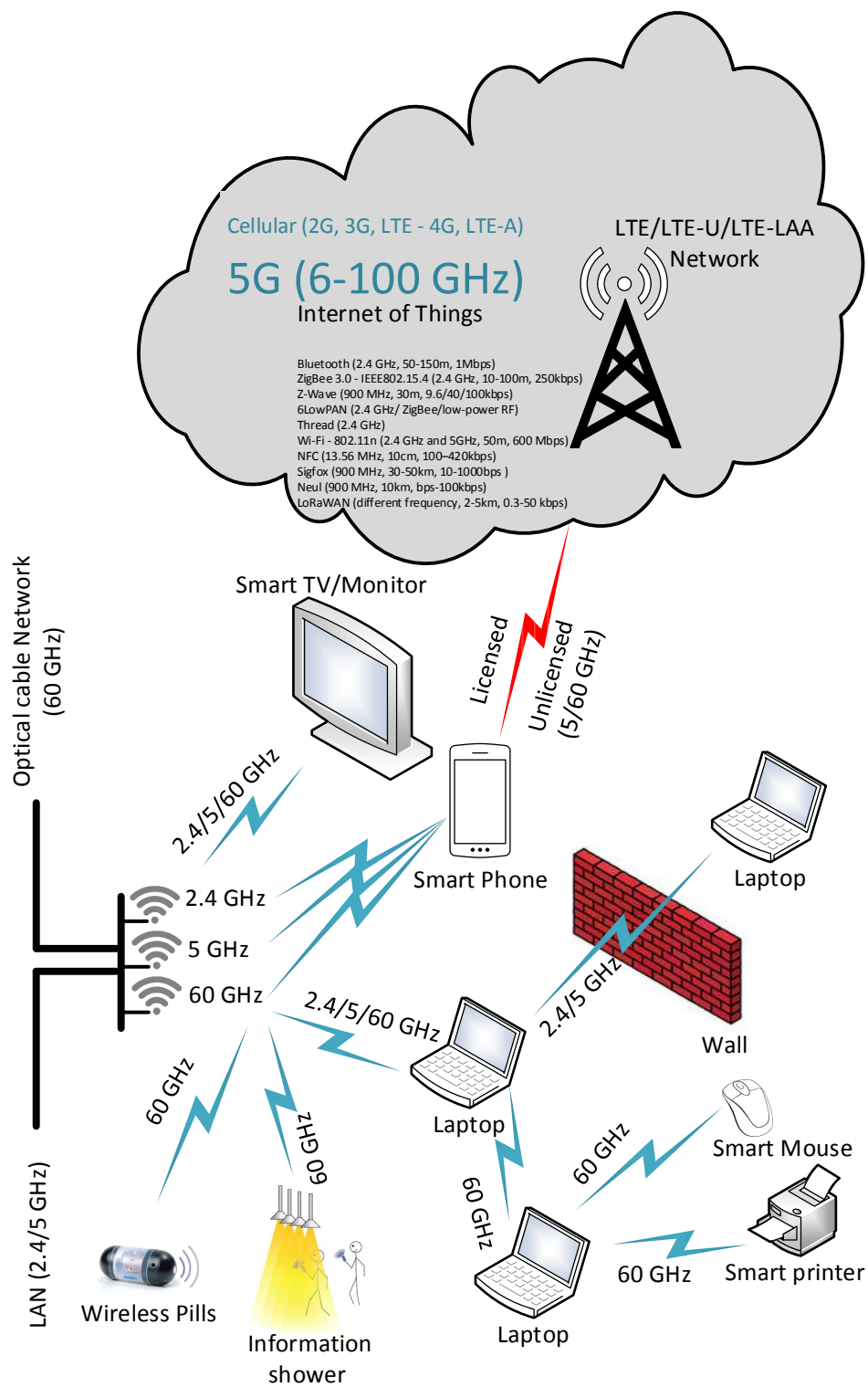


Figure 2.1 An example of cmWave and mmWave networks.

2.1 Technological advantages at 60 GHz frequency

2.1.1 Ease to reuse frequencies due to the high signal attenuation

The signal attenuation due to free space path loss (PL) propagation at distance d is given by [6] :

$$PL(d) [dB] = 10 \log_{10} \frac{P_t}{P_r} = -10 \log_{10} \left[\frac{G_t G_r \lambda^2}{4\pi^2 d^2} \right] \quad (2.1)$$

The description of equation 2.1 is defined in [6] and noted that the free space propagation loss is 20 dB / decade (20 dB loss for 10 m transmitter receiver separation distance) with 5 mm wavelength. Moreover, due to oxygen (O_2) absorption, the signals at 60 GHz is attenuated more than 12 dB / Km in addition with the free space [7] as shown in Fig. 2.2 and the O_2 absorption at 60 GHz at 7 m is around 20 dBm. The Fig. 2.2 gives an idea to investigate if there is any theoretical observation of additional losses at 60 GHz due to O_2 and H_2O in underground mine environment where 100% humidity exists. The additional oxygen absorption loss along with the free space loss reduce the range of 60 GHz communication systems and reduces the interference for a condensed network compared with range of lower frequencies. So, it permits the reuse of the spectrum and thus a better use of resources. This is to note that the path loss due to water vapour (wv) can be calculated as $L_{wv}(dB) = V \text{ (dB/Km)} \times d \text{ (Km)}$ [7] where V is the absorption value due to water vapour and d is the distance. With 42% of humidity, a temperature of 20°C and a vapour concentration 7.5 g/m^3 , the water vapour absorption is 0.1869 dB/Km. With 100% humidity and 20°C temperature, the vapour concentration is found to be 12.85 g/m^3 . Thus, the water vapour absorption is calculated as 0.42 dB/Km which is negligible for a short range distance (<10 m). The temperature with 6°C also makes negligible signal attenuation at 60 GHz. The penetration losses with brick and concrete walls are > 20 dB [7] which may have an advantages for small cell deployment.

2.1.2 Minimize the electronic circuits package size

The size of the components (antennas, RF circuitry lines) is directly related to the wavelength of operation of the circuit. Circuits operating at 5 mm wavelength which reduces the size of the system design.

2.1.3 High data rates

The capacity is related to the system bandwidth according to Shannon [8] given by the following equation

$$C = W \log_2(1 + SNR) \quad (2.2)$$

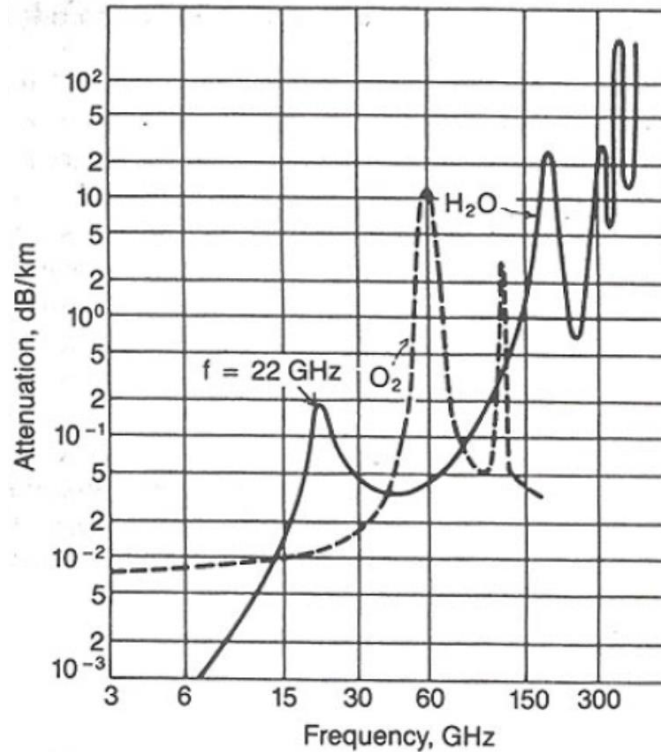


Figure 2.2 Signal attenuation caused by oxygen and water vapour ($T=20^{\circ}\text{C}$, water content = 7.5 g/m^3)

where C is the capacity, W is the bandwidth, SNR is the received signal to noise ratio. Since the 60 GHz technology uses high system bandwidth (i.e., around 2 GHz), a high data rate with a reasonable SNR is guaranteed.

2.2 60 GHz standards

IEEE 802.15.3c

The task group 3 (TG3) of IEEE 802.15 was mandated to develop a high rate ($>20 \text{ Mbps}$) wireless personal area networks (WPAN) in 2003. Three different physical layer specifications have been defined in 2009 [9]; a single carrier (SC) mode, a high speed interface (HSI) mode and an audio/visual (AV) mode. The SC and HSI modes use phase shift keying (PSK) or quadrature amplitude modulation (QAM) where AV mode uses orthogonal frequency division multiplexing (OFDM). The SC/HSI modes are considered for lower power battery operated equipment such as phone, camera, etc. whereas AV mode better deals with multipath distortion which can offer greater coverage. However, IEEE 802.15.3c standard with SC is aimed at Gbps data transfer over a few meters in 2009 [1]. The IEEE 802.15.3c radio

channel assignments are shown in Table 2.1.

Table 2.1 IEEE 802.15.3c RF channel assignment.

Channel	Start frequency	Center frequency	Stop Frequency
1	57.240 GHz	58.320 GHz	59.400 GHz
2	59.400 GHz	60.480 GHz	61.560 GHz
3	61.560 GHz	62.640 GHz	63.720 GHz
4	63.720 GHz	64.800 GHz	65.880 GHz

WirelessHD

WirelessHD was founded to promote a specification for consumer electronics for short range (10 m) high definition multimedia data transmission over an ad-hoc network at 60 GHz frequency band. In April 2010, the standard specified a physical layer capable of 7.138 Gbps and enhanced by using 4x4 spatial multiplexing techniques to reach a 28.552 Gbps [1, 10].

ECMA-387

The first edition of the ECMA-387 high rate 60 GHz PHY, MAC and HDMI PAL standard for short-range unlicensed communications was published in December 2008 and the second edition in 2010. Based on the complexity and power consumption, three types of devices (i.e. Type A, Type B and Type C) were specified. Type A represented the most complex and power-hungry device type, intended to deliver video/data even without LOS by employing a beamforming technique. Type B represented moderate complexity and power consumption devices and designed to deliver video/data in LOS without using beamforming. Finally, Type C devices are the least complex and have the lowest power consumption, and has been designed for data delivery over the very short range (less than 1 meter). The ECMA-387 defines four radio channels with a separation of 2.160 GHz [11].

Wireless Gigabit Alliance / WiGig

In 2009, the wireless Gigabit Alliance was aimed to develop specifications for audio/video and data transmission for personal computers, consumer electronics, and mobile industries in 60 GHz frequency band [12].

IEEE 802.11.ad

Task group ad (Tad) of IEEE 802.11 developed a standard for wireless local area network (WLAN) based on the modification of 802.11 MAC and PHY layer to enable their operation at 60 GHz frequency band. WiGig defined a short range (1 m - 10 m) wireless data transfer at a data rate up to 6.75 Gbps over an ad-hoc network. LOS to NLOS switching operation

is using beam steering techniques for higher data rate. In 2012, the final specification was published [13]. More information is provided in Appendix D.

2.3 60 GHz applications in indoor and outdoor

Radio at 60 GHz has technological advantages to provide a high speed data service than the lower frequencies. Some applications such as uncompressed high definition (HD), video streaming, synch and go file transfer and wireless gaming [14] have been discussed in various standards and industry alliances. Uncompressed video streaming is emerging as one of the most attractive application [1]. The 60 GHz indoor/outdoor applications are given below :

1. Wireless Display
 - Projection in conference room, auditorium etc.
 - In-room gaming.
 - Streaming from camcorder.
 - Professional HDTV.
2. Distribution of HD video
 - Video streaming around the home.
 - Large vehicle applications (e.g. airplane, ferry).
 - Wireless networking for office.
 - Remote medical assistance.
3. Rapid upload/download
 - Rapid file transfer/sync.
 - Downloading movie content to mobile device.
 - Police surveillance data transfer.
4. Backhaul
 - Mesh backhaul
 - Point-to-point backhaul
5. Outdoor
 - Real time video communication in stadium.
 - Public safety.

2.4 60 GHz applications in Underground Mine

Nowadays, the short range wireless communication offers huge possibilities to provide seamless multimedia services. Recently, the 60 GHz band has generated significant interest because of expected high data rates (i.e. > 1 Gbps) for short range communications in indoor environments [15].

Consequently, the utility of wireless communication is essential requisite particularly for safety and productivity in an underground mine [16, 17]. Along with the multimedia (Voice, Video, and data) service, wireless communication is used for geolocalization of miners and equipment, real-time portable video monitoring, speedy rescue operation of trapped miners under debris in this particular environment. For instance, a vehicular wireless communication system could provide, data communication between a central server and mobile vehicles, as well as vehicle to vehicle cooperative communication solutions when an accident or disaster is a concern. Along with the use of well-known TTE (Through The Earth) systems for vehicle tracking, monitoring, and controlling in the mining industry, other systems such as Radio-Frequency IDentification (RFID), Zigbee wireless systems, the Wireless Sensor Network (WSN), and Wi-Fi systems are also convenient for these purposes. Possible vehicular location tracking solutions could be implemented with a chip or tags implemented in miners bodies or installed in moving machines [18]. The use of the Internet of Things (IoT) and aerial drones is also a possible future application for a faster wireless safety system. However, the lower frequency bands are not enough to provide a large amount of multimedia services to a dense network in a larger gallery length. The Tri-band (2.4 GHz, 5.8 GHz and 60 GHz) solutions however could provide a reliable wireless system to fulfill the mining industry requirements. Therefore, it is important to find a suitable frequency for the required services including the optimum attenuation, lower interference, and high accuracy of geolocation in a dense network, which will help to design a scalable wireless communication device for underground mining environment.

At the 60 GHz band, the features such as low interference, unlicensed spectrum, larger bandwidth, low-cost, smaller chip scale package size, phase array and beamforming capability could possibly fulfil many of the mining industries demands, particularly for a dense mesh network in a larger tunnel length (i.e., > 100 m), where a compatible high speed (i.e., > 1 Gbps) wireless system is necessary. In this kind of hazardous confined environment a 60 GHz band is most suitable, for a network with small cell mobile backhaul to be used, and for applications such as video monitoring, remote control of vehicles, real-time mobile 3-D mapping and creating virtual environments, cooperative robotic system for remote operation of mineral extraction, etc. Particularly, a 60 GHz band could improve scalability and extension of future cooperative robotic system development for vehicular applications.

High camera resolution requires high-speed data transmission that may be possible with high bandwidth. The frequency window around 60 GHz band can also play an important role since it has unlicensed 7 GHz bandwidth. High camera resolution images can also be useful for extracting mineral examination by using advanced image processing techniques. On the other hand, since short distances are involved, a 60 GHz system uses low power consumption, which is an advantage in underground mine tunnels, since the deployment of the power supply is a complicated process. On

the other hand, low-cost and low-power 60 GHz phased array small cell technology is of interest for mobile backhaul particularly in this confined environment.

However, the 60 GHz band suffers from dispersion, absorption, scattering, and attenuation due to its 5 mm wavelength, and the heterogeneous and complex structure of the mine surface creates further complication in terms of radio propagation.

2.5 Wireless propagation phenomena

In wireless communication, the radio channel can be described as a multipath propagation channel where signals reach the receiver antenna by two or more paths [7]. The propagation of radio waves is generally described with three basic mechanisms, such as reflection, diffraction, and scattering of electromagnetic waves from various objects in the propagation environment. Propagation models are particularly based on the physics of reflection, scattering, and diffraction. These three propagation mechanisms of electromagnetic waves are shown in Fig. 2.3 corresponding to the underground mine rough surface. At 60 GHz, the wavelength is 5 mm, and thus any object of the rough surface larger than 5 mm can be considered as a flat surface. Since surface roughness is irregular, three propagation phenomena can perform randomly, since within a small scale area ($< 1 \text{ cm}^2$) the object could be larger than λ or lower than the λ or larger than λ with sharp edges, but it is expected to have mostly scattering. Therefore, due to surface roughness a single reflection, multiple reflections and diffractions as well as scattering can be present during the interaction of an electromagnetic (EM) wave on the mine surface.

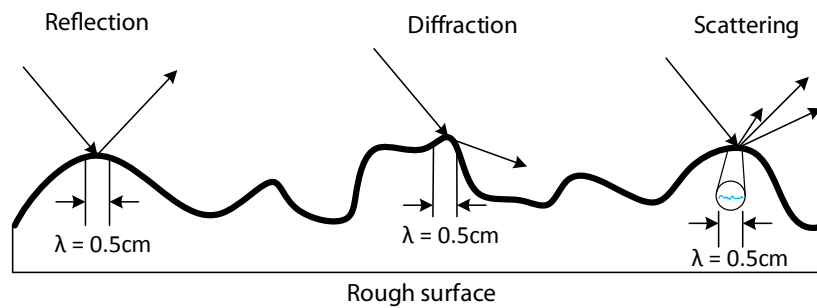


Figure 2.3 Reflection, diffraction and scattering.

Reflection

Reflection occurs when an electromagnetic wave interacts on a large dimension of an object compared to the wavelength. It can change the direction according to the Fresnel reflection

law. It also depends on the permittivity, permeability, conductivity as well as the incident angle. Reflection can be modeled using the Geometrical Optics (GO) theory. The Fresnel reflection coefficients (Γ) for smooth surfaces provide only the specular reflections which is related to the material properties, incident angle (θ_i), polarization (vertical, horizontal) of the wave and the frequency as defined in [6, 19].

Diffraction

Diffraction appears when any obstacle comes between transmitter and receiver during electromagnetic wave propagation. Basically it happens when a radio wave interacts sharp irregularities (edges) of a dense obstacle with large dimensions compared to the propagated wavelength shown in Fig. 2.3. As a result, diffracted waves arise in any possible direction from the surface. It is possible that the diffracted waves bend around the obstacle and provide an almost artificial LOS between transmitter and receiver [7]. Diffraction phenomenon particularly depends on the geometry of the surface object, incident angle, amplitude, phase as well as the polarization of the incident wave. Diffraction can be modeled using the Geometrical Theory of Diffraction (GTD) or the Uniform Theory of Diffraction (UTD) [6].

Scattering

Scattering is the most important phenomenon, particularly at high frequency wave propagation environments. It happens when the object dimensions are small compared to the wavelength and where the number of obstacles per unit volume is large. In other words, scattering is an interaction between an electromagnetic wave and an arbitrarily shaped obstacle. Larger than the wavelength and regularly shaped objects can be demonstrated using reflection and diffraction approximations, and only smaller than the wavelength and irregularly shaped objects cause scattering [6]. During scattering, the incident energy is distributed in all angular directions in coherent and incoherent ways and it is difficult to compute those directions using deterministic ray optical theories.

2.6 State of the art of wireless channel characterization and model

Prior to design a wireless system and predict its capacity, it is required to have the channel characterization and modeling. Multiple radio waves usually travel over different paths in the propagation medium due to reflection, diffraction and scattering phenomena in different directions, delays and amplitudes. This is indeed called multipath propagation and the channel is the multipath channel. If the surface is rough enough to scatter, the reflected, scattered and diffracted paths may be added constructively or destructively at the receiver which provides signal power variations.

Multipath channel characterization and modeling perform major contribution for any wireless system design [1, 14, 20]. Radio wave propagation, particularly in an underground mine is very com-

plex in nature and diverse in practice, which makes it an interesting research problem especially at 5 mm wavelength. It is required to have a realistic channel model in order to properly capture the key channel effects and to have a simple model. A radio channel model can provide particular information of RF propagation and also allows to examine and theoretically predict the system performance without having further experiments.

In the context of the 60 GHz channel, wideband (i.e., around 2 GHz bandwidth) systems are considered in general. Directional antenna concepts are usually used for this kind of design. Moreover, the polarization and scattering effects are challenging to investigate the channel characterization in a practical point of view as the scattering makes multipath arrivals in different directions at the receiver and the polarization of the signal at the receiver depends on the material properties, the incident angles and the geometry of the object which performs scattered wave.

There are different modeling approaches reported in the literature. Reflection from the floor, wall and obstacle, and diffraction around the corner of the furniture are major constraints to simplify a channel model. In general, there are two categories of modeling, namely deterministic and stochastic models [1, 14]. Deterministic model approaches can be further divided into subgroups such as empirical (based on measurement) approach and ray tracing approach. The empirical approach is partially acceptable due to its simplicity. The ray tracing approach is based on ray optical theory and usually considered for indoor but it is usually complex and computationally expensive for confined environments [1, 14].

Stochastic Modeling is the most popular approach in the channel modeling community. Compared to the deterministic modeling, stochastic modeling has lower complexity and can provide sufficiently accurate channel information. Stochastic models are derived based on the measurements collected in an array of locations with a small fraction of grid points within the environment. To provide a statistical representation of the channel, associated statistical channel parameters are used to generate the channel impulse response (CIR) [1, 14].

2.6.1 Background study

In wireless communication system design, the mathematical demonstration that characterize the propagation channel, is necessary. Characterization and modeling of a channel can be studied by a time invariant system illustrated in Fig. 2.4 for single input and single output communication system which consists of single antenna at the transmitter and single antenna at the receiver and additive noise. This noise can be thermal noise, impulsive noise, multiple access interference and can be ignored for simplicity. The received signal, $y(t)$ is the convolution of the transmitted signal $x(t)$ and the channel impulse response $h(t)$ and can be written as $y(t) = x(t) * h(t)$. In a linear time invariant system, the convolution of the transmitted signal with the channel can be written as

a product in the frequency domain (using Fourier transformation), $Y(f) = X(f)H(f)$.

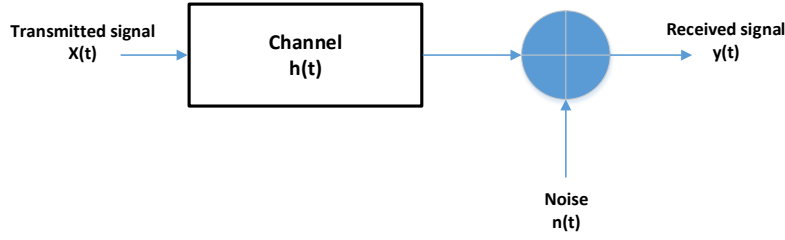


Figure 2.4 Block diagram of a channel model.

For linear time variant system (frequency dispersion - mobility and signal amplitude fluctuation - fading) the following input-output relationship can be used by using the Inverse Fourier Transform of $Y(f)$ [7] :

$$y(t) = \int_{-\infty}^{+\infty} X(f)H(f, t)\exp(j2\pi ft)df \quad (2.3)$$

Generally, the channel transfer function, $H(\cdot)$ is a function of frequency, time and distance. If a signal is transmitted through a linear time-varying channel, the received signal as a function of time (t) and space (d) can be expressed as [7] :

$$y(t, d) = \int_{-\infty}^{+\infty} h(\tau, d, t)x(t - \tau)d\tau \quad (2.4)$$

where τ is the multipath delay. During multipath propagation, the total electromagnetic field is the summation of direct and multipath components. Each multipath component can be characterized by its amplitude, phase and time of arrival (TOA). Therefore, for a finite bandwidth and discrete time variant channel, the impulse response in a specific position can be written as

$$h(\tau, d, t) = \sum_{i=1}^N a_i(t, d)e^{j\theta_i(t, d)}\delta\{\tau - \tau_i(t, d)\} \quad (2.5)$$

where N is the number of multipath components, a_i , θ_i and τ_i are the i^{th} time variant amplitude, phase and path delay, respectively.

2.6.2 Related underground mine measurements

Some studies led by the LRTCS-UQAT, located in Val-d'Or, have been performed in order to design and improve mining industry wireless communications systems. For more than a decade, a

former gold mine named CANMET, which is now an experimental mine, has been used for several measurement campaigns for wireless channel characterization. This mine environment, different from the indoor environment (e.g., office, corridor), is affected by multiple reflections, scattering, and diffraction due to surface roughness and narrow passages [21, 22, 23, 24, 25].

So far, experiment with different frequencies and galleries have been performed in CANMET and the results are listed in Table 2.2. Comparative results of this research show that as the operating frequency increases and as the antenna half-power beamwidth (HPBW) decreases, a lower value of RMS delay spread is obtained. The values of the path-loss exponents are found to be around 2. The value of τ_{rms} particularly depends on the antenna HPBW, the topology of the experiment, gallery curvature, and operating wavelength as well as the Tx - Rx distance.

In addition, measurements with a heavy vehicle between the Tx and Rx with inside and outside of the 40 m gallery have been carried out in a frequency range between 2 GHz and 6 GHz and reported in [26]. The results showed that the path loss exponent is found to be approximately 2.23 and 1.96 when a scoop vehicle was inside and outside of the gallery, respectively. Furthermore, the average values of RMS delay spread inside and outside of the mine were found to be approximately 5.02 ns and 3.85 ns, respectively [26]. Therefore, for vehicle to vehicle communication application in underground mine, with the above scenarios, measurements with 60 GHz frequency can be performed to characterize the channel.

Experimental work carried out in different mines and tunnels were reported in [27, 28, 29, 30]. Emslie et al. [28] compared theoretical and measured results in a coal mine at 200-4000 MHz and noted that the increase of signal loss was caused by surface roughness and the tilt of tunnel walls.

2.6.3 Related 60 GHz indoor measurements with and without use of different antenna polarizations

Several experimental works on indoor environments using 60 GHz band listed in [1], particularly in [2] and [39] reported a path loss exponent of less than 2 with fading between 0.14 and 2.14 dB. Moreover, a 1 ns RMS delay spread has been achieved with a fan-pen antenna configuration. Channel fading and dispersion effects are also well defined by Geng [40], where the obtained path loss component is less than the free space value, due to the waveguide effect in an indoor environment.

Su Khiong Yong noted that polarization changes with respect to the reflection and incident angles as well as the surface roughness [1]. Zhao et al. [41] noted co- and cross-polarization patterns of the antennas and multipath propagation which could change the polarization states (from vertical to horizontal and vice versa) are the main reason for signal depolarization. No obvious difference

Table 2.2 CANMET underground mine experimental results in Line of Sight (LOS).

Reference	Gallery (m)	fc (GHz)	BW (GHz)	A_{tx}	A_{rx}	Tx - Rx (m)	A_{tg}	A_{rg}	n	$\overline{\tau_{rms}}$ (ns)
[21]	40	2.4	0.2	Omni	Omni	~ 70	0	0	2.16	15-37
[31]	40	2.4	0.1	2x2 Omni	2x2 Omni	~ 26	2.5	2.5	1.76	3.23
[24]	40	2.4	0.1	2x2 Patch	2x2 Patch	~ 25	6-9	6-9	1.73	N/A
[32]	40	2.45	0.2	4x4 Patch	4x4 Patch	~ 30	7	7	1.29	1.38
[33]	40	5.8	0.2	2x2 Patch	2x2 Patch	~ 11	12	12	2.1	N/A
[34]	40	6.6	7	2x2 Patch	2x2 Patch	~ 10	12	12	1.42	N/A
[35]	40	60.5	7	2x2 Patch	2x2 Patch	~ 10	10	10	1.48	7.65
[36]	40	60.5	7	2x2 Patch	2x2 Patch	~ 10	24	24	1.36	1.85
[37]	70	2.4	0.2	Omni	Omni	~ 23	0	0	2.04	6.31
[38]	70	3.5	3	Omni	Omni	~ 15	0	0	1.47	11.8
[22]	70	5.8	0.2	Omni	Omni	~ 22	0	0	2.22	5.11
[37]	70	5.8	0.2	Omni	Omni	~ 23	0	0	2.22	6.14
[23]	70	6.5	7	Horn	Horn	~ 10	6-14	6-14	2	2.09
[23]	70	6.5	7	Omni	Horn	~ 10	1	6-14	1.99	7.79
[23]	70	6.5	7	Omni	Omni	~ 10	1	1	2.11	9.74
[37]	70	60	2	Horn	Horn	~ 6	20	20	1.68	2.41

Note : n is the path loss exponent. $\overline{\tau_{rms}}$ is the mean RMS delay spread. A_{tx} and A_{rx} are the transmitter (Tx) and receiver (Rx) antennas, respectively. A_{tg} and A_{rg} are the Tx and Rx antenna gains in dBi, respectively. Tx - Rx is the maximum transmitter receiver separation distance.

between vertically and horizontally polarized received power at 5.3 and 61.7 GHz in LOS corridor has been obtained, but a significant difference found in NLOS [41].

Measurement results show that, in LOS, the directional circularly polarized antennas reduce RMS delay spread compared to the omnidirectional and the directional linearly polarized antennas. In LOS environments, the received signal is dominated by the LOS component, which is not depolarized. Conversely, in hallway corners, reception is primarily due to reflection, diffraction, and scattering, which depolarizes the transmitted signal and high RMS delay spread is observed [42].

The performance of 60 GHz wireless communications in the library, hallway, and residential environments, using circular polarization, gave a better result in terms of bit error rate (BER) due to a reduction of the multipath effect than linear polarization [43]. Measurement results show that the number of strong reflection waves depends on the polarization type (i.e., horizontal and vertical). Moreover, the received cross-polarized signal power is found to be small but not negligible [44]. Antenna imperfections such as channel XPD (Cross Polarization Discrimination) and polarization mismatch are interference for polarization diversity or dual polarization transmission system. The Angle of Arrival (AoA) of the strong reflected waves depends on the polarization type due to the variation of the reflection coefficient with different polarizations [44]. Manabe [45] found that the

RMS delay spread for circular polarization is about half of the one obtained with linear polarization in an indoor environment. He also showed that its value with horizontal polarization (H) is slightly lower than with vertical (V) polarization. However, the IEEE 802.15.3c Task Group demonstrated in 2009 that the mismatch of polarization characteristics of transmitting and receiving antennas can result in large degradation of the received power by 10-20 dB [46]. Similarly, Zhao et al. [41] noted that vertical polarization applied in the transceiver gives higher received power in the shadowing region compared to horizontal polarization.

2.6.4 Related antenna polarization measurements in underground mine

A very significant amount of theoretical and experimental studies has been made on the polarization effect in underground mine and tunnels. Cawley et al. [47] defined that different polarizations have different coupling losses, attenuations and bend losses. Zhang et al. [48] also analyzed different polarization losses at 900 MHz.

So, polarization characteristics are very important for 60 GHz WLAN systems and need to be properly addressed in the channel model. In the case of an underground mine environment, this channel characteristic is obvious due to surface roughness and narrow passage galleries, and the receiver may experience different dominant power with different polarizations.

The polarimetric measurements and channel characterizations are motivated by the Co (HH and VV) polarization radiation patterns of the antennas and the different magnitude of the floor, wall and ceiling roughness. Polarization can also be changed by the rough surface specially with rock walls. Thus, an underground mine rough walls can change polarization type and the new polarized signal can not be received at the single polarized antenna at the receiver which tends to decrease the capacity of the WLAN system. Therefore, polarization characteristics based on wave propagation in different gallery dimensions could be an interesting topic in underground mine wireless communication research.

2.7 State of the art of scattering analysis

Scattering phenomena due to the high roughness of mine surface may cause a non-negligible scattered multipath contribution at the receiver. Standard theoretical scattering models available in literature based on different techniques such as Kirchhoff Model consists of the Geometrical Optics Model, Physical Optics Model by using ray optics to estimate the electric field on a surface and the Small Perturbation Model is dominated by the coherent component of scattering [49]. The scattering patterns for a Kirchhoff model surface are dominated by the diffuse components. The small perturbation approximation requires small standard deviation of heights and correlation length with

respects to the wavelength. Therefore, based on the explanation and validation of models, Kirchhoff scattering model is suitable for a very rough surface, whereas Physical Optics Model is mostly considered for average roughness and small perturbation approximation is well suited for small roughness. A suitable analytical approach of Kirchhoff scattering approximation commonly found in the literature is widely used for scattering analysis [50]. Non specular, specular and diffused scattering analysis and measurement at THz frequency are reported in [51, 52, 53, 54]. The multiplication of the reflection coefficients (derived from the Fresnel equations) with the Rayleigh roughness factor is considered as the extension of the Kirchhoff theory of scattering [50]. This theory is thoroughly implemented in THz communication for home environment [51]. Also, backscattering measurement procedure and measured reflected signal from building in urban areas have been analyzed at 4 GHz frequency and have been found that the reflected energy is between 20 to 30 dB higher than the diffused scattered energy [55]. This is to note that the diffused energy is particularly depends with the wavelength.

2.8 State of the art of scattering analysis based on reflection coefficients

So far, few experimental investigations of reflection characteristics of interior and exterior of homes and office buildings at different frequencies have been published [56, 57, 58, 59, 60, 61, 62]. Earliest experimental study of reflection, scattering and transmission characteristics of building materials at 60 GHz by Langen *et al.* [60] demonstrated the measurement procedures and exhibited power dependent scattering of building materials. The authors also noted that, depending on the reflection profile shapes, either Fresnel model or the multiple reflection model can be proposed. Another measurement campaign was conducted in an office building by Sato *et al.* [59] at 60 GHz frequency and results have been compared with multilayer dielectric models. Measurements of common flooring materials is carried out in [58] to analyse the frequency dependencies on the reflection coefficients of the materials. Recently, Zhao *et al.* [57] reported measurements of outdoor mm-Wave cellular communications at 28 GHz in New York city and found that outdoor building materials are more reflective (reflection coefficient of 0.896 for tinted glass at 10° incident angle) than indoor ones. Moreover, it was reported in [61] and [62] that, multipath reflections from buildings caused at least 15 dB additional pathloss over line of sight signals against 15 to 20 dB in office environments. Some works with the wireless channel characterization at 60 GHz in underground mine has been done, however, no experimental investigation of the reflection coefficients for propagation in underground mines has been reported so far. The objective in this issue is to study of the scattering phenomena of the mine floor and the wall surfaces relative to the reflection coefficients.

2.9 State of the art of angular spread analysis

Some experiments of angle of arrival (AoA) have been reported in the literature for indoor [44, 63, 64, 65] and outdoor [66, 67] environments. Hao et al. [68] reported that multipath comes along the LOS direction in the hallway and the angular spread is smaller than that of the rooms. Moreover, it is mentioned that, by increasing the distance along the hallway, the angular spread increases due to more multipath coming from different directions. Higher angular constriction results were also observed for close distances in the hallway. Spencer et al. [69] observed uniform distribution of angular arrivals of a cluster and showed that the multipath arrivals within a cluster have a Laplacian distribution having standard deviations of angular spread of 22° to 26° . Plattner [70] showed also that the multipath reflections follow a geometric law to estimate the delay spread in an indoor environment. Loni et al [71] noted that the angular spread values for indoor environments are higher than those for outdoor environments showing that multipath comes from multiple directions in an indoor environment. In addition, the AoA shape factors in an indoor environment relate to a specific area and correlation between the environment and the multipath channel structure as shown in [72].

2.10 State of the art of channel modeling

Propagation characteristics in underground mine and tunnels are site specific and depend on the employed frequency band. Recent surveys of wireless communications and propagation modeling in underground mines and tunnels have been reported in [27, 73, 74]. Several channel modeling approaches such as numerical methods for Maxwell equation, wave guide and ray approach are reported in [48, 75, 76, 77, 78, 79, 80, 81, 82]. A theoretical and a ray optical theory have been developed by Ndoh et al. [76] and Fono et al. [77], respectively as for deterministic modeling to characterize the CANMET underground mine channel. Prediction of amplitude, arrival time and the RMS delay spread were modelled both in narrow band and wide band cases using the theoretical ray optical method in [48]. As in open literature, waveguide approach gives analytical solution for smooth walls and ceiling. Since the surface roughness of the underground mine is higher than the wavelength, and the gallery walls contain metallic pipes, nets, arches preventing collapse and various kinds of objects mounted on the walls and ceiling, ray tracing approach might not be appropriate since large number of reflected, diffracted and scattered rays and higher computational time. As referenced in literature, radio wave propagation modeling approaches using electromagnetic theory for rectangular, circular, semi circular tunnels might be useful. Using ray frustum technique and Fast Fourier Transform (FFT), a temporal millimeter wave propagation model for tunnels is reported in [83]. However, the problem can be partially solved for the best fitted approach so far

by using a hybrid modeling approach or empirical based statistical model for multipath simulation. The statistical model can be obtained by using the performance of multipath arrivals and amplitudes [22].

2.11 Measurement approaches

In order to characterize the underground mine channel at 60 GHz frequency, measurement approaches can be used to obtain the channel impulse responses [84]. The first approach is to transmit a series of very short periodic RF pulses and measure the impulse response of the channel on the receiver. The second approach is for wideband measurement using the principles of spread-spectrum technology and it is based on the pseudorandom bit sequences as direct-sequence spread-spectrum (DSSS) communications. The impulse response of the channel can be obtained by correlating the received signal with a replica of the pseudorandom sequence. The third approach is based on frequency domain measurement technique using a vector network analyzer which sweeps the channel with equal increments frequency samples and measures the similar number of complex samples of the frequency response $H(f)$. Given the availability of a network analyzer operating up to 70 GHz in LRTCS laboratory, it was decided to use the frequency domain measurement technique to obtain the channel impulse response.

The propagation channel in underground mine is a time variant due to environmental effects and narrower gallery dimensions. The duration of the measurement is proportional to the number of frequency samples. For several GHz band measurements, the duration of the measurement is of the order of few seconds. A Vector Network Analyzer (VNA) was used to record transmission scattering parameters. During the channel measurement, port 1 of VNA was connected to the transmitting antenna and port 2 was connected to the receiving antenna. The S21 parameter represents the entire system transfer function ($H(f)$) including the measuring equipment and the channel being measured.

2.11.1 Large scale ($< 10\text{ m}$ at 60 GHz) measurement approach

Large scale channel characterization consists of path loss (PL) and fading of the channel. PL is defined as the ratio of the received signal power to the transmitted signal power, which describes the attenuation of the mean power as a function of distance travelled. PL is necessary for the link budget analysis and network planning in order to ensure the targeted coverage. The distance power loss coefficient at 60 GHz is approximately 22 dB in office environment as reported by ITU [1, 85]. It is

known that the path loss can be modeled as a function of distance using the following relationship

$$PL_{dB} = 10\log_{10}(d_0) + 10n\log_{10}(d/d_0) + \delta_\sigma \text{ [dB]} \quad (2.6)$$

where $10\log_{10}(d_0)$ is the PL at the reference distance d_0 in dB and n is the PL exponent. δ_σ is the Gaussian random variable in dB with standard deviation σ .

PL at 60 GHz also has additional losses due to oxygen absorption and rain attenuation, but negligible for the short range radio link. It makes a promising candidate for indoor rather than outdoor applications. Large scale fading signifies the average signal power variations over an area due to the constructive and destructive behavior of the multipath, particularly in an underground mine where dynamic multipath behaviour exists [1, 86]. Therefore, a large scale measurement approach was conducted and presented in Chapter 5.

2.11.2 Small scale (1 cm^3) measurement approach

Small-scale fading is caused by the multipath signals that arrive at the receiver with random phases that add constructively or destructively within a small scale area compared of a grid separated by a half of the operating wavelength. To investigate the rapid changes in signal amplitude over a smaller distance (less than 10 wavelengths), a 3D measurement approach was conducted. The channel parameters such as mean delay and root mean square delay spread are demonstrated in [86, 87] and more explanations are in Chapter 5.

2.11.3 Scattering measurement approach

Since the objects on the rough surface in the underground mine are smaller than the 5 mm wavelength, scattering phenomenon occurs during wave propagation. To analyze the effect of scattering, a measurement approach was conducted and presented in Chapter 4. Extraction of the statistical parameters and comparison with the known Kirchhoff scattering approximation are presented. Moreover, to investigate scattering behavior, reflection coefficient measurements were carried out and extracted parameters are compared with available scattering models.

2.11.4 Angular dispersion measurement approach

To characterize the scattering phenomenon and angular spread of multipath in the underground mine, an angle of arrival measurement approach was conducted and presented in Chapter 6. The measurement results provide an idea of multipath angular spreads. The multipath shape factor is analyzed which characterizes the scattered channel and provides more relative information regar-

ding the transmitter receiver link lobes. The analysis of the results could help to understand the feasibility of beamforming technology in the underground mine.

2.11.5 Antenna polarization measurement approach

The use of polarization concept has gained attention in wireless communication. Measurements with different antenna polarizations (VV, HH) were considered to investigate for this particular multipath environment where different roughness and different gallery dimension exhibit an impact on the scattered channel. Moreover, antenna radiation patterns can have an effect on the scattered channel.

2.12 Difference between other CANMET 60 GHz experimental works

The 60 GHz previous experimental results performed in CANMET underground mine galleries are listed in Table 2.3. In this thesis, wireless scattered channel experiments, with different antenna polarizations, provide the use to determine whether dual or single and which type of polarization those would be best suited to use of polarization diversity. Different antenna configurations contribute to the decision to use directional or Omnidirectional antenna in underground mine galleries. A combination of gallery dimensions, antenna configurations, and polarizations, as well as 3D small scale experiments, provide more information on channel characteristics compared to other works. Particularly, the advantage of AoA experimental work is to have information of angular spread and angular dependencies of multipath arrivals on the scattered channel. Different gallery depths with different antenna configurations in conjunction with different antenna polarization experiments provide much more channel information for statistical modeling.

Table 2.3 Difference between other CANMET 60 GHz experimental works with this work

Ref.	Gallery depths	Polarization	A	n	$\overline{\tau_{rms}^l}$	3D $\overline{\tau_{rms}^s}$	AoA	S	Model
[35]	40 m	×	×	✓	✓	×	×	×	×
[88]	70 m	×	×	✓	✓	×	×	×	×
[37]	70 m	×	×	✓	✓	×	×	×	×
This work	40 m, 70 m	✓	✓	✓	✓	✓	✓	✓	✓

Note : n is the path loss exponent. A is the antenna configurations (i.e, Horn - Horn, Horn - Omni etc.). S is the scattering experiments. The τ_{rms}^l and τ_{rms}^s are the large scale and the small scale RMS delay spread, respectively.

2.13 Summary and benefits of the thesis

Based on this research work the following list is given as for the benefits of the thesis, in other words, what kind of information will be available.

- Which antenna configuration is useful for underground mine environment.
- Which antenna polarization is useful to design antenna in underground mine environment.
- What could be the expected antenna beamwidth.
- What are the temporal and angular dispersion characteristics to help wireless system designer.
- An idea of having statistical modeling of scattered channel.
- An idea of having high frequency wireless channel coexistence based on practical LTE-U and WiFi channel sharing experiment.

Therefore, measurement approaches have been carried out in CANMET experimental mine in order to investigate the scattering, polarization effect those are described later in this thesis. The motivation is to do in-depth research in this area. However, 60 GHz channel characteristics and modeling in underground mine based on scattering and polarization effect is not yet carried out and published according to the open access literature review.

CHAPTER 3 MEASUREMENT SETUP AND PROTOCOLS

A 60 GHz frequency domain measurement system was used to perform channel characteristics in underground mine environment.

3.1 Underground mine galleries and environment

Two measurement zones (i.e., 40 m and 70 m levels) were used in the CANMET mine, located in Val-d'Or, Quebec, as shown in Fig. 3.1 and 3.2. From surface roughness measurements (explained

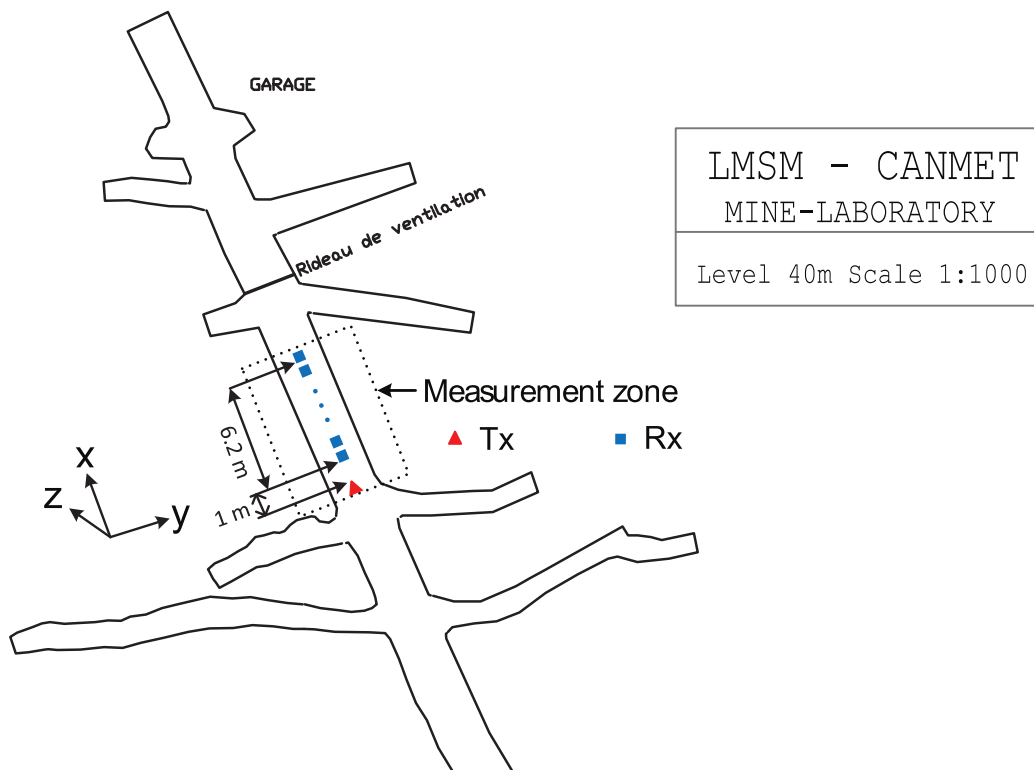


Figure 3.1 Measurement zone at 40 m level.

in Chapter 4), the maximum and average roughness thickness of the side walls are around 37 cm and 20 cm, respectively. The ceilings are especially rougher. Some metallic pipes are present in the corner of the gallery at 70 m. Digital photographs of both environments are shown in Fig. 3.3. The floor is mostly covered with water puddles at 70 m, whereas it is more dry and mostly covered with dust on the floor at 40 m galley.

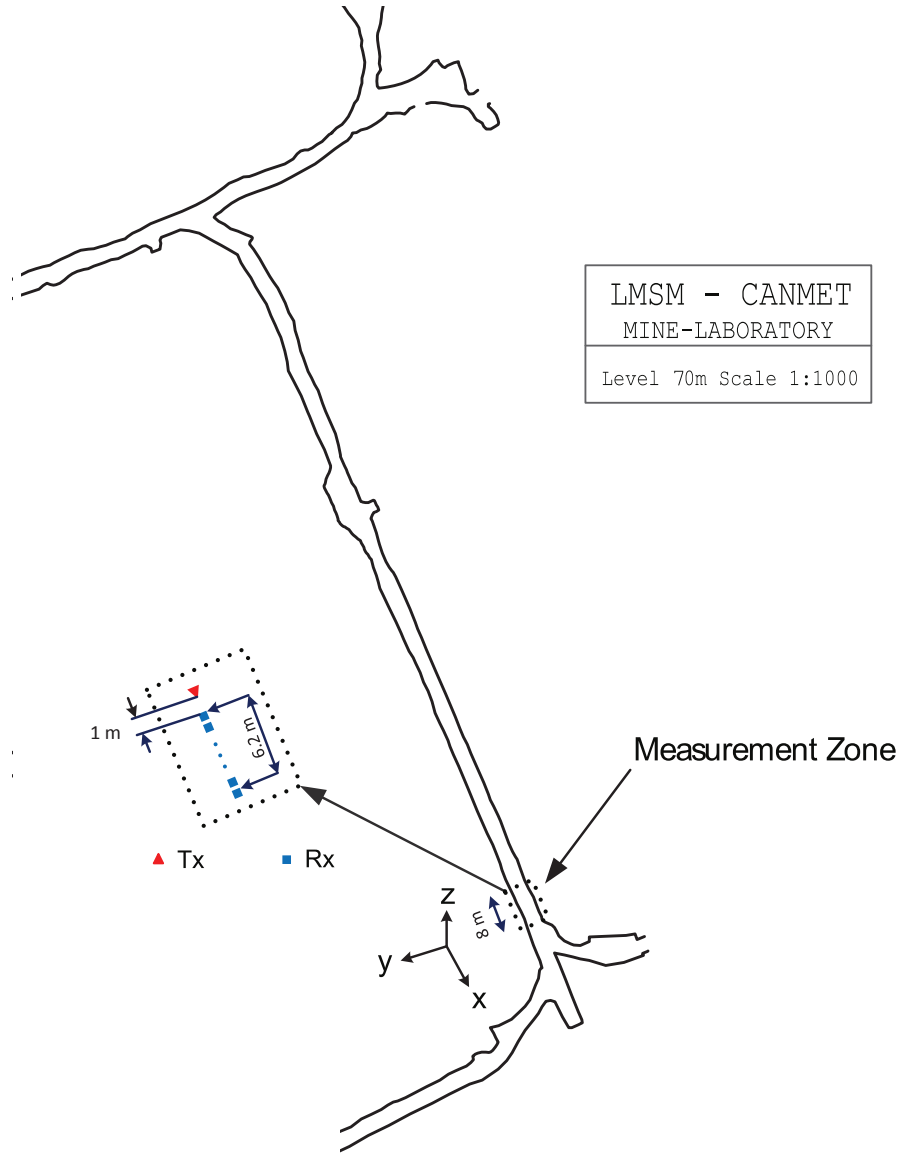


Figure 3.2 Measurement zone at 70 m level.

The humidity in both galleries were found to be around 100 percent. The temperature varied between 6°C and 7°C and the minimum temperature was felt at 70 m. The presence of large amounts of dust in the air at 70 m compared to the 40 m gallery also observed. Large machinery noise caused by the air ventilation system was also observed in both environments. This kind of phenomena in the mine environment may constitute a signal fluctuation and unexpected behavior of wireless propagation in the 60 GHz frequency band. The dimensions of the mine galleries at both levels are listed in the Table 3.1. The value of the length is an approximate straight line of sight distance before a curvature [17, 22]

Table 3.1 Approximate dimensions of mine galleries.

Depth (m)	Height (m)	Width (m)	Length (m)
40	5	5	30
70	2.5-3	3	70



(a) 40 m



(b) 70 m

Figure 3.3 (a) 40 m and (b) 70 m galleries.

3.2 Measurement setup and campaigns

A 60 GHz channel measurement setup was implemented in the CANMET underground mine in cooperation with the LRTCS laboratory and used for the measurement campaigns in both mine levels. The setup was based on frequency domain measurements using a 60 GHz cable architecture. The illustration of the measurement setup is shown in Fig. 3.4. A Vector Network Analyzer (ANRITSU MS 4647A) with a frequency band range of 40 MHz to 70 GHz has been used as a two-port network measurement system for transmission and reception of the radio signal. The Power Amplifier (CBM 57653/015-03 CERNEX) was used with a gain of 30 dB. Since we had a high loss (almost 36.8 dB) for the 4.6 m cable, even with a Low Noise Amplifier (CBL 57653/055-01 CERNEX) with 30 dB gain, the level of the signal was not strong enough especially in the 70 m gallery. Hence, a second Low Noise Amplifier (QuinStar, Serial N11328) was added with a gain of 18 dB to enhance the signal power. The frequency range was then selected, following the IEEE Standard 802.15.3c, between 57.24 GHz to 59.4 GHz (channel 1). Experiments with other channels in this standard have also been taken into account during measurements, but high attenuation of the radio signal was observed because of the 61 GHz upper frequency range of the QuinStar LNA. The transmit power was set at 4 dBm. Horn and Omnidirectional antennas were used in order to make

directional and omnidirectional propagation scenarios between the transmitter and receiver. Horn antenna presents a half-power beam width (HPBW) of about 12° in azimuth and elevation planes. Since the Pyramidal Horn antenna is vertically polarized, the electromagnetic (EM) field radiation is mostly directive in the HH (Tx as Horizontal and Rx as Horizontal) case, whereas some ripples have been found in the VV (Tx as vertical and Rx as vertical) case. The omnidirectional antenna (vertically polarized), has an HPBW of 360° in azimuth and $\sim 40^\circ$ in elevation direction. Moreover, 8 dB below from the peak values the omnidirectional antenna covers $\sim 40^\circ$ in the elevation direction. In order to find the polarization effect in the underground mine, horizontal polarization of the omnidirectional antenna was used to see if there was an influence between horizontal and vertical polarizations considering the geolocation links between moving miners. An similar experimental

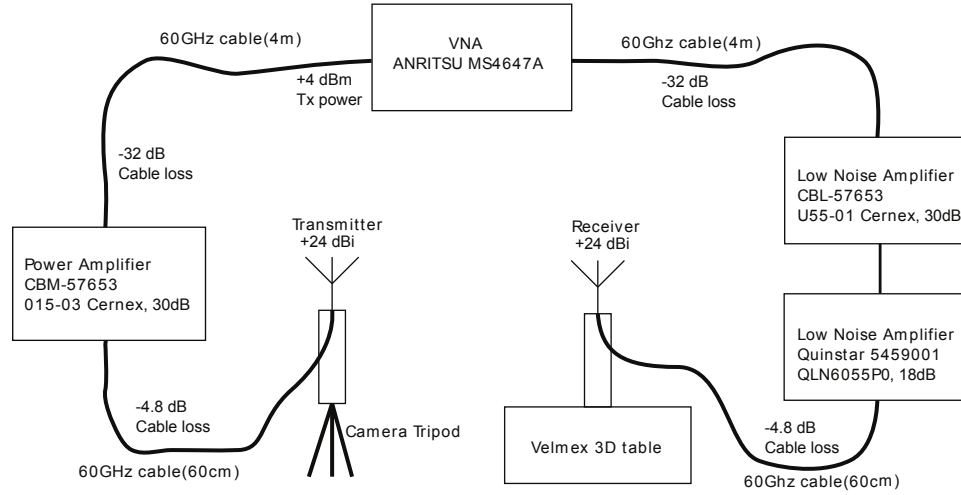


Figure 3.4 Measurement setup.

setup has been used for all antenna configurations (Horn-Horn, Horn-Omni, Omni-Horn) and polarizations (VV, HH). The polarization of the antenna has been changed from vertical to horizontal and vice versa manually using a shift of 90° .

A laser and a camera tripod were used in order to have accurate and fixed placement of the transmitter and receiver in case of line of sight (LOS) condition. No measurements have been carried out in NLOS situation due to unavailability of the radio signal. Indeed, the channel considered for the geolocation links between miners and the transmitter and receiver was in the middle of the gallery widths at heights of approximately 1.5 m in both galleries. The complete list of the measurement campaign parameters is shown in Table 3.2. The data acquisition was completed by connecting a computer to the VNA via a GPIB interface. A Labview program was used to control the whole measurement procedure and a MATLAB program was employed to move the VELMEX 3D positioning table.

Table 3.2 Parameters of 60 GHz channel measurements

Mine Level	40 m, 70 m
Frequency range	57.24 GHz-59.4 GHz
Center frequency	58.32 GHz
Bandwidth	2.16 GHz
Tx power	+4 dBm
Tx/Rx height	~1.5 m/~1.5 m
Sweep points	2000
Sampling frequency	1.08 MHz
Power amplifier gain	30 dB
Low noise amplifier gain	18 dB and 30 dB
Pyramidal Horn antenna	Gain 24 dBi, HPBW 12°
Omnidirectional antenna	Gain 3 dBi
Polarization	HH, VV
60 GHz cable	Loss 7.86 dB/m

The Vector Network Analyzer (VNA) with 1 kHz IFBW (i.e., the intermediate frequency bandwidth) permits a one channel (S_{21}) full sweep time of around 6 s for 2000 points which provides a stable state for the frequency response of the channel. The standard VNA system noise floor (e.g., -10 dBm source power, 10 Hz IFBW) is -107 dBm [89]. Therefore, with 1 kHz IFBW, the VNA dynamic range (i.e., the difference between the maximum rated source power and the specified noise floor) was 87 dB (e.g., narrowing IFBW to 1/10 IFBW decreases by 10 dB the receiver noise floor). SOLT (short-open-load-thru) calibration were performed for the measurement system with 2.16 GHz bandwidths, 2000 sweep points spaced by 1.08 MHz [21]. The measurements were conducted as continuous wave measurements, where 2000 samples were transmitted separately on the channel to have a power delay profile at the receiver. At both mine levels, the transmitter and receiver antennas were always pointed directly at each other using a laser as shown in Fig. 3.3. The channel was static in all conditions. The antenna far field region d_f from the transmitter antenna aperture has been calculated using the equation $d_f = \frac{2D^2}{\lambda}$, where D is the physical dimension (diameter) of the antenna. For our measurements, d_f of the Horn and Omni directional antennas were 0.83 m and 0.58 m, respectively. Over the air calibration measurement was set 1 m distance to remove system losses and antenna effects, which was also been used for the post processing of channel impulse responses. During the measurements two fixed references, a 2 m long plane of wood on the floor and a rope were used outside the channel in order to ensure maximum accuracy of LOS. Signifi-

cant time was spent to place two fixed and parallel pieces of wood on the ground as rails to move the trolley easily. The Velmex Stepping Controller was able to move the receiver via a MATLAB program with a precision of 2.5 mm. For each measurement point, several snapshots were taken to have a local average in order to eliminate the time varying fading.

3.3 Velmex 3D experimental table

The Table as shown in Fig. 3.5 used to support a load of 2 Kg with movements along the x, y and z axis with a step of mm range [90]. x and y axis maximum ranges were 1.5 m and 1 m, respectively. In the z axis, the maximum displacement of the load (i.e., antenna, motor, etc.) were between 250 and 500 mm. The load with an antenna along the z axis were able to rotate in azimuth direction between 0° and 360° . It has been used to have channel measurements in the underground mine and perfectly placed on the trolley to move along the gallery tunnels.

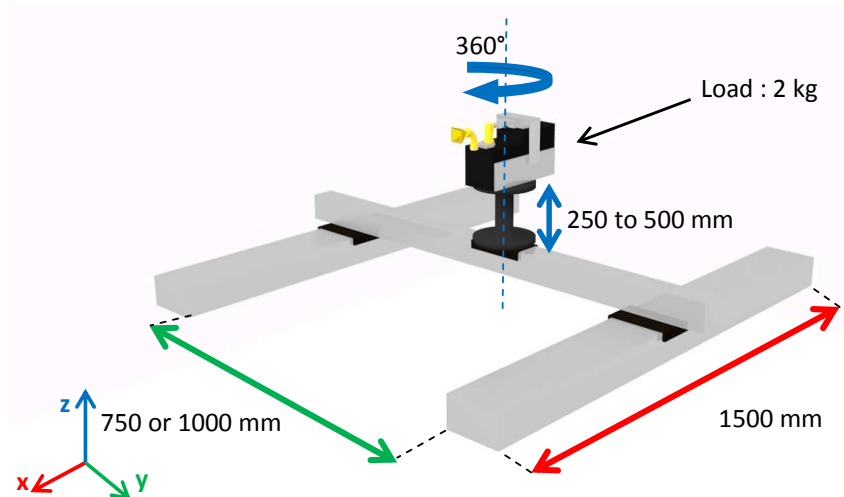


Figure 3.5 Illustration of the Velmex 3D table.

3.4 mmWave measurement prerequisites for underground mine

- Before going to the underground mine, all necessary measurements should be done outside in indoor to be familiar with the measurement procedures. Calibration, table movement, antenna alignments, path loss and delay spread calculations should be performed.
- A SOLT calibration of the system including cables, amplifiers, etc., excluding the antennas has to be performed. Verify transmitter (Tx) and receiver (Rx) positions on the gallery by looking from a 50 m distance for example. To observe multipath characteristics from the floor, wall, and ceiling, it is important to check the heights of the Tx and Rx in order to be in the middle of the gallery in the elevation direction because the Velmex table height is around 1 m and it has

metallic rods. If the height of the receiver is 1.2 m, some reflection may come from the Velmex table itself.

- It is required to put a long wood piece along the axis in order to move the Velmex table smoothly followed by the LOS direction. Wooden rails could be a perfect choice for mmWave measurements, particularly in this kind of confined environment.
- First measurements has to be taken at a reference distance of 1 m (as an example) in order to remove the antenna effects and cable losses.
- If the transmitter remains fixed and the receiver moves, since the table length is around 1.5 m, each grid point separation can be less than 20λ (10 cm). It could be more precise but required to see the data recording time. The recording time and one table movement time are necessary to cover within a period of one day time.
- It is required to check the direct path (i.e., delay and amplitude) at each distance particularly once the Velmex table moves (not the linear track) from one position to another. Once Velmex table is moved to the second position, the distance between the last measurement point of the first position and the first measurement of the second position should remain a Tx - Rx separation distance of 20λ . It would be perfect if a colored spray is used to mark the previous and current table positions.
- It is required to check if the received power is reasonably acceptable at a certain distance from the transmitter. Necessary to calculate the data recording and calibration time and should cover at least two table movements within a day time.
- The measurements of each scenario should be performed within one day if possible. If not, recording at night time could be an alternative procedure by using automation scripting.
- For proper alignment of the transmitter and receiver, it is necessary to use a laser and verify that the laser works with an acceptable azimuth and elevation angle drift. Moreover, the camera tripod head type should pan and tilt in 3 directions (x, y and z coordinates).
- At least four persons are required during the measurement campaign to avoid misalignment along the x, y and z directions. One person should stand at the transmitter to check LOS with laser pointer once the Tx and Rx antennas change from V to H manually without changing the physical position and heights of the Tx and Rx, one person should stand at the receiver to check carefully the antenna alignment once the Velmax table moves, one person should monitor the impulse response of the channel at each distance, during the movement of Rx and changes of antenna polarizations or antenna configurations, in the laptop either any signal received or not. One person should prepare the plans of the next measurements, and the validation of the recorded data instantly on site not outside of the mine.
- It is required to clean the track rods and put oil in a timely manner to move the linear track easily.
- It is mandatory to have a commercial software or predefined post processing structures for real-

the x direction did not change the direction of the antenna directivity, y and z movement offset were required to compensate for misalignment. Recording of grid points followed a trajectory having the profile of a square wave (defined by the Velmex table). The measurement procedure is explained more in Chapter 5.

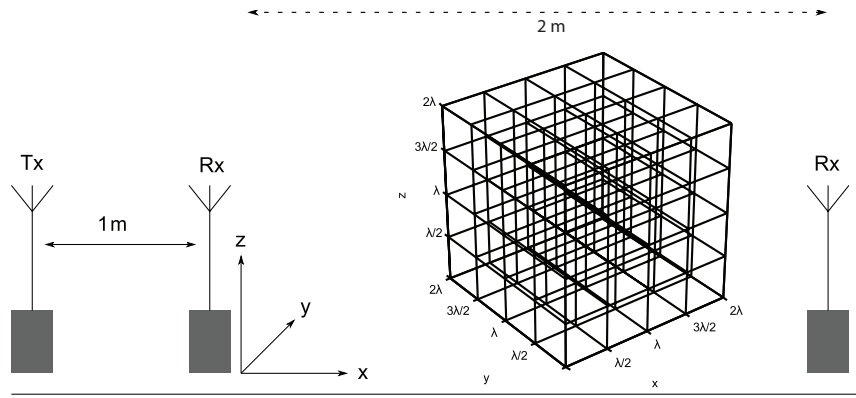


Figure 3.7 3D small scale measurement procedure.

3.5.3 Scattering

For wall surface measurements, a mine wall area of $1.5m \times 5m$ (as $z \times x$) was used to measure manually the surface heights with a grid spacing of 10 cm by using a fixed rope. Another measurement procedure was carried out to find reflection coefficients in a particular reflected angle. The frequency response of the channel was measured with a defined test area of the underground mine floor and wall using two step processes. The measurement procedures are described more in Chapter 4.

3.5.4 Angle of Arrivals (AoA)

During AoA measurements at each position of both galleries, the transmitter was fixed and the receiver was moved in azimuth directions from -90° to 90° with a step of 5° as well as along the x direction. Along the z directions, six consecutive measurements were taken at each position separated by $\lambda/2$ with 15 snapshots in different time instants. The measurement procedure is explained more in Chapter 6.

3.6 PDP post processing procedure

To obtain the power delay profile (PDP) of each receiver position, firstly, an average of 15 snapshots was performed. Secondly, over the air calibration was done by dividing the results of the frequency

response (S_{21}) of 1 m to all measurement points in order to remove the antenna effect and the cable loss. Thirdly, using the Inverse Fast Fourier Transform (IFFT), the time domain normalized magnitudes of the complex impulse responses were obtained from the calibrated frequency responses. An example of a PDP post processing is illustrated later in Fig. 5.1.

CHAPTER 4 SCATTERING ANALYSIS

In order to investigate the multipath behavior of 60 GHz channel at 5 mm wavelength with a centimeter range surface roughness of the mine walls, scattering measurements procedure was conducted. Surface roughness parameters such as standard deviation of heights and correlation coefficients were extracted from the surface height measurements, in order to use into Kirchhoff scattering approximation (KA) theory and to characterize scattering phenomenon in one single Radar Cross Section (RCS) scattering behavior. Angular dependent received power obtained from the simulation and the measurements and the results were analyzed in this Chapter.

Reflection coefficients are obtained from individual reflected and line of sight (LOS) signals with a particular reflective angle then compared with theoretical models. The results suggest a distinguishable reflection and scattering characteristics between mine wall and floor. Measurement results show that, in specular directions, the path loss difference between the LOS and the reflected signal lies between 11 dB and 18 dB. On both surfaces of wall and floor, strong reflections in specular directions and scattering in non specular directions were observed. Moreover, the wall surface of the mine produces more scattering with strong reflections than the floor surface. These reflection coefficient parameters are useful to estimate the multipath signal strength of the deterministic channel modeling approach of the underground mine.

4.1 Scattering analysis based on Kirchhoff approximation (KA)

Scattering phenomenon of the underground mine environment which can be described by the KA theory. The KA can be employed to find a model that can be used to generate the impulse responses of the channel. Measurements are necessary for the KA model verification. Therefore, to validate KA in an underground mine, surface height measurements were carried out. The surface roughness parameters were extracted. The channel measurements were performed and validated with the model.

4.1.1 Kirchhoff scattering theory

Beckmann and Spizzichino derive an analytical description of the electromagnetic field scattered from a rough surface [50]. A schematic illustration of the corresponding geometry is given in Fig 4.1, where θ_1 is the incident angle, θ_2 is the azimuth angle referred as reflection angle and θ_3 is the elevation angle of the scattered signal. Scattered field over the entire surface needs to be considered in order to obtain the scattering coefficient ρ with the assumption of a Gaussian height distribution.

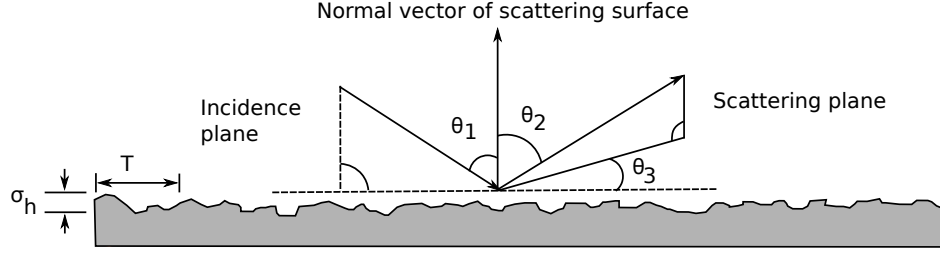


Figure 4.1 Rough surface scattering geometry.

Such surface is characterized by its heights standard deviation σ_h and its surface correlation length T . Knowing the angles θ_1 , θ_2 and θ_3 , the average scattering coefficient for an infinite surface can be derived as (for a roughness factor g is equal to 1 or less than 1)

$$\langle \rho \rho^* \rangle_\infty = e^{-g} \cdot \left(\rho_0^2 + \frac{\pi T^2 F^2}{A} \sum_{m=1} \frac{g^m}{m! m} e^{-\frac{v_{xy}^2 T^2}{4m}} \right) \quad (4.1)$$

where ρ_0^2 describes the scattering in specular direction and the second term of equation 4.1 is defined as diffuse scattering. The Rayleigh roughness factor g is an indicator for the relative surface roughness at a given wavelength, and the illustration shows in Fig. 4.2 that the incident power dissipated once the value of g is higher than the value of 1 [50]. Other parameters of this equation are given below

$$\rho_0 = \text{sinc}(v_x l_x) \cdot \text{sinc}(v_y l_y), \quad (4.2)$$

$$v_x = k \cdot (\sin(\theta_1) - \sin(\theta_2) \cos(\theta_3)), \quad (4.3)$$

$$v_y = k \cdot (-\sin(\theta_2) \sin(\theta_3)), \quad (4.4)$$

$$v_{xy} = \sqrt{v_x^2 + v_y^2}, \quad (4.5)$$

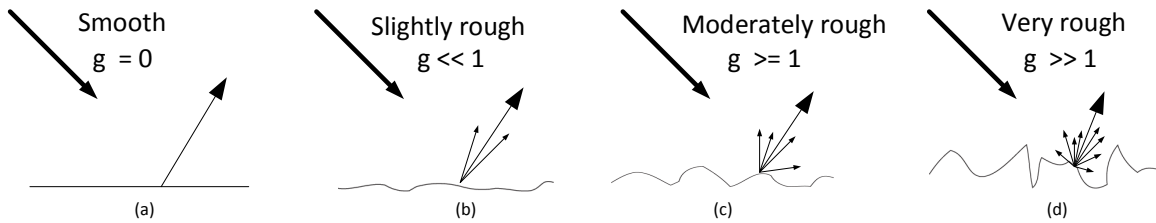


Figure 4.2 Rough surface scattering behaviour according to the value of roughness factor g .

$$v_z = 2k \cos(\theta_1), \quad (4.6)$$

$$F = \frac{1 + \cos(\theta_1) \cos(\theta_2) - \sin(\theta_1) \sin(\theta_2) \cos(\theta_3)}{\cos(\theta_1)(\cos(\theta_1) + \cos(\theta_2))}, \quad (4.7)$$

$$g = k^2 \sigma_h^2 (\cos(\theta_1) + \cos(\theta_2))^2. \quad (4.8)$$

where $k = 2\pi/\lambda$ is the wave number and $A = l_x \times l_y$ is the surface area. The value of l_x and l_y of the scattering surface has to be chosen large compared to wavelength (λ) and correlation length (T). When $g \gg 1$, the special case of KA scattering becomes :

$$\langle \rho \rho^* \rangle_\infty = \frac{\pi T^2 F^2}{A v_z^2 \sigma^2} e^{-\frac{v_{xy}^2 T^2}{4 v_z^2 \sigma^2}} \quad (4.9)$$

This is to note that $\langle \rho \rho^* \rangle_\infty$ does not depend on the material properties.

4.1.2 Surface height characteristics

In order to extract the surface roughness parameters from the mine wall, a 40 m underground level CANMET gold mine gallery (in Val-d'Or) was considered and shown in Fig 4.3.

4.1.3 Height measurement

A mine wall area of $1.5m \times 5m$ was used to measure manually the surface height with a grid spacing of 10 cm by using a fixed rope. The measurement procedure is shown in Fig 4.4. These heights are considered as an initial guess for surface characteristics. Though the horizontal and vertical resolution of height measurement is 10 cm, the surface heights were assumed to be symmetric in the whole gallery in 40 m mine gallery. It was also assumed that the roughness of the walls, ceiling and floor have different characteristics in nature.

4.1.4 Roughness characterization

4.1.4.1 Height distribution

The surface height distribution describes the Two-dimensional variation in surface elevation and azimuth above an arbitrary plane. A higher resolution will provide more accurate surface roughness, which is defined by the standard deviation of the surface height distribution. This parameter has more importance in statistical methods for roughness purpose. It is more sensitive than the arithmetic average of heights. The surface height distribution of the measured area is obtained by processing the measured surface roughness data using $h_{x,y} = h_{max} - h_{x,y}(measured)$ and by set-



Figure 4.3 Wall surface height measurement at 40 m mine gallery.

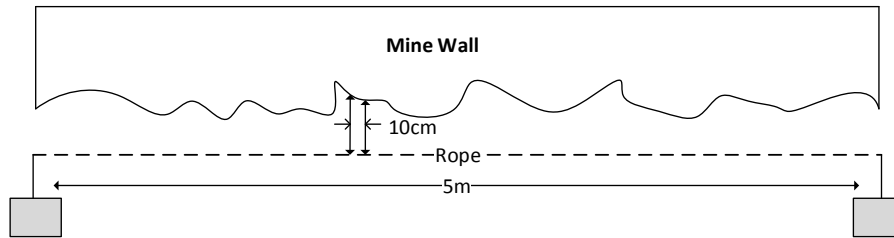


Figure 4.4 Height measurement procedure.

ting the offset to a zero mean value. Fig. 4.5 shows the color map of the spatial distribution of the wall surface. Maximum and average height are found to be 37.5 cm and 20.5 cm, respectively. Then the Kolmogorov-Smirnov test was used to fit with normal distribution and to find statistical parameters. Therefore, the wall surface is Gaussian with 6.0658 cm standard deviation (σ_h) according to the fitting. The histogram and Cumulative distribution function of measured data and corresponding fittings are shown in Fig. 4.6a.

4.1.4.2 Height correlation

The correlation length describes how strongly the surface heights of neighbouring points are correlated. In other terms, the correlation length provides information whether the surface consists of densely packed irregularities or slowly varying features. It can be defined as the distance between two statistically independent points. Generally, the autocorrelation decreases when the dis-

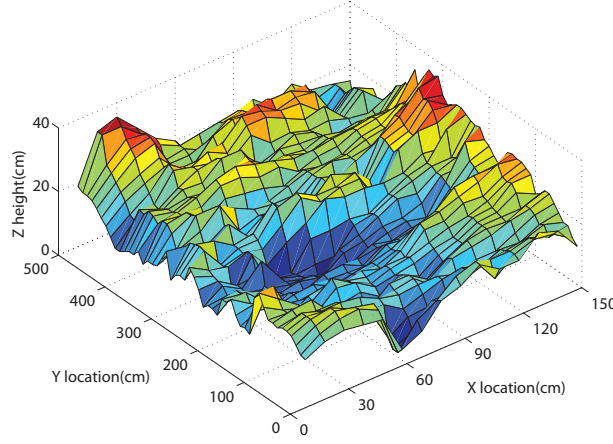


Figure 4.5 3D color map of measured surface height distribution.

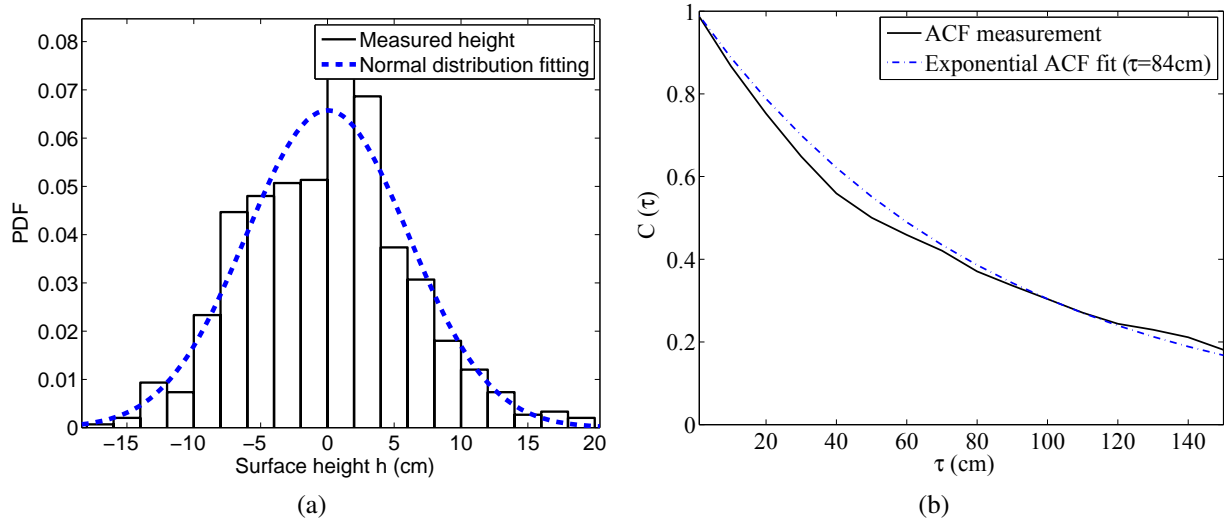


Figure 4.6 (a) CDF of measured surface heights (b) Auto correlation function of the heights $C(\tau)$.

tance increases and is determined empirically using the auto correlation function (ACF), equals to $C(\tau) = \langle h_1 h_2 \rangle / \langle h_1^2 \rangle$, where h_1 and h_2 are two heights and τ is the distance between them. For instance, the discrete one-dimensional auto correlation function $C(\tau)$ can be determined from two dimensional ($N \times M$) discrete heights $h_{x,y}$ and is given by,

$$C(\tau) = \sum_{\tau=1}^N \sum_{x=1}^N \left[\frac{\sum_{y=1}^{M-\tau} h_{x,y} h_{x,y+\tau}}{\sum_{y=1}^M h_{x,y}^2} \right] \quad (4.10)$$

where $x = 1, 2, \dots, N$ and $y = 1, 2, \dots, M$. The correlation length is then defined as the value of τ at which the autocorrelation coefficient $C(\tau)$ drops to e^{-1} . According to exponential fitting (Fig. 4.6b), correlation length T is found to be 84 cm. In the present investigations, the standard deviation of heights and corresponding correlation length at 70 m mine level gallery surface have not been measured experimentally, but the values determined by 40 m gallery have been used as initial guess parameters to model for 70 m gallery.

4.1.5 Scattered power measurement setup and procedure

As reference, there are some backscattering measurement technique illustrated in literature [91, 92]. In order to find backscattered power from the wall, a 60 GHz measurement system setup was used as described in Fig. 3.4. A LABVIEW program was employed to control the whole measurement procedure and MATLAB program was applied to rotate the antenna using Velmex 3D table with a step of 5° . The purpose of the measurement was to validate the KA model and

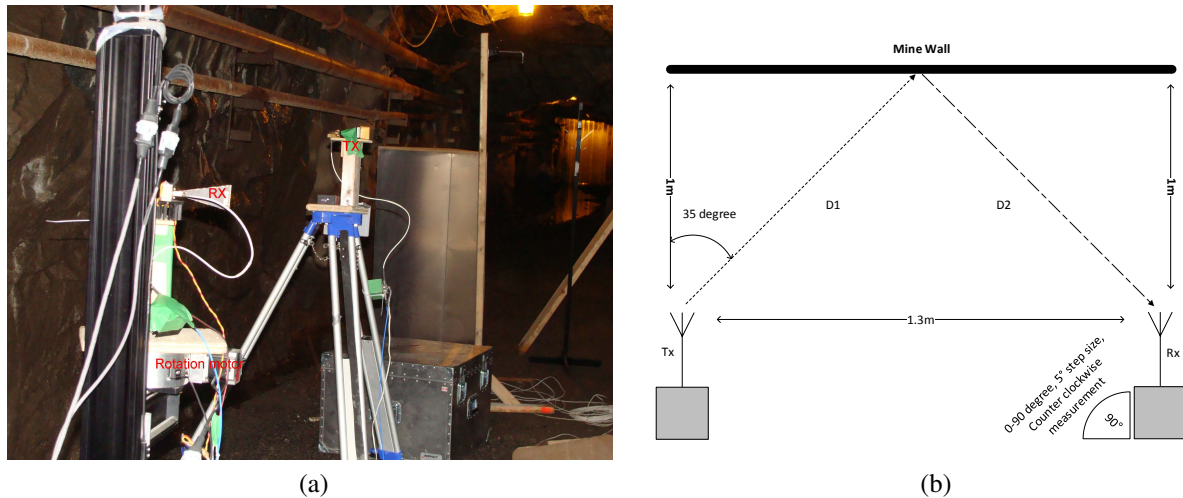


Figure 4.7 (a) Digital photograph for scattering measurement at 70 m mine gallery (b) Illustration of the measurement procedure.

to develop a framework for the application of a ray tracing model suitable for the underground mine. The measurements were part of an experimental program in the CANMET mine mainly directed at scatter measurements from wall surface at 70 m gallery. Figs. 4.7a and 4.7b show the experimental arrangements those were used to measure the scattered signal from the wall. In order to make a far field region of the horn antennas, Tx and Rx were set at 1 m away from the wall. Tx was fixed with 35° incident angle and Rx moved from 3 m to 1 m in order to get scattered signal from the wall, then Tx Rx separation distance was set at 1.3 m. This is to note that it was necessary to have a specular reflection direction less than 35° to achieve smaller Tx Rx separation

distance and maximum amplitude at the receiver. For the Tx Rx separation distance of > 3 m, no scattered signal from the wall and between 2 m and 3 m no strong scattered signal from the wall were observed since the angle of incidence is 35° . Since it was not in LOS direction, no LOS or direct path was observed during measurements. As in Fig. 4.7b, $(D1 + D2)$ was calculated from the geometry of the illustration and found to be 2.3854 m. An azimuth incident angle of 35° was set at the transmitter and the receiver was rotated from 0 to 90° along the counter clockwise azimuth direction. The rotation was used to observe the angular dependency of the scattered power from the wall.

4.1.6 Implementation and discussion

Fig. 4.8 shows the KA model of wall scattering which consists of a one radar cross section (RCS) for one single ray. RCS is defined as two times of correlation length T . A free space propagation from the transmitter to the scattering point and from the scattering point to the receiver was considered. According to the value of T and σ_h obtained from surface height measurements, and with $\theta_1 = 35^\circ$, the min and max values of roughness factor g are found $3.8514e^3$ and $1.8813e^4$, respectively which are much more greater than 1. For this condition scattering coefficient for infinite surface $\langle \rho \rho^* \rangle_\infty$ was considered (equation 4.9) since it is as special case ($g \gg 1$) of equation 4.1. It was also observed that T and σ_h of roughness are the main parameters for the simulation process. Simulation results show that increasing the correlation length with a fixed roughness value, there is less scattering behaviour at the receiver end and incident energy of the signal is scattered mostly if σ_h increases with a given correlation length. The finite scattering coefficient $\langle \rho \rho^* \rangle_{TE/TM}$ by multiplying conventional Fresnel reflection coefficient $r_{TE/TM}$ at 35° incident angle is determined as

$$\langle \rho \rho^* \rangle_{TE/TM} = (r_{TE/TM} \cdot r_{TE/TM}^*) \cdot \langle \rho \rho^* \rangle_\infty \quad (4.11)$$

The received power is then calculated within a given area of A ($l_x \times l_y$) by multiplying the finite scattering coefficient as [50, 91]

$$P_r = P_t G_t G_r \left(\frac{\lambda}{4\pi(D1 + D2)} \right)^2 \cdot \langle \rho \rho^* \rangle_{TE/TM} \quad (4.12)$$

The angular dependent scattered received power corresponding to θ_2 and θ_3 is shown in Fig. 4.9a. It was observed that, the scattered power is mostly in specular direction in θ_2 and found broad angular range in θ_3 direction. According to the measurement results, pathloss was calculated from equation 4.13, where N is the value of the sweep points and $H(f)$ is the transfer function of the channel. At

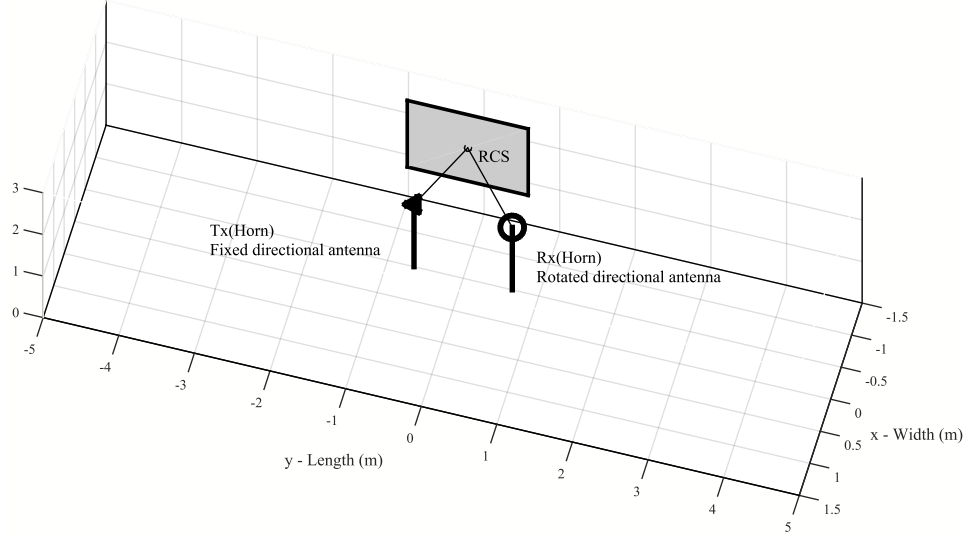


Figure 4.8 3D kirchhoff scattering model for mine.

each angle, $H(f)$ was calculated by averaging 5 snap shots taken from different time instances.

$$PL(dB) = -10\log_{10} \left[\frac{1}{N} \sum_{i=1}^N |H(f_i)|^2 \right] \quad (4.13)$$

The received power is then determined as

$$P_r(dBm) = P_t(dBm) - PL(dB) \quad (4.14)$$

The received signal from measurements was found between 0° and 90° where peaks were distinguishable from scattered power from wall. It can be noted that the dynamic range of the measuring equipment was sufficient to enable scattering power to have values well above -100 dB. Angular dependencies from measurements and simulations both were considered for azimuth angle of θ_2 direction. Antenna polarization was considered as HH (Horizontal-Horizontal) for both simulation and measurements. KA Simulation profile were defined as $[T, \sigma, \theta_i]$. Two simulation profile were used, $[T = 84, \sigma = 6, \theta = 35^\circ]$ and $[T = 90, \sigma = 6.5, \theta_i = 35^\circ]$ and corresponding comparison plot is shown in Fig. 4.9b. Result of measured received power was found to be approximately equal to the backscattered power from KA model as shown in Fig. 4.9b. It has been satisfied that simulation parameters $[T, \sigma]$ can be adjusted with the measured surface roughness parameters. The measurements were subsequently repeated for the far-field region, in which the receiver-wall distance was reduced gradually. Moreover, cross polarization measurements of transmitter and receiver antennas were performed with no significant reflected signal obtained. The results are not included since to

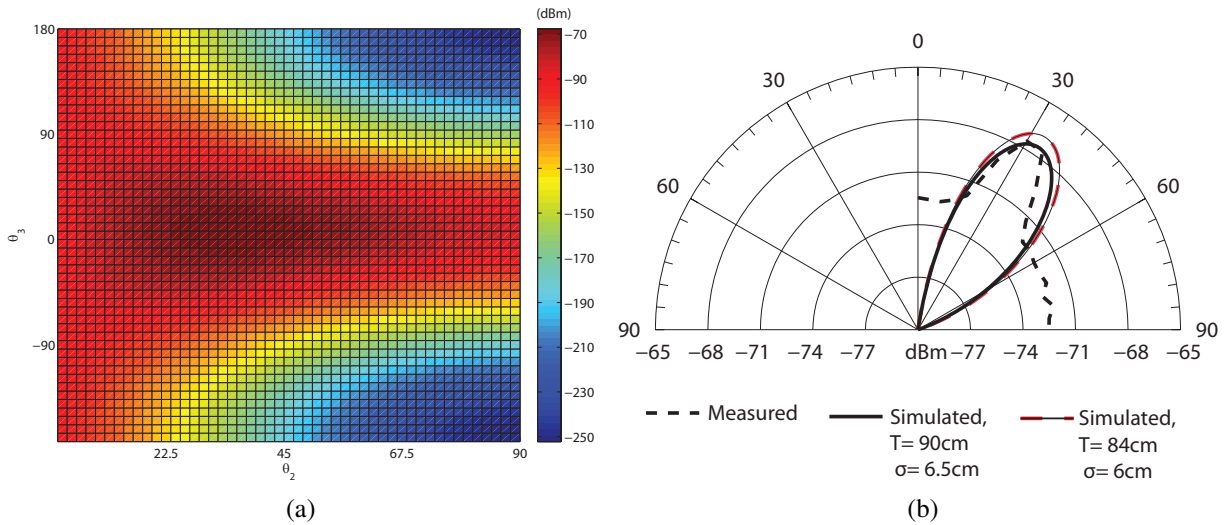


Figure 4.9 (a) Simulated angular dependent scattered received power (b) Measured and simulated scattered received power.

achieve the only cross polarized reflected signal from the wall, it is necessary to remove antenna cross polarized power from the measurements and need more investigation in this issue. It is clear that a fair agreement between simulated and measured values exists where the scattered power is above -100 dB. The peak of scattered power was found to be -98 dB (i.e., 4 dB above the noise level). It is useful to point out that incident power is scattered significantly around the specular direction of the reflected signal. The incident power is distributed around the scattering point and the scattered angular range around is about 10° . In order to compare with LOS measurement, a 30 dB difference was found between LOS and the scattered signal. This LOS measurement was a part of the scattering measurement campaign. Hence, one can conclude that there is an additional loss of the incident power during scattering from the wall due to absorption and roughness of the wall. This scattering phenomenon can make more emphasis on power delay profile simulation for the mine tunnel using KA model.

4.2 Scattering analysis based on reflection coefficients

The characteristics of reflection from the rough surface at 5 mm wavelength are necessary to be investigated. Indeed, reflection coefficients are key to the design a scattered channel model in an underground mine with rough surfaces.

4.2.1 Reflection models

Since the underground mine surface is rough and the wavelength (λ) is 5 mm, a single reflection or multiple reflections can be present during interaction of electromagnetic (EM) wave to the mine surface. A schematic illustration of the multiple reflections, e.g. refers as scattering geometry, is given in Fig 4.10, where θ_i is the incident angle and θ_r is the specular reflected angle.

4.2.1.1 Fresnel model

The Fresnel reflection coefficients (Γ) for smooth surfaces provide only the specular reflections. They are related to the material properties, which depend on the incident angle (θ_i), the polarization (vertical, horizontal) and the frequency defined as [19], [93]

$$\begin{aligned}\Gamma_{\parallel} &= \frac{\eta_2 \cos \theta_t - \eta_1 \cos \theta_i}{\eta_2 \cos \theta_t + \eta_1 \cos \theta_i} \\ \Gamma_{\perp} &= \frac{\eta_2 \cos \theta_i - \eta_1 \cos \theta_t}{\eta_2 \cos \theta_i + \eta_1 \cos \theta_t}\end{aligned}\quad (4.15)$$

The E-field component that is parallel to the plane of incidence which has vertical polarization of an antenna refers as parallel reflection coefficient (Γ_{\parallel}), whereas the E-field which is perpendicular to the incident plane has horizontal polarization of an antenna and is defined as perpendicular reflection coefficient (Γ_{\perp}). The wave impedances ($\eta_{1,2}$) and the transmitted wave angle (θ_t) are expressed in [19].

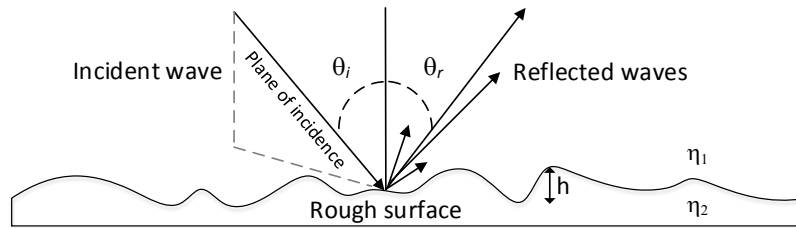


Figure 4.10 Rough surface reflection geometry.

The wave impedances ($\eta_{1,2}$) and the transmitted wave angle (θ_t) are expressed as

$$\begin{aligned}\eta_{1,2} &= \sqrt{\frac{jw\mu_{1,2}}{\sigma_{1,2} + jw\varepsilon_{1,2}}} \\ \cos \theta_t &= \sqrt{1 - \left(\frac{k_1}{k_2}\right)^2 (\sin \theta_i)^2} \\ k_{1,2} &= w\sqrt{\mu_{1,2}\varepsilon_{1,2} - \frac{j\mu_{1,2}\sigma_{1,2}}{w}}\end{aligned}\quad (4.16)$$

where 1 and 2 are the free space medium and the medium of the interacted object, respectively. The permittivity ($\varepsilon_{1,2}$), the permeability ($\mu_{1,2}$), and the conductivity ($\sigma_{1,2}$) are the dielectrics properties of the material.

4.2.1.2 Gaussian rough surface scattering model

The rough surface produces diffuse reflection, in which incident energy is distributed over the specular direction as described in [19, 50, 93]. Giving the critical height (h_c) of the surface, the dependency on the surface roughness can be defined by the Rayleigh criterion as $h_c = \lambda/(8 \cos \theta_i)$. When the height (h) of a given rough surface is defined as the minimum to maximum surface protuberance, as shown in Fig. 4.10, it is considered smooth if $h < h_c$ and rough if $h > h_c$. In the considered underground mine, h is used to be greater than 1 cm which implies an environment with rough surface. Then, the scattering loss factor (ρ_s) with the standard deviation of surface heights (σ_h) will be given by

$$\rho_s = \exp \left[-8 \left(\frac{\pi \sigma_h \cos \theta_i}{\lambda} \right)^2 \right] \quad (4.17)$$

4.2.1.3 Modified Gaussian rough surface scattering model

The scattering loss factor ρ_s is reported in [93] as modified Gaussian rough surface scattering loss factor given by

$$\rho_{sm} = \exp \left[-8 \left(\frac{\pi \sigma_h \cos \theta_i}{\lambda} \right)^2 \right] I_0 \left[8 \left(\frac{\pi \sigma_h \cos \theta_i}{\lambda} \right)^2 \right] \quad (4.18)$$

where $I_0(z)$ is the modified Bessel function of zeroth order.

4.2.2 Experimental setup and procedure

Digital photographs of measurement campaigns of the floor and the wall of that gallery are shown in Figs. 4.11 and 4.12. The measurement point of the reflection coefficient on the floor was mostly

covered with small rock tiles (dimension was approximately less than 1 cm and the form like crystal and round) and was wetted, covered with mud and mostly flatted. For the wall, which was entirely less wetted with rough surface in which the rock shape form consists like plates with large heights (average 20 cm) and sharp edges.

4.2.2.1 Procedure

A measurement procedure was carried out to find reflection coefficients in a particular reflected angle. The reflection profile has been measured with a defined test area of the underground mine floor and wall using two step processes, as depicted in Figs. 4.13 and 4.14. For a particular incident angle, the first step consisted of recording the frequency response of the line of sight (LOS) signal as shown in Fig. 4.13. Secondly, the frequency response of the reflected signal (REF) from the surface point was recorded as shown in Fig 4.14, in which Rx remained fixed and the Tx moved from 0° to 75° with a step of 15° keeping the distance $(D_1 + D_2)$ constant. D_1 and D_2 are the distances between Tx and the surface point and between the surface point to Rx, respectively. In order to make a far field region of the horn antennas, Tx and Rx were set with a separation of at 1 m. For the floor measurements, Rx was fixed with a wood at an angle of 60° and the Tx was vertically moved. For the wall measurements, the Rx remained fixed at 45° angle and the Tx was moved horizontally, and Tx and Rx were placed 1 m away from the wall. Tx and Rx positions and incident angles were assumed to be fairly accurate during measurements due to mechanical and automatic movement apparatus constraints. Physical distances D_1 , D_2 and D_{LOS} were measured from the site in order to verify with recorded propagation delays.

4.2.3 Measurement results

Measurements were performed for perpendicular (horizontal antenna polarization) and parallel (vertical antenna polarization) polarizations for the floor and wall surfaces. For each incident angle, an average of 10 LOS and 10 REF channel impulse responses have been recorded. For the post processing of the measured data, LOS and reflected channel impulse responses are shifted by 1 m reference measurement delay, samples for perpendicular polarization for the wall surface are given in Figs. 4.15 and 4.16. Fig. 4.15 shows a delay of 0.46 ns for LOS measurement at 0° and a delay of 3.2 ns at 45° . The delay of reflected signal with all incident angles remains almost fixed values between 7.4 ns to 7.8 ns. LOS and REF delays were compared with calculated physical delays and agreed fairly. Moreover, those delays are being used to calculate measured distances D_1 , D_2 and D_{LOS} to find $|\Gamma|$. Fig. 4.16 shows the maximum amplitude that has been obtained at 45° compare to 0° , since the incident and reflected angles corresponded to the specular direction at 45° . Pathloss has been calculated from equation 4.13, where N is the value of the sweep

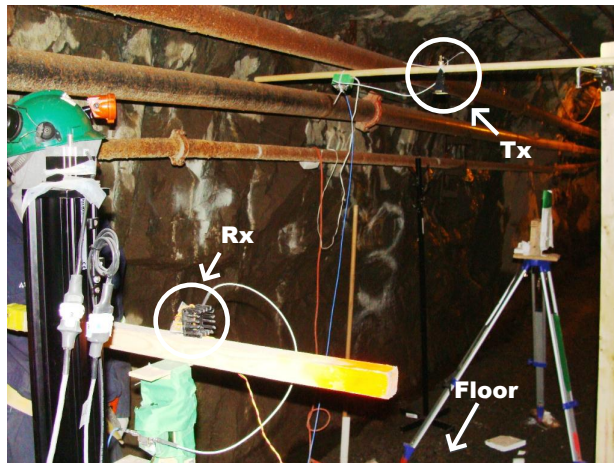


Figure 4.11 Reflection measurement campaign of the floor.



Figure 4.12 Reflection measurement campaign of the wall.

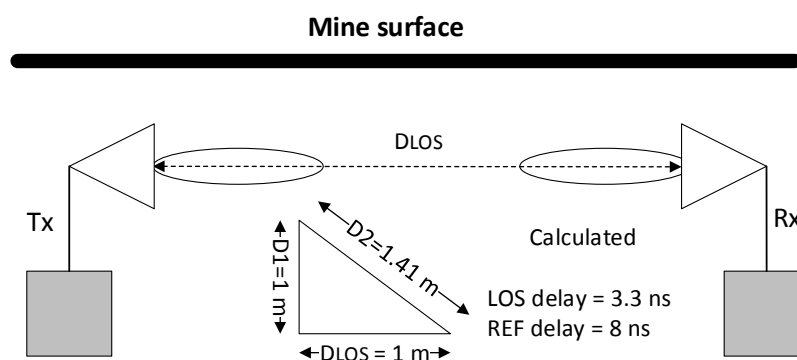


Figure 4.13 Illustration of the Line of Sight signal measurement procedure.

points and $\overline{H(f)}$ is the average (i.e., 10 snap shots) transfer function of the channel. Each measured reflection coefficient was obtained by using (4.19) with the associated measured received power

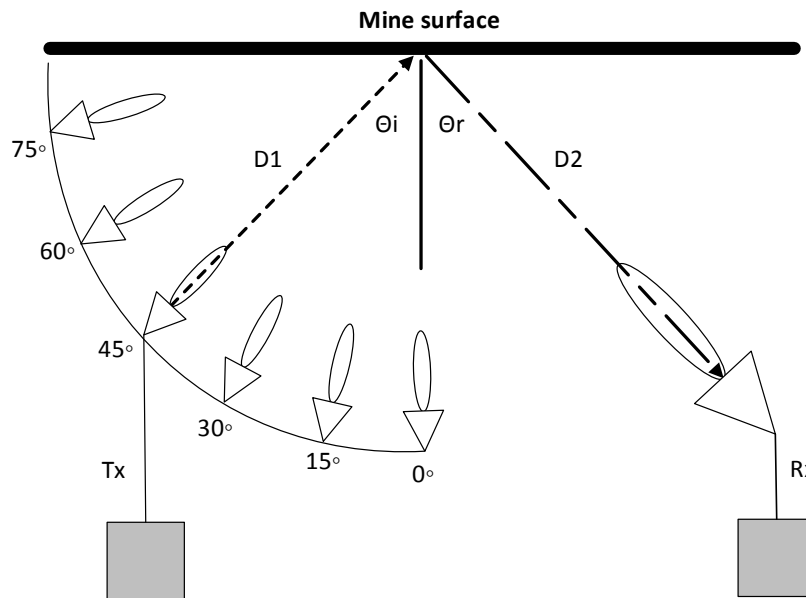


Figure 4.14 Illustration of the reflected signal measurement procedure.

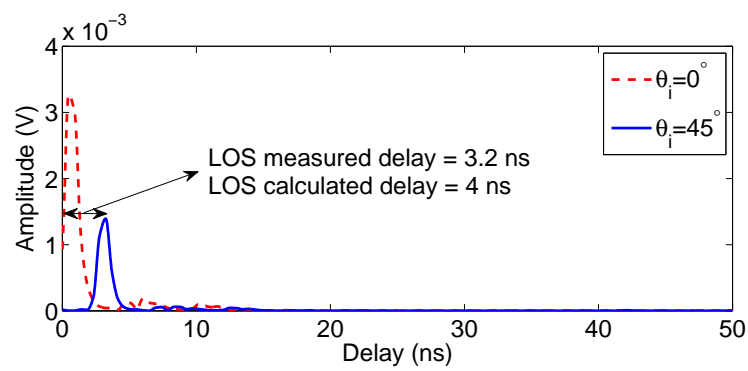


Figure 4.15 Channel impulse response of LOS signal for the wall surface.

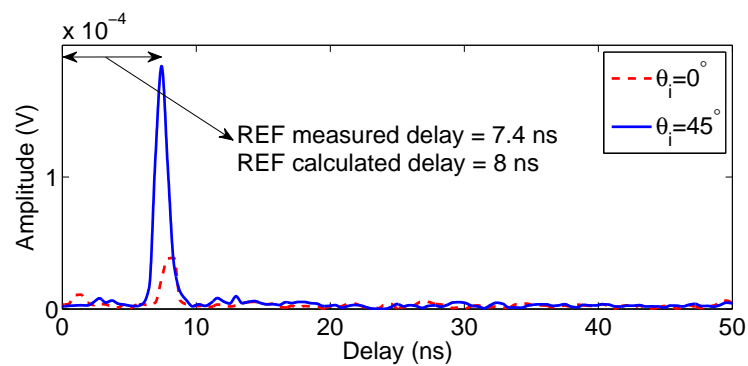


Figure 4.16 Channel impulse response of REF signal for the wall surface.

$(P_r(dBm) = P_t(dBm) - PL(dB))$ and values of D_1 , D_2 and D_{LOS} .

$$\{|\Gamma_{\parallel}|, |\Gamma_{\perp}|\} = \frac{D_1 + D_2}{D_{LOS}} \sqrt{\frac{P_{TREF}}{P_{TLOS}}} \quad (4.19)$$

Table 4.1 gives the predicted Fresnel reflection coefficients with the measured values. The permittivity (ϵ) and conductivity (σ) for the floor (limestone [56]) and the wall (Granite [60]) are assumed as 7.51, 0.03 S/m and 5.5, 0.215 S/m, respectively. Measured values exhibited additional losses of reflected signals from the wall and the floor compared to smooth surfaces due to absorptive surface material and power dissipation. It is useful to point out that the average pathloss difference between LOS and reflected signals for the wall and for the floor is found to be around 19 dB and the maximum and minimum values of the pathloss differences are listed in Table 4.2. The measured values of D_1 and D_2 and PL differences at each θ_i , have significant impact on reflection coefficient measurements. For example, in case of $|\Gamma_{\perp}|$ of the wall surface, the $D_1 + D_2$ value lies between around 2.08 m to 2.5 m, if PL difference is low at a particular θ_i and the $|\Gamma|$ value will experience higher value. Figs. 4.17 and 4.18 show the measured reflection coefficients for perpendicular and parallel polarization for wall and floor surfaces with different incident angles of θ_i , respectively. According to the surface height measurements of the wall surface (large scale range, i.e., $1.5\text{ m} \times 5\text{ m}$ area) with 10 cm grid spacing, the σ_h and T were found to be 6 cm and 84 cm, respectively [94]. The wall surface consists of a bunch of tilted rock plates (with maximum heights much higher than the wavelength) and sharp rock edges. However, in small scale area ($50\text{ mm} \times 50\text{ mm}$), it is assumed that the wall surface consists of tangent planes with a roughness less than λ and a correlation length much greater than λ . This may produce strong reflections (specular) as well as strong scattered (non specular) signals. Measurement results show high fluctuations of the reflection coefficient and strong reflections. With zero σ_h , the $|\Gamma|$ is independent of the λ . In the considered environment, the wall surface has a σ_h , exhibiting reflection coefficients that are functions of the λ . According to Kirchhoff theory, if $T \gg \lambda$, the reflections will be in specular directions. If $T > \lambda$, more diffuse components will be produce across specular directions. If the value of σ_h is constant at a particular incident angle in a given area, either it has $T > \lambda$ or $T \gg \lambda$, the maximum amplitude of reflection coefficients remains constant. Fig. 4.19 shows the predicted $|\Gamma|$ for the considered surface material

Table 4.1 Comparison of reflection coefficients of Wall and Floor.

Surface	$ \Gamma_{\parallel} $		$ \Gamma_{\perp} $	
	Fresnel	Measured	Fresnel	Measured
Wall ($\theta_i = 45^\circ$)	0.247	0.1267	0.536	0.2445
Floor ($\theta_i = 60^\circ$)	0.155	0.1389	0.691	0.2656

Table 4.2 Pathloss difference values of Wall and Floor in dB.

Surface	PL($ \Gamma_{\parallel} $)		PL($ \Gamma_{\perp} $)	
	Min	Max	Min	Max
Wall	18	23	13	21
Floor	16	22	11	26

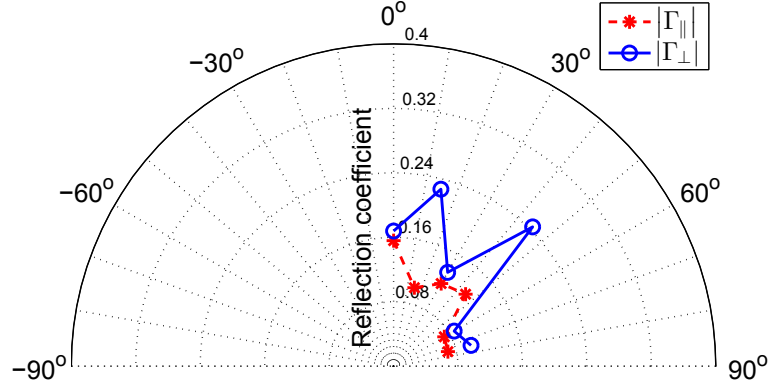


Figure 4.17 Measured reflection coefficients for the wall surface.

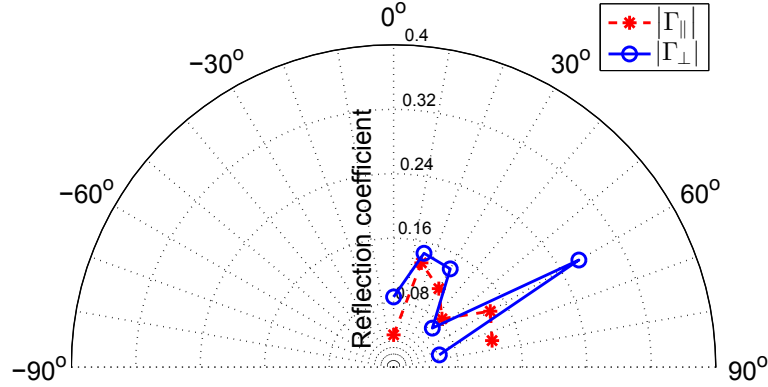


Figure 4.18 Measured reflection coefficients for the floor surface.

(i.e. granite) of the wall with $\theta_i = 45^\circ$ and $T = 10\lambda$, considering the roughness between 0 to 50 mm. According to the predicted reflection coefficients and the measured scattering limit (between maximum and minimum value) of the wall, the appropriate scattering model can be chosen for the wall surface.

On the other hand, the floor was mostly flat and filled with mud containing small rocks. By considering a small scale area ($50\text{ mm} \times 50\text{ mm}$), it may also assumed that, σ_h is less than λ and the value of T is higher than the wall surface height. Measurement results show strong reflections mostly in

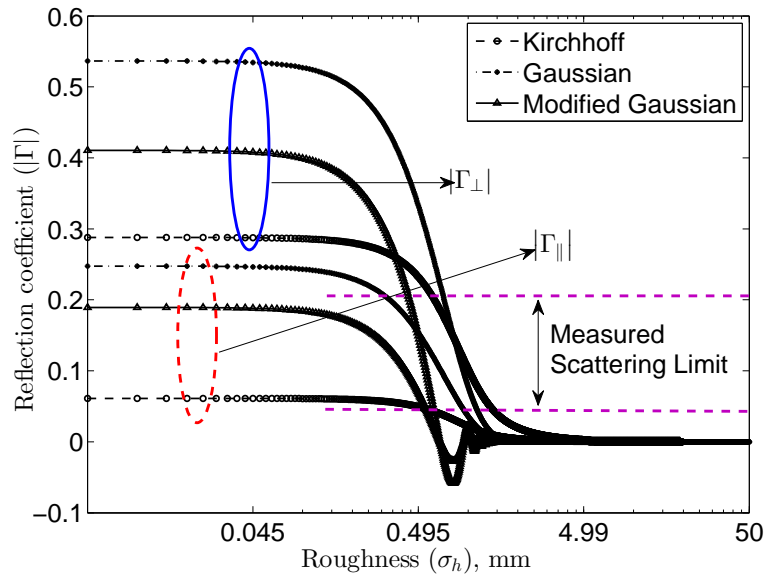


Figure 4.19 Predicted reflection coefficients for the wall surface.

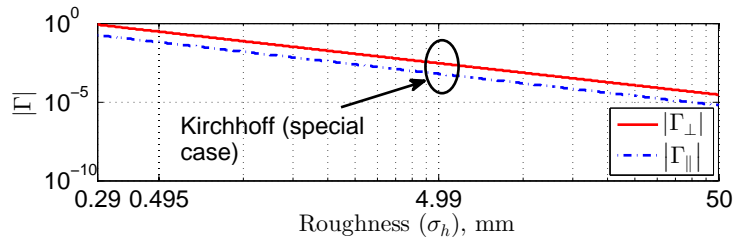


Figure 4.20 Predicted reflection coefficients for the wall surface with the special case of Kirchhoff model.

specular directions and low scattering in non specular ones. Less variability of $|\Gamma|$ compared to the wall has been observed due to the fact of lossy surface (which absorbs power), and its structural characteristics and higher correlation length of surface heights. Since the measured scattering limit of $|\Gamma|$ for the floor (with both polarizations) in specular and non specular directions is between 0.0591 to 0.2656 (as shown in Fig 4.18), it can be modelled with one of the scattering models used for the wall as shown in Fig. 4.19. If the surface roughness is higher than 5 mm then the special case of KA can be used to model as shown in Fig. 4.20. Girders and pipes may have significant scattering effect on the propagation, since the directional antennas have 12° HPBW, however, no effect has been observed during the measurements because they were outside the propagation area. Therefore, the reflection coefficients in an underground mine wall and floor surfaces have been

measured to find possible scattering models. According to the results, specular reflections of the wall and floor are strong and scattering phenomena has been found in non specular directions. This scattering phenomena exhibits to choose an available appropriate scattering model for the mine surface. Moreover, a wall surface of the mine is more reflective and scattered than lossy floor surface. The results can be used for scattered channel modelling purpose. Further investigations may be carried out to determine the reflection coefficients associated with mine floors, walls and ceilings into different frequencies and different areas and make a statistical distribution.

CHAPTER 5 CHANNEL CHARACTERIZATION WITH DIFFERENT ANTENNA POLARIZATIONS

In this chapter polarimetric large scale and small scale characterization of the wireless channel at 60 GHz band with different antenna configurations at 40 m and 70 m gallery depths in an underground mine are addressed. Large scale case, around a 10 m Tx-Rx separation distances was considered, which characterize the power Vs distance and delay spread Vs distance relationships. For the small scale case within a fraction of λ of Tx-Rx distance, a 3D grid measurements were considered, which characterize the channel as the power and delay spread versus distance relationship as well. It also characterizes the signal fading due to a random movement of the receiver (for example attached with mine workers) with a directive Tx Rx antennas. In addition, based on different antenna polarizations with different antenna configurations at 60 GHz in the CANMET underground mine have not been addressed so far as discussed in section 5.3.1 of this chapter.

5.1 Large scale characterization with different antenna polarizations.

The path loss represents the signal power attenuation in the channel in decibels and usually obeys the power distance law [93].

For the large scale case, 32 measurement locations were considered with a separation of 40λ (i.e., 20 cm), covering 1 m to 7.2 m. At each location, three consecutive measurements were taken, separated by $\lambda/2$ (2.5 mm) have a local average which eliminates the spatial small scale fading. The measurement configurations are listed in Table 5.1.

Table 5.1 Large scale measurement configurations

Mine Level	Antenna Configuration	Polarization
40	Directional - Directional (D - D)	VV, HH
40	Omnidirectional - Directional (O - D)	VV, HH
70	Directional - Directional (D - D)	VV, HH
70	Directional - Omnidirectional (D - O)	VV, HH

5.1.1 Post processing

To obtain the Power Delay Profile (PDP) for each Rx position, firstly, an average of 15 snap shots of the frequency response ($H(f)$) were performed. Secondly, to remove the antenna effect and the cable loss, over the air calibration (i.e., a division of the complex frequency response of 1 m for all complex frequency responses) was performed. Finally, Inverse Fast Fourier Transform (IFFT) of the calibrated frequency responses were then performed and the normalized PDPs were obtained. The multipath detection process was performed by the procedure described in [22]. The 1.08 MHz sweep frequency gave a temporal range of 925 ns (corresponding to the inverse of the sweep frequency), which was sufficient to observe the largest multipath excess delay (i.e., approximately 30 ns) through all sets of measurements.

Fig. 5.1 shows an example of the post-processed normalized PDP. The strongest peak of the PDP power corresponds to the first observable path. As expected in the 70 m D - D_{VV} configuration, at 3 m Tx - Rx distance, the first path was observed at a delay of about 9.7 ns. A decrement of multipath component powers with various propagation delays can be seen in Fig. 5.1. The threshold value for multipath detection was set to -25 dB. The dynamic range of the measurement was around 40 dB.

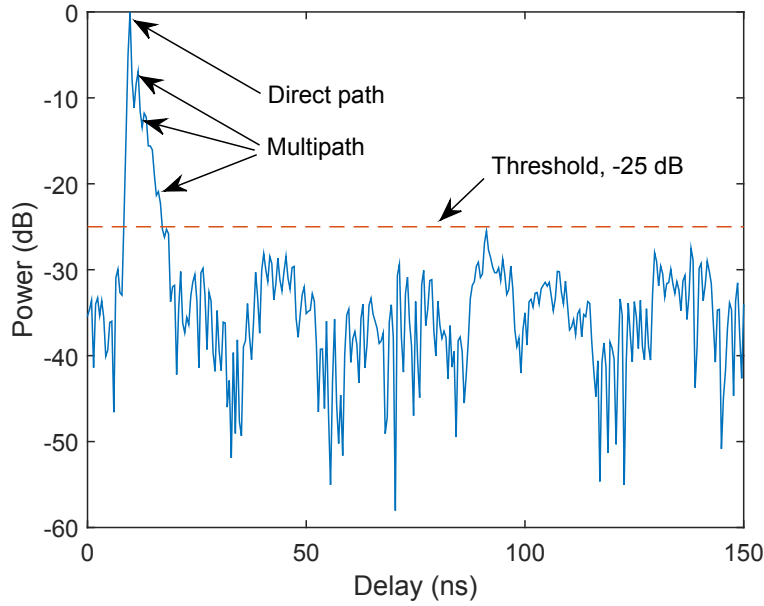


Figure 5.1 An example of a PDP.

Results of large scale (i.e., < 10 m) characterization have been analyzed by the value of path loss exponent and signal fading. The average path loss at distance $d_p(x)$ was calculated by summing all incoming multipath by the following equation, where $d_p = 1.2, 1.4, 1.6 \dots, 7.2$ and the consecutive measurement points $\{x_1, x_2, x_3\}$ are $\{0, 0.005, 0.010\}$. The free space path loss at reference

distance of 1 m (i.e., d_0) with 58.32 GHz center frequency was set to 67.76 dB [93, 95, 96].

$$PL_{dB}(d_p) = 67.76 \text{ (dB)} + \frac{1}{K} \sum_{j=1}^K \sum_{i=1}^L |a_i(d_p, x_j)|^2 \delta\{\tau - \tau_i(d_p, x_j)\} \quad (5.1)$$

where K and L are the total number of consecutive measurement points along the x direction and the total number of multipath, respectively. a_i and τ_i are the i^{th} path amplitude and delay, respectively.

By computing the deviation of path loss with respect to the linear regression line, the value of the fading was estimated from the measurements. These deviations were then fitted with a zero mean normal distribution to obtain the fading parameter.

The average path loss for any arbitrary distance between Tx and Rx can be modeled by a lognormal (normal in dB) random distribution [93] :

$$PL_{dB}(d) = PL_{dB}(d_0) + 10n \log_{10} \left(\frac{d}{d_0} \right) + S_{\sigma}(dB) \quad (5.2)$$

where n denotes the rate at which the received power decreases with the distance between antennas. $PL_{dB}(d_0)$ is the free space path loss at reference distance d_0 and S_{σ} is a fading parameter with a zero mean Gaussian random variable in dB with a standard deviation of σ_{dB} .

5.1.2 Path loss

The linear least square regression method was used to find the values of n and σ_{dB} . Fig. 5.2 shows scatter plots of the path loss in dB according to the Tx - Rx distance with different antennas and polarizations and the values obtained are summarized in Table 5.2.

The path loss exponent (n) values obtained are smaller which is close to the value found in free space (i.e., $n = 2$). This result can be explained by the phenomena of waveguiding where a direct path and a very slightly delayed path (or paths) from the surface combine at the Rx in such a way where waves guide along the x direction. This guided effect can be affected by the antenna radiation pattern and the surface roughness, particularly at 5 mm wavelength. For a small Tx - Rx distance, the reflected/scattered waves, in particular, are caught by the antenna side lobes of the directional antenna. It is important to note that the waveguide effect is more dominant in the narrow gallery (70 m) than in the wide one (40 m). The increase of the waveguide effect in the narrow gallery implies a lower value of n .

A differential value of n between VV and HH polarization may be caused by the different magni-

tude and the higher inclination of the roughness, antenna radiation pattern, and the dielectric properties of the surface material. According to the radiation patterns of the Horn antenna as shown in Fig. 5.14, with D - D_{HH} configuration ; attenuated diffused scattered waves may arrive from the walls caught by the antenna side lobes more often when compared to the D - D_{VV} one. In the case of D - D_{VV} , multipath with higher amplitudes by the antenna side lobes may arrive from the reflective floor and ceiling. On the other hand, vertically polarized Omnidirectional antenna waves propagate in an azimuth plane with a wider angle of HPBW, and correspondingly resulting in a higher number of multipath with higher amplitudes from the surrounding surface. In the case of the horizontal polarization, the waves propagated in the elevation plane with a wider angular range, and a slightly lower number of multipath components arrived from the surrounding surface. Hence, the VV polarization provides more multipath components and less value of path loss exponent than the HH polarization.

Table 5.2 Large scale measurement results.

L	A	P	n	σ_{dB}	τ_{rms} (ns)		$\bar{\tau}$ (ns)		τ_{max} (ns)		B_{c90} (MHz)	
					μ	σ	m	s	μ	σ	μ	σ
40 m	D - D	VV	1.87	1.76	1.86	0.38	0.38	0.1	28.06	7.15	26.44	2.09
		HH	2.18	1.39	1.83	0.43	0.33	0.14	26.25	5.82	44.69	34.11
	O - D	VV	1.10	1.12	2.66	0.56	2.06	0.69	11.51	3.58	30.76	14.85
		HH	1.97	1.59	2.04	0.41	1.52	0.53	6.53	1.91	37.75	15.43
70 m	D - D	VV	1.48	1.39	1.22	0.23	0.30	0.11	10.15	3.21	105.31	10.04
		HH	1.80	2.05	1.12	0.37	0.23	0.10	20.11	7.64	97.45	8.91
	D - O	VV	1.15	1.53	1.40	0.59	0.60	0.30	9.89	7.47	88.19	28.46
		HH	1.98	1.13	0.97	1.33	0.22	0.26	7.33	11.31	172.73	81.14

Note : L is the mine gallery levels, A is the antenna configurations, P is the antenna polarization types. Moreover, D - D, D - O and O - D are Horn-Horn, Horn-Omni and Omni-Horn antenna configurations, respectively.

According to the results, a better radio coverage can be achieved with VV polarization in this underground mine than in the free space situation. Without the polarization effect, results show path loss exponents ranging between 1.4 and 1.8 for different kinds of indoor and underground mine environments [39, 72, 97, 98, 99, 100]. The directivity of the Horn antenna has a significant impact on the maximum receiving power due to a lower value of HPBW. The obtained values in both galleries imply that the Horn-Horn antenna configuration gives the best results for high speed wireless communication systems in mine environments due to antenna directivity and lower signal degradation. In addition, the use of both polarizations in the system may help to enhance the

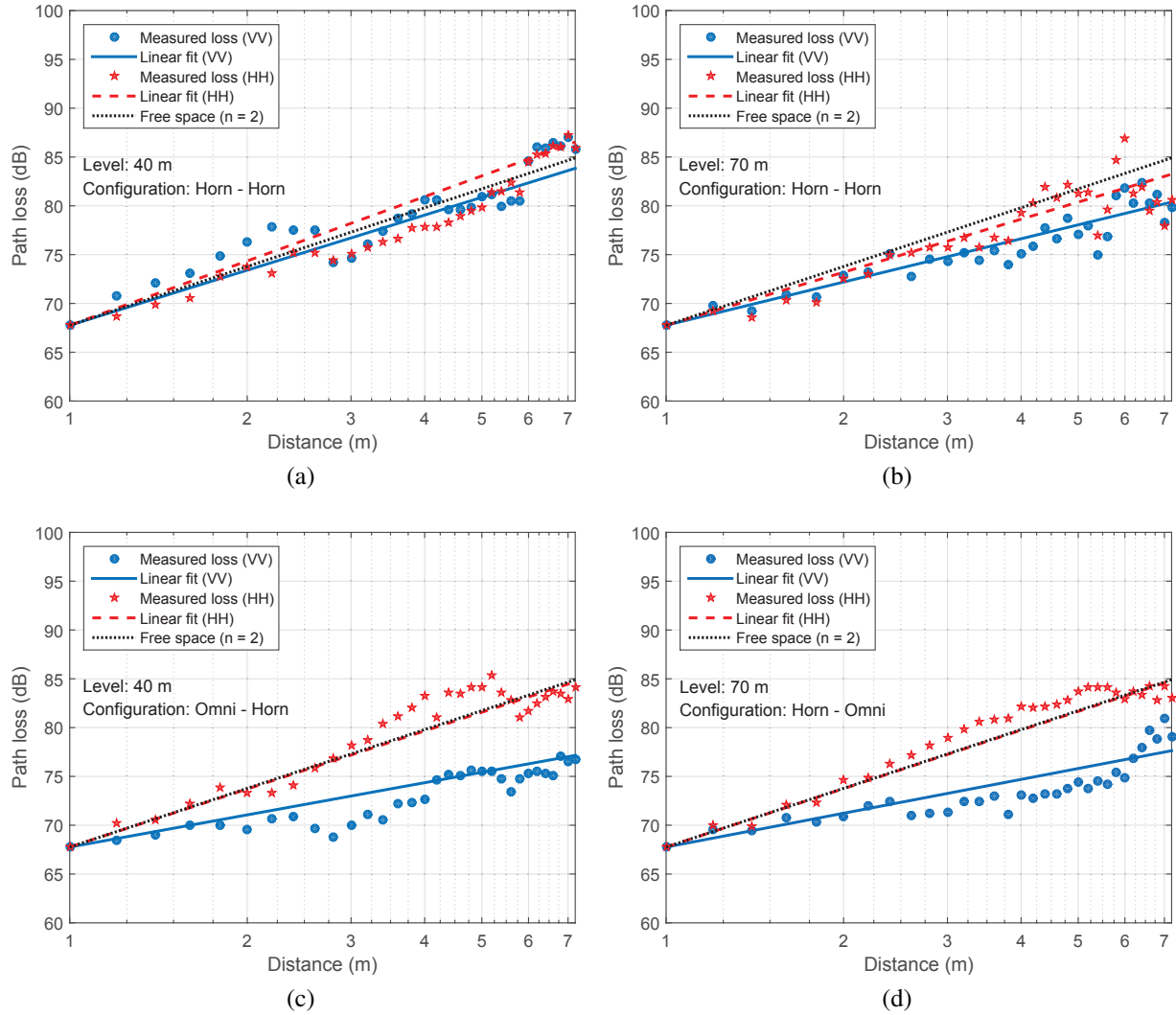


Figure 5.2 Scatter plot of path loss as a function of Tx - Rx separation distance with different antenna and polarization configurations. (a) and (b) are the Horn-Horn configurations at 40 m and 70 m, (c) and (d) are the Omni-Horn at 40 m and Horn-Omni at 70 m gallery, respectively.

capacity. Omnidirectional antennas are not very effective at 60 GHz because of lower directivity and gain compared to the directional antennas, but they might be appropriate for the wider signal coverage.

5.1.3 Interference fading

Interference fading can be characterized by increasing and decreasing signal losses, when the Rx is driven at a LOS direction in the presence of fixed objects (rough walls, metallic pipes and nets, ventilation system at the ceiling, water puddles etc.) in the environment. Sharp edged rocks that are

larger than the wavelength (5 mm) can increase the effects of large-scale radio signal fading due to reflection, diffraction, and scattering, in which the signal power variations along a wireless link can be characterized by statistical distributions. In order to quantify this, the deviations of the path-loss values from the linear regression line were calculated and the standard deviation of the variations (σ_{dB}) was estimated. The obtained results of σ_{dB} are summarized in Table 5.2. An example of the cumulative distribution of fading between the fitted and the measured data is then plotted in Fig. 5.3. Large scale fading in underground mines is usually found to be normally distributed [23]; this was seen to be consistent in all of our configurations.

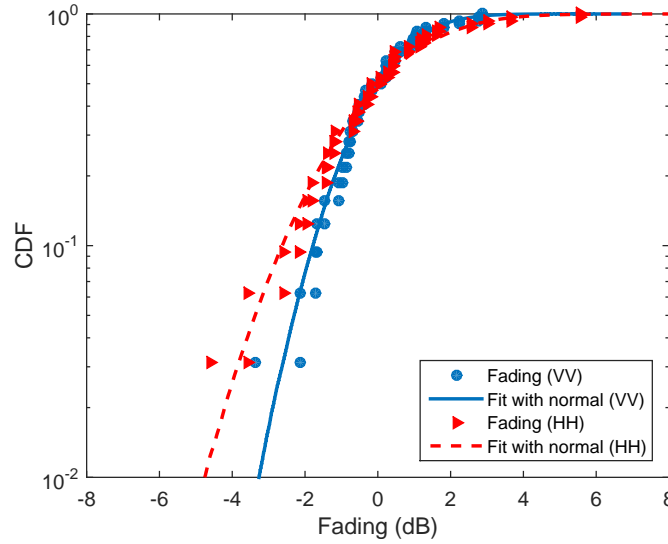


Figure 5.3 An example of shadow fading CDF fitted with the normal distribution at 70 m (Horn-Horn).

5.1.4 Delay spread

Table 5.2 shows the time dispersion parameters from the large scale measurements (between 1 m and 7.2 m distance). The time dispersion parameters extracted from the PDPs, are defined in equations 5.7, 5.8 and 5.9 of section 5.2.1. These results show that a higher value of RMS delay spread implies a lower path loss exponent value. The use of vertical polarization provides a higher values of RMS delay spread than horizontal ones. Moreover, a higher gallery dimension provides higher values of τ_{rms} and τ_{max} corresponding to a lower value of B_{c90} .

5.2 Small scale characterization

Since the presence and absence of multipath amplitudes and delays at 5 mm wavelength may arise the reflected/scattered waves from the surrounding rough surface, a 3D small scale measurement ($x \times y \times z$) was considered. Therefore, two measurement locations (i.e., 1 m and 3 m) were considered and the measurement configurations are listed in Table 5.3. At 40 m D - O case, HH polarization has been considered to characterize the channel with horizontal polarization configuration in a small scale area.

Table 5.3 Small scale measurement configurations

Mine Level	Antenna Configuration	Polarization
40	Directional - Directional (D - D)	VV
40	Directional - Omnidirectional (D - O)	HH
70	Directional - Directional (D - D)	VV
70	Directional - Omnidirectional (D - O)	VV

The grid positions can be defined as $d_{x,y,z}$. The measured channel transfer function can also be defined as $H(f, t, d_{x,y,z})$, where $x = x_1 \dots x_5$, $y = y_1 \dots y_5$, $z = z_1 \dots z_5$. Therefore, for a position $d_{x,y,z}$ the averaged measured channel impulse response can be calculated as follows :

$$h(\tau; d_{x,y,z}) = IFFT \left[\frac{1}{M} \sum_{j=1}^M H(f_i, t_j, d_{x,y,z}) \right] \quad (5.3)$$

where M is the number of snapshots taken at each time t , τ is the path delay and i is frequency sample index with $i = 1, 2, \dots, 2000$. The PDP can be calculated as

$$P(\tau; d_{x,y,z}) = |h(\tau; d_{x,y,z})|^2 \quad (5.4)$$

The PDP can be defined as follows [93, 101] :

$$P(\tau; d_{x,y,z}) = \sum_{i=1}^N |a_i(d_{x,y,z})|^2 \delta\{\tau - \tau_i(d_{x,y,z})\} \quad (5.5)$$

where N is the number of multipath components, a_i and τ_i are the i^{th} path amplitude and delay, respectively.

5.2.1 Channel parameters

The time dispersion parameters of the channel such as the mean excess spread ($\bar{\tau}$), the maximum excess delay (τ_{max}) and the root mean square (RMS) delay spread (τ_{rms}) [93, 102] have been extracted from the PDPs followed by the equation 5.5. The τ_{rms} can be expressed as :

$$\tau_{rms} = E_d\{\tau_{rms}(d_{x,y,z})\} \quad (5.6)$$

where $E_d\{\cdot\}$ is defined as the mean value of τ_{rms} collected from every grid points ($d_{x,y,z}$). The $\tau_{rms}(d_{x,y,z})$ at each point is mathematically defined as :

$$\tau_{rms}(d_{x,y,z}) = \sqrt{\tau^2 - (\bar{\tau})^2} \quad (5.7)$$

where $\bar{\tau}$ is the mean excess delay and its first and second moments ($n=1, 2$) expression is given below :

$$\bar{\tau}^n = \left[\sum_{i=1}^N a_i^2 \tau_i^n \right] / \left[\sum_{i=1}^N a_i^2 \right], \quad n = 1, 2 \quad (5.8)$$

where N is the total number of paths, τ_i and a_i are the i^{th} path delay and amplitude, respectively.

The coherence bandwidth (B_c) is defined as the range of frequency components in which the amplitudes are correlated strongly [103]. The frequency correlation function $R(\Delta f)$ of the channel can be obtained from the Fast Fourier Transform of the PDP (only taken multipath and without the noise) as [104, 105] :

$$R(\Delta f) = FFT [P(\tau; d_{x,y,z})], \quad \Delta f = 1 \dots P \quad (5.9)$$

where Δf is the frequency separation of $H(f; d_{x,y,z})$ and P is the total number of sweep point. The minimum frequency separation of $|R(\Delta f)|$ has been calculated as B_c , where B_c can be defined as 90% below from the value of $|R(\Delta f)|_{\Delta f=P/2}$. An example of the correlation function of the frequency deviation is shown in Fig. 5.4.

5.2.2 Small scale fading and delay-spread statistics

5.2.2.1 Fading

In order to evaluate 3D small-scale (i.e., 1 cm^3) fading statistics in a local area, the normalized multipath total powers (e.g. the power summation of all multipath components) were extracted from the PDPs. Examples of the spatial distribution of normalized total multipath power at each receiver location at 3 m distance is shown in Fig. 5.5 and 5.6. It can be seen that the signal power

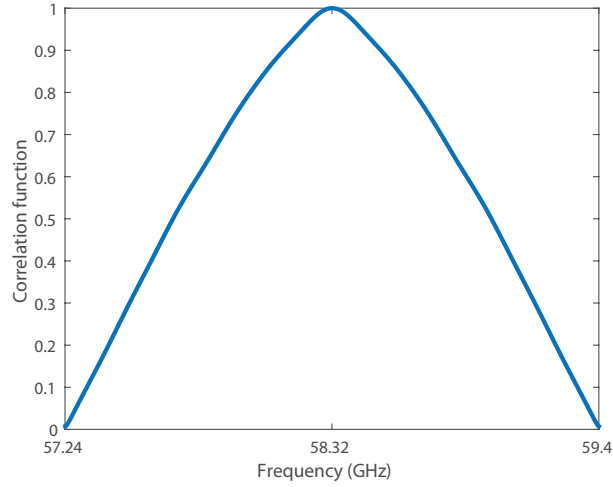


Figure 5.4 An example of correlation function of the frequency deviation at 70 m (Horn-Omni).

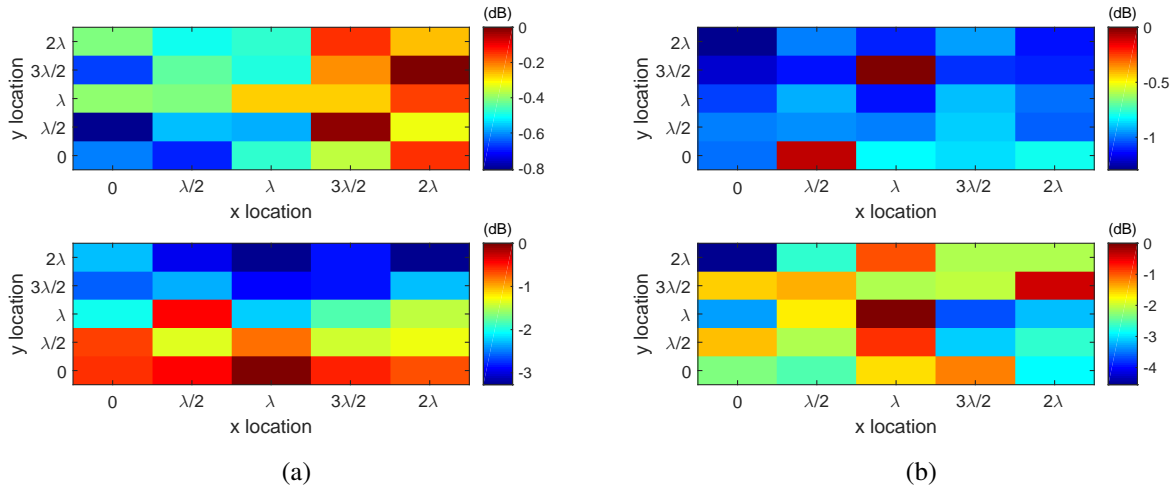


Figure 5.5 An example of a spatial distribution of total multipath power with $x \times y$ and $z = \lambda$ (which is aligned) for different antenna configurations. (a) 40 m (the upper plot is $D - D_{VV}$ and the lower plot is $D - O_{HH}$) and (b) 70 m (the upper plot is $D - D_{VV}$ and the lower plot is $D - O_{VV}$).

is mostly distributed throughout the grid points at 70 m. These power variations may have been caused by environmental factors such as the narrow passage with rough surface. At 40 m, the power is mostly directive due to smaller signal fluctuation and larger gallery dimension. It was observed that the average small scale fading ranges from 1 to 2 dB and 3 to 5 dB for Horn-Horn and Horn-Omni configurations, respectively. This implies that the Rx may experience, at most, an additional 1 to 5 dB loss when it moves by a particular cubical area (i.e., 1 cm^3). The Rx antenna height along the z direction also contributes to power variations with a step of $\lambda/2$. The multipath

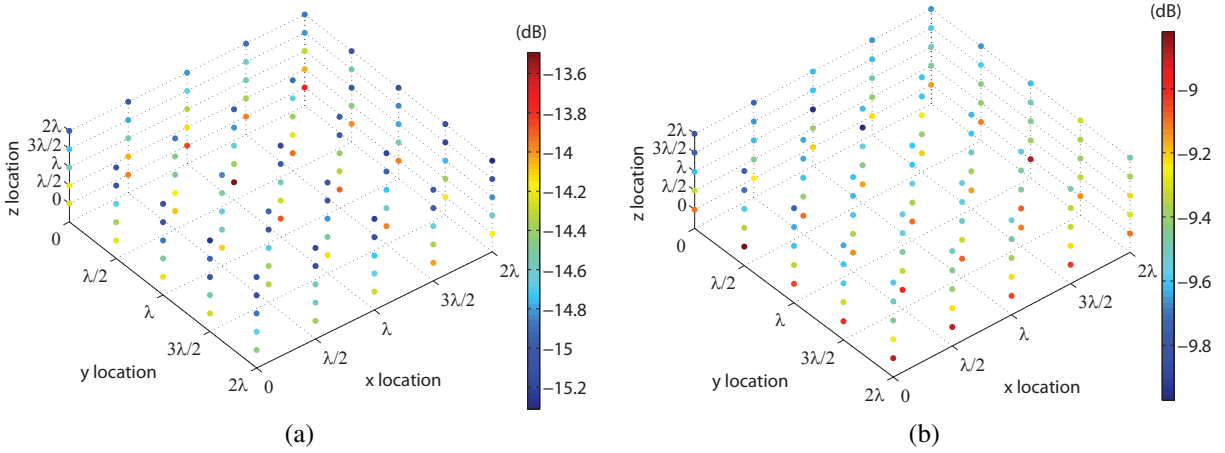


Figure 5.6 An example of a spatial distribution of total multipath power with $x \times y \times z$. (a) 40 m $D - D_{VV}$ and (b) 70 m $D - D_{VV}$.

total power at different Rx heights resulted in a directive propagation phenomena also at 40 m. Moreover, variations around 2 dB and 4 dB were observed for Horn-Horn and Horn-Omni antenna configurations, respectively. Therefore, in a small cubical area (i.e., 1 cm^3), the 1 to 5 dB amplitude fading of Rx displacement would be present in the mine environment at 60 GHz. In summary, multipath fading within a small scale area at 60 GHz is lower than the lower operating frequencies such as 2.4 GHz.

The distribution of small scale multipath amplitudes of the LOS channel can be modeled as a Rician distribution which characterizes the stronger LOS path and the scattered multipath. This is why to find statistical characteristics of the amplitude fading, different known distributions have been compared. To identify the best-fitted distribution with the experimental results, the Kolmogorov-Smirnov Test (KST) was performed by having the lower value of the k . Fig. 5.7 shows an example of measured cumulative distribution functions (CDF) of multipath amplitude fading, which fit with the Rician distribution. A comparative study of all configurations showed that Rician distributions matched in both galleries, since the Tx were Directional Horn antenna in the LOS direction, and a strong dominant direct path and scattered multipath arrived at the Rx [7].

5.2.2.2 Delay spread

The mean and standard deviation of $\bar{\tau}$ (the mean excess delay), τ_{rms} (RMS delay spread), τ_{max} (the maximum excess delay) and channel coherence bandwidth (B_{c90}) for different antenna configurations were computed from the PDP of each measurement of the 3D grid points and are summarized in Table 5.4. According to the results of the D - D configuration, the 40 m gallery provided a higher

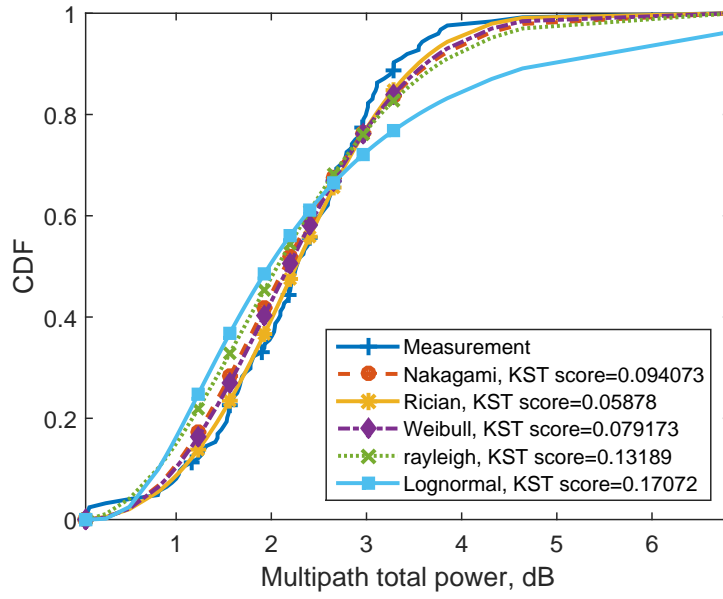


Figure 5.7 An example of small scale fading distribution with $D - O_{VV}$ configuration at 70 m.

Table 5.4 Small scale measurement results

Configuration	τ_{rms} (ns)		$\bar{\tau}$ (ns)		τ_{max} (ns)		Bc_{90} (MHz)	
	μ	σ	μ	σ	μ	σ	μ	σ
40 m $D-D_{VV}$	1.20	0.14	0.48	0.10	22.15	0.38	34.86	2.4
40 m $D-O_{HH}$	1.11	0.36	0.47	0.26	11.13	9.42	45.78	14.27
70 m $D-D_{VV}$	0.77	0.51	0.36	0.27	9.05	11.39	130.76	11.14
70 m $D-O_{VV}$	1.62	0.71	0.89	0.45	9.07	9.62	58.59	32.25

τ_{rms} value than the 70 m gallery due to the higher gallery dimensions that cause higher path delays. The results of 40 m $D-O_{HH}$ show that the τ_{rms} value is lower which may have been caused by the Horn and Omnidirectional antennas' HPBW's (in the azimuth plane with horizontal-horizontal case) of 12° and $\sim 40^\circ$, respectively. The horizontal polarization of the Omnidirectional antenna was used to observe any influence with horizontal polarization for a geolocation links between moving miners. For the 70 m $D-O_{VV}$ case, on average, higher numbers of multipath components were observed compared to all configurations and it provided a higher value of τ_{rms} . This is due to the use of Omnidirectional antenna at the Rx, the presence of narrower gallery dimension, and metallic pipes beside the LOS, which may have added a higher number of multipath with higher amplitudes at the Rx.

Ben Mabrouk et al. [35] reported an RMS delay spread is approximately 7 ns. Since this experiment was with MIMO channels with 60° HPBW of antennas in a different environmental topology, a higher number of multipath may have arrived at the Rx with larger amplitudes and delays. On the other hand, an RMS delay spread of around 2 ns is reported in [37] by using a Horn antenna of 16° HPBW. The differences between the obtained results due to the distinct HPBW. Hence, the time dispersion results of the polarimetric measurements depend on a specific environment and antenna radiation pattern.

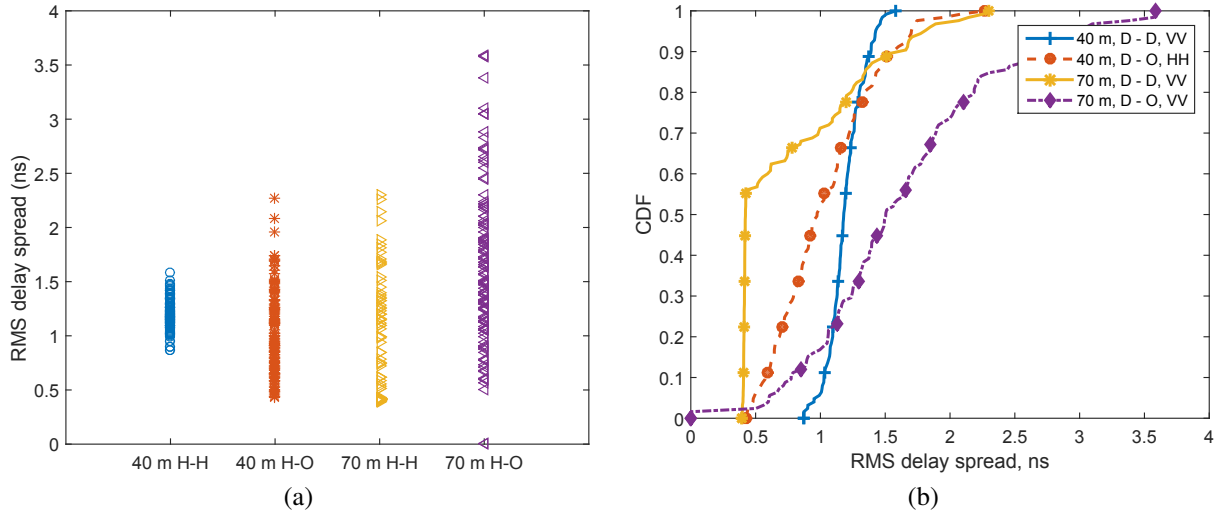


Figure 5.8 (a) RMS delay spread values with different antenna configurations. Note : the measurements at 3 m Tx Rx separation distance consisting of 125 ($5 \times 5 \times 5$) points and (b) CDF of RMS delay spread values.

The RMS delay spread values of 3D grid points at 40 m and 70 m are shown in Fig. 5.8a. These results show that the Horn-Omni configuration provide a higher time dispersive phenomena compared to Horn-Horn due to the use of Omnidirectional antenna which provide a higher fluctuation of multipath amplitudes with a higher value of HPBW. Moreover, with a Horn-Horn configuration, a higher time dispersive channel was observed in the VV case at 70 m compared to 40 m due to the narrow gallery with a different roughness magnitudes.

The empirical CDF of the value of τ_{rms} is illustrated in Fig. 5.8b. It seems that the standard deviation of RMS delay spread does not vary. The radiation pattern of the directional antenna in both Tx and Rx has a major advantage to reduce the number of multipath components in the underground mine gallery, and consequently maximizes the data transfer rate.

For small scale amplitude fading and time dispersion characteristics, the 3D grid measurement procedure is more effective since it eliminates the antenna misalignment issues in the underground

mine particularly at millimeter wave.

Table 5.4 shows the different values for channel coherence bandwidth. At 70 m, the mean coherence bandwidth of the Horn-Horn configuration is greater than the Horn-Omni configuration due to the small number of multipath in the channel. Overall, a smaller standard deviation for the value of coherence bandwidths has been observed with D - D compared to D - O.

This is to note that, to design a wireless communication system, the symbol length (T_s) is necessary to define according to the value of RMS delay spread [106]. If the Inter Symbol Interference (ISI) exists in the system, need an equalizer to have reliable wireless communication. The explanation is given below :

$$T_s > 10 \times \tau_{rms} \text{ (No ISI)} \quad (5.10)$$

$$T_s < 10 \times \tau_{rms} \text{ (ISI)} \quad (5.11)$$

This is also to have a relationship between coherence bandwidth and system data rate by applying :

$$R = W/2 \quad (5.12)$$

where R and W are the data rate and coherence bandwidth, respectively [106]. Measurement results show that the coherence bandwidth with D - D communication system provides around 100 MHz and 40 MHz at 70 m and 40 m galleries, respectively. For a reliable underground communication system in the CANMET underground mine the large scale and small scale results show that the signal undergoes frequency selective fading due to the smaller coherence bandwidth of the channel compared to the signal bandwidth (2.16 GHz), indicate an equalizer (adaptive tapped delay filter) will be needed in the Rx. As well, the data rate of the system, on average, would be less than 50 Mbps and 20 Mbps for 70 m and 40 m galleries, respectively.

5.3 Antenna polarizations effect

It is important to investigate time dispersion characteristics with different antenna polarizations for the scattered channel, since scattering phenomenon with different antenna polarizations may change the multipath arrival, amplitude, and the change of state from H to V or vice versa. The time resolution which is the inverse of the bandwidth, is taken as 0.46 ns to consider all detected paths. The extracted number of multipath components and RMS delay spread with respect to Tx - Rx distance, as illustrated in Fig. 5.9, employ the procedure described in [22, 93]. Results show that the relationship between the number of multipath and the distance exhibits a random behavior and observed a little trend of decrement in the 40 m gallery in both polarization configurations. In the 70 m gallery, the number of paths remains random and observed a little trend of constant. The number

of multipath were found less valued at 70 m gallery than 40 m gallery. Moreover, the horizontal polarization of the Omnidirectional antenna configuration results exhibited less multipath compared to the vertical polarization. The RMS delay spread values were found to behave randomly according to Tx - Rx distance.

Fig. 5.9b shows the results that a wider gallery dimension and a VV polarization provide a higher RMS delay spread than a narrower gallery and a HH polarization, respectively. The difference between VV and HH polarization value occurred due to horizontal antenna polarization of the Omnidirectional antenna has a HPBW of around 40° . Accordingly, results of the total multipath power (i.e., summation of all incoming multipath power) of the signal show a less multipath addition at the Rx with *HH* exhibiting higher degradation of the signal power reception according to Tx - Rx compared to the *VV* polarization.

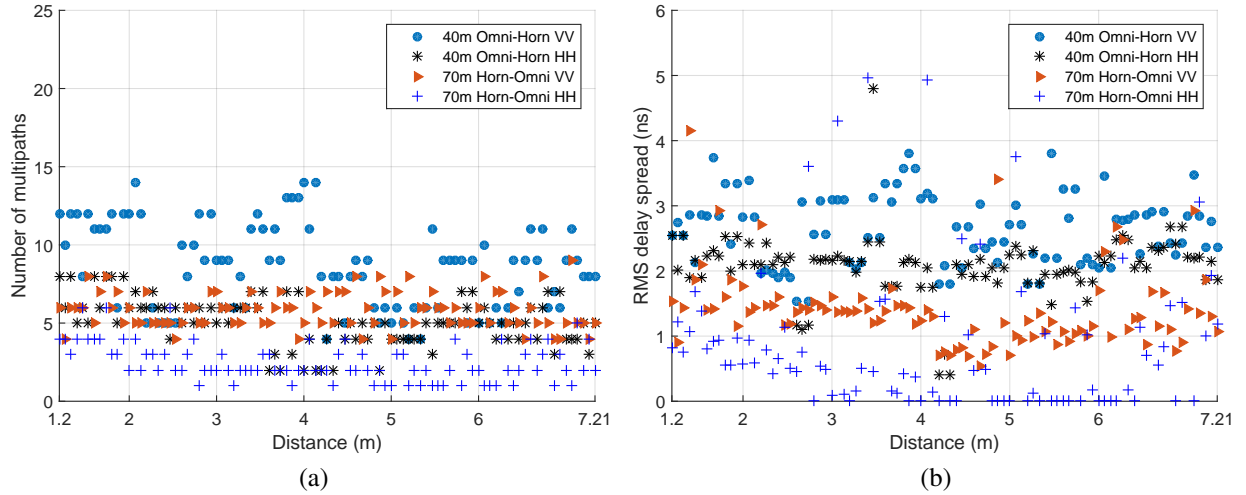


Figure 5.9 Scatter plot of time dispersion characteristics with different antenna and polarization configurations. (a) the number of multipath, (b) the RMS delay spread, with respect to Tx Rx separation distance.

The mean (μ) and the standard deviation (σ) of the time dispersion characteristics of the channel such as RMS delay spread (τ_{rms}), mean access delay ($\bar{\tau}$), maximum access delay (τ_{max}) and coherence bandwidth ($B_{c0.9}$) results are listed in Table 5.2. Results suggest that a wider gallery dimension provides a higher RMS delay spread than a narrower gallery. In both galleries, the VV polarization also provides a higher RMS delay spread than the HH polarization.

The mean value of $B_{c0.9}$ remains around 30 at 40 m gallery for VV polarization. In the 70 m gallery, the $B_{c0.9}$ fluctuates a little and the average value remains around 90 MHz with VV polarization. This difference occurred due to the wider gallery dimension at 40 m compared to the 70 m level. The Fig. 5.10 shows the CDF of coherence bandwidths. This is to note that once the horizontal

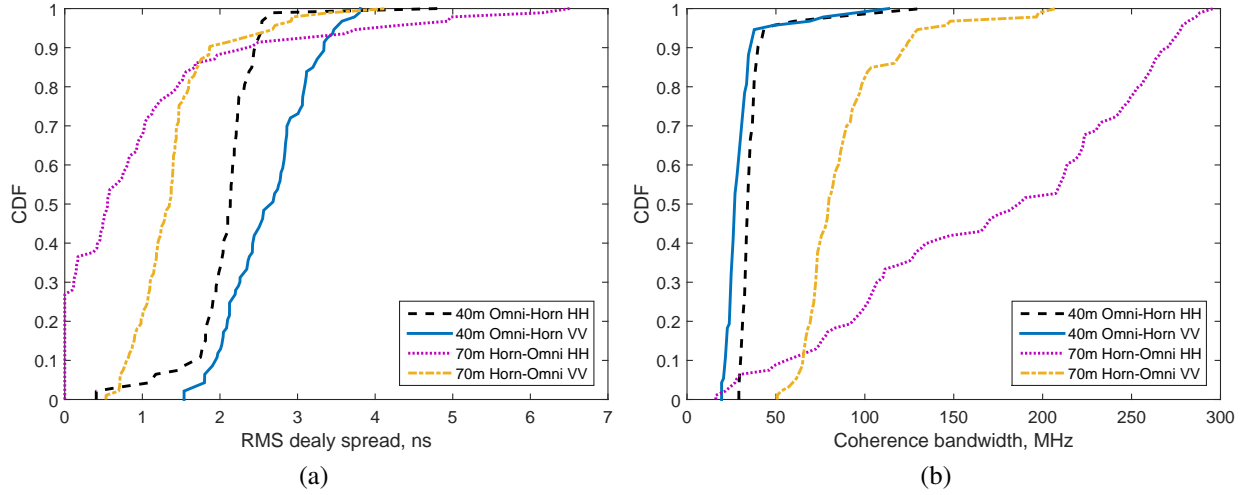


Figure 5.10 CDF of RMS delay spread and coherence bandwidth (i.e. $B_{c0.9}$) in both galleries. (a) the RMS delay spread, (b) the coherence bandwidth.

polarization of the antennas was used the values of the coherence bandwidths were observed a higher fluctuation from the median values, since the radiation pattern of the omnidirectional antenna provides sometimes one or two paths in a certain distance.

5.3.1 Comparison with other results

Experimental results in CANMET underground mine with different system setups and configurations are listed in Table 5.5. Ben Mabrouk et al. [35] reported an average of 7.65 ns RMS delay spread value in the 40 m gallery, where 50° HPBW rectangular patch (2x2) antennas with 10 dBi gain in both Tx and Rx sides of a 2x2 MIMO system were used. In this paper, a lower value of RMS delay spread of 2.63 ns has been found in the same gallery when a SISO configuration has been employed with a 12° HPBW Rx pyramidal Horn antenna (24 dBi gain) and a Tx Omnidirectional antenna (3 dBi).

The lower antenna gain provides a wider HPBW [107], resulting in the probability of having a higher number of multipath. Similarly, the experimental setup that has been used in [37] with Horn antennas and the results are listed in Table 5.5 and provide a differential value of RMS delay spread with this work due to the fact of HPBW. With 5 mm λ , the scattering phenomenon will be present, and the incident wave could change its polarization and interference of scattered waves could occur due to the coherent phenomenon. Therefore, different antenna configurations and polarizations results particularly provide an information of the scattering point of view where it can be concluded that dual polarized antenna systems at the Tx and Rx side would be the good choice for the underground mine gallery wireless system to enhance the performance and capacity.

Table 5.5 Comparison of CANMET underground mine experimental results.

Reference	Mine gallery	Frequency (GHz)	Antenna system	Polarization	BW (GHz)	A_{tx}	A_{rx}	H_{tx}	H_{rx}	$\overline{\tau_{rms}}$ (ns)
[35]	40 m	60	MIMO	Vertical	7	Patch (2x2)	Patch (2x2)	50°	50°	7.65
[37]	70 m	2.46	SISO	Vertical	0.2	Omni	Omni	360°	360°	6.31
		5.8	SISO	Vertical	0.2	Omni	Omni	360°	360°	6.14
		60	SISO	Vertical	2	Horn	Horn	16°	16°	2.14
In this paper	40 m	60	SISO	Vertical	2.16	Omni	Horn	360°	12°	2.63
		60	SISO	Horizontal	2.16	Omni	Horn	$\simeq 40^\circ$	12°	2.044
	70 m	60	SISO	Vertical	2.16	Horn	Omni	12°	360°	1.39
		60	SISO	Horizontal	2.16	Horn	Omni	12°	$\simeq 40^\circ$	0.97

Note : In [35] a 2×2 MIMO antenna system configuration was used. In [37] and in this paper, the used Horn antennas have a 16° (from [107]) and 12° (from Millitech) of HPBW, respectively. A_{tx} and A_{rx} are the Tx and Rx antennas, respectively. H_{tx} and H_{rx} are the Tx and Rx azimuthal HPBW, respectively.

In the considered measurement scenarios ; surface wall, floor, and ceiling have different values of roughness and different gallery dimensions, and the use of different antenna polarizations therefore could provide an impact on the time dispersion parameters on the channel. This impact can be characterized by the differential values of τ_{rms} .

In the considered mining environment, surface wall, floor and ceiling have different values of roughness and therefore will have different impact on the channel parameters for to use of different polarizations.

5.3.2 Impact of antenna polarizations on the scattered channel

To analyze the impact of the antenna polarizations on the channel, the analytical explanations have been carried out. A spherical coordinate system of the Tx and Rx antenna is illustrated in Fig. 5.11. The $\Omega = (\theta, \phi)$ corresponds to the coordinate point on a spherical surface of the antenna, where $\theta \in [0, \pi]$ and $\phi \in [0, \pi]$ (for Omnidirectional $\phi \in [-\pi, \pi]$) are the elevation and azimuth angles, respectively. An illustration of the line of sight (LOS) path and the scattered path with Horn antenna as a Tx and Omnidirectional antenna as a Rx is shown in Fig. 5.13. The channel parameters of l^{th} multipath is $\{L, a_l, \tau_l, \Omega_{T,l}, \Omega_{R,l}\}$, where L is the number of scattered paths, a_l is the path amplitude, τ_l is the time of arrival (TOA), $\Omega_{T,l}$ is the direction of departure (DOD) and $\Omega_{R,l}$ is the direction of arrival (DOA), respectively. The channel parameters of the LOS path is $\{a_0, \tau_0, \Omega_{T,0}, \Omega_{R,0}\}$.

A modified impulse response of the scattered channel as described in [108], by adding the polari-

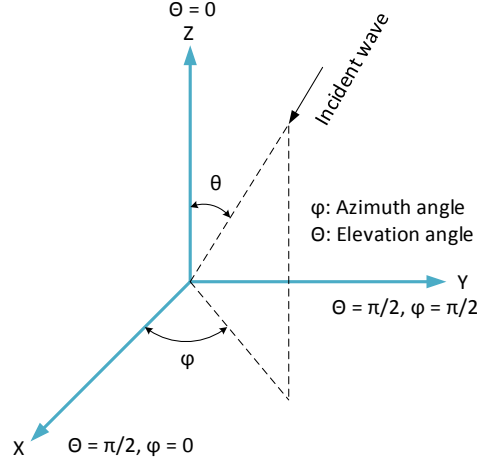


Figure 5.11 The spherical coordinates of the transmitter and receiver antennas.

zations and reflection coefficients is obtained as a function of delay, DOD, and DOA :

$$h(\tau, \Omega_T, \Omega_R) = h_{los}(\tau, \Omega_T, \Omega_R) + h_s(\tau, \Omega_T, \Omega_R) \quad (5.13)$$

$$h_{los}(\tau, \Omega_T, \Omega_R) = a_0 \delta(\tau - \tau_0) \delta(\Omega_T - \Omega_{T,0}) \delta(\Omega_R - \Omega_{R,0}) \quad (5.14)$$

$$h_s(\tau, \Omega_T, \Omega_R) = \sum_{l=1}^L a_l \delta(\tau - \tau_l) \delta(\Omega_T - \Omega_{T,l}) \delta(\Omega_R - \Omega_{R,l}) \quad (5.15)$$

$$a_l = \{a_{l,V} \cdot \Gamma_{\parallel} \cdot \rho\}; \{a_{l,H} \cdot \Gamma_{\perp} \cdot \rho\} \quad (5.16)$$

$$\Omega_{T,l} = \{\Omega_{T,l,V}\}; \{\Omega_{T,l,H}\} \quad (5.17)$$

$$\Omega_{R,l} = \{\Omega_{R,l,V}\}; \{\Omega_{R,l,H}\} \quad (5.18)$$

$$\tau_l = \{\tau_{l,V}\}; \{\tau_{l,H}\} \quad (5.19)$$

where the equation 5.14 corresponds to the LOS path and the equation 5.15 corresponds to the scattered paths. The a_l is the l^{th} scattered path amplitude. The $a_{l,V}$ and $a_{l,H}$ are the vertical and horizontal polarized amplitudes of the l^{th} path, and Γ_{\parallel} , and Γ_{\perp} are the corresponding reflection coefficients, respectively. The ρ is the scattering coefficient of the rough surface that can be estimated from scattering models as described in [109]. It is assumed that all scattered paths are received at the receiver within an angular range of Ω_R . The $\Omega_{T,l}$, $\Omega_{R,l}$ and τ_l consist of vertical and horizontal DOD, DOA and delay, respectively, and shown in the equations 5.17, 5.18 and 5.19. The power delay profile of the scattered channel can be defined as

$$P(\tau, \Omega_T, \Omega_R) = \mathbb{E}\{|h(\tau, \Omega_T, \Omega_R)|^2\} \quad (5.20)$$

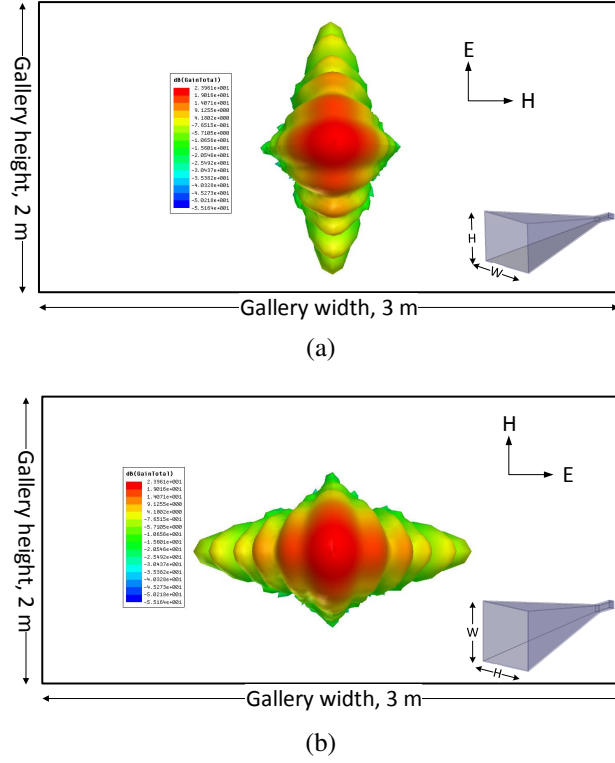


Figure 5.12 3D simulated Horn antenna radiation pattern with different polarizations with an approximation of the 70 m gallery dimensions. a) Vertical and b) Horizontal orientation, respectively.

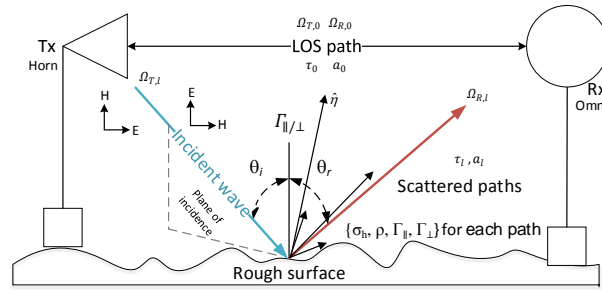


Figure 5.13 An illustration of the LOS path and the scattered paths with Horn and Omnidirectional antenna configurations by considering a rough surface, where σ_h and ρ are the standard deviation of the surface heights and scattering coefficient, respectively. The θ_i and θ_r are the incident and reflected angles, respectively. The \hat{n} is the tangent plane of the surface.

5.3.2.1 Experimental explanations

It is assumed that the channel fading is Rician distribution since Tx and Rx are in LOS. Hence, that the scattered channel can be characterized by the Rician K-factor, where K is the ratio between the power of the LOS path and the power sum of the scattered paths (vertical or horizontal) [110] and

given below :

$$K_V = \frac{|a_{0,V}|^2}{\sum_{l=1}^L |a_{l,V}|^2} \quad (5.21)$$

$$K_H = \frac{|a_{0,H}|^2}{\sum_{l=1}^L |a_{l,H}|^2} \quad (5.22)$$

K_f can be used to characterize the channel as an impact factor due to the use of vertical and horizontal antenna polarizations on the scattered channel and is given below :

$$K_f = \frac{K_V}{K_H} \quad (5.23)$$

The Co-polarization ratio (CPR) which characterize also the channel, defined as the ratio between the received power by using an antenna in vertical and the received power by using an antenna in horizontal [110] and given below :

$$CPR = \frac{|a_{l,V}|^2}{|a_{l,H}|^2} \quad (5.24)$$

The average CPR value and the correlation coefficient of the power between HH and VV polarization with Omni - Horn configuration at 40 m gallery reported in [110]. Although the mean values of the K-factor were around 25 dB for both polarizations, a lower value of the standard deviation of VV polarization was observed compared to HH one. Moreover, the average CPR value was found to be around 6 dB and a correlation coefficient of the received power between HH and VV polarization was found to be 0.8649 as reported in [110] implying a higher amplitude correlation between them.

Fig. 5.14 shows the radiation patterns of the Directional and omnidirectional antennas. The vertical polarization of the Directional antenna consists some ripples in the side lobes which may produce strong reflection/scattering from the surface compared to the horizontal polarization of the antenna. The horizontal polarization of the omnidirectional antenna consists gain fluctuations above $\pm 45^\circ$ which may produce higher multipath amplitude variations at the receiver.

5.3.2.2 Conceptual explanations

The results of time dispersion, K-factor, and CPR (reported in [110]) demonstrate that the use of vertically polarized antennas at the Tx and Rx sides shows a probability of a higher value of RMS delay spread than the use of horizontally polarized antennas. The explanations are described below :

- Antenna gains are higher in vertically polarized antennas (Horn and Omni) between $\pm 20^\circ$ and $\pm 60^\circ$ than the horizontal one. In addition, the used Omnidirectional antenna gains both in azimuth and elevation directions in a range of -40° to $+40^\circ$ are not same.

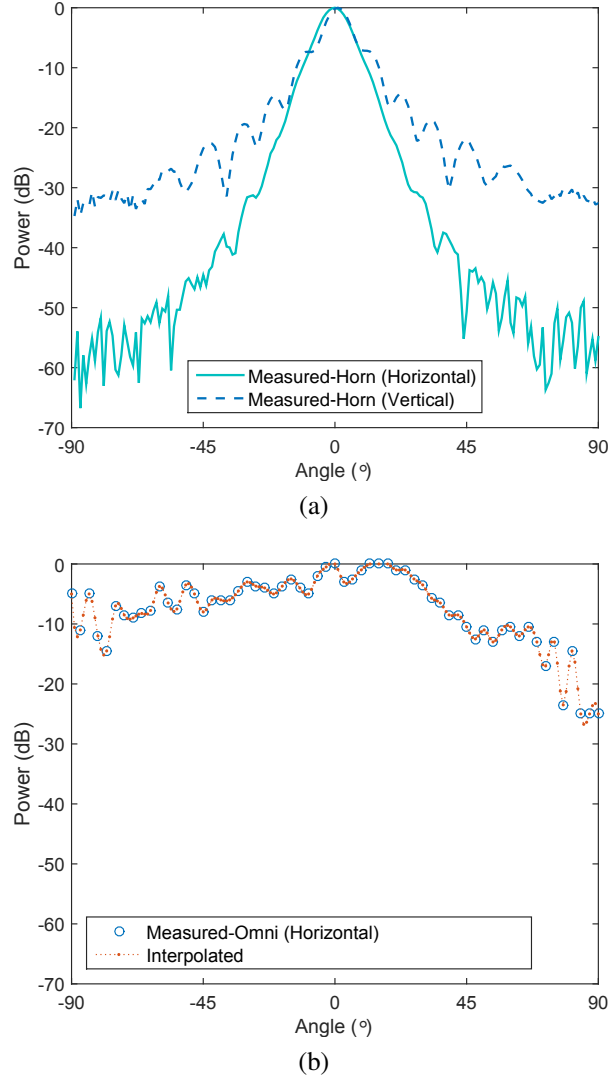


Figure 5.14 Measured 2D antenna radiation patterns with different polarizations. a) Horn and b) Omnidirectional (horizontal polarization - elevation direction). Note : in the vertical polarization (azimuth direction) of the Omnidirectional antenna consists between 0 dB and -3 dB.

- In the CANMNET gallery, the roughness magnitudes of the floor and ceiling are less than the value obtained for walls.

5.3.2.3 Geometrical explanations

The impact of antenna polarizations on the scattered channel can be characterized by the parameters,

$$\{H, W, \theta_i, \varepsilon, \sigma, \sigma_h, \alpha\} \quad (5.25)$$

where H and W are the height and width of the galleries, θ_i is the incident angle, ε and σ are the permittivity and conductivity of the material, σ_h and α are the standard deviation of roughness and percentage of polarization state change (from V to H and vice versa), respectively. Since rough surface could change the polarization state once EM wave interacts with the surface materials, the use of α would be useful to characterize the scattered channel.

Since commercial software is not fit to simulate the PDP within the underground mine gallery due to surface roughness, the hypothesis based on the geometrical explanation of the antenna polarizations impact could instead be described by the relationship of the gallery dimension and material properties in a particular incident angle. For instance, with $H > W$ and around $\varepsilon_r \gtrsim 60$ conditions, the simulation results show that the use of VV configuration provides a higher value RMS delay spread than the use of HH . Therefore, the conditions could be clarified with two factors based on assumptions of the gallery dimensions.

Firstly, antenna side lobes are towards the ceiling and the floor with vertically polarized antenna and provide a higher path delay. This condition can be clarified by that the higher amplitudes of multipath provide a higher value of RMS delay spread of the channel with the same value of TOAs while lower values of the TOA provide a lower value of RMS delay spread with the same amplitudes.

Secondly, the higher values of the permittivity of underground mine surface material (i.e., estimated as around $\varepsilon_r \gtrsim 60$ since plasterwork rough and rockwool have $\varepsilon_r \geq 30$ with 5 mm wavelength [60]) contribute a lower value of Γ_{\parallel} . This can be clarified by an example of the reflection (according to the Fresnel theory) such as with a range of θ_i around between 50° and 70° ; the 77.5 value of ε_r , the Γ_{\parallel} (vertical) provides <10 dB power loss; whereas 7.5 value of ε_r , the Γ_{\parallel} (vertical) provides a notch of ~ 30 dB power loss.

A $D - O$ configuration (a Tx - Rx distance of 7 m are considered in a geometry based simulation with the antenna radiation patterns as shown in Fig. 5.14. The simulation process was implemented in order to find the impact of the antenna radiation patterns and polarization on a scattered channel and described in Appendix C. With the Ω_T values between $\pm 70^\circ$ and $\pm 20^\circ$, the set of impact parameters $\{H = 3 \text{ m}, W = 2 \text{ m}, \theta_i = (\sim 50^\circ \text{ to } \sim 80^\circ), \varepsilon_r = 77.5, \sigma = 0.03, \sigma_h = 0.5 \text{ mm}, \alpha = 10\}$, and the use of free space propagation; the use of vertically polarized antennas provide around 0.0155 ns RMS delay spread whereas a lower value of 0.0114 ns obtained with horizontally polarized antennas. It has been observed that conductivity does not provide a strong impact between V and H polarizations.

In addition, the value of scattering coefficients (σ) which are based on Gaussian rough surface Scattering Model, modified Gaussian rough surface scattering Model or Kirchhoff scattering Model provide only a reduction of path amplitudes by multiplying it with Fresnel reflection coefficients

[109] and correspond to a lower value of RMS delay spread compared to the use of Fresnel reflection coefficients. The roughness magnitude of the mine surface within a small square area (e.g., 10 mm^2) of a facet is assumed to be less than 0.5 mm for the above models. For a higher value of roughness (i.e., $> 0.5 \text{ mm}$), the Kirchhoff scattering Model is useful to consider.

In summary, the inhomogeneous material properties of the underground mine gallery surface and its corresponding values of reflection coefficients Γ_{\parallel} and Γ_{\perp} , gallery dimensions, Tx and Rx heights, grazing angles, incident angles (θ_i), reflected angles (θ_r), DODs, and DOAs have a direct impact on the value of the RMS delay spread of the scattered channel.

5.4 Wireless InSite Simulation results

In order to explain the difference between the measurement results obtained in [35, 88, 111] and this work, a simulation scenario was carried out. The simulation scenario as shown in Fig. 5.15 is based on 70 m gallery and considered as a smooth surface. The Wireless InSite software has a parameter to deal with the surface roughness, but at 60 GHz with 6 cm roughness, it is not compatible to do a simulation scenario which is highly related to the incident angle of the ray launching approach. Moreover, it does not support MIMO configurations as well. Therefore, the Single Input Single Output (SISO) configurations were used for all setup.

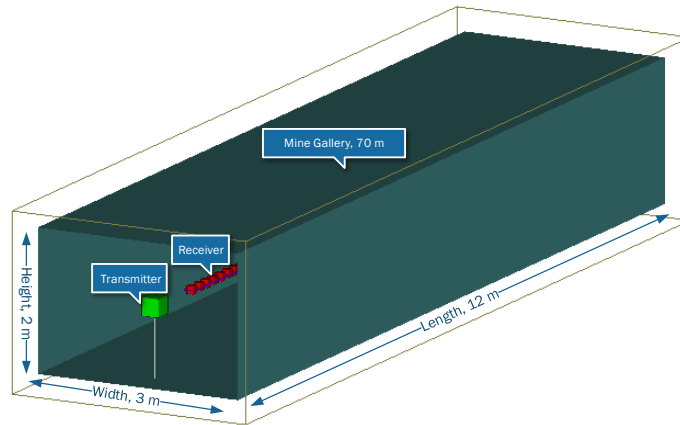


Figure 5.15 Mine model (70 m gallery).

The simulation parameters are listed in the Table 5.6. In addition, the 3D simulated antenna radiation patterns such as vertical and horizontally polarized pyramidal horn antennas are illustrated in Fig. 5.16 and 5.17. Moreover, to understand the graphical view of the scenarios the 3D radiation pattern of Omni (V) - Omni (V), Horn (V) - Horn (V), Horn (H) - Omni (H) antenna configurations

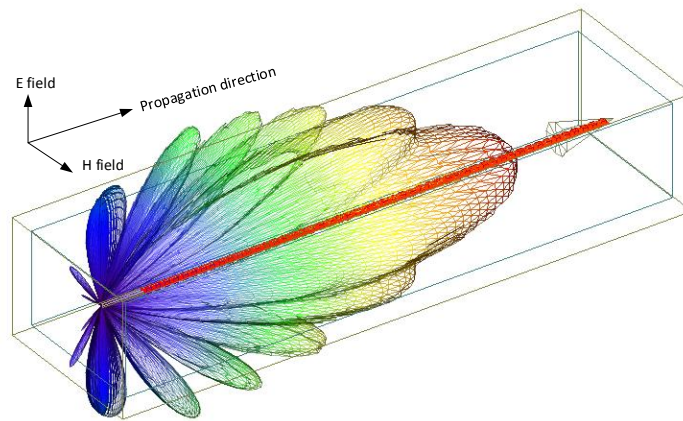


Figure 5.16 3D vertical Horn antenna radiation pattern.

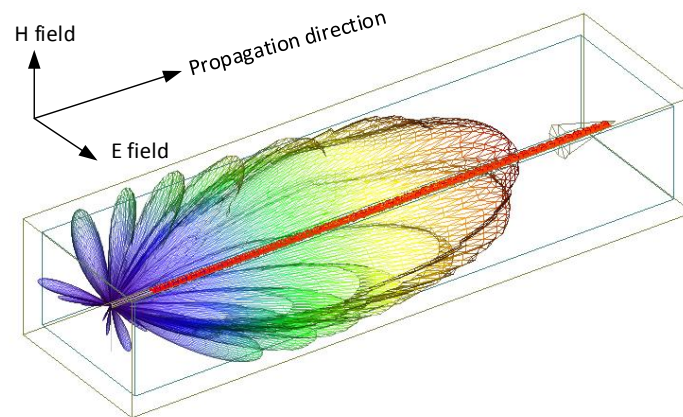
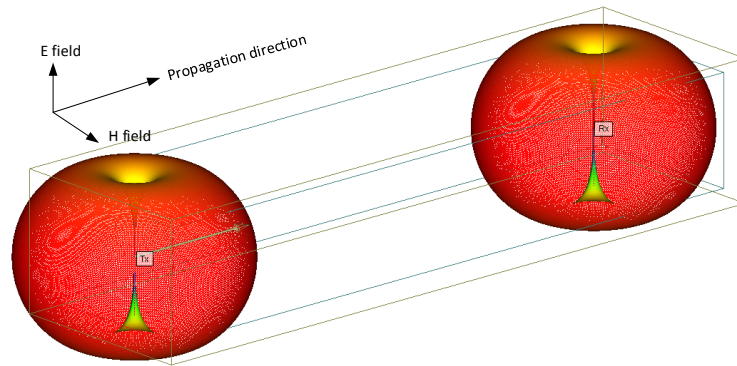


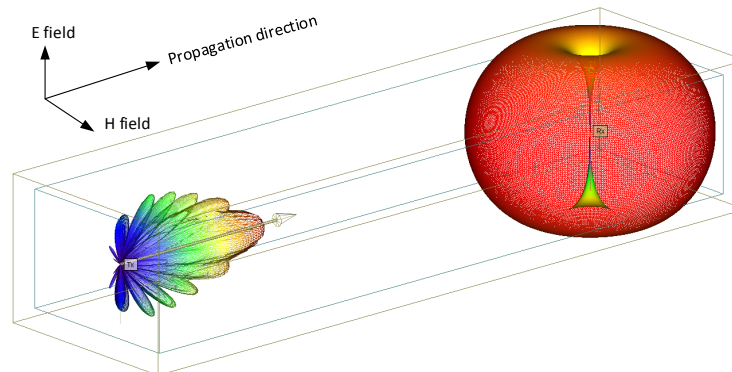
Figure 5.17 3D horizontal Horn antenna radiation pattern.

are shown in Fig. 5.18.

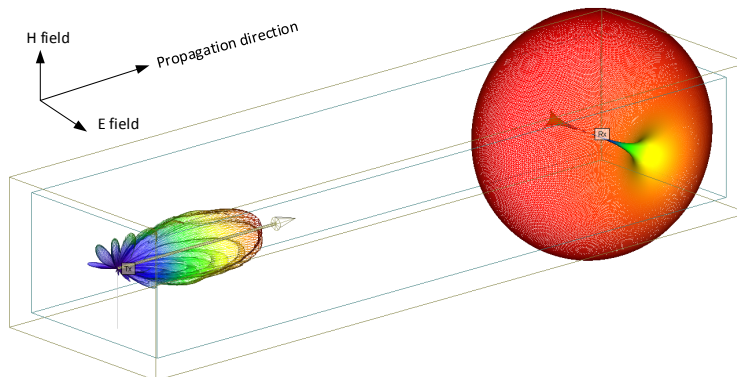
The simulation results are listed in Table 5.7 and illustrated in Fig. 5.19. Results show that the use of a higher antenna gain yields a lower value of the RMS delay spread. For the setup of 7, 2×2 antenna rectangular patch having around 50° of HPBW antennas provide a higher value (i.e., 0 - 1 ns) of RMS delay spread compared to our setups 1 to 5. The results also show that no significant difference between Horn (V) - Omni (V) and Omni (V) - Horn (V) antenna configurations (setup 4 and 5). Higher RMS delay spread value was obtained between Horn - Horn and Horn - Omni with vertical polarization (i.e., setup 1 and 3). Horn - Horn with horizontal polarization gives a little higher value of RMS delay spread than vertical polarization, since the gallery width is higher than the height. Due to the roughness of the wall and different measurement locations in the mine,



(a) Minemodel-V-pol-Omni(Tx)-Omni(Rx)



(b) Minemodel-V-pol-Horn(Tx)-Omni(Rx)



(c) Minemodel-H-pol-Horn(Tx)-Omni(Rx)

Figure 5.18 3D antenna radiation pattern with different antenna configurations.

VV polarization configurations may provide a higher value of the RMS delay spread than HH. Moreover the reason could be the metallic nets on the ceilings and the flatness of the floor could provide a strong reflected wave than rough walls which dissipate power. Using different frequencies such as 60 GHz and 2.4 GHz with a bandwidth of 2.16 GHz and 200 MHz, The average RMS value was around 1.19 ns and 1.94 ns, respectively (i.e., setups 8 and 9). For the setups of 1 and 6, a Horn antenna having around 16° of HPBW provides a higher value of the RMS delay spread compared

Table 5.6 Channel simulation parameters

Mine Level	70 m
Frequency range	57.24 GHz-59.4 GHz
Center frequency	58.32 GHz
Bandwidth	2.16 GHz
Tx power	+4 dBm
Tx/Rx height	~ 1 m/ ~ 1 m
Pyramidal Horn antenna (this work)	Gain 24 dBi, HPBW 12°
Pyramidal Horn antenna ([88, 111])	Gain 20 dBi, HPBW 16°
Rectangular 2x2 patch antenna ([35])	Gain 10 dBi, HPBW 50°
Omnidirectional antenna	Gain 3 dBi
Polarization	VV, HH
Roughness	zero
Tx - Rx Max Distance	10 m
Grid	0.20 m
Permittivity	5.5
Conductivity	1e-003 S/m
2.4 GHz center frequency	2.4 GHz
2.4 GHz bandwidth	200 MHz

to the setup 1 having around 12° of HPBW.

5.5 Rician K-factor and Co-polarization ratio results

The experimental results of the Rician K-factor and the co-polarization ratio (CPR) are obtained from the measurements conducted at 40 m CANMET underground mine gallery with Horn and Omnidirectional antennas with Horizontal (H) and Vertical (V) polarizations. Results suggest that the VV polarization offers a larger number of multipath components than the HH polarization, a correlation coefficient of about 0.86 between them, and an average CPR of about 6 dB. Furthermore, the average value of the Rician K-factor shows little or no difference between the HH and VV polarizations.

In this particular 5 mm wavelength, the multipath fading can be modeled by Rician distribution. Most commonly used Rician K-factor which determines how much dominant is the LOS component compared to the other multipath components. In other words, higher values of the K-factor

Table 5.7 Simulation results

N	F_c	T_a	R_a	P	T_{HPBW}	R_{HPBW}	G_t	G_r	τ_{rms}
1	58.32	Horn	Horn	VV	12°	12°	24	24	$4.1142e^{-04}$ -0.1165
2	58.32	Horn	Horn	HH	12°	12°	24	24	0.0013-0.1624
3	58.32	Horn	Omni	VV	12°	360°	24	3	0.0108-0.4346
4	58.32	Horn	Omni	HH	12°	40°	24	3	0.0178-0.4202
5	58.32	Omni	Horn	VV	360°	12°	3	24	0.0107-0.4332
6	58.32	Horn	Horn	VV	16°	16°	20	20	$9.1351e^{-04}$ -0.3974
7	58.32	Patch	Patch	VV	50°	50°	10	10	$5.1853e^{-04}$ -0.9993
8	58.32	Omni	Omni	VV	360°	360°	3	3	0.7281-3.2474
9	2.4	Omni	Omni	VV	360°	360°	Auto	Auto	1.5228-2.3144

Note : N is the number of antenna configurations, F_c is the center frequency, T_a is the transmitter antenna type, R_a is the receiver antenna type, P is the antenna polarization configuration type, T_{HPBW} is the transmitter antenna azimuthal HPBW, R_{HPBW} is receiver antenna azimuthal HPBW, G_t is the transmitter antenna gain, G_r is the receiver antenna gain, τ_{rms} is the RMS delay spread.

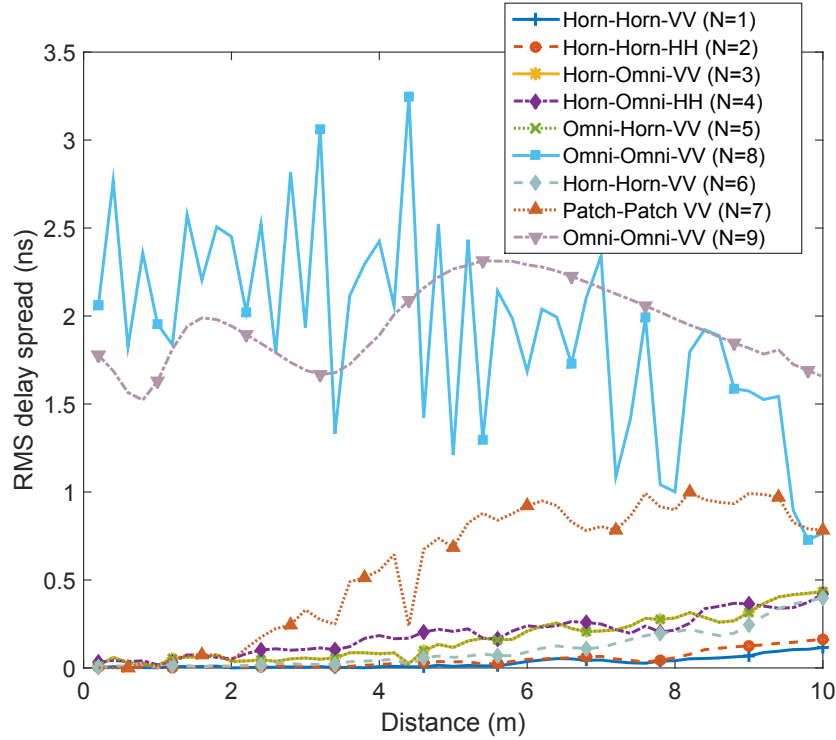


Figure 5.19 Illustration of the simulation results with different setups listed in Table 5.7

demonstrate lower values of multipath amplitudes [93].

K-factor measurement techniques in the home and office environments at 60 GHz reported in [112] revealed that the K-factor lies between 6.35 dB and 15.1 dB with an average of 9.89 dB. The authors also mentioned that a larger K-factor indicates higher losses of reflected signal strength caused by lossy scattering objects. In an aircraft cabin, K-factor measurement results at 2.4 GHz, 3.52 GHz, and 5.8 GHz suggested its value lies between 8 dB and 12 dB [113]. In an underground mining environment over a frequency range of 2 to 10 GHz, LOS measurements revealed an average K-factor value of around 18 dB at transmitter receiver separation distances between 2 m to 7 m with 1 m steps [114]. It was also mentioned there that high measured values of the K-factor show a better fit with the Lognormal distribution. The gallery walls are more absorbent thereby causing lower multipath signal strength. Moreover, no correlation was found between the K-factor and transmitter receiver separation distance. Cellular mobile communication channel measurements with different antenna polarizations were investigated in [115] to report that co-polar channel components have the same power on average. Measured values from 0.86 to 0.96 of the correlation coefficient of different streets between horizontal and vertical polarization received powers were reported in [116].

However, the K-factor and the CPR have never been investigated so far in an underground mine environment at 60 GHz.

5.5.1 K-factor

Several methods have been proposed to estimate the K-factor such as the moment of the signal fading variations over time, space or frequency, using the I and Q components, or the maximum likelihood (ML) [114]. The received signal fading can be also characterized by the Rician probability density function (PDF) of the random amplitude of x , which is given by

$$p(x) = \frac{x}{\sigma^2} e^{-\frac{(x^2+A^2)}{2\sigma^2}} I_0\left(\frac{Ax}{\sigma^2}\right) \quad (5.26)$$

where A is the peak amplitude of the dominant component and σ^2 is the variance of the multipath components. $I_0(\cdot)$ is the modified Bessel function of order 0. Therefore, the K-factor is given by

$$K(\text{dB}) = 10\log_{10}\left(\frac{A^2}{2\sigma^2}\right) \text{ dB} \quad (5.27)$$

which is defined by the power ratio between the LOS and the multipath component.

Consequently, in order to find the K-factor values, the relative signal amplitudes at the receiver at each distance and the corresponding number of multipath components have to be determined. Fig. 5.20 plots the number of multipath components in the VV and HH polarization configurations

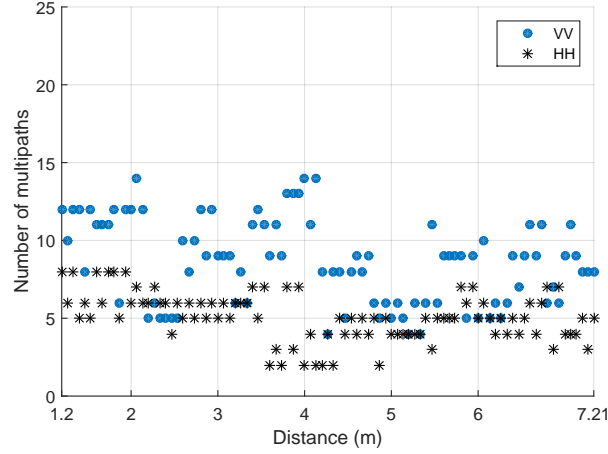


Figure 5.20 Number of the multipath components (with Omni - Horn configuration at 40 m gallery).

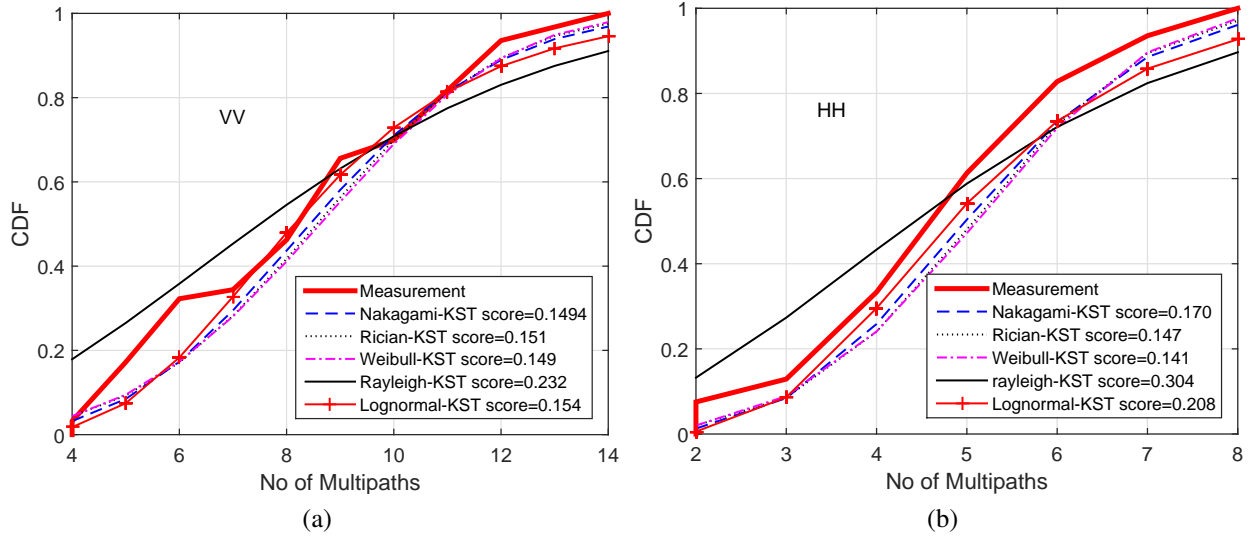


Figure 5.21 Kolmogorov-Smirnov test (KST) scores with different distributions of the number of multipath components for (a) the VV and (b) the HH configurations (with Omni - Horn configuration at 40 m gallery).

versus the transmitter receiver separation distances. The results suggest that the VV polarization offers a larger number of multipath components than the HH polarization. Indeed, the vertically polarized antenna radiates over 360° in azimuth and $\sim 40^\circ$ in the elevation (along the x direction of Fig. 3.6) directions. Results show that once the transmitter receiver separation distance increases, the number of multipath components decreases slightly.

Fig. 5.21 shows the Kolmogorov-Smirnov Test (KST) results for the number of multipath components, to find the best fitted distribution among Rayleigh, Rice, Nakagami, Weibull, and Lognormal.

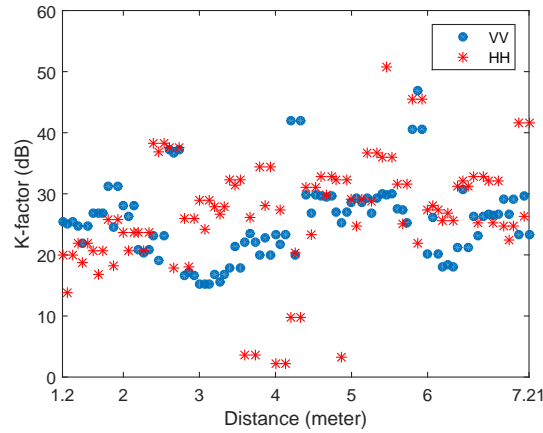


Figure 5.22 K-factor values (in dB) versus the transmitter receiver separation distance (with Omni - Horn configuration at 40 m gallery).

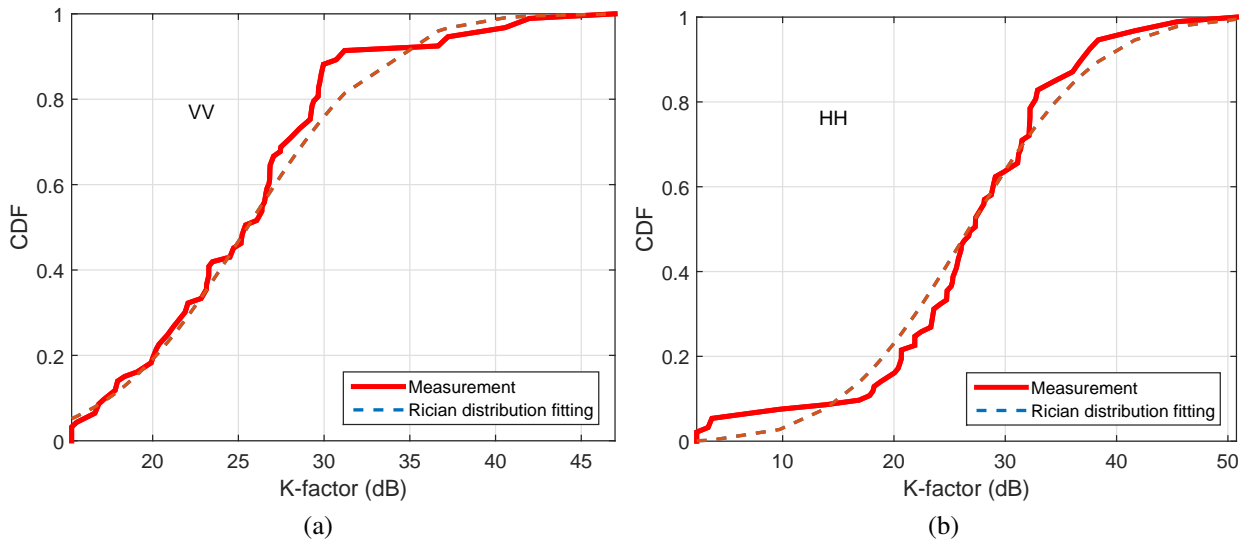


Figure 5.23 Rician distribution fitting of K-factor results (with Omni - Horn configuration at 40 m gallery) for (a) VV and (b) HH configurations.

The fitting results suggest that Weibull is the best fitted distribution for both the VV and HH configurations.

Fig. 5.22 shows the measured K-factor values in dB versus the transmitter receiver separation distances. The plots suggests no correlation between the K-factor and the transmitter receiver separation distance. It can be noted that, at 4 m distance with HH polarization presents lower value of K-factor, which described that a lower number of multipath components with a higher amplitude may cause the lower value of K-factor due to the rough surface and higher inclination of the surface.

Fig. 5.23 shows the Rician distribution fitting results of the measured K-factor values with the HH and VV polarizations. The estimated statistical parameters are listed in the Table 5.8. The mean values are almost the same (i.e., around 25 dB where [114] reported around 18 dB over a frequency range of 2 to 10 GHz) for both polarization configurations whereas a difference is found in the standard deviations. Indeed, the HH polarization results in higher fluctuations of the reflected signal and the receiver may experience multipath from different angles with higher amplitudes.

Table 5.8 Rician distribution fitting of K-factor values (with Omni - Horn configuration at 40 m gallery)

Polarization	Statistical parameters (dB)			
	A	σ	μ	σ^2
VV	24.68	6.44	25.54	40.05
HH	24.92	9.52	26.83	83.53

5.5.2 Co-polarization ratio

Vertical and horizontal polarized waves are independent of each other. The two co-polar components P_{VV} and P_{HH} are independent but related to the environment and the number of multipath components received by the receiver. The co-polarization ratio (CPR) is defined as in equation 5.24.

which characterizes the significant decimal difference between the vertical and horizontal multipath component amplitudes. Since, the surface of the environment is rough and since the roughness values of the floor, the wall, and the ceilings are different from each other, then the reflected and scattered multipath total powers are different. The CPR value could be different at each distance and may follow linear power degradation versus the transmitter-receiver separation distance. Due to the rough surface, the CPR values are also related to the gallery curvature.

Fig. 5.24 shows the CPR value in dB versus the transmitter-receiver separation distance. Results at 1.2 to 3 m suggest that, the CPR value remains below 4 dB. However, at 3 to 7 m, the CPR value increases to about 8 dB on average. In contrast, the average CPR value remains close to 6 dB.

Fig. 5.25 plots the KST results for the measured CPR values to identify the best fitted distribution, namely the Rician distribution.

The correlation coefficient between P_{VV} and P_{HH} also characterizes how strongly they are correlated with each other. The Pearson correlation coefficient r was used to find the coefficient between

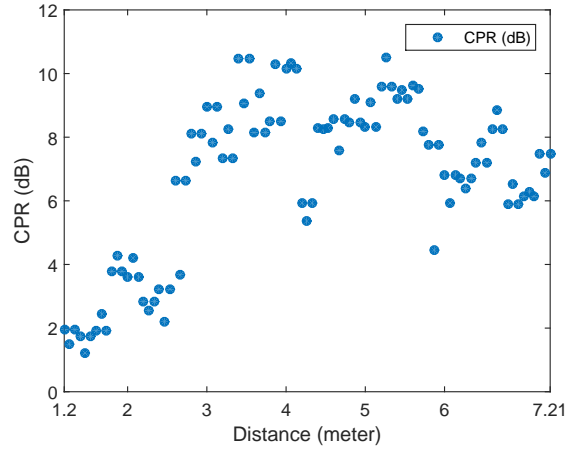


Figure 5.24 CPR versus the transmitter-receiver separation distance.

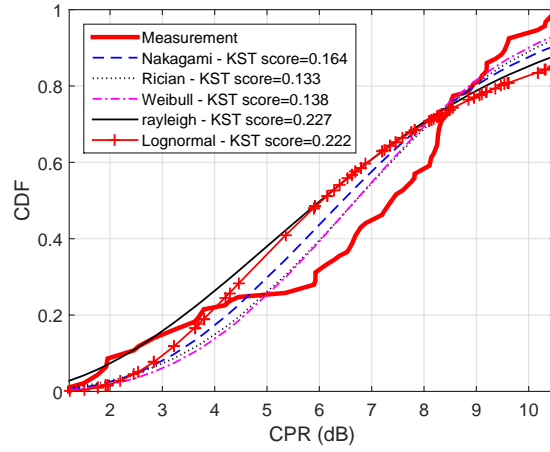


Figure 5.25 Kolmogorov-Smirnov test for the measured CPR values.

x and y those are equivalent to P_{VV} and P_{HH} , respectively and can be written [117, 118] as

$$r_{xy} = \frac{\sum_{i=1}^n (x_i - \bar{x})(y_i - \bar{y})}{(n-1)\sigma_x\sigma_y} \quad (5.28)$$

where x and y are the P_{VV} and P_{HH} , respectively, n is the total number of measurements. σ_x and σ_y are the standard deviations of x and y , respectively.

The measured r_{xy} value of 0.8649 satisfied with the outdoor street experimental results reported in [116].

In summary of section 5.5, time dispersion results were extracted and results show that a vertical

antenna polarization provides a larger number of reflected paths than horizontal polarization. The measured Rician K-factor values have found an average of 25 dB for both polarizations whereas a higher value of standard deviation found with the HH polarization. The CPR value remains around 6 dB and analyzed that its value depends on the roughness and the gallery curvature. Furthermore, high correlation between the total multipath powers of P_{VV} and P_{HH} over both polarizations was reported.

CHAPTER 6 ANGLE OF ARRIVAL ANALYSIS

In general, 60 GHz directive antenna system allows beamforming technology, and due to the mineworkers mobility concern, the 5 mm wavelength could be a better candidate for accurate geo-location service in this particular confined environment. The experimental mine consists of rough surfaces which can be affected by the reflections and the scattering at this particularly wavelength of 5 mm. The angular dependencies are necessary during the investigation of wireless system design in underground mine. This measurement campaign is particularly motivated due to the different roughness magnitude of the floor, wall and ceiling. In this chapter, angular dispersion measurement results of 60 GHz radio wave propagation in different real underground mine level depths are presented. The characterization of the multipath arrivals at the receiver is based on statistical analysis of the multipath shape factors.

6.1 Measurement setup and experimental protocol

A similar experimental system setup was used as shown in Fig. 3.4. The Velmex table having the capability to do 3D measurements along the x and z directions simultaneously. During AoA

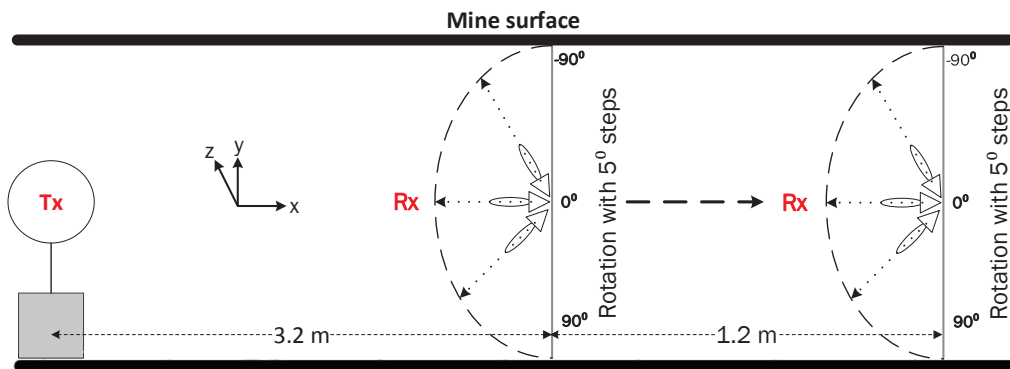


Figure 6.1 AoA measurement procedure with Omnidirectional antenna at the Tx and directional horn antenna at the Rx.

measurements in the 70 m gallery, the Rx was moved from 3.2 m to 4.4 m along the x axis as shown in Fig. 6.1. The separation of two successive positions was 40λ . At 40 m gallery, the Rx moved from 3 m to 4 m separated by 1 m along the x axis. For both galleries, a 1 m reference measurement (so called over the air calibration) was used to remove the antenna side lobe effect and the system losses. Along the elevation direction (i.e. z axis), six consecutive measurements

were taken at each position separated by $\lambda/2$ to have an average of spatial fading and to reduce the antenna misalignment issue (due to rough floor). A higher magnitude of Rx power was observed to be approximately at 3 m from the Tx and the length of the linear track in the Velmex table was around 1.5 m. At each position of both galleries, the Rx was moved in azimuth directions from -90° to 90° with a step of 5° with an accurate programmable Velmex linear track in order to have the azimuthal coverage of 180° . The measurements were conducted particularly to evaluate the scattering effect and to obtain the angular characteristics of multipath. A HPBW for the rotational antenna is larger than the step size (5°) of the measurement which offers a sufficient angular space to receive strong multipath at the Rx. At each position, 15 snap shots for different time instances in order to have a local average which eliminates the time varying small scale fading.

A record of 26,640 measurements (37 angles x 6 grids x 15 snapshots x 8 separation distances) at 70 m gallery were taken continuously around 9 hours. Six hours accessible time inside the mine and Velmex table movements (e.g., 4 m to 5.5 m) required another 2 hours limit the recording of measurement samples. Due to the limitation of time and CANMET experimental mine was supposed to close at that time, measurements with larger distances were not conducted.

6.1.1 Post processing

Firstly, for angular dispersion measurements, the 37 frequency responses were obtained at each position by averaging 15 snapshots. Therefore, 1776 (8 and 6 positions along the x-axis and z-axis, respectfully) and 666 (3 and 6 positions along the x-axis and z-axis, respectfully) frequency responses were stored for post-processing to investigate the angular power dependencies at 70 m and 40 m gallery, respectively.

Secondly, the OTA (over the air) calibration of data was performed by dividing of 1 m complex-valued frequency response with all complex-valued frequency responses of the measurements.

Finally, using the Inverse Fast Fourier Transform (IFFT), the normalized channel impulse responses $h(\tau; d)$ with 0.46 ns time resolution were obtained from the OTA calibrated frequency responses using the procedure employed in [22].

Therefore, for a position d , the channel impulse responses $h(\tau; d)$ were obtained leading to the PDPs calculated by $P(\tau; d) = |h(\tau; d)|^2$. The noise threshold level was set to -25 dB. The noise floor was around -100 dB. The dynamic threshold as described in [119] and a modification is described in Appendix B. The dynamic threshold can be more useful due to the lower multipath amplitudes in higher multipath arrivals.

6.2 Angular dispersion characteristics

This section investigates the angular characteristics of the channel in the 70 m and 40 m level galleries. The multipath shape factors are introduced by the angular distribution of the multipath power $p(\theta)$ where θ is the angle of measurements. Statistical modeling of the angle of arrivals of an indoor multipath channel has been reported in [69]. In [120] and [68], the theory and experimental results of multipath shape factors such as the angular spread (Λ), angular constriction (γ), direction of maximum fading (θ_{max}) and maximum AoA direction of the angular distribution of the multipath power have been described. Shape factor theory has been considered herein since it can provide more information on multipath arrivals where scattering is of high concern. The shape factor parameters were extracted from the recorded Power Angular Profiles (PAPs) in order to characterize the distribution of the multipath power and to investigate reflection/scattering phenomenon in the galleries. First, the individual amplitude (a) and delay (τ) from the channel impulse response $h(\tau)$ were extracted. Second, at a certain distance, the average values of PAPs have been calculated as [72] [68]

$$p(\theta) = \frac{1}{M} \sum_{k=1}^M \left(\sum_{i=1}^N |a_i(\theta, z_k)|^2 \delta \{ \tau - \tau_i(\theta, z_k) \} \right) \quad (6.1)$$

where M and N are the number of measurement points along the z direction denoted as z_k ($k = 1, 2, \dots, 6$) and the number of sweep points ($i = 1, 2, \dots, 2000$), respectively. The values of θ are used from $-\pi/2$ to $\pi/2$ with 5° angular resolution. In order to calculate the shape factor value of the multipath, the n -th Fourier complex coefficient F_n of $p(\theta)$ has been calculated using

$$F_n = \int_0^{2\pi} p(\theta) e^{jn\theta} d\theta \quad (6.2)$$

The four multipath shape factors are described in detail in the following subsections.

6.2.1 Angular spread

The multipath concentration along a single azimuthal direction is defined by the shape factor angular spread (Λ) [68] as

$$\Lambda = \sqrt{1 - \frac{\|F_1\|^2}{\|F_0\|^2}} \quad (6.3)$$

where F_1 and F_0 are the first and second order Fourier transform defined by equation 6.2. Angular spread characterizes the multipath power by the ranges from zero to one. A value of zero represents one single multipath from a single direction and a value close to unity denotes multipath coming from multiple directions.

6.2.2 Angular constriction

The angular constriction (γ) specifies how multipath components are distributed along the two directions (towards -90° and 90° from 0°) and is defined [68] as

$$\gamma = \frac{\|F_0 F_2 - F_1^2\|}{\|F_0\|^2 - \|F_1\|^2} \quad (6.4)$$

where F_0 , F_1 and F_2 are obtained from equation 6.2. The values of γ range from zero to one, one denoting the multipath energy equally distributed in two directions and close to zero specifying that multipath energy is distributed in different directions.

6.2.3 Maximum fading angle

Maximum fading angle (θ_{max}) provides the azimuthal direction of maximum fading in which receiver will not receive multipath components in that direction and is defined [68] as

$$\theta_{max} = 1/2 \text{ Phase}\{F_0 F_2 - F_1^2\} \quad (6.5)$$

6.2.4 Maximum AoA direction

Maximum AoA represents the angular direction of the strongest multipath component at the receiver [68]. A typical value at a short distance is 0° and for a little longer distance typically its value is $+/- 5^\circ$. These values depend particularly on the antenna alignment and the propagation environment.

The adjacent spread of power, arriving in the azimuth or elevation directions can be defined as a lobe [4]. The azimuth and elevation lobes can be different and depend on the antenna radiation patterns which define a propagation route. The mean direction of arrival of a lobe ($\bar{\theta}$) defines the precise direction of lobe arrivals as

$$\bar{\theta} = \sum_k \frac{p(\theta_k)\theta_k}{p(\theta_k)} \quad (6.6)$$

where k remains from $-\pi/2$ to $\pi/2$.

6.3 Results and discussions

Since the underground mine surface is rough and consists of sharp rock edges, the shape of each PAP is affected particularly by the grazing angles (i.e., around $\pm 30^\circ$) of the multipath on azimuth and elevation directions at 60 GHz corresponding to a wavelength of 5 mm which is larger than

the magnitude of the surface roughness. Currently, there are no PAP experiments carried out for other frequencies such as 2.4 GHz and 5.8 GHz (in CANMET mine) but it is assumed that the multipath profile would be different at lower frequencies since its behavior depends on the operating frequency and on the magnitude of the roughness. For a lower frequency (e.g., 2.4 GHz), the magnitude of the surface roughness is lower than the 12 cm wavelength of the signal and it is highly probable that PAPs would be different from the ones obtained using a 60 GHz carrier frequency.

6.3.1 70 m gallery results

From the measurement results in the 70 m gallery, the PAPs and extracted multipath shape factor values at each distance are shown in Fig. 6.2 and listed in Table 6.1, respectively. Moreover, in Appendix A, the results at each distance along the x and z directions are illustrated. For a fixed distance, the obtained lobes were constituted by the average (6 points along the z direction \times 15 snap shots) of 90 PAPs. According to visual observation of multipath arrivals of 7 PAPs results, scattering exists in the underground mine environment and the PAPs will differ from those obtained with the smooth surface with zero roughness.

In order to explain, a comparison of multipath arrivals between rough and smooth surfaces was considered. By using the Wireless InSite software, a simulation scenario with a 3 m width and a 2 m height of a rectangular straight tunnel were carried out. The simulation parameters and the protocols are the same as the ones used in the experiments where an Omni - Omni antenna configuration was considered (during measurements, the horn antenna at the receiver has been rotated with 5° step). The surface roughness value was set to zero. Specular reflections and diffractions are considered for simulation purposes. The material properties were as defined in [121]. Fig. 6.3 shows the comparison of the measured and simulated PAP results. Simulated PAPs at each distance are illustrated in Fig. 6.4. Results show that a difference of the multipath angle of arrivals exists between

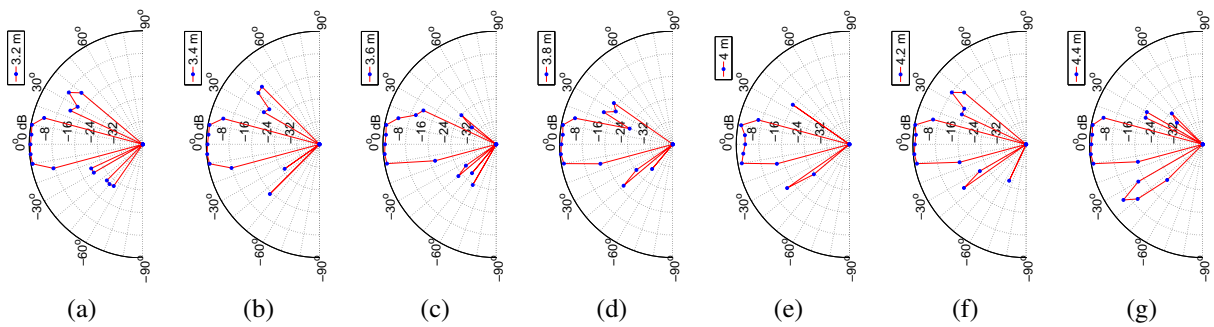


Figure 6.2 Normalized PAPs according to transmitter receiver separation distance between 3.2 m and 4.4 m with a step of 40λ at 70 m gallery.

Table 6.1 AoA statistical parameters of 70 m gallery according to transmitter receiver separation distances. Λ and γ are dimensionless, θ_{max} , max AoA and Lobe angles are in degree, Peak Avg. values are in dB.

Distance	Λ	γ	θ_{max}	max AoA	Lobe angles	Peak Avg.
3.2 m	0.3063	0.8532	-89	-5	-49.99, -27.48, 0.54, 30.78	7.34
3.4 m	0.2950	0.8603	-83	-5	0.40, 36.17	7.87
3.6 m	0.2481	0.8539	84	-5	-38.11, 3.42, 35	8
3.8 m	0.2450	0.8926	89	-5	-38.45, 2.93, 31.5	8.13
4 m	0.2347	0.9069	87	10	-36.15, 0.82	8.79
4.2 m	0.2955	0.8527	-86	10	-33.56, 1.01, 31.44	7.84
4.4 m	0.3038	0.9069	82	-5	-36.18, 1.37, 27.57, 40	7.63

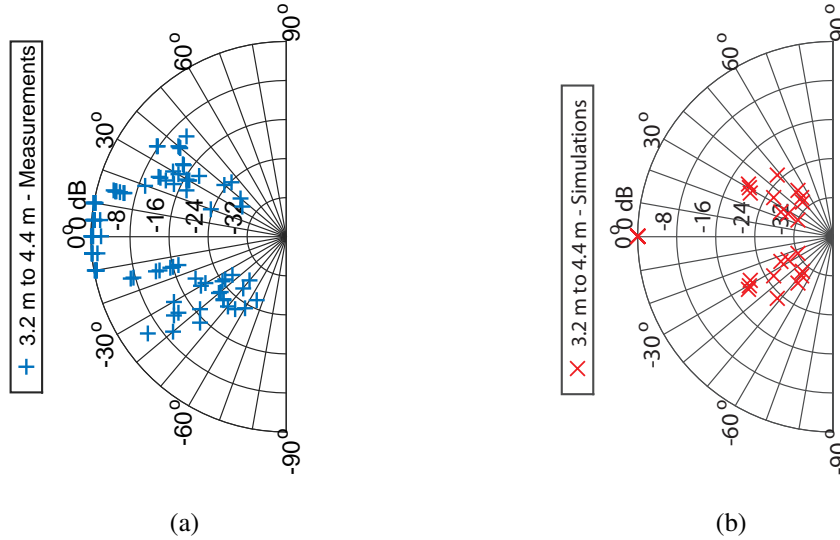


Figure 6.3 Normalized measured and simulated PAPs at 70 m level gallery. a) and (b) based on rough surface (with around 6 cm on magnitude) and zero roughness, respectively.

the choice of smooth and rough surfaces implying the existence of scattering in the underground mine environment.

As such, the roughness of the surface produces scattering, changing the amplitudes and the angles of multipath arrivals along the x, y and z directions of Rx. Due to time constraints, the angular measurements along the y direction were not conducted. It has been observed for each PAP that the probability of having individual multipath arrival and amplitude, at each specific angle, is random.

Measurement results show a small change in the values of Λ with the distance particularly due to the straight vein of the gallery. Its value lies between 0.2347 and 0.3038 within a 3.2 m to 4.4 m link

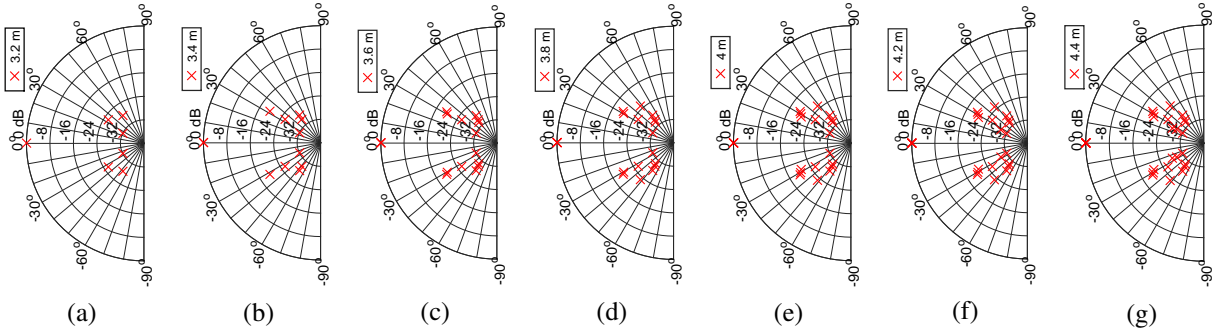


Figure 6.4 AoA simulation results with Omnidirectional antennas both at the Tx and the Rx at 70 m gallery.

distance, which corresponds to a range of values of Λ close to zero suggesting that the multipath does not come from multiple directions (coming only from two or three directions and not from one direction). Moreover, it has been observed that within a 40λ distance (for example, at 3.4 m and 3.6 m distance in Fig 6.2b and 6.2c), the value of Λ varies, referring to the deviation of path arrivals caused by the surface roughness. As the reference, the experimental results in an indoor environment reflect somehow our results as reported in [68], in which the multipath is accumulated in the main lobe, giving rise of similar trend of angular spread values once the Rx location is closer to Tx.

As an example, geometrical analysis of Fig. 6.2 shows that at a 3.2 m distance with a fixed height of 3 m, the reflected path from the wall may have traveled 3.88 m and 4.38 m distances with respective angles of $\pm 34^\circ$ and $\pm 42.92^\circ$ corresponding to mine gallery widths of 2.2 m and 3 m, respectively. The dominant lobe (consisting of several paths) is arriving along the LOS direction within a resolution angle of $\pm 30^\circ$ while the other three lobes (consisting also of several paths) arrived at angles of -49° , -27° and 30° . These lobe arrivals results show a difference where a smooth surface is considered. Accordingly, at a 3.4 m distance, only one strong reflected dominant lobe arriving at an angle of 36° caused by the metallic pipe of the gallery.

Angular constriction (γ) values are close to the value of 1 which indicates that multipath power is distributed around in both directions of the main lobe. These results are attributed to the rough walls, ceiling, and floor, and correspond to strong reflected waves arriving from angles corresponding to approximately $\pm 30^\circ$ (towards -90° and $+90^\circ$ from LOS angle) compared to the dominant path as shown in Fig. 6.2.

Maximum fading angle (θ_{max}), results show a value with variation according to Tx - Rx distance caused by the rough surface of the gallery. At 4.2 m as seen in Fig. 6.2f, since the maximum power of the multipath consists of a lobe of $+31.44^\circ$. By considering the vector sum of multipath power,

the maximum fading angle would be -86° .

For maximum AoA results show that its value lies between -5° and $\pm 10^\circ$ which is obvious at short Tx - Rx distance. Observations at each $\lambda/2$ separation distance along the z axis indicates that the values of maximum AoA are not varying significantly. This is to note that, some lobes and paths (as shown in Figs. 6.2c and 6.2f) lie between 60° and 65° , indicating the scattering or diffraction phenomenon on the interaction points of the rough surface when the surface is close to the Rx which yields to a larger AoA.

The peak of the strongest multipath power is deduced from all pointing angles of the Rx. The ratio between maximum power and average multipath power is defined as peak avg. and listed in Table 6.1. The received power of the dominant path (along the LOS) does not change significantly and is around 5 dB. At 3.2 m and 3.4 m (Figs. 6.2a and 6.2b) the power at the positive link lobe of 30° remains almost the same, but at the 3.6 m location the power degrades around 14 dB. This is to note that two or three side lobes and those paths arrived around $\pm 30^\circ$ and one main lobe which consists several paths arrived around $\pm 15^\circ$.

The distribution of path arrivals with respect to angles extracted from 42 PAPs (6 points along the z axis \times 7 points along the x axis) is shown in Fig. 6.5a. Zero mean Laplacian and Gaussian distributions fittings provide the standard deviations (defined as an angular spread, σ_θ) of 9.66° and 14.33° , respectively. Curve fitting, uses the least square method, closely matches with the Gaussian distribution. The Laplacian Probability Density Function (PDF) peak at 0° (AoA) is much higher than the Gaussian peak and does not correspond to the measured PDF (number of occurrences of path arrival angles). It indicates that the number of occurrences of path arrivals within that angle is not too high and that it does not consist of sharp peak caused by the scattering. This is to note that, an extension of the Saleh-Valenzuela (S-V) model introduced by Spencer [69] shows that the angle of arrival within a multipath cluster is assumed to have a zero-mean Laplacian distribution. Moreover, Zhang et al. [122] observed that the azimuth AoA follows a Laplacian distribution and the elevation AoA follows a Gaussian distribution in indoor environments.

At each distance, the Gaussian distribution fitting and the corresponding AoA standard deviation values are shown in Fig. 6.5b and 6.5c. The results show that when the distance increases, the value of the standard deviation becomes smaller due to a larger incident angle implying a lower value of σ_θ and tends to be smaller at farther distances along the x direction of the gallery.

6.3.2 40 m gallery results

Fig. 6.6 illustrates the average PAPs at 3 m and 4 m Tx - Rx distance. Results show that a wider gallery dimension provides a larger angular spread of multipath arrivals by comparing 40 m and 70

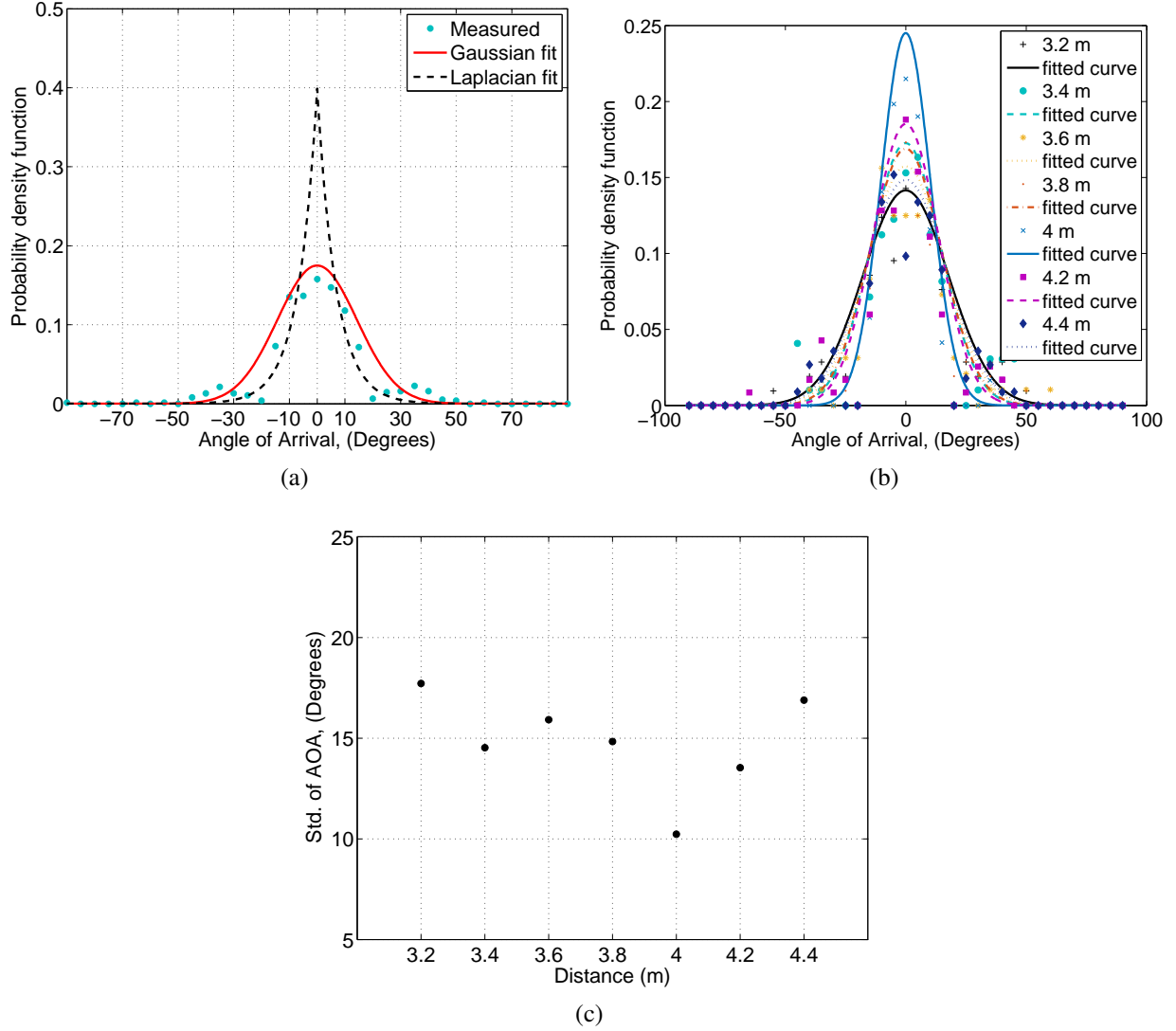


Figure 6.5 Distribution fitting of relative path arrivals with respect to the angles at 70 m gallery. Superimposed by the best fitted Gaussian distribution ($\sigma_{\theta} = 14.33^{\circ}$) is illustrated in (a), (b) illustrates the Gaussian distribution fitting of 7 PAPs of different distances and (c) is the standard deviation of AoA according to Tx Rx separation distances.

Table 6.2 AoA statistical parameters of 40 m gallery according to transmitter receiver separation distance. Λ and γ are dimensionless, θ , max AoA and Lobe angles are in degree, Peak Avg. values are in dB.

Distance	Λ	γ	θ_{max}	max AoA	Lobe angles	Peak Avg.
3 m	0.3890	0.7684	78.9464	5	-76.14, -53.40, -2.99, 43.87	8.6639
4 m	0.1722	0.9707	88.60	0	0.0327	10.10

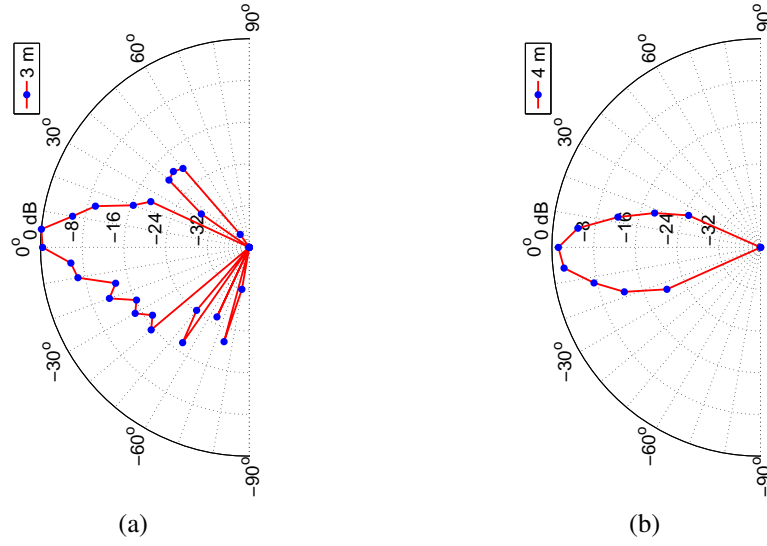


Figure 6.6 Normalized PAPs according to the transmitter receiver separation distance of 3 m and 4 m at 40 m gallery.

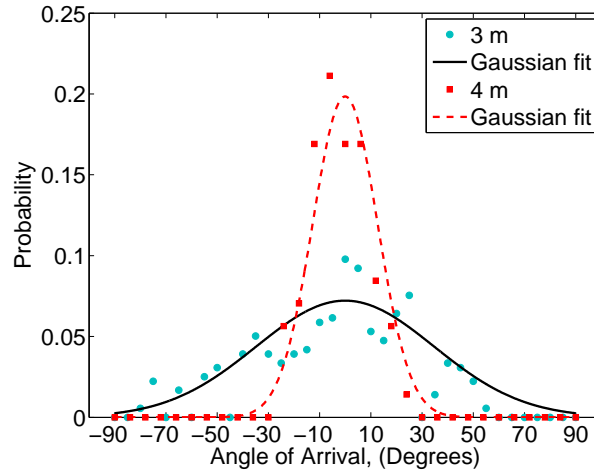


Figure 6.7 Gaussian distribution fitting, $\sigma_\theta = 34.75^\circ$ at 3 m and $\sigma_\theta = 12.63^\circ$ at 4 m.

m results. As well, due to the higher incident angles, the larger Tx - Rx distance of 4 m provides the less angular spread of multipath arrivals as shown in Fig. 6.6b. The extracted statistical parameters of AoA are listed in Table 6.2.

Geometrically, with a Tx - Rx distance of 3 m, the reflected path could travel 5.8 m with an arrival angle of $\pm 59^\circ$, but due to scattering and diffraction phenomena in the wider gallery, multipath arrived with large angles and the lobe angles are around 43° , -53° and -76° . The angular constriction value at 3 m is lower than the 70 m level gallery (at 3.2 m) indicating that multipath power is distri-

buted more in different directions. Gaussian curve fitting provides the standard deviations of 34.75° and 12.63° for the angle of arrivals at 3 m and 4 m as shown in Fig. 6.7, respectively. Moreover, the angular spread of the LOS lobe of the 40 m gallery is larger than at the one at 70 m gallery indicating that more multipath is arriving in different directions. At 4 m Tx - Rx distance, no side lobes were observed which indicates that all multipath are concentrated along the LOS direction and yields a higher peak average value. In addition, side lobes at 3 m travel larger distances with higher signal power attenuation and provide an absence of multipath or a lobe at the receiver for a 4 m link distance.

6.3.3 Comparison with other experiments

As a reference, Forooshani et al. [27] reported 10° and 3° at 50 m and 200 m link distances (i.e., the roughness of the surface is less than 1 cm and much lower than the wavelength) at a lower frequency, respectively. Their results mentioned that the angular spread becomes insignificant as Tx - Rx distance increases. A comparison with our experiments is indeed relevant since the tunnel dimensions and the roughness of the surface are different (as the parameters to be considered for short range link distances) and listed in Table 6.3. In contrast, at closer distances around 1 - 10 m, the angular spread becomes larger with larger gallery dimensions and its value depends on operating wavelength as well as on the surface roughness. It is noted that within a short range of link distance the angular spread decreases sharply as distance increases as reported in [123] (i.e., 10 to 50 m 30° to 13°) and CANMET 40 m results (i.e., at 3 to 4 m 34.75° to 12°).

Table 6.3 A comparison with different angle of arrival experimentsl results.

Location	Environment	H (m)	W (m)	F (GHz)	M/E	Angular spread
[27]	Underground mine (small tunnel)	5.1	3.8	2.8-5	Multimode Model	15.3° (10-50 m)
[27, 123]*	2 way tunnel (large subway tunnel)	6.1	8.6	2.8-5	Experiment	10° (50 m), 3° (200 m)
CANMET **	Underground mine	3	2	57.24-59.4	Experiment	14.3° (3.2-4 m)
CANMET **	Underground mine	5	5	57.24-59.4	Experiment	34.75° (3 m), 12° (4m)

Note : H is the height, W is the width, F is the frequency, M/E is method/experiment.

* Angular power spectrum theory was used to calculate angular spread as in [124] page 121 and in [123].

** The angles of multipath arrival fits with Gaussian distribution and σ_θ was used to calculated the value of angular spread [69].

In order to make more analysis, the average PAP at 3.2 m and PAPs along the z directions are plotted in the Fig. 6.8. Figs. in Appendix A are illustrated other results with different transmitter

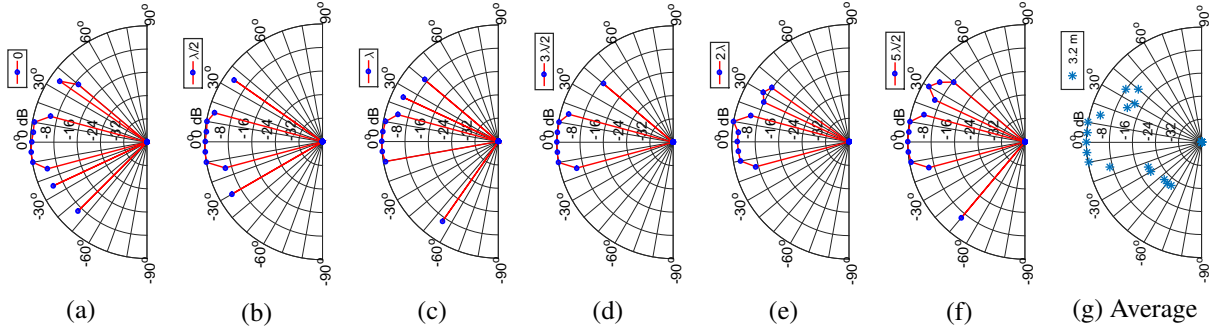


Figure 6.8 Measured normalized PAPs according to transmitter receiver separation distances of 3.2 m along the z directions with a step of $\lambda/2$ at 70 m gallery.

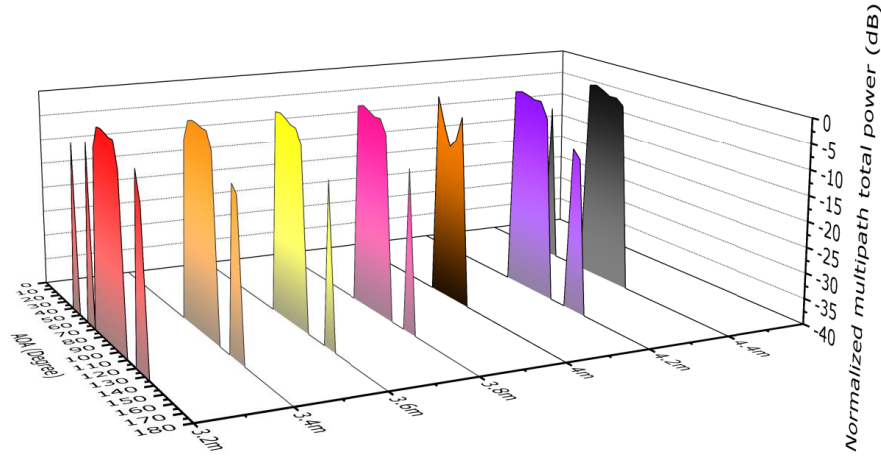


Figure 6.9 Measured PAPs at $z = 0$ for all Tx Rx separation distances.

receiver separation distances. According to the observation, the absence or presence of multipath in a particular angle exists within a $\lambda/2$ Tx Rx separation distance and overall considered as random angle of arrival. This is to note that the average of the 6 PAPs produced 4 angular link lobes.

Moreover, the PAPs along the x direction (at $z = 0$) are plotted in Fig. 6.9. The results also show that the presence and absence of the multipath particularly at 3.8 m and 4 m distances. The Table in Appendix A shows the multipath shape factor results at the receiver positions from 0 to $5\lambda/2$ along the z directions and from 3.2 m to 4.4 m along the x direction are listed. It can be noted that at $z = 0$, the angular spread value (Λ) at 4 m (i.e., 0.1391) is less than the one at 3.8 m (0.1993).

CHAPTER 7 STATISTICAL MODELING

In this chapter, statistical modeling approach has been considered by using multipath arrivals and amplitudes where no multipath clustering has been found in the underground mine environment. For the statistical modeling, the impulse responses were generated based on different amplitude models, and RMS delay spread values were generated and compared with the measured RMS delay spread values. Angular dispersion parameters could be included in this modeling approach. The measurement configurations are listed in Table 7.1.

Table 7.1 Measurement configurations.

Mine Level	Antenna configuration	Polarization
40	Omnidirectional - Directional (O - D)	VV, HH
70	Directional - Omnidirectional (D - O)	VV, HH

7.1 Modeling process

The PDPs with 0.46 ns time resolution (defined as path index) of the impulse responses were obtained from the recorded frequency responses using the procedure employed in [22]. The complete flow chart of the statistical modeling process is illustrated in Fig. 7.2.

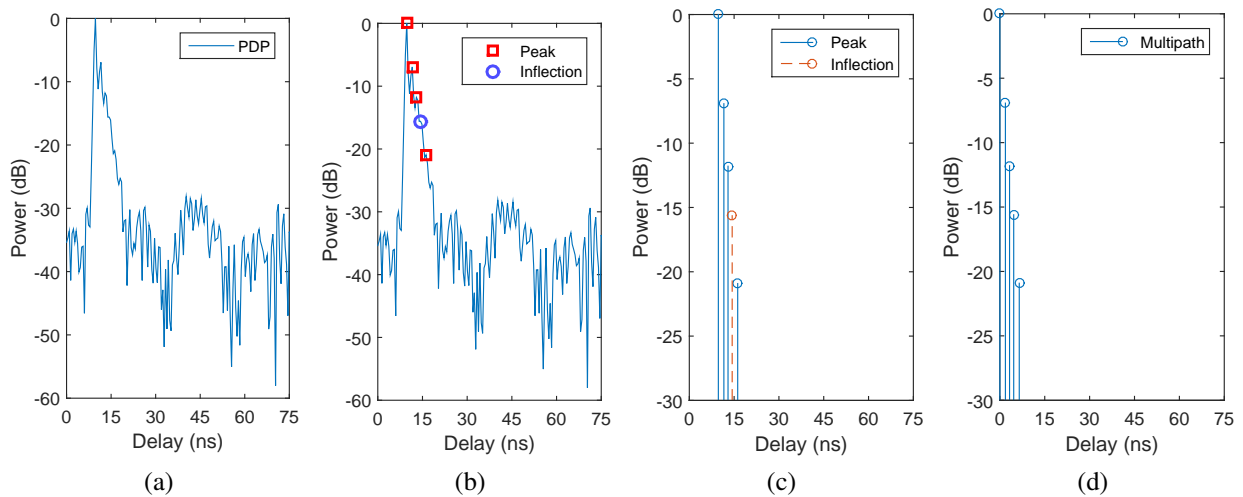


Figure 7.1 An example of a PDP post processing. (a) the recorded signal, (b) peaks and inflection detection, (c) final detected dominant path and multipath, and (d) shifted power delay profile.

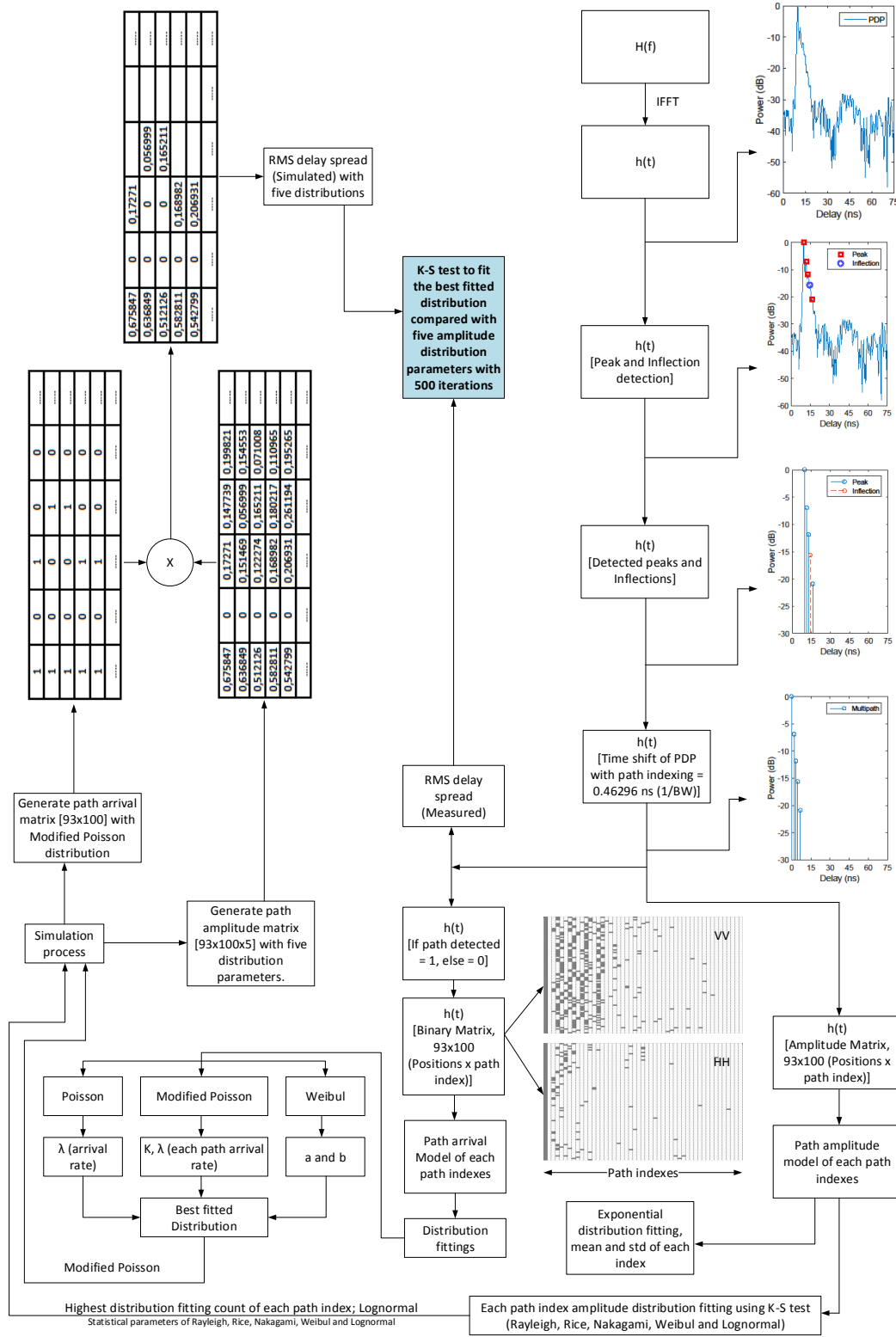


Figure 7.2 Flowchart of the statistical modeling.

7.1.1 Path arrival modeling

A simple path arrival model is a poisson process which can characterize the random arrivals of paths [84]. Some studies in indoor and underground mine environments suggest that modified poisson distribution is closely fit with empirical measurement results as described in [22] and [125]. This phenomena can be explained that the arrival of paths are not totally random (e.g., fixed average arrival rate λ), it can be poisson process where probability of having a path in index i is given by λ_i (e.g., individual arrival rate of paths) [84]. The Fig. 7.3 illustrates an example of the probability of path occupancy for 40 m_{O-D} configuration for each path index of 0.46 ns delay. Results show that in the first path index the probability of having a path is 1 for all configurations. It can be noticed that for the second path index no path arrivals is observed in all configurations, since the path index delay time resolution (i.e., 1/BW) is lower than the second path arrival time coming from the surfaces of the galleries. The results from the 3rd to maximum number of path index, provide the probability of having a path is increasing some while and decreases gradually until the maximum path delay. This can clarify that the probability of having maximum multipath consists in a certain delay. On the other hand, the 70 m_{D-O} configuration shows that the probability of having a path between the 3rd to the maximum number of path index are fluctuating and the mean delay of paths are less than 40 m_{O-D}. This might be caused by the smaller gallery dimension and the use of Horn antenna at the transmitter in the 70 m gallery. Figs. 7.4 and 7.5 show the examples of the distribution of the number of paths occurrence for 2nd to 5th, 10th, 15th and 20th path index with HH and VV configurations, respectively, where path arrival of first index is always present. An example of the comparison between empirical results with Poisson, modified Poisson and weibull distribution and corresponding minimum mean square error (MMSE) values are shown in Figs. 7.6 and 7.7. The results suggest that the modified Poisson distribution offers the best fit for all antenna and polarization configurations.

7.1.2 Path amplitude modeling

The amplitude fluctuations of each path as a statistical distribution which can be classified into Rayleigh, Rice, Nakagami, Weibul and Lognormal distributions. The linear relative amplitudes of each path index are determined and compared with the theoretical five distributions by using Kolmogorov-Smirnov (KS) test.

Rayleigh fading model of multipath amplitudes at the receiver usually describes the received signal, where all the components are non-LOS and non-specular. Moreover, once a large number of reflecting, diffracting, and scattering waves contributes to the received signal at a receiver in the shadow region. It can also describe where the extreme multipath situations exist [7]. However, if an LOS component or a strong specular component exist in the channel then the Rice distribution

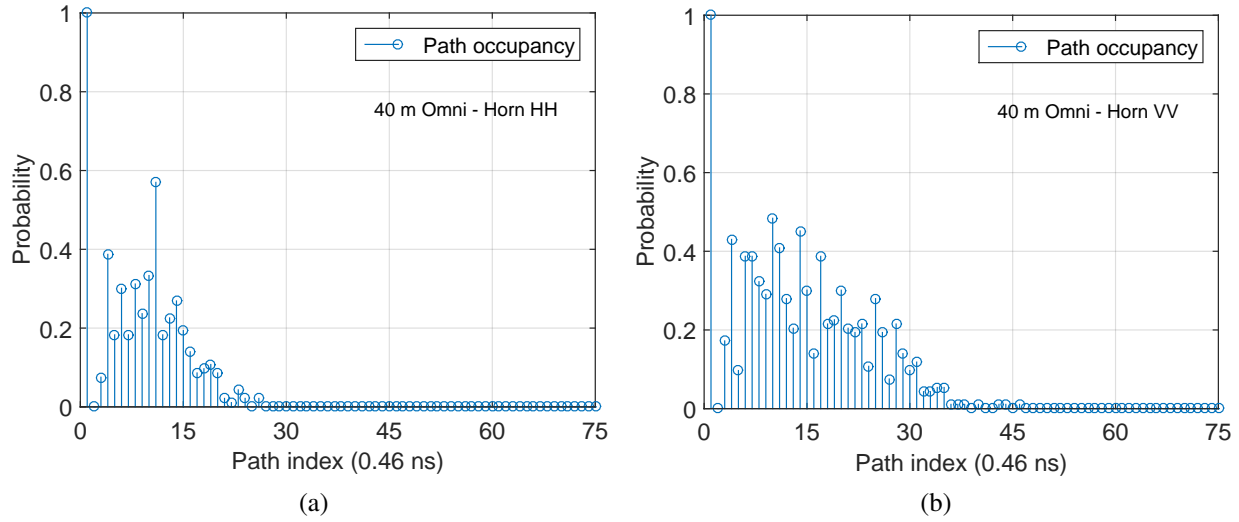


Figure 7.3 Probability of path occupancy as a function of path index with different antenna polarization configurations. (a) and (b) are the 40 m_{O-D_{HH}} and 40 m_{O-D_{VV}} configurations, respectively.

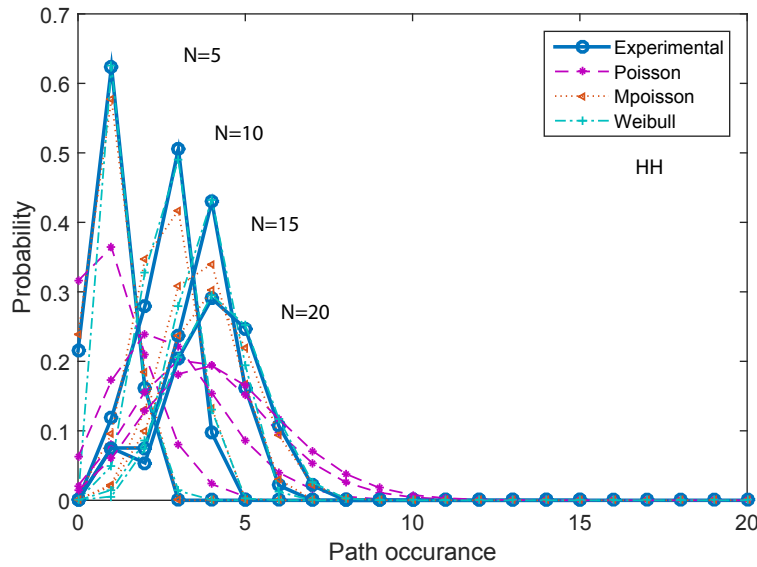


Figure 7.4 An example of path arrival distribution of 40 m_{O-D_{HH}} configuration, where N in the total number of considered path indexes without considering the first path occurrence at first path index.

describes the amplitude fading.

The KS test results identify the best-fitted distribution and results show that each path index is followed Lognormal distribution since higher bandwidth (i.e., 2.16 GHz) causes an average of received signal power over a wide frequency spectrum which makes stable signal strength [84]. An example of amplitude distributions of first path index of different polarization configurations is shown in Fig.

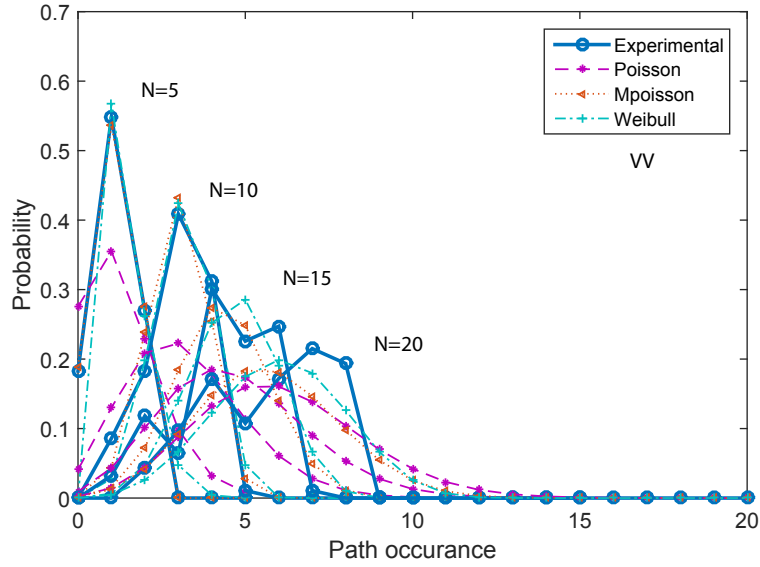


Figure 7.5 An example of path arrival distribution of 40 $m_{O-D_{VV}}$ configuration, where N in the total number of considered path indexes without considering the first path occurrence at first path index.

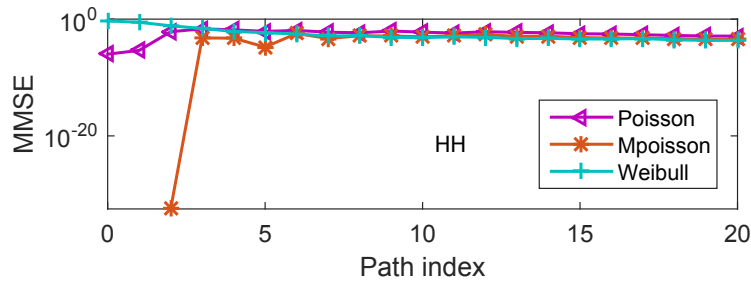


Figure 7.6 An example of the MMSE of three distributions compared to measurement results of 40 $m_{O-D_{HH}}$.

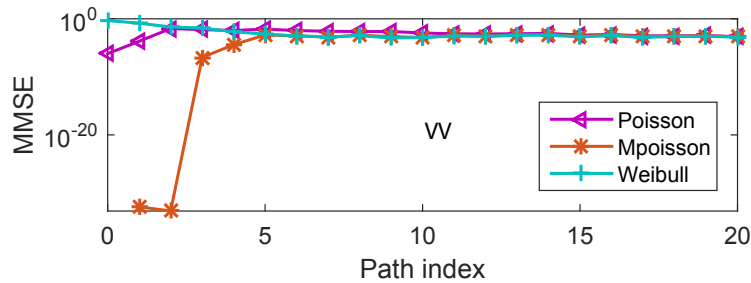


Figure 7.7 An example of the MMSE of three distributions compared to measurement results of 40 $m_{O-D_{VV}}$.

7.8. To explain large scale amplitude variations of the signal in a multipath fading environment, the lognormal distribution has often been used. Zhang [126] reported that if an LOS propagation path exists, along with a limited number of multipath components the Lognormal distribution can be described [7]. Moreover, multiple reflections in the fading phenomenon can be characterized as a multiplicative process. The signal amplitude multiplication gives a rise to a lognormal distribution as an additive process results in a normal distribution (the central limit theorem) [7].

The mean and standard deviation of the amplitudes of each path index are then fitted with a curve fitting technique expressed as $y = y_0 + ae^{xb}$. Where y_0 and a are constants, b is the decay rate and x is the vector of path indexes. The fitting results are listed in Table 7.2. An example of the exponential curve fitting of path amplitudes mean and standard deviation as a function of path index is shown in Fig. 7.9 for 40 m_{O-D} configuration.

Table 7.2 Path amplitude model parameters for all configurations.

Configuration	Mean			Standard deviation		
	y_0	a	b	y_0	a	b
40 m _{O-D_{VV}}	$-1.34993e^{-7}$	0.51262	-0.1515	-0.00373	0.10059	-0.05076
40 m _{O-D_{HH}}	$-3.1573e^{-9}$	0.27231	-0.18273	-0.00118	0.07592	-0.0813
70 m _{D-O_{VV}}	$-4.21703e^{-9}$	0.54885	-0.16382	$-6.48911e^{-4}$	0.10527	-0.09462
70 m _{D-O_{HH}}	$-1.48148e^{-8}$	0.32241	-0.16896	0.00128	0.08923	-0.13113

Results show that the received power is concentrated on the initial path and presents slower and faster rates of decay in the 40 m and 70 m galleries, respectively. In the 40 m gallery, the results exhibit a wide spread of power with respect to delay compared to the one in the 70 m gallery. A slower decay rate of the amplitudes is observed for the *VV* polarization (both mean and standard deviation) as compared to the *HH* polarization. Moreover, a slower decay rate at 40 m was also observed as compared to the 70 m gallery, due to the presence of higher number of multipath with longer delays in the wider gallery.

It has been observed that between the 10th and 15th path index, the mean and standard deviation of the path amplitudes are higher than the neighboring path indexes. This can be explained that the Horn antenna side lobes (either in Tx or Rx side) lie between around $\pm 20^\circ$ and $\pm 60^\circ$ provide a higher value of amplitude variations on the channel. This amplitude variation is higher with vertical polarization compared to horizontal polarization and this is indeed seen in Fig. 7.9. With this angular window of the Horn antenna, the difference between LOS and first order reflected path is approximately less than 10 ns. Therefore, there is a high probability of having higher amplitude variation within this particular angular and temporal window.

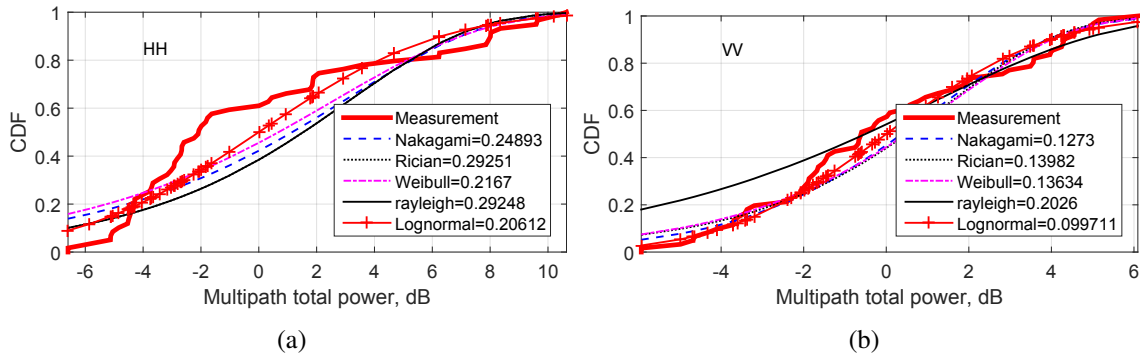


Figure 7.8 An example of Kolmogorov-Smirnov (KS) test and corresponding K values with different antenna polarization configurations at 40 m. (a) and (b) are the HH and VV polarization of first path index according to the amplitude of 40 m_{O-D} configuration, respectively.

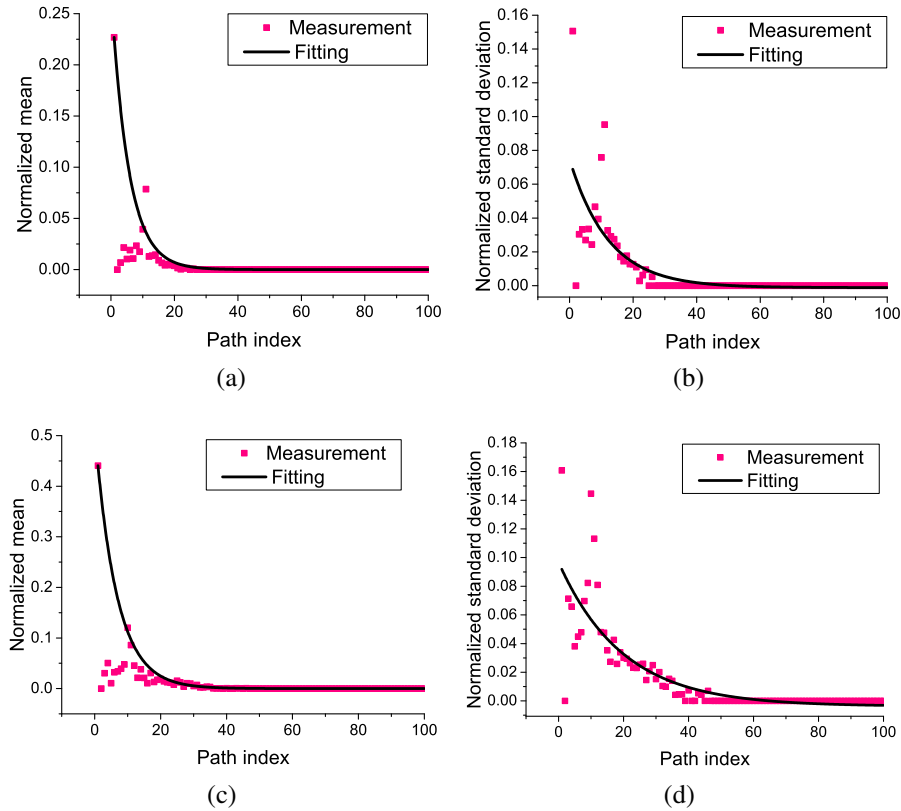


Figure 7.9 An example of normalized mean and standard deviation of amplitude with different polarization configurations of 40 m gallery. (a) and (b) are the mean and standard deviation of 40 m_{O-D_{HH}}, (c) and (d) are the mean and standard deviation of 40 m_{O-D_{VV}}, respectively.

7.1.3 Simulation of impulse responses

The simulation procedure of impulse response generation of the channel is given below :

- Generation of a path arrival model for each path index using the best-fitted distribution of multipath arrivals. The best-fitted distribution is found to be a modified Poisson distribution and its corresponding optimal values of the constant K are obtained as described in [125] and [22].
- Generation of five sets of amplitude model (Rayleigh, Rice, Nakagami, Weibull, and Lognormal) for each path index.
- Combination of the generated path arrival model and the five sets of amplitude models are considered to generate five sets of simulated impulse response models.
- Calculation of 500 iterated RMS delay spread values using the five sets of simulated impulse response models and comparing these with the measured RMS delay spread values using the KS test to identify the best performance score of the simulated impulse response models.

An example of a KS test and corresponding k values are shown in Fig. 7.10. The performance score, with the five sets of amplitude models for all configurations, is given in Table 7.3. The performance scores show that the Lognormal distribution is the best fit for the amplitude model.

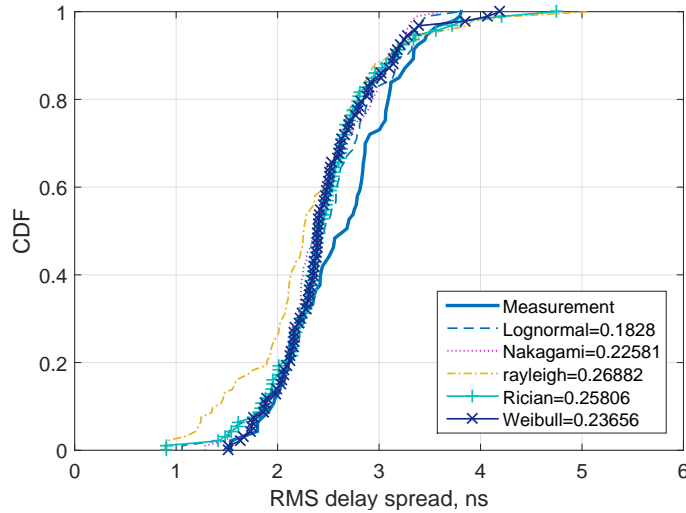


Figure 7.10 An example of kolmogorov-Smirnov (KS) test and corresponding k values between measured and simulated RMS delay spread of 40 m_{O-D_{VV}} configuration.

Experiments in different gallery depths with different antenna and polarization configurations also provide much more channel information for statistical modeling. For instance, lower fluctuation of path occupancies and slower decay rates are observed in 40 m as compared to 70 m galleries. Additionally, no differences in best-fitted distributions of path amplitudes and arrivals were observed between VV and HH in either gallery. The angular characteristics can be integrated into path arrival

Table 7.3 Performance results compared to experimental RMS delay spread.

40 m	Omni-Horn (HH)	Omni-Horn (VV)
Lognormal	226	205
Nakagami	44	110
Rayleigh	83	53
Rician	115	59
Weibull	32	73
70 m	Horn-Omni (HH)	Horn-Omni (VV)
Lognormal	240	151
Nakagami	91	106
Rayleigh	17	74
Rician	66	98
Weibull	94	101

and amplitude models in order to have an effective and robust statistical model for the underground mine environment.

This Chapter presents the statistical channel modeling at 60 GHz for two different namely an underground mine at 40 m and 70 m level depths. Statistical simulation of impulse responses were conducted and compared with measured impulse responses based on RMS delay spread. Performance results suggest that the Lognormal distribution matches better for multipath amplitude distribution and modified poisson distribution performs best fits for the multipath arrivals. Results show a little or no clustering of path arrivals observed in all configurations.

These measurement results can be used subsequently to build an empirical model based on statistical parameters for underground mine wireless channel. However, wireless propagation modeling in underground mine is a challenge and the deterministic modeling is not feasible due to the effect of scattered paths.

CHAPTER 8 CONCLUSION AND FUTURE WORK

8.1 Summary of measurement results

The 60 GHz channel measurements were conducted in CANMET underground mine and extracted channel parameters were analyzed. The main research findings are pointed below :

Multipath phenomena : The measurement results for less than 10 m Tx Rx separation distance with different antennas such as Horn - Horn, Horn - Omni, Omni - Horn with different antenna polarizations show that the path loss exponents are less and close to the free space. A waveguide effect occurs due to the multipath addition at the receiver. This effect is dominant in vertically polarized antennas and Omni - Horn antenna configuration. Moreover, the wider gallery provides a less waveguide effect than the narrower gallery. The directional antenna provides less multipath than the omnidirectional antenna. 3D small scale measurement results show that the small scale fading lies between 1 and 5 dB and 40 m gallery provides a directive propagation phenomenon compared to the 70 m gallery. Rician distribution provides a better fit with the measured small scale power distributions.

Scattering : The scattered power of the walls has been analyzed by the proper measurement arrangements. Scattering along the specular direction from the rough surface can be modeled by the Kirchhoff Approximation (KA). Surface roughness measurements have been conducted and found to be around 6 cm in order to validate the KA model. A fair agreement has been observed between KA model and measurement results. The KA scattering approach could be useful to develop a simulation tool for a mine gallery where roughness magnitude is much higher than the wavelength. Results also show that the specular reflections on the wall and floor are strong and scattering phenomenon exists in nonspecular directions and exhibit to choose an appropriate known different scattering models.

Angular characteristics : The angle of arrival (AoA) results show that the multipath arrivals in the channel are affected by the surface roughness of the mine. The angular spread decreases for larger transmitter receiver separation distances as observed at a short distance (i.e. 3.2 m to 4.4 m). The angular characteristics of the multipath provide a difference compared to a smooth surface due to scattering caused by the rough surfaces. The AoA shape factor values show a correlation between the gallery dimensions i.e. higher gallery dimension provides higher angular spread and lower angular constriction. The standard deviations of the path arrival distribution with respect to the angles were found to be around 18° (at 3.2 m) and 34° (at 3 m) in the 70 m and the 40 m galleries, respectively implying that a larger gallery dimension makes a higher value of angular spread. Shape factor parameter values may help

to estimate an angular resolution for the antenna designers.

Temporal characteristics : The time dispersion results with different antennas and polarizations (less than 10 m Tx Rx separation distances) show that a higher RMS delay spread value provides a lower path loss exponent value. A higher value of gallery dimension provides a higher value of the RMS delay spread and a vertically polarized directional antenna provides more multipath than the horizontal one.

Statistical modeling Impulse responses were simulated based on the statistical parameters of the measured path amplitudes and path arrivals and compared with measured and simulated RMS delay spread values. The Lognormal distribution of the multipath amplitudes of each path index and the modified Poisson distribution of multipath arrivals are the best-fitted distributions for Horn - Omni and Omni - Horn configurations. Moreover, exponential distributions were fitted with the amplitudes of each power delay profile (PDP). Lower fluctuation of path occupancies and the slower decay rate were observed at 40 m compared to the 70 m gallery, no difference of fitted distributions of path amplitudes and arrivals was observed between VV and HH as well as between 40 m and 70 m gallery.

8.2 General conclusion

Few multipath with lower amplitudes along with direct path were observed in Horn - Horn configuration in both galleries. For Horn - Omni and Omni - Horn configurations around 2 to 5 multipath with higher amplitudes along with direct path were found. Angular and time dispersion results of the channel are suitable for the use of beamforming technology. Consequently, a directional vertically polarized Horn - Horn antenna configuration with the narrow beam is suitable for underground mine wireless system design.

Results also suggest that, with antenna beam steering using phased arrays maybe useful for accurate geolocation and reliable for high-speed data link in an underground mine. The vertically polarized antenna constitutes the best candidate since the underground mine floor usually remains almost flat to move heavy vehicles along the gallery. Therefore, for geolocation applications with mmWave may imply a positioning system with a higher precision and accuracy.

These measurement results can also be used as an empirical model for an underground mine wireless channel in 60 GHz band. However, wireless propagation modeling in underground mines remains a challenge and deterministic modeling is not feasible due to the effect of scattering.

8.3 Future work

Firstly, cross polarization measurements could be an interesting measurement approach in order to investigate the XPD (cross polarization discrimination) existence in this particularly confined environment where the surface roughness is much higher than the wavelength.

Secondly, measurements with different antenna polarizations such as linear, dual and circular could be an interesting future work to investigate the proper antenna polarization selection.

Thirdly, AoA results can be implemented into the statistical model of the wireless channel.

Fourthly, channel measurements and analysis with different frequency bands such as 28 GHz, 73 GHz with beamforming technology by integrating the channel sharing approach could provide an advanced future research work for underground mine wireless communication system design perspective.

8.3.1 High frequency (e.g., 60 GHz) channel sharing

Considering the future underground mine wireless communication system design issue which could be a combination of frequency bands of available standards such as LTE, 802.11n, 802.11ad (60 GHz). However, LTE system performance has been conducted in CANMET underground mine reported in [127] and mentioned that the LTE - MIMO system at 2.4 GHz is useful for underground mining applications in the presence of higher number of multipath which enhance the system capacity.

According to the future work extension of underground mine wireless communication system, the real LTE-U wired setups, developed at Ericsson, Ottawa laboratory, were used in order to verify the 5 GHz channel coexistence between LTE-U and Wi-Fi. The future work based on this setup could be the combination of LTE/LTE-U, 802.11ad and other mmWave unlicensed bands, particularly those are feasible for underground mine wireless communication system design.

The background study of channel coexistence, experimental setup, LTE small cell and Wi-Fi products, IEEE 802.11ad, LTE-U, carrier aggregation, co-existence, channel measurement parameters, duty cycle, throughput calculation are explained in Appendix D.

Two LTE-U measurement setups with Ericsson small cell radio base stations (RBSs) such as Radio dot system (RDS) and RBS Pico 6402 products as shown in Fig. D.11 and 8.1. The explanation of the RDS setup is included in Appendix D and illustrated in Fig. D.11. The LTE-U wired setup architecture with a Pico 6402 product, a Wi-Fi access point (AP) and a Wi-Fi station (STA) shown in the Fig. 8.1 and the explained in Appendix D. The performance results of the channel sharing by using QXDM and Bandwidth Monitor are illustrated in Figs. D.12 and D.13, respectively and

LTE-U and WiFi Coexistence laboratory setup

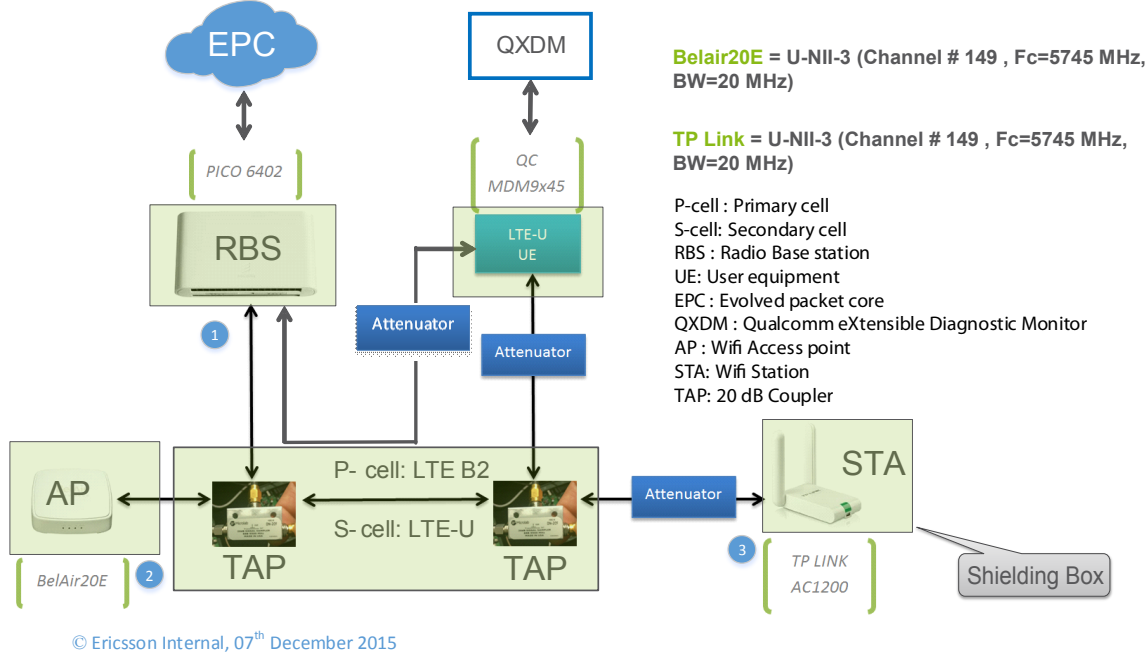


Figure 8.1 LTE-U wired setup with Pico 6402 small cell product.

explained in Appendix D. The post processed performance results based on UDP and TCP protocol are illustrated in Fig. D.14.

In underground mine, the LTE band performs better with multiple antennas, and raise the capacity, recorded in [127]. For high frequency use cases, where the antennas are more directive and perform less multipath in the channel, the beamforming technology would be a better candidate for underground mmWave wireless system deployment.

Concerning the necessity of lower and higher frequency channel sharing in the underground mine gallery, few observations are identified, such as by keeping the coverage and geolocation facility as a high priority and data offloading on demand.

For lower frequency bands, the investigation of LTE-U and Wi-Fi at 5 GHz channel in a dense confined environment and feasibility of the massive MIMO antenna configurations can be the challenges. For higher frequency bands, as an example, RDS with 60 GHz can be useful for underground mine wireless system development by using unlicensed frequency bands, because RDS particularly designed also where the radio signals are not reachable and it may perform very well

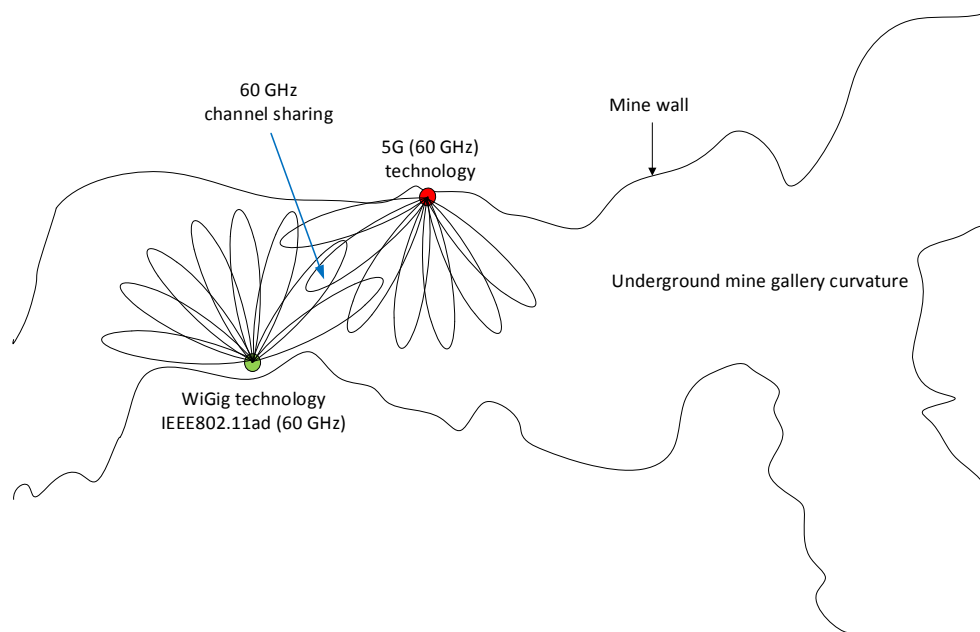


Figure 8.2 An example of a high frequency (i.e., 60 GHz) channel sharing scenario in an underground mine gallery.

in underground mine, while a higher number of mine workers present in a narrower gallery which can be considered as very dense 60 GHz network.

Concerning the setup for higher frequency bands, it is necessary to have the compatible RF cables, bidirectional TAP, power combiners/splitters/dividers. For a fair channel sharing algorithm development using multiple narrow antenna beams, dynamic channel and antenna beam selection increases the complexity.

Fig. 8.2 shows an illustration of unlicensed 60 GHz deployment scenario by considering a channel sharing between WiGig and 5G technologies. Utilizing the beamforming technology, RDS (60 GHz) with phased array multiple antennas (180 degree sector panel) can provide a channel sharing mechanism for underground mine galleries as shown in Fig. 8.2 [128]. Few remarks for channel sharing between WiGig and 5G at 60 GHz can be identified, such as different physical layer specification, on demand dynamic link and frequency selections, network deployment for larger gallery length (i.e., 200 m). However, it can also be deployed in the forest, condensed areas and stadium to ensure high-speed consistent performance (i.e., Gbps) by expecting a better radio performance with future 5G access technology at 60 GHz than WiGig.

REFERENCES

- [1] S. K. Yong, P. Xia, and A. V. Garcia, *60 GHz Technology for Gbps WLAN and WPAN : From Theory to Practice*. Wiley, 2011.
- [2] P. Smulders, "Exploiting the 60 GHz band for local wireless multimedia access : prospects and future directions," *IEEE Communications Magazine*, vol. 40, no. 1, pp. 140 – 7, 2002.
- [3] Y. H. G. Wu and M. Inoue, "An ATM-based indoor millimeter-wave wireless LAN for multimedia transmissions," *IEICE Transactions on Communications*, vol. 8, p. 1740 – 1751, August 2000.
- [4] M. Samimi, K. Wang, Y. Azar, G. Wong, R. Mayzus, H. Zhao, J. Schulz, S. Sun, F. Gutierrez, and T. Rappaport, "28 GHz angle of arrival and angle of departure analysis for outdoor cellular communications using steerable beam antennas in new york city," in *2013 IEEE 77th Vehicular Technology Conference (VTC Spring)*, June 2013, pp. 1–6.
- [5] M. Akdeniz, Y. Liu, M. Samimi, S. Sun, S. Rangan, T. Rappaport, and E. Erkip, "Millimeter wave channel modeling and cellular capacity evaluation," *IEEE Journal on Selected Areas in Communications*, vol. 32, no. 6, pp. 1164–1179, June 2014.
- [6] T. Rappaport, *Wireless communications : principles and practice*, ser. Prentice Hall communications engineering and emerging technologies series. Prentice Hall PTR, 2002.
- [7] J. Schothier, "WP3-study : the 60 GHz channel and its modelling," in *IST-2001-32686 Broadway*.
- [8] J. Proakis, *Digital communications*. McGraw-hill, 2001.
- [9] "IEEE standard for information technology– local and metropolitan area networks– specific requirements– part 15.3 : Amendment 2 : Millimeter-wave-based alternative physical layer extension," *IEEE Std 802.15.3c-2009 (Amendment to IEEE Std 802.15.3-2003)*, pp. 1–200, Oct 2009.
- [10] (2016) The WirelessHD website. [Online]. Available : www.wirelesshd.org
- [11] (2016) The ECMA website. [Online]. Available : www.ecma-international.org
- [12] (2016) The WiGig website. [Online]. Available : <http://www.wi-fi.org/discover-wi-fi/wigig-certified>
- [13] "IEEE standard for information technology–telecommunications and information exchange between systems–local and metropolitan area networks–specific requirements–part 11 : Wireless LAN medium access control (MAC) and physical layer (PHY) specifications amendment 3 : Enhancements for very high throughput in the 60 GHz band," *IEEE Std 802.11ad-*

- 2012 (Amendment to IEEE Std 802.11-2012, as amended by IEEE Std 802.11ae-2012 and IEEE Std 802.11aa-2012), pp. 1–628, Dec 2012.
- [14] R. Kraemer and M. Katz, *Short-Range Wireless Communications : Emerging Technologies and Applications*, ser. Wiley-WWRF series. Wiley, 2009.
 - [15] S. K. Yong, P. Xia, and A. V. Garcia, *60 GHz Technology for Gbps WLAN and WPAN : From Theory to Practice*. Wiley, 2011.
 - [16] R. R. Murphy, J. Kravitz, S. L. Stover, and R. Shoureshi, “Mobile robots in mine rescue and recovery,” *IEEE Robotics Automation Magazine*, vol. 16, no. 2, pp. 91–103, June 2009.
 - [17] C. Nerguizian, C. L. Despins, S. Affes, and M. Djadel, “Radio-channel characterization of an underground mine at 2.4 GHz,” *IEEE Transactions on Wireless Communications*, vol. 4, no. 5, pp. 2441–2453, 2005.
 - [18] A. Maity, “Project Report on Wireless Communication in Underground mines,” Department of Mining Engineering, Asansol Polytechnic, India, Tech. Rep., May 2015.
 - [19] O. Landron, M. J. Feuerstein, and T. S. Rappaport, “Comparison of theoretical and empirical reflection coefficients for typical exterior wall surfaces in a mobile radio environment,” *IEEE Transactions on Antennas and Propagation*, vol. 44, no. 3, pp. 341 – 351, 1996.
 - [20] P. Pagani, *Ultra Wide Band Radio Propagation Channel*. Wiley, 2010.
 - [21] C. Nerguizian, C. L. Despins, S. Affes, and M. Djadel, “Radio-channel characterization of an underground mine at 2.4 GHz,” *IEEE Transactions on Wireless Communications*, vol. 4, no. 5, pp. 2441–2453, 2005.
 - [22] M. Boutin, A. Benzakour, C. Despins, and S. Affes, “Radio wave characterization and modeling in underground mine tunnels,” *IEEE Transactions on Antennas and Propagation*, vol. 56, no. 2, pp. 540–549, Feb 2008.
 - [23] Y. Rissafi, L. Talbi, and M. Ghaddar, “Experimental characterization of an UWB propagation channel in underground mines,” *IEEE Transactions on Antennas and Propagation*, vol. 60, no. 1, pp. 240–246, Jan 2012.
 - [24] I. Ben Mabrouk, L. Talbi, B. Mnasri, M. Nedil, and N. Kandil, “Experimental characterization of a wire-less MIMO channel at 2.4GHz in underground mine gallery,” *Progress in Electromagnetics Research Letters*, vol. 29, pp. 97 – 106, 2012.
 - [25] A. Chehri, P. Fortier, and P.-M. Tardif, “Measurements and modeling of Line-of-Sight UWB channel in underground mines,” in *GLOBECOM - IEEE Global Telecommunications Conference*, San Francisco, CA, United states, 2007.
 - [26] Y. Coulibaly, D. Gilles, H. Nadir, and A. Dodji, “Experimental characterization of the UWB channel for an underground mining vehicle,” in *2013 7th European Conference on Antennas and Propagation (EuCAP)*, April 2013, pp. 2331–2334.

- [27] A. Forooshani, S. Bashir, D. Michelson, and S. Noghianian, "A survey of wireless communications and propagation modeling in underground mines," *IEEE Communications Surveys Tutorials*, vol. 15, no. 4, pp. 1524–1545, Fourth 2013.
- [28] A. Emslie, R. Lagace, and P. Strong, "Theory of the propagation of uhf radio waves in coal mine tunnels," *IEEE Transactions on Antennas and Propagation*, vol. 23, no. 2, pp. 192–205, Mar 1975.
- [29] Y.-P. Zhang, Y. Hwang, and R. Kouyoumjian, "Ray-optical prediction of radio-wave propagation characteristics in tunnel environments," *IEEE Transactions on Antennas and Propagation*, vol. 46, no. 9, pp. 1337–1345, Sep 1998.
- [30] M. Lienard and P. Degauque, "Natural wave propagation in mine environments," *IEEE Transactions on Antennas and Propagation*, vol. 48, no. 9, pp. 1326 – 39, Sept. 2000.
- [31] Y. Coulibaly, B. Mnasri, M. Nedil, I. B. Mabrouk, L. Talbi, and T. A. Denidni, "Experimental characterization of a MIMO underground mine channel at 2.45 GHz," *Progress In Electromagnetics Research B*, no. 50, pp. 219 – 234, 2013.
- [32] M. Ghaddar, M. Nedil, I. B. Mabrouk, and L. Talbi, "Multiple-input multiple-output beam-space for high-speed wireless communication in underground mine," *IET Microwaves, Antennas Propagation*, vol. 10, no. 1, pp. 8–15, 2016.
- [33] B. Mnasri, M. Nedil, N. Kandil, L. Talbi, and I. Ben Mabrouk, "Experimental characterization of wireless MIMO channel at 5.8 GHz in underground gold mine," *Progress In Electromagnetics Research C*, vol. 36, pp. 169 – 180, 2013.
- [34] I. B. Mabrouk, J. C. Reyes-Guerrero, M. Nedil, and L. Talbi, "Line of sight MIMO-UWB short range communication in underground mine tunnel," in *2015 9th European Conference on Antennas and Propagation (EuCAP)*, May 2015, pp. 1–4.
- [35] I. Ben Mabrouk, J. Hautcoeur, L. Talbi, M. Nedil, and K. Hettak, "Feasibility of a millimeter wave mimo system for short range wireless communications in an underground gold mine," *IEEE Transactions on Antennas and Propagation*, vol. 61, no. 8, pp. 4296–4305, Aug 2013.
- [36] M. Ghaddar, L. Talbi, M. Nedil, I. B. Mabrouk, and T. A. Denidni, "Mm-waves propagation measurements in underground mine using directional mimo antennas," *IET Microwaves, Antennas Propagation*, vol. 10, no. 5, pp. 517–524, 2016.
- [37] N. Hakem, G. Delisle, and Y. Coulibaly, "Radio-wave propagation into an underground mine environment at 2.4 GHz, 5.8 GHz and 60 GHz," in *The 8th European Conference on Antennas and Propagation (EuCAP 2014)*, April 2014, pp. 3592–3595.
- [38] A. Chehri, P. Fortier, and P. M. Tardif, "Cthp1-8 : Measurements and modeling of Line-of-Sight UWB channel in underground mines," in *IEEE Globecom 2006*, Nov 2006, pp. 1–5.

- [39] P. F. Smulders, "Statistical characterization of 60 GHz indoor radio channels," *IEEE Transactions on Antennas and Propagation*, vol. 57, no. 10 PART 1, pp. 2820 – 2829, 2009.
- [40] S. Geng, J. Kivinen, and P. Vainikainen, "Propagation characterization of wideband indoor radio channels at 60 GHz," in *IEEE 2005 International Symposium on Microwave, Antenna, Propagation and EMC Technologies for Wireless Communications*, Piscataway, NJ, USA, 2005, pp. 314 – 17.
- [41] X. Zhao, S. Geng, L. Vuokko, J. Kivinen, and P. Vainikainen, "Polarization behaviours at 2, 5 and 60 GHz for indoor mobile communications," *Wireless Personal Communications*, vol. 27, no. 2, pp. 99 – 115, 2003.
- [42] T. Rappaport and D. Hawbaker, "Wide-band microwave propagation parameters using circular and linear polarized antennas for indoor wireless channels," *IEEE Transactions on Communications*, vol. 40, no. 2, pp. 240 – 5, 1992.
- [43] F. Yildirim, A. S. Sadri, and H. Liu, "Polarization effects for indoor wireless communications at 60 GHz," *IEEE Communications Letters*, vol. 12, no. 9, pp. 660 – 662, 2008.
- [44] H. Sawada, H. Nakase, S. Kato, M. Umehira, K. Sato, and H. Harada, "Polarization dependence in double directional propagation channel at 60 GHz," in *IEEE International Symposium on Personal, Indoor and Mobile Radio Communications, PIMRC*, 2009, pp. 3010–3014.
- [45] T. Manabe, K. Sato, H. Masuzawa, K. Taira, T. Ihara, Y. Kasashima, and K. Yamaki, "Polarization dependence of multipath propagation and high-speed transmission characteristics of indoor millimeter-wave channel at 60 GHz," *IEEE Transactions on Vehicular Technology*, vol. 44, no. 2, pp. 268 – 74, 1995.
- [46] A. Maltsev, R. Maslennikov, A. Lomayev, A. Sevastyanov, and A. Khoryaev, "Statistical channel model for 60 GHz WLAN systems in conference room environment," *Radioengineering*, vol. 20, no. 2, pp. 409 – 22, 2011.
- [47] J. Cawley, "An assessment of leaky feeder radio systems in underground mines," in *U.S. Department of the Interior Bureau of Mines*, 1989, pp. 25–1.
- [48] Y. Zhang, G. Zheng, and J. Sheng, "Radio propagation at 900 MHz in underground coal mines," *IEEE Transactions on Antennas and Propagation*, vol. 49, no. 5, pp. 757 – 62, 2001.
- [49] V. Gupta and R. Jangid, "Microwave response of rough surfaces with auto-correlation functions, RMS heights and correlation lengths using active remote sensing," *Indian Journal of Radio and Space Physics*, vol. 40, no. 3, pp. 137 – 46, 2011.
- [50] P. Beckmann and A. Spizzichino, *The Scattering of Electromagnetic Waves from Rough Surfaces*, ser. International Series of Monographs on Electromagnetic Waves. Pergamon Press, 1963, vol. 4.

- [51] R. Piesiewicz, C. Jansen, D. Mittleman, T. Kleine-Ostmann, M. Koch, and T. Kurner, "Scattering analysis for the modeling of THz communication systems," *IEEE Transactions on Antennas and Propagation*, vol. 55, no. 11, pp. 3002 – 9, 2007.
- [52] S. Priebe, M. Jacob, C. Jansen, and T. Kurner, "Non-specular scattering modeling for THz propagation simulations," Rome, Italy, 2011, pp. 1 – 5.
- [53] S. Priebe, M. Jacob, and T. Kurner, "Polarization investigation of rough surface scattering for THz propagation modeling," Rome, Italy, 2011, pp. 24 – 28.
- [54] C. Jansen, S. Priebe, C. Moller, M. Jacob, H. Dierke, M. Koch, and T. Kurner, "Diffuse scattering from rough surfaces in THz communication channels," *IEEE Transactions on Terahertz Science and Technology*, vol. 1, no. 2, pp. 462 – 72, 2011.
- [55] A. Noerpel, M. Krain, and A. Ranade, "Measured scattered signals at 4 GHz confirm strong specular reflections off buildings," *Electronics Letters*, vol. 27, no. 10, pp. 869 – 71, 1991.
- [56] O. Landron, M. J. Feuerstein, and T. S. Rappaport, "Comparison of theoretical and empirical reflection coefficients for typical exterior wall surfaces in a mobile radio environment," *IEEE Transactions on Antennas and Propagation*, vol. 44, no. 3, pp. 341 – 351, 1996.
- [57] H. Zhao, R. Mayzus, S. Sun, M. Samimi, J. Schulz, Y. Azar, K. Wang, G. Wong, F. Gutierrez, and T. Rappaport, "28 GHz millimeter wave cellular communication measurements for reflection and penetration loss in and around buildings in new york city," in *2013 IEEE International Conference on Communications (ICC)*, June 2013, pp. 5163–5167.
- [58] J. Ahmadi-Shokouh, S. Noghianian, and H. Keshavarz, "Reflection coefficient measurement for north american house flooring at 57-64 GHz," *IEEE Antennas and Wireless Propagation Letters*, vol. 10, pp. 1321 – 4, 2011.
- [59] K. Sato, T. Manabe, T. Ihara, H. Saito, S. Ito, T. Tanaka, K. Sugai, N. Ohmi, Y. Murakami, M. Shibayama, Y. Konishi, and T. Kimura, "Measurements of reflection and transmission characteristics of interior structures of office building in the 60-GHz band," *IEEE Transactions on Antennas and Propagation*, vol. 45, no. 12, pp. 1783–1792, Dec 1997.
- [60] B. Langen, G. Lober, and W. Herzig, "Reflection and transmission behaviour of building materials at 60 GHz," in *Personal, Indoor and Mobile Radio Communications, 1994. 5th IEEE International Symposium on Wireless Networks - Catching the Mobile Future.*, Sep 1994, pp. 505–509 vol.2.
- [61] E. Violette, R. Espeland, R. DeBolt, and F. Schwering, "Millimeter-wave propagation at street level in an urban environment," *IEEE Transactions on Geoscience and Remote Sensing*, vol. 26, no. 3, pp. 368–380, May 1988.

- [62] A. Maltsev, R. Maslennikov, A. Sevastyanov, A. Khoryaev, and A. Lomayev, "Experimental investigations of 60 GHz WLAN systems in office environment," *IEEE Journal on Selected Areas in Communications*, vol. 27, no. 8, pp. 1488–1499, October 2009.
- [63] Y. Jiang, K. Li, J. Gao, and H. Harada, "Antenna space diversity and polarization mismatch in wideband 60 GHz-millimeter-wave wireless system," in *2009 IEEE 20th International Symposium on Personal, Indoor and Mobile Radio Communications*, Sept 2009, pp. 1781–1785.
- [64] C. Liu, E. Skafidas, and R. Evans, "Angle of arrival extended S-V model for the 60 GHz wireless indoor channel," in *Telecommunication Networks and Applications Conference, 2007. ATNAC 2007. Australasian*, Dec 2007, pp. 181–185.
- [65] C. Park and T. S. Rappaport, "Short-range wireless communications for next-generation networks : Uwb, 60 GHz millimeter-wave WPAN, and ZigBee," *IEEE Wireless Communications*, vol. 14, no. 4, pp. 70–78, August 2007.
- [66] E. Ben-Dor, T. Rappaport, Y. Qiao, and S. Lauffenburger, "Millimeter-wave 60 GHz outdoor and vehicle AOA propagation measurements using a broadband channel sounder," in *2011 IEEE Global Telecommunications Conference (GLOBECOM 2011)*, Dec 2011, pp. 1–6.
- [67] T. Rappaport, E. Ben-Dor, J. Murdock, and Y. Qiao, "38 GHz and 60 GHz angle-dependent propagation for cellular and peer-to-peer wireless communications," in *2012 IEEE International Conference on Communications (ICC)*, June 2012, pp. 4568–4573.
- [68] H. Xu, V. Kukshya, and T. Rappaport, "Spatial and temporal characteristics of 60 GHz indoor channels," *IEEE Journal on Selected Areas in Communications*, vol. 20, no. 3, pp. 620–630, Apr 2002.
- [69] Q. Spencer, B. Jeffs, M. Jensen, and A. Swindlehurst, "Modeling the statistical time and angle of arrival characteristics of an indoor multipath channel," *IEEE Journal on Selected Areas in Communications*, vol. 18, no. 3, pp. 347–360, March 2000.
- [70] A. Plattner, N. Prediger, and W. Herzig, "Indoor and outdoor propagation measurements at 5 and 60 GHz for radio LAN application," in *IEEE MTT-S International Microwave Symposium Digest, 1993*, June 1993, pp. 853–856 vol.2.
- [71] Z. Loni, R. Ullah, and N. Khan, "Analysis of fading statistics based on angle of arrival measurements," in *2011 International Workshop on Antenna Technology (iWAT)*, March 2011, pp. 314–319.
- [72] N. Moraitis and P. Constantinou, "Indoor channel measurements and characterization at 60 GHz for wireless local area network applications," *IEEE Transactions on Antennas and Propagation*, vol. 52, no. 12, pp. 3180–3189, 2004.

- [73] S. Yarkan, S. Guuzelgooz, H. Arslan, and R. Murphy, "Underground mine communications : A survey," *IEEE Communications Surveys Tutorials*, vol. 11, no. 3, pp. 125–142, rd 2009.
- [74] A. Hrovat, G. Kandus, and T. Javornik, "A survey of radio propagation modeling for tunnels," *IEEE Communications Surveys Tutorials*, vol. 16, no. 2, pp. 658–669, Second 2014.
- [75] M. Ndoh and G. Delisle, "Underground mines wireless propagation modeling," in *IEEE 60th Vehicular Technology Conference, 2004. VTC2004-Fall. 2004*, vol. 5, Sept 2004, pp. 3584–3588 Vol. 5.
- [76] M. Ndoh, G. Delisle, and R. Le, "An approach to propagation prediction in a complex mine environment," in *17th International Conference on Applied Electromagnetics and Communications, ICECom 2003*, Oct 2003, pp. 237–240.
- [77] V. Fono, L. Talbi, and N. Hakem, "Propagation modeling in complex rough environment based on ray tracing," in *2013 IEEE Antennas and Propagation Society International Symposium (APSURSI)*, July 2013, pp. 1924–1925.
- [78] Z. Sun and I. Akyildiz, "Channel modeling and analysis for wireless networks in underground mines and road tunnels," *IEEE Transactions on Communications*, vol. 58, no. 6, pp. 1758–1768, June 2010.
- [79] S. Zhang, "The multipath propagation model of rectangular tunnel channel," in *TEN-CON '02. Proceedings. 2002 IEEE Region 10 Conference on Computers, Communications, Control and Power Engineering*, vol. 2, Oct 2002, pp. 1016–1019 vol.2.
- [80] J. Boksiner, C. Chrysanthos, J. Lee, M. Billah, T. Bocskor, D. Barton, and J. Breakall, "Modeling of radiowave propagation in tunnels," in *Military Communications Conference, 2012 - MILCOM 2012*, Oct 2012, pp. 1–6.
- [81] Z. Xingqi and C. Sarris, "A high-accuracy adi scheme for the vector parabolic equation applied to the modeling of wave propagation in tunnels," *IEEE Antennas and Wireless Propagation Letters*, vol. 13, pp. 650–653, 2014.
- [82] G. Ke, Z. Zhangdui, B. Ai, R. He, B. Chen, Y. Li, and C. Briso Rodriguez, "Complete propagation model in tunnels," *IEEE Antennas and Wireless Propagation Letters*, vol. 12, pp. 741–744, 2013.
- [83] C. Kwon, H. Kim, H. Lee, H. H. Choi, W.-J. Byun, and K. Kim, "A temporal millimeter wave propagation model for tunnels using ray frustum techniques and FFT," *International Journal of Antennas and Propagation*, vol. 2014, pp. 172 924–172 933, 2014.
- [84] K. Pahlavan and A. Levesque, *Wireless Information Networks*, ser. Wiley Series in Telecommunications and Signal Processing. Wiley, 2005.
- [85] J. S. Seybold, *Introduction to RF Propagation*. Wiley, 2005.

- [86] F. P. Fontán and P. M. Espiñeira, *Modelling the Wireless Propagation Channel : A simulation approach with Matlab*, ser. Wireless Communications and Mobile Computing. Wiley, 2008.
- [87] P. Smulders, “Exploiting the 60 GHz band for local wireless multimedia access : prospects and future directions,” *IEEE Communications Magazine*, vol. 40, no. 1, pp. 140 – 7, 2002.
- [88] Y. Coulibaly, G. Delisle, and N. Hakem, “Comparison of small-scale parameters at 60 GHz for underground mining and indoor environments,” in *2013 Proceedings of the International Symposium on Antennas Propagation (ISAP)*, vol. 02, Oct 2013, pp. 693–696.
- [89] (2016) The Anritsu website. [Online]. Available : <http://www.anritsu.com>
- [90] (2016) The LRTCS website. [Online]. Available : <http://lrtc.ca/en/about.aspx>
- [91] G. Conway, L. Schott, and A. Hirose, “Measurement of surface reflection coefficients via multiple reflection of microwaves,” *Review of Scientific Instruments*, vol. 65, no. 9, pp. 2920 – 2920, 1994.
- [92] M. Al-Nuaimi and M. Ding, “Prediction models and measurements of microwave signals scattered from buildings,” *IEEE Transactions on Antennas and Propagation*, vol. 42, no. 8, pp. 1126 – 37, 1994.
- [93] T. Rappaport, *Wireless communications : principles and practice*, ser. Prentice Hall communications engineering and emerging technologies series. Prentice Hall PTR, 2002.
- [94] S. Md Tariq, C. Despins, S. Affes, and C. Nerguizian, “Rough surface scattering analysis at 60 GHz in an underground mine gallery,” in *2014 IEEE International Conference on Communications Workshops (ICC)*, June 2014, pp. 724–729.
- [95] M. Samimi, K. Wang, Y. Azar, G. N. Wong, R. Mayzus, H. Zhao, J. K. Schulz, S. Sun, F. Gutierrez, and T. S. Rappaport, “28 GHz angle of arrival and angle of departure analysis for outdoor cellular communications using steerable beam antennas in new york city,” in *2013 IEEE 77th Vehicular Technology Conference (VTC Spring)*, June 2013, pp. 1–6.
- [96] A. A. M. Saleh and R. Valenzuela, “A statistical model for indoor multipath propagation,” *IEEE Journal on Selected Areas in Communications*, vol. 5, no. 2, pp. 128–137, 1987.
- [97] C. Lounis, N. Hakem, G. Delisle, and Y. Coulibaly, “Large scale characterization of an underground mining environment for the 60 GHz frequency band,” in *2012 International Conference on Wireless Communications in Unusual and Confined Areas (ICWCUCA)*, Aug 2012, pp. 1–4.
- [98] S. Geng, J. Kivinen, and P. Vainikainen, “Propagation characterization of wideband indoor radio channels at 60 GHz,” in *IEEE 2005 International Symposium on Microwave, Antenna, Propagation and EMC Technologies for Wireless Communications*, Piscataway, NJ, USA, 2005, pp. 314 – 17.

- [99] S. Piersanti, L. A. Annoni, and D. Cassioli, "Millimeter waves channel measurements and path loss models," in *IEEE International Conference on Communications*, Ottawa, ON, Canada, 2012, pp. 4552 – 4556.
- [100] T. Zwick, T. Beukema, and H. Nam, "Wideband channel sounder with measurements and model for the 60 GHz indoor radio channel," *IEEE Transactions on Vehicular Technology*, vol. 54, no. 4, pp. 1266–1277, 2005.
- [101] H. Yang, P. F. M. Smulders, and M. H. A. J. Herben, "Channel characteristics and transmission performance for various channel configurations at 60 GHz," *EURASIP Journal on Wireless Communications and Networking*, vol. 2007, no. 1, pp. 43–43, Jan. 2007.
- [102] N. Moraitis and P. Constantinou, "Measurements and characterization of wideband indoor radio channel at 60 GHz," *IEEE Transactions on Wireless Communications*, vol. 5, no. 4, pp. 880 – 889, 2006.
- [103] M. Al-Nuaimi and A. Siamarou, "Coherence bandwidth characterisation and estimation for indoor rician multipath wireless channels using measurements at 62.4GHz," *IEE Proceedings of Microwaves, Antennas and Propagation*, vol. 149, no. 3, pp. 181–187, Jun 2002.
- [104] M. Varela and M. Sanchez, "RMS delay and coherence bandwidth measurements in indoor radio channels in the UHF band," *IEEE Transactions on Vehicular Technology*, vol. 50, no. 2, pp. 515–525, Mar 2001.
- [105] B. Fleury, "First- and second-order characterization of direction dispersion and space selectivity in the radio channel," *IEEE Transactions on Information Theory*, vol. 46, no. 6, pp. 2027–2044, Sep 2000.
- [106] H. Kim, *Wireless Communications Systems Design*. Wiley, 2015.
- [107] W. L. Stutzman and G. A. Thiele, *Antenna Theory and Design*. Wiley, 2012.
- [108] H. Yang, M. H. A. J. Herben, I. J. A. G. Akkermans, and P. F. M. Smulders, "Impact analysis of directional antennas and multiantenna beamformers on radio transmission," *IEEE Transactions on Vehicular Technology*, vol. 57, no. 3, pp. 1695–1707, May 2008.
- [109] S. Tariq, C. Despins, S. Affes, and C. Nerguizian, "Scattering effect based on measurements of reflection coefficients at 60 GHz in an underground mine gallery," in *2014 IEEE 25th Annual International Symposium on Personal, Indoor, and Mobile Radio Communication (PIMRC)*, Sept 2014, pp. 217–221.
- [110] S. A. M. Tariq, C. Despins, S. Affes, and C. Nerguizian, "Experimental results of Rician K-factor and co-polarization ratio of 60 GHz wireless channel in an underground mine gallery," in *2015 IEEE International Conference on Ubiquitous Wireless Broadband (ICUWB)*, Oct 2015, pp. 1–5.

- [111] N. Hakem, G. Delisle, and Y. Coulibaly, "Radio-wave propagation into an underground mine environment at 2.4 GHz, 5.8 GHz and 60 GHz," in *2014 8th European Conference on Antennas and Propagation (EuCAP)*, April 2014, pp. 3592–3595.
- [112] I. Sarris and A. Nix, "Ricean k-factor measurements in a home and an office environment in the 60 GHz band," in *16th IST Mobile and Wireless Communications Summit, 2007*, July 2007, pp. 1–5.
- [113] Y. Zhou, C. Zhou, Y. Zhang, L. Xiao, L. Huang, and S. Zhou, "Rician K-factor analysis of in-cabin distributed MIMO system measurements," in *2011 International Conference on Wireless Communications and Signal Processing (WCSP)*, Nov 2011, pp. 1–4.
- [114] B. Nkakanou, N. Hakem, and Y. Delisle, "Evaluation of ricean K-factor of an ultra-wideband channel in an underground mine," in *2012 IEEE Antennas and Propagation Society International Symposium (APSURSI)*, July 2012, pp. 1–2.
- [115] H. Asplund, J.-E. Berg, F. Harrysson, J. Medbo, and M. Riback, "Propagation characteristics of polarized radio waves in cellular communications," in *2007 IEEE 66th Vehicular Technology Conference, 2007. VTC-2007 Fall.*, Sept 2007, pp. 839–843.
- [116] W. C. Lee and Y. Yeh, "Polarization diversity system for mobile radio," *IEEE Transactions on Communications*, vol. 20, no. 5, pp. 912–923, Oct 1972.
- [117] W. Xu, Y. Hung, M. Niranjan, and M. Shen, "Asymptotic mean and variance of gini correlation for bivariate normal samples," *IEEE Transactions on Signal Processing*, vol. 58, no. 2, pp. 522–534, 2010.
- [118] R. A. Fisher, "On the 'probable error' of a coefficient of correlation deduced from a small sample," *Metron*, vol. 1, pp. 3–32, 1921.
- [119] A. Benzakour, S. Affes, C. Despins, and P.-M. Tardif, "Wideband measurements of channel characteristics at 2.4 and 5.8 GHz in underground mining environments," in *Vehicular Technology Conference, 2004. VTC2004-Fall. 2004 IEEE 60th*, vol. 5, Sept 2004, pp. 3595–3599.
- [120] G. Durgin and T. Rappaport, "Theory of multipath shape factors for small-scale fading wireless channels," *IEEE Transactions on Antennas and Propagation*, vol. 48, no. 5, pp. 682–693, May 2000.
- [121] M. Ndoh and G. Y. Delisle, "A modern approach to complex propagation problems in confined media," in *presented at the URSI General Assembly*, Maastricht, The Netherlands, 2002, pp. 314 – 17.
- [122] Y. Zhang, A. Brown, W. Malik, and D. Edwards, "High resolution 3-D angle of arrival determination for indoor UWB multipath propagation," *IEEE Transactions on Wireless Communications*, vol. 7, no. 8, pp. 3047–3055, August 2008.

- [123] C. Garcia-Pardo, J.-M. Molina-Garcia-Pardo, M. Lienard, D. Gaillot, and P. Degauque, "Double directional channel measurements in an arched tunnel and interpretation using ray tracing in a rectangular tunnel," *Progress In Electromagnetics Research M*, vol. 22, pp. 91 – 107, 2012.
- [124] A. F. Molisch, *Wireless Communications*. Wiley, 2010.
- [125] R. Ganesh and K. Pahlavan, "Statistical modelling and computer simulation of indoor radio channel," *IEE Proceedings I Communications, Speech and Vision*, vol. 138, no. 3, pp. 153–161, June 1991.
- [126] W. Zhang and N. Moayeri, "Classification of statistical channel models for local multipoint distribution service using antenna height and directivity," in *IEEE 802.16.1pc-00/07*, 2000.
- [127] I. Mabrouk, L. Talbil, M. Nedil, and T. Denidni, "On the performance of MIMO systems for LTE downlink in underground gold mine," *Progress In Electromagnetics Research Letters*, vol. 30, pp. 59 – 66, 2012.
- [128] "The IMEC website," IMEC, Tech. Rep., 2016. [Online]. Available : <http://www2.imec.be/content/user/File/NEW/Research/Wireless%20Communication/60%20GhZ/60GhZ%20SMALL%20CELL%20TECHNOLOGY%20.pdf>
- [129] (2016) The TP-LINK website. [Online]. Available : www.tp-link.com
- [130] K. Haneda, L. Tian, H. Asplund, J. Li, Y. Wang, D. Steer, C. Li, T. Balercia, S. Lee, Kim, Y., A. Ghosh, T. Thomas, T. Nakamura, Y. Kakishima, Y. Imai, H. Papadopoulos, T. S. Rappaport, M. K. Samimi, S. Sun, O. Koymen, S. Hur, J. Park, C. Zhang, E. Mellios, A. F. Molisch, A. S. Ghassamzadah, and A. Ghosh, "Indoor 5G 3GPP-like channel models for office and shopping mall environments," in *2016 IEEE International Conference on Communications Workshops (ICCW)*, May 2016.
- [131] "5G channel model for bands up to 100 GHz," Aalto University, BUPT, CMCC, Nokia, NTT DOCOMO, New York University, Ericsson, Qualcomm, Huawei, Samsung, Intel, University of Bristol, KT Corporation, University of Southern California, Tech. Rep.
- [132] "METIS channel models," METIS, Tech. Rep., 2015. [Online]. Available : https://www.metis2020.com/wp-content/uploads/METIS_D1.4_v3.pdf
- [133] (2016) The qualcomm website. [Online]. Available : <https://www.qualcomm.com/invention/technologies/lte/unlicensed>
- [134] Y. Lan, L. Wang, H. Jiang, K. Takeda, H. Harada, T. Wenfang, L. Qiang, and S. Nagata, "A field trial of unlicensed LTE (U-LTE) in 5.8 GHz band," in *Vehicular Technology Conference (VTC Fall), 2015 IEEE 82nd*, Sept 2015, pp. 1–5.

- [135] A. Babaei, J. Andreoli-Fang, and B. Hamzeh, "On the impact of LTE-U on WiFi performance," in *2014 IEEE 25th Annual International Symposium on Personal, Indoor, and Mobile Radio Communication (PIMRC)*, Sept 2014, pp. 1621–1625.
- [136] A. Bhorkar, C. Ibars, and P. Zong, "On the throughput analysis of LTE and WiFi in unlicensed band," in *2014 48th Asilomar Conference on Signals, Systems and Computers*, Nov 2014, pp. 1309–1313.
- [137] E. Almeida, A. M. Cavalcante, R. C. D. Paiva, F. S. Chaves, F. M. Abinader, R. D. Vieira, S. Choudhury, E. Tuomaala, and K. Doppler, "Enabling LTE/WiFi coexistence by LTE blank subframe allocation," in *2013 IEEE International Conference on Communications (ICC)*, June 2013, pp. 5083–5088.
- [138] F. Liu, E. Bala, E. Erkip, M. C. Beluri, and R. Yang, "Small-cell traffic balancing over licensed and unlicensed bands," *IEEE Transactions on Vehicular Technology*, vol. 64, no. 12, pp. 5850–5865, Dec 2015.
- [139] A. Al-Dulaimi, S. Al-Rubaye, Q. Ni, and E. Sousa, "5g communications race : Pursuit of more capacity triggers LTE in unlicensed band," *IEEE Vehicular Technology Magazine*, vol. 10, no. 1, pp. 43–51, March 2015.
- [140] W. J. Hillery, N. Mangalvedhe, R. Bartlett, Z. Huang, and I. Z. Kovacs, "A network performance study of LTE in unlicensed spectrum," in *2015 IEEE Globecom Workshops (GC Wkshps)*, Dec 2015, pp. 1–7.
- [141] S. Choi and S. Park, "Co-existence analysis of duty cycle method with Wi-Fi in unlicensed bands," in *2015 International Conference on Information and Communication Technology Convergence (ICTC)*, Oct 2015, pp. 894–897.
- [142] R. Zhang, M. Wang, L. X. Cai, X. Shen, L. L. Xie, and Y. Cheng, "Modeling and analysis of MAC protocol for LTE-U co-existing with Wi-Fi," in *2015 IEEE Global Communications Conference (GLOBECOM)*, Dec 2015, pp. 1–6.
- [143] M. Labib, J. H. Reed, A. F. Martone, and A. I. Zaghloul, "Coexistence between radar and LTE-U systems : Survey on the 5 GHz band," in *2016 United States National Committee of URSI National Radio Science Meeting (USNC-URSI NRSM)*, Jan 2016, pp. 1–2.
- [144] H. Ko, J. Lee, and S. Pack, "A fair listen-before-talk algorithm for coexistence of LTE-U and WLAN," *IEEE Transactions on Vehicular Technology*, vol. PP, no. 99, pp. 1–1, 2016.
- [145] M. R. Khawer, J. Tang, and F. Han, "usicic 2014 ;a proactive small cell interference mitigation strategy for improving spectral efficiency of LTE networks in the unlicensed spectrum," *IEEE Transactions on Wireless Communications*, vol. 15, no. 3, pp. 2303–2311, March 2016.

- [146] Y. Li, F. Baccelli, J. G. Andrews, T. D. Novlan, and J. Zhang, "Modeling and analyzing the coexistence of Wi-Fi and LTE in unlicensed spectrum," *IEEE Transactions on Wireless Communications*, Feb 2016.
- [147] (2016) The 3GPP website. [Online]. Available : www.3gpp.org
- [148] (2016) The Ericsson website. [Online]. Available : www.ericsson.com
- [149] "IEEE standard for information technology–telecommunications and information exchange between systems–local and metropolitan area networks–specific requirements part 11 : Wireless lan medium access control (MAC) and physical layer (PHY) specifications amendment 10 : Mesh networking," *IEEE 802.11n-2009*, pp. 1–372, Sept 2011.
- [150] (2016) The Ericsson website. [Online]. Available : http://www.ericsson.com/res/site_JP/press/2012/doc/cg_wifi120927_eg.pdf
- [151] (2016) The spiceworks website. [Online]. Available : <https://community.spiceworks.com/reviews/60156-ericsson-ap-6321-indoor-wireless-access-point>
- [152] T. Nitsche, C. Cordeiro, A. B. Flores, E. W. Knightly, E. Perahia, and J. C. Widmer, "Ieee 802.11ad : directional 60 GHz communication for multi-gigabit-per-second Wi-Fi [invited paper]," *IEEE Communications Magazine*, vol. 52, no. 12, pp. 132–141, December 2014.
- [153] R. Zhang, M. Wang, L. X. Cai, Z. Zheng, X. Shen, and L. L. Xie, "LTE-unlicensed : the future of spectrum aggregation for cellular networks," *IEEE Wireless Communications*, vol. 22, no. 3, pp. 150–159, June 2015.
- [154] A. Bhorkar, C. Ibars, and P. Zong, "Performance analysis of LTE and Wi-Fi in unlicensed band using stochastic geometry," in *2014 IEEE 25th Annual International Symposium on Personal, Indoor, and Mobile Radio Communication (PIMRC)*, Sept 2014, pp. 1310–1314.
- [155] D. Park and J. G. Park, "An enhanced ranging scheme using WiFi RSSI measurements for ubiquitous location," in *Computers, Networks, Systems and Industrial Engineering (CNSI), 2011 First ACIS/JNU International Conference on*, May 2011, pp. 296–301.
- [156] (2015) The airccse website. [Online]. Available : <http://airccse.org/journal/jwmn/7415ijwmn09.pdf>
- [157] (2016) The 3GPP website ed impact. [Online]. Available : http://www.3gpp.org/ftp/tsg_ran/WG1_RL1/TSGR1_83/Docs/R1-156622.zip
- [158] (2016) The LTE-U forum website. [Online]. Available : www.lteuforum.org
- [159] A. Molisch, *Wireless Communications*. Wiley-IEEE Press, 2005.
- [160] P. Dhakal, D. Riviello, F. Penna, and R. Garello, "Impact of noise estimation on energy detection and eigenvalue based spectrum sensing algorithms," in *2014 IEEE International Conference on Communications (ICC)*, June 2014, pp. 1367–1372.

- [161] N. Rupasinghe and . Güvenç, “Licensed-assisted access for WiFi-LTE coexistence in the unlicensed spectrum,” in *Globecom Workshops (GC Wkshps)*, 2014, Dec 2014, pp. 894–899.
- [162] S. K. Baghel, M. A. Ingale, and G. Goyal, “Coexistence possibilities of LTE with ISM technologies and gnss,” in *2011 National Conference on Communications (NCC)*, Jan 2011, pp. 1–5.
- [163] N. C. S. M. S. Rathi, N. Malik, “Throughput for TDD and FDD 4G LTE systems,” *International Journal of Innovative Technology and Exploring Engineering (IJITEE)*, vol. 3, no. 12, May 2014.
- [164] (2016) The Ericsson review website. [Online]. Available : http://www.ericsson.com/res/thecompany/docs/publications/ericsson_review/2014/er-radio-dot.pdf

APPENDIX A ANGULAR DISPERSION RESULTS

Table A.1 AoA statistical parameters of 70 m gallery according to transmitter receiver separation distance. Λ and γ are dimensionless, θ_{max} and Max AoA in degrees ($^{\circ}$).

Distance(m)	Rx heights	Λ	γ	θ_{max}	Max AOA
3.2	0	0.3384	0.8674	89.9999	-5
	$\lambda/2$	0.2719	0.9183	-87.0038	-5
	λ	0.3393	0.8016	82.2243	-5
	$3 \lambda/2$	0.2193	0.9414	-80.1655	-5
	2λ	0.2487	0.9671	-80.0564	10
	$5\lambda/2$	0.3508	0.8466	-89.9924	0
3.4	0	0.2498	0.9519	-78.6010	-5
	$\lambda/2$	0.2890	0.8679	81.1848	-5
	λ	0.3546	0.8238	-86.5999	-5
	$3 \lambda/2$	0.2758	0.9464	-74.9121	-5
	2λ	0.2897	0.9511	-74.8779	10
	$5\lambda/2$	0.2821	0.8891	-83.8207	5
3.6	0	0.2162	0.9504	-77.4137	-5
	$\lambda/2$	0.1885	0.9840	-83.2274	-5
	λ	0.1878	0.9839	-83.3974	-5
	$3 \lambda/2$	0.2909	0.9025	67.8465	10
	2λ	0.2543	0.9349	80.7350	10
	$5\lambda/2$	0.2908	0.8820	83.7951	10
3.8	0	0.1993	0.9612	-80.1074	-5
	$\lambda/2$	0.2080	0.9554	-81.4771	-5
	λ	0.1812	0.9814	-83.7275	-5
	$3 \lambda/2$	0.3531	0.5827	-65.6226	0
	2λ	0.2772	0.9101	87.7662	10
	$5\lambda/2$	0.3076	0.8772	87.5770	10
4	0	0.1391	0.9960	89.8487	-10
	$\lambda/2$	0.2816	0.9720	-76.3528	35
	λ	0.2120	0.9530	82.0005	-5
	$3 \lambda/2$	0.2615	0.9554	77.5925	10
	2λ	0.1581	0.9897	-89.8708	10
	$5\lambda/2$	0.2223	0.9547	81.2754	10
4.2	0	0.2383	0.9605	-76.4890	-5
	$\lambda/2$	0.2619	0.9537	-77.5668	10
	λ	0.2818	0.8994	-88.2090	-5
	$3 \lambda/2$	0.2123	0.9622	-78.7241	10
	2λ	0.3663	0.7975	80.6157	10
	$5\lambda/2$	0.3378	0.9092	-85.7707	10
4.4	0	0.2764	0.9519	76.4647	-5
	$\lambda/2$	0.3521	0.8367	87.2880	10
	λ	0.2822	0.9463	82.5325	-5
	$3 \lambda/2$	0.2859	0.9601	76.9167	10
	2λ	0.3161	0.9227	82.7628	-5
	$5\lambda/2$	0.2893	0.9313	83.9356	10

Normalized Line of sight (LOS) lobes are maximum at each distance. Strong reflections from the metallic pipe of the tunnel have been observed at each distance around 40° . Some other reflections have also observed coming from the rough walls in different angles. Following figures show that

the normalized PAPs according to transmitter receiver separation distances between 3.2 m and 4.4 m with different distances in z directions with a step of $\lambda/2$ at 70 m gallery.

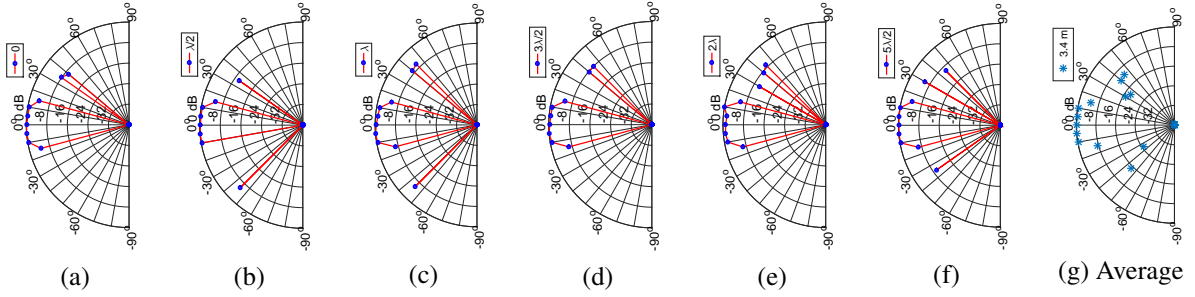


Figure A.1 Normalized PAPs according to transmitter receiver separation distance at 3.4 m with different distances in z directions with a step of $\lambda/2$ at 70 m gallery.

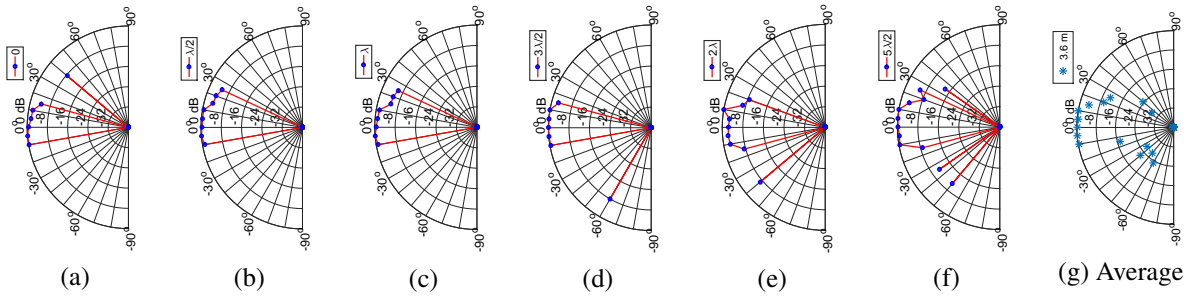


Figure A.2 Normalized PAPs according to transmitter receiver separation distance at 3.6 m with different distances in z directions with a step of $\lambda/2$ at 70 m gallery.

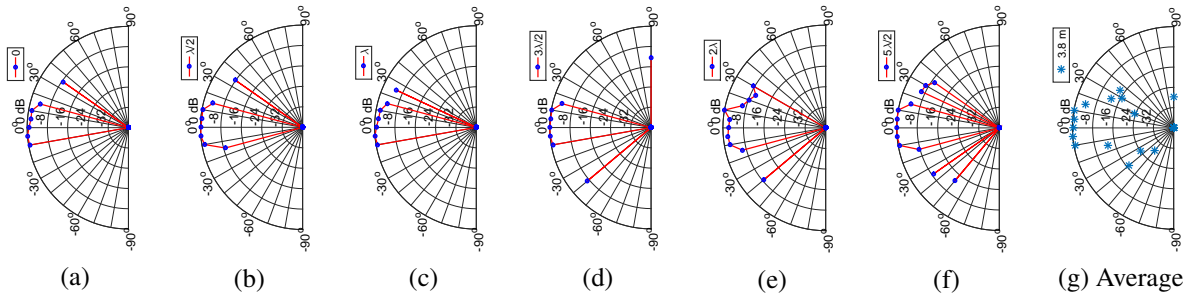


Figure A.3 Normalized PAPs according to transmitter receiver separation distance at 3.8 m with different distances in z directions with a step of $\lambda/2$ at 70 m gallery.

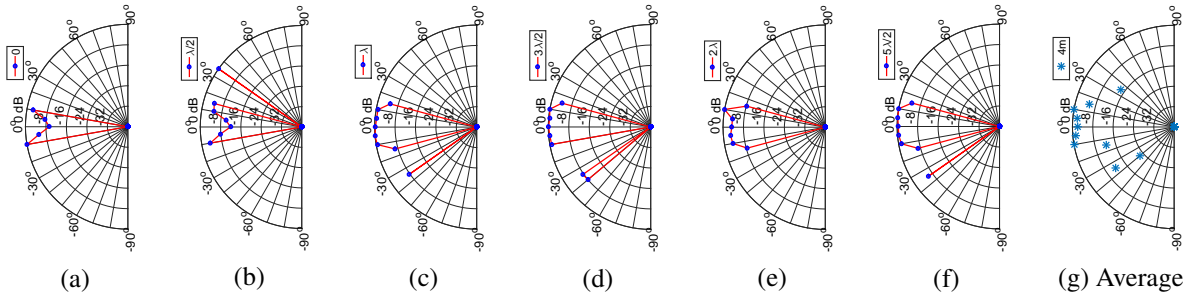


Figure A.4 Normalized PAPs according to transmitter receiver separation distance at 4 m with different distances in z directions with a step of $\lambda/2$ at 70 m gallery.

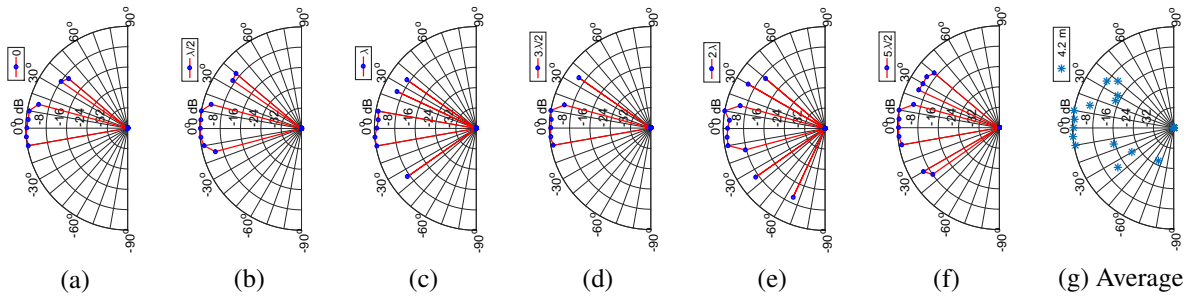


Figure A.5 Normalized PAPs according to transmitter receiver separation distance at 4.2 m with different distances in z directions with a step of $\lambda/2$ at 70 m gallery.

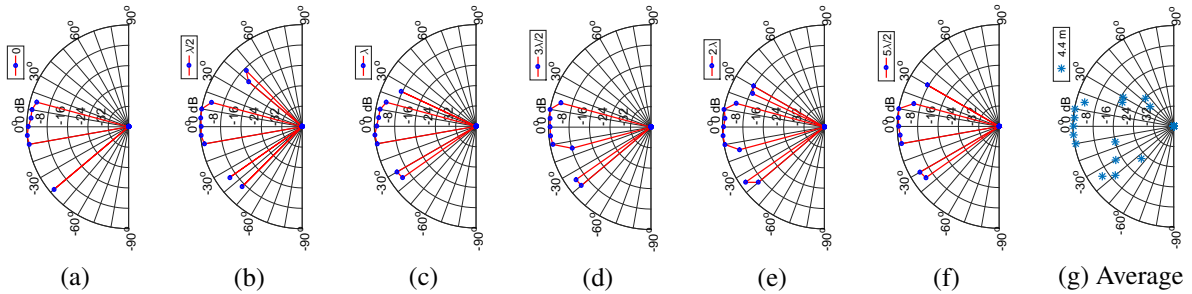


Figure A.6 Normalized PAPs according to transmitter receiver separation distance at 4.4 m with different distances in z directions with a step of $\lambda/2$ at 70 m gallery.

APPENDIX B DYNAMIC THRESHOLD

A modified dynamic threshold (Th_d) could be used as defined in [119] given by

$$\text{Th}_d [dB] = 20 \log_{10} \{ \overline{W} + K \times \text{std}(W) \} \quad (\text{B.1})$$

where W is the the linear amplitude of the noise defined by the time delays, processed as $\{A_{max}(t_{id}) + T_{th}(t_{id})\}$ to 800 ns, $A_{max}(t_{id})$ is the time ID of the highest peak and $T_{th}(t_{id})$ is the threshold time ID which was set to 100 ns. The K value could defined by a visual inspection of the measured and calculated largest path delay.

The threshold was necessary to verify with the maximum access delay, where the maximum travelling time of a path based on the specular reflection from the wall. An example of $\text{Th}_d [dB]$ calculation is given below :

$$\text{Th}_d [dB] = 20 \times \log_{10}(\text{mean}(\text{noise}) + K \times \text{std}(\text{noise})); \quad (\text{B.2})$$

$$\text{Th}_d [dB] = 20 \times \log_{10}(\text{noise}_{mean}) + 20 \times \log_{10}(1 + (3 \times \text{noise}_{std}/\text{noise}_{mean})); \quad (\text{B.3})$$

$$\text{Th}_d [dB] = -33.4667 \text{ dB} + 8.0169 \text{ dB} \quad (\text{B.4})$$

$$\text{Th}_d [dB] = -25.4498 \text{ dB} \quad (\text{B.5})$$

Here, before normalization of the PDP, another threshold (Th) was processed between the highest peak and the VNA dynamic range of 107 dB, in which all PDPs necessary to satisfy $\text{Th}_d < \text{Th}$.

The maximum access delay condition could be followed according to the propagation geometry, for example, at 2.6 m Tx Rx separation distance, the maximum specular reflection path delay was 10.56 ns, and the measured largest path delay was found around 11 ns.

APPENDIX C SCATTERING SIMULATION PROCEDURE

The simulation geometries are illustrated in Fig. C.1 and C.2, and the simulation steps are given below :

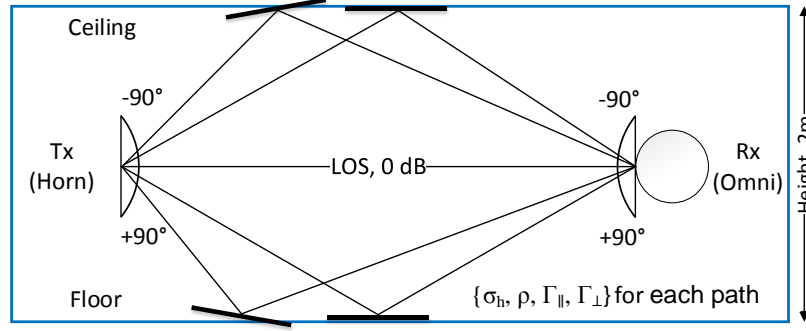


Figure C.1 Simulation geometry (2D gallery height with Ceiling and Floor) with VV configuration based on the 70 m gallery dimension by using Vertical cross section between the antenna radiation pattern and the gallery height.

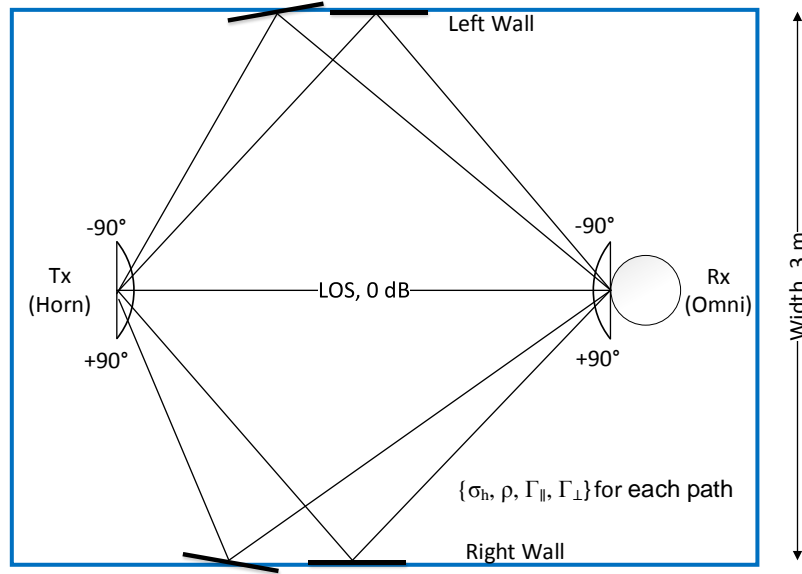


Figure C.2 Simulation geometry (2D gallery width Left Wall and Right Wall) with VV configuration based on the 70 m gallery dimension by using Vertical cross section between the antenna radiation pattern and the gallery width.

- The angles of $\Omega_{T,l}$ and $\Omega_{R,l}$ were between -90° and $+90^\circ$ in 2D plane where $\phi = 0^\circ$ as shown in Fig. 5.14. The angles were selected between $\pm 20^\circ$ and $\pm 60^\circ$ with 10° step size.

- Two gallery geometries (i.e., height and width) were selected as shown in Fig. C.1 and C.2. Transmitter and receiver were located in the middle of the gallery.
- 70 m gallery dimension was at 2 m in height and 3 m in width. 40 m gallery dimension was at 5 m in height and 5 m in width.
- The normalized LOS path has been selected as antennas maximum gain of 0 dB.
- The traveling distance (D_l) and delay of the l^{th} scattered path were calculated by using the geometry according to the gallery height and width as shown in Fig. C.1 and C.2.
- The power of the l^{th} path was calculated as the summation of the antenna gains of corresponding angles of $\Omega_{T,l}$, $\Omega_{R,l}$ (as shown in Fig. 5.14) and the free space loss ($-10 \times n_{v,h} \times \log_{10}(D_l)$), where $n_v = 1.15$ and $n_h = 1.98$.
- Five paths were selected as a set of scattered path. At each set, the third path was considered as reflected path. First, second, fourth and fifth paths are weighted by a five random values (i.e., between 0 to 1) and a linear average value of four paths was calculated and added with the third path by considering that weighted four paths were added constructively at the receiver.
- The calculated power of the l^{th} path was multiplied by the corresponding value of $\{\Gamma \times \rho\}$, where ρ and Γ were calculated as described in [109]. Since σ_h is randomly selected between 0.2 mm to 5 mm, the value of the scattering coefficient ρ was random. To calculate the ρ , any model could be used as described in [109]. For this simulation Kirchhoff scattering coefficient was considered since the gallery heights measurements were conducted. The Fresnel reflection coefficients Γ_{\parallel} and Γ_{\perp} were calculated according to the $\Omega_{T,l}$ angles (i.e., as the incident angles of θ_i shown in Fig. 5.13) and as described in [109]. To consider the scattering phenomena with the rough surface, the θ_i and θ_r were followed as Snell's law and considered that the surface plane was tilted by the rough surface plane shown in Fig.C.1 and C.2.
- Finally the RMS delay spread at each distance was calculated from the power delay profiles of the ceiling, floor, left wall and right wall.

The geometrical illustration of the simulation is shown in Fig. C.3 and given below :

$$a = \sqrt{b^2 - c^2} \quad (C.1)$$

$$b = \frac{c}{\sin^{-1}(90^\circ - \theta_T)} \quad (C.2)$$

$$c = L/2 \quad (C.3)$$

$$d = d_{tot} - a \quad (C.4)$$

$$e = \sqrt{c^2 + d^2} \quad (C.5)$$

$$\theta_r^{sm} = \theta_R \quad (C.6)$$

$$\theta_i^{sm} = \theta_T \quad (C.7)$$

$$\theta_R = 90^\circ - \tan^{-1}\left(\frac{c}{d}\right) \quad (C.8)$$

$$\theta_i^s = \frac{\theta_i^{sm} + \theta_r^{sm}}{2} \quad (C.9)$$

where L is the gallery width or height. θ_i^s is the incident angle of the path.

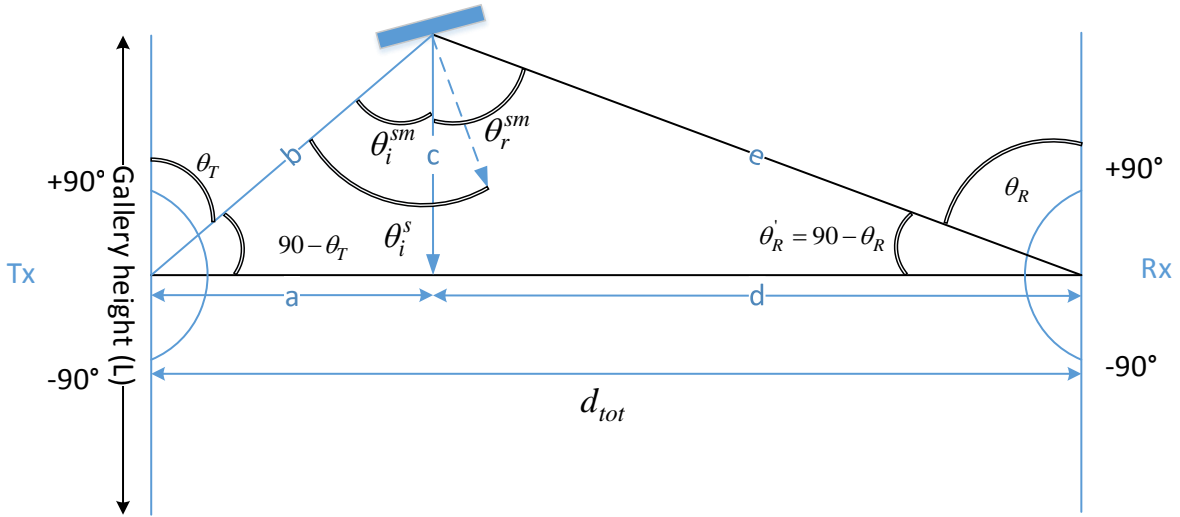


Figure C.3 Geometry of scattered ray tracing simulation.

APPENDIX D LTE-U SMALL CELL AND WIFI CHANNEL SHARING EXPERIMENTAL INFORMATION

An investigation of 60 GHz wireless channel sharing (as an approach of future work) based on the experiment over LTE, LTE-U, WiFi bands :

Tri-band (2.4 GHz, 5 GHz, and 60 GHz) system design is highlighted recently. The application of the Tri-band can combine the advantage of the coverage with 2.4/5 GHz and high data rate at 60 GHz on demand. As an example, the commercial product of TP-LINK, Talon AD7200 is capable of up to 800 Mbps in 2.4 GHz, 1733 Mbps in 5 GHz, and 4600 Mbps at 60 GHz (WiGig) [129]. Therefore, multi-gigabit 802.11ad WiGig solution are attractive for industries to have a seamless connection at speeds up to 4.6 Gbps.

An investigation to cover 5G requirements for cellular networks has been conducted both on measurement and ray-tracing simulation at 2.5 GHz, 28 GHz, and 60 GHz [130]. Both indoor office and shopping mall environments have been investigated at expected 5G enabled frequencies, including 2.9 GHz, 3.5 GHz, 6 GHz, 14 GHz, 15 GHz, 20 GHz, 28 GHz, 29 GHz, 60 GHz, and 73 GHz and some preliminary analysis of large scale channel characteristics has been summarized in [131, 132].

Based on the open literature reviews, another high-speed data transfer solution, developed by Qualcomm, is the combination of two existing technologies LTE and Wi-Fi as LTE in unlicensed spectrum (LTE-U) [133] of 5 GHz. Within a time sharing basis of the small cell network with LTE-U allows a cell phone to use LTE unlicensed 5 GHz carrier with Wi-Fi network. It uses control channels over LTE and transfer also voice and data over LTE-U. Wi-Fi (IEEE 802.11 standard) bands are suitable to be use as an unlicensed band for radio access with LTE-U, and LTE-U band (5 GHz) performance over Wi-Fi (5 GHz) is better due to the advantages of LTE-U access technology, medium access control, mobility management, and excellent coverage. Therefore, available spectrums in 5 GHz make an attention for LTE-U. Wi-Fi devices are already deployed, but LTE-U small cell and LTE-U capable user equipment (UE) devices are required in order to have a coexistence mechanism. Multiple LTE-U operators may use the same spectrum to provide data service and may cause severe RF interference with Wi-Fi. A proper channel selection is necessary to be used by LTE-U to minimize Wi-Fi RF interference. If all channels are occupied by the Wi-Fi, and LTE-U is forced to use the same channel, then Wi-Fi will back off once its interference level is above the energy detection threshold (-62 dBm). Therefore, a proper co-existence mechanism is necessary to have a considerable interference caused by LTE-U on Wi-Fi channel.

Background study of LTE-U and Wi-Fi channel sharing :

Along with LTE-U forum activities, research has been conducted to have a fair and reliable co-existence between LTE-U and Wi-Fi technology.

In [134], the field trial in thinly dispersed network deployment suggested that a better performance of LTE-U than Wi-Fi can be observed and interference handling technology is necessary for the use of unlicensed spectrum. It has been noted that the reason for better performance of LTE coverage and capacity is expected due to more advanced PHY/MAC design of LTE than Wi-Fi, such as, e.g., robust control channel protection to guarantee the coverage with a low-SINR, robust channel coding, longer cyclic prefix (CP) in OFDM to better overcome multipath fading, and better retransmission mechanism, and so on.

A comparison of LTE and Wi-Fi MAC and PHY layer are well explained in [135] and mentioned orthogonality is not maintained properly in Wi-Fi technology due to different subcarrier spacing and lack of synchronization into the OFDM transmission. For MAC layer comparison, multiple access, channel usage, channel access, collision avoidance and co-existence mechanisms are different for LTE and Wi-Fi. Moreover, a numerical analysis suggests that the currently proposed period in an LTE protocol is too short to access a Wi-Fi channel and its listening time will be higher during the channel sharing.

A stochastic analysis is presented in [136] and it is stated that Wi-Fi performance can be degraded by LTE-U in dense networks due to persistent transmissions. A better co-existence can be achieved by reducing LTE-U transmission power and increasing ED threshold for Wi-Fi.

In [137], it is mentioned that if Wi-Fi (contention based access) coexists with LTE (scheduled channel access) in an unlicensed band, the performance of the Wi-Fi will severely degraded. A simple coexistence mechanism has been proposed based on blanking some LTE subframes for Wi-Fi transmission to improve the performance of Wi-Fi.

F. Liu et al. [138] proposed a channel access mechanism for dual band femtocell (DBF) to access an unlicensed band. A traffic balancing algorithm has been described to use both licensed and unlicensed bands, which is based on an algorithm that searches for the optimal power allocation in the licensed band and the optimal channel time usage in the unlicensed band. Moreover, a practical algorithm is proposed to tune the unlicensed band channel usage time for LTE-U.

In [139], a new adaptive listen before talk (LBT) mechanism is derived for both Wi-Fi and LTE-U technologies. The 802.11e standard employs LBT functionality with CSMA/CA which senses the spectrum and solves the radio self-coexistence issues in the overlapping spectrum. A significant degradation in the performance of Wi-Fi systems is reported during the same channel sharing because Wi-Fi changes to silence mode due to CSMA/CA. The LTE performance variation is around 4%

while Wi-Fi performance degrades about 70% to 90%. A non-coordinated and coordinated coexistence models are also proposed for new LTE-U and Wi-Fi sharing systems and can be implemented in the radio access technology (RAT).

Moreover, Hillery et al. [140] shows that unlicensed LTE performs better than Wi-Fi in outdoor environments. The coexistence using a static muting approach on LTE-U has been studied to have fairness with Wi-Fi network.

In [141], the collisions during Wi-Fi and duty cycle (DC) devices co-existence are shown and stated the cumulated collision for Wi-Fi device decreases as the DC-on time is increased.

In [142] a friendly coexistence mechanism of LTE-U with Wi-Fi is reported and mentioned that by adjusting a period of LTE-U and Wi-Fi transmissions, and proposed spectrum sensing, Wi-Fi protection can be provided up to certain degree.

Since the LTE-U (5 GHz) band occupied by the different radar system and by the 802.11 technology and a survey about the RF regulations and the different radar types within the different sub-bands of the 5 GHz band are presented in [143]. Spectrum sharing techniques are also introduced. The summary of the regulations includes limiting the transmit power, limiting the UNII device to be used indoors only, using dynamic frequency selection, using listening before the talk and transmission power control as well as restricting the power leakage to neighbor bands.

Since LTE does not sense for channel availability before transmissions, the LTE interference severely affects the Wi-Fi. A fair listen before talk (F-LBT) algorithm for the coexistence of LTE-U and Wi-Fi is proposed and improves the total system throughput while providing the fairness between LTE-U and Wi-Fi [144].

In [145], the multi-operator LTE-U co-channel interference co-ordination mechanism is presented. It is highlighted that using CSAT overall system performance could be degraded when multi-operator LTE-U small cells share the same unlicensed channel without any CSAT gating cycle co-ordination for LTE-U transmissions.

Moreover, LTE can improve transmission and coverage probability of Wi-Fi by adopting a shorter transmission duty cycle, lower channel access priority, or more sensitive clear channel assessment (CCA) thresholds [146]. However, in order to have a fair sharing mechanism between LTE-U and Wi-Fi, a laboratory setup with a wired connection is necessary. The following sections are giving more explanation of the setup and necessary information underlying the research and development of underground mine wireless system design.

LTE small cell :

LTE (Long Term Evolution) is defined as an evolution of both radio and core network [147]. 3GPP release 8 introduced the E-UTRAN (Evolved Universal Terrestrial Access Network), which is the accessible part of the IP-based Evolved Packet System (EPS), consists of high spectral efficiency, high peak data rates, short round trip time (RTT) as well as flexibility in bandwidths. EPS provides real-time services carried by the IP, for example, an IP will be assigned once the mobile device is switched on and released, once switched off.

The LTE radio access network is based on

- OFDMA (Orthogonal Frequency Division Multiple Access)
- Higher order modulation (up to 64QAM)
- Large bandwidths (up to 20 MHz)
- MIMO (up to 4x4)

Radio dot system product :

Ericsson small cell Radio Dot System (RDS) offers an indoor solution with a compact and flexible mounting facility [148]. Fig. D.1 shows a RDS product and its main features are ; deployment advantages where radio signal usually not reachable, able to connect through Power over Ethernet (PoE) LAN cables (Category 5/6/7), carrier aggregation facility, supports LTE/Wi-Fi, MIMO, possible to use as LTE-U (5 GHz).



Figure D.1 Radio Dot System

RBS Pico 6402 :

Figure D.2 Pico RBS 6402

The RBS 6402 is another small cell Radio Base station (RBS) of Ericsson [148]. The Fig. D.2 shows an RBS Pico 6402 product and its main features are ; covers indoor environments such as shopping mall, train station up to 5 Km square area, low energy consumption, MIMO, carrier aggregation upto 300 Mbps speed, supports 10-bands, supports LTE, WCDMA and Wi-Fi and mixed-mode capabilities, plug-and-play installation in ten minutes, supports LTE-U (5 GHz) functionality.

Wi-Fi products :

Supporting IEEE 802.11n standard product operates on both the 2.4 GHz and the 5 GHz bands is based on the previous 802.11 standards by adding multiple-input multiple-output (MIMO) and 40 MHz channels to the PHY layers, and frame aggregation to the MAC layer. MIMO significantly increases data throughput as the number of data streams are increased. In MAC layer, the frame aggregation technique is used which combines multiple frames into one large frame before the transmission and increases the channel utilization and improves the MAC throughput [149].

BelAir20E :

Belair 20E is an Ericsson Carrier-Grade Wi-Fi Solution [148, 150]. The Fig. D.3 shows a Wi-Fi access point and the its features are given below

- Supports 2.4/5 GHz IEEE 802.11 b/g/n certified
- 2x2 MIMO with 2 spatial streams
- 300 Mbps per radio



Figure D.3 BelAir 20E

Ericsson AP 6321 :

Figure D.4 Ericsson AP 6321

The AP 6321 is an Ericsson's product using the latest 802.11ac Gigabit WLAN which supports data rates of over 1 Gbps. It provides a cost-effective service such as Hot zone, 3G, and 4G traffic offload. It operates in both 2.4 GHz and 5 GHz operation simultaneously with 3x3 MIMO and 3 spatial streams per band. The 5 GHz radio supports 80 MHz bandwidth and 256 QAM modulation rates, resulting a 1.3 Gbps system data rate. In addition, the 2.4 GHz radio supports the robust, high-performance 802.11n standard. Supporting 40 MHz channel bandwidth, 2.4 GHz radio enables 450 Mbps speed. It has integrated wireless point-to-point, point-to-multipoint or mesh and gigabit Ethernet wired backhaul connection features [148, 151].

IEEE 802.11ad :

IEEE 802.11ad standard supports unlicensed 60 GHz band and makes a transformation from the use of omnidirectional to directional wireless radio channel [13, 152].

With a new physical layer of 802.11 operating at 60 GHz named as WiGig, with a rate of 7 Gbps. It has high signal attenuation factor due to higher oxygen absorption and typically used for 10 m distance. It has an additional attenuation of 22 dB compared to the 5 GHz band.

At 60 GHz, the received signal is dominated by the line of sight (LOS) path and first order reflections. Concrete materials can easily create a blockage. Thus, 60 GHz link is more suitable to use in indoor environments where sufficient reflectors are available to avoid blockage. The IEEE 802.11ad takes an advantage of beamforming with quasi-optical propagation behavior, low reflectivity, and high attenuation.

Therefore, IEEE 802.11ad introduces beamforming (BF) mechanism and hybrid medium access control (MAC) to facilitate directional point to point radio communication link.

Moreover, multiple phased antenna arrays also enable high gain coverage in all directions not as like as MIMO, but like a set of additional sectors (i.e., narrow beam) with only one antenna array used at a time.

LTE-U :

A small cell can support both LTE (licensed spectrum) and LTE-U (unlicensed spectrum), which reduces the cost of the service operators. LTE-U currently uses the 5 GHz band to co-exist with Wi-Fi and provides a low-cost wireless data traffic to the user. Moreover, in Heterogeneous Networks (HetNet), LTE-U supports data offloading from a macro cell to a small cell. The current LTE licensed cellular networks restrict to fulfil the higher data traffic demand of users, LTE-U is then acceptable in 3GPP [147], which operates as a supplemental downlink carried by the unlicensed secondary carrier (S-cell), and uplink carried by primary licensed LTE carrier (P-cell). Once the P-cell and S-cell both are employed in the small cell network the user equipment (UE) uses carrier aggregation (CA) to have a higher throughput. Concerning the 5 GHz band in LTE-U which is used already deployed by Wi-Fi operator implying 802.11 protocols, a co-existence between LTE-U and Wi-Fi is then necessary to have fairness.

Fifth-generation (5G) network deployment issues also motivate to combine a significant amount of unlicensed spectrum (6 - 100 GHz) of both Wi-Fi and LTE technologies. Following this issue, specifically the 5 GHz band the LTE in the unlicensed band has a physical layer topology to access Wi-Fi spectrum. The 3GPP radio access network (RAN) under the LTE-U forum focuses on the

capacity, coverage, cell coordination and cost reduction [147]. Therefore, the ongoing research activities and product developments of coexistence, fairness, impact between LTE-U and Wi-Fi at 5 GHz are necessary to characterize and investigate the existing problems to propagate a motivation for further research activities on 5GPPP channel sharing.

Carrier aggregation :

LTE-Advanced uses carrier aggregation (CA) to increase the bandwidth, and thereby increase the bitrate. CA can be used for both FDD and TDD. Component carrier (CC) is defined as for each aggregate carrier and the bandwidths are used (1.4, 3, 5, 10, 15 or 20 MHz). The Fig. D.5 shows the same frequency and different frequency band allocations for FDD. For TDD, the number of CCs and the bandwidths of each CC will be same for downlink and uplink. Fig. D.6 shows the use of CA in intra band (contiguous), intra band (non-contiguous), and inter band (non-contiguous) [147].

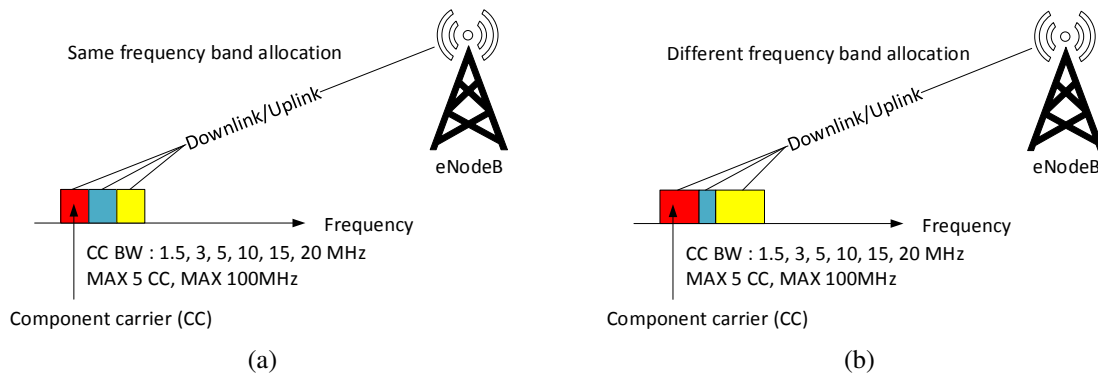


Figure D.5 (a) Same frequency band allocation, (b) Different frequency band allocation.

Co-existence :

In 3GPP R13, studies are carried out on co-existence about the carrier sense adaptive transmission (CSAT) and listen before talk (LBT) coexistence mechanism for a fair channel sharing between LTE-U and Wi-Fi [147]. In [153], LTE-U duty cycling and LTE-U CSAT coexistence mechanism have been presented and showed that LTE-U can gain higher throughput than Wi-Fi in small cell deployment. A. Bhorkar et. al. [154] analyzed a stochastic geometry for a fair coexistence. The hidden node issue reduces the system performance but the channel selection mechanisms can solve this issue. However, a fair and better performance for both LTE-U and Wi-Fi can be achieved by

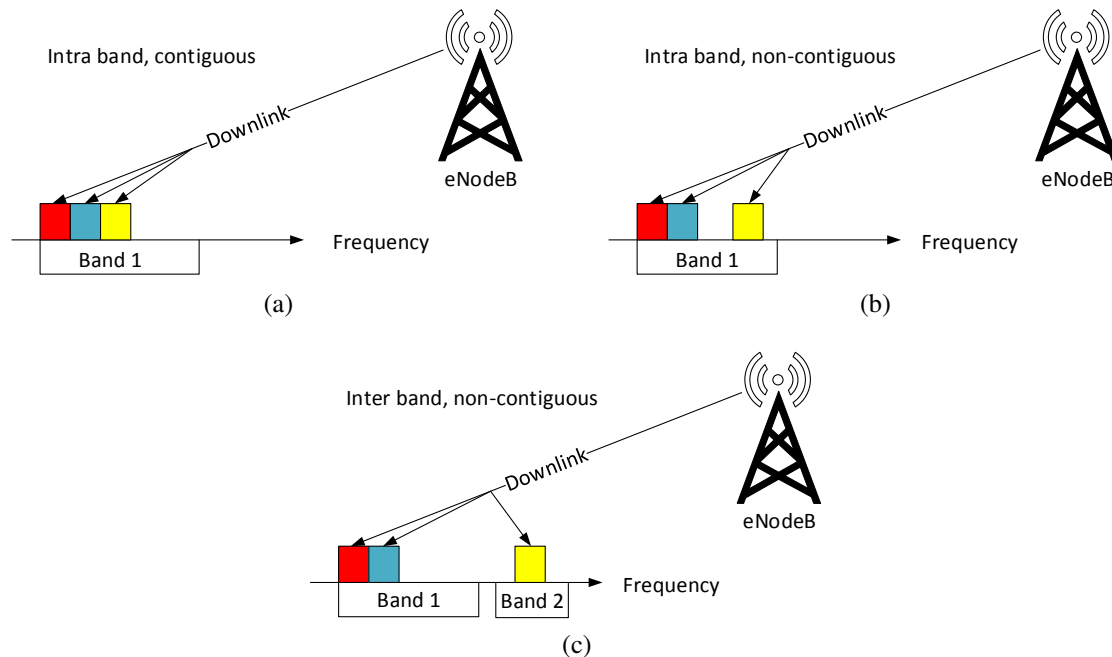


Figure D.6 (a) Intra band (contiguous) (b) Intra band (non-contiguous) (c) Inter band (non-contiguous).

combining listen before talk, channel access priority, and a smart choice of the energy detection (ED) threshold reported in [154].

Fig. D.7 shows the general demonstration of illustrations of co-existence between LTE-U and Wi-Fi networks. Fig. D.7a shows two different LTE and Wi-Fi networks work independently. Fig. D.7b shows that user equipment (UE) can get both channel access from different networks independently, but UE can get the same facility through only LTE-U network (licensed and unlicensed) and throughput will be higher by using the carrier aggregation process shown in Fig D.7c. Fig. D.7d shows that if a Wi-Fi uses the same channel, the sharing can be possible between LTE-U and Wi-Fi access by using ON and OFF periods in the time domain. Simply once LTE-U channel is switched off, Wi-Fi will get access the channel and share the same channel by using a smooth fairness coexistence mechanism.

Channel measurement parameters :

RSSI Receive Strength Signal Indicator (RSSI) measures the average total RF energy (channel power) at the antenna port, including noise, serving cell power, interference power and can

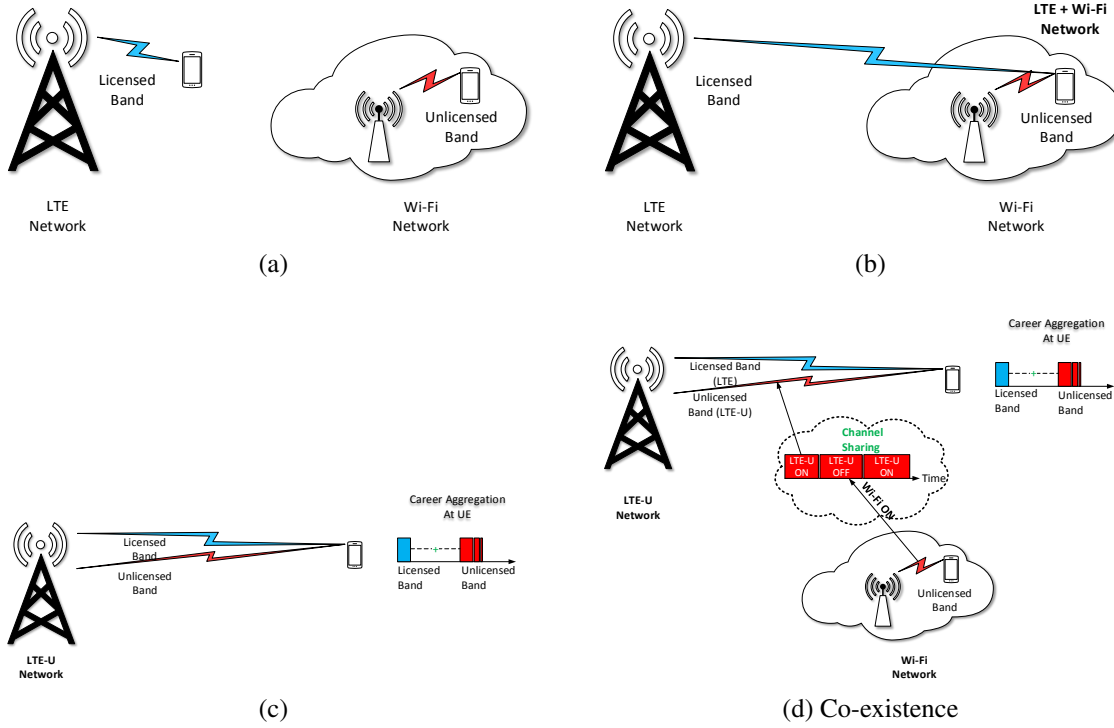


Figure D.7 LTE, LTE-U and Wi-Fi networks

be determined within a distance d by the free space formula [155]

$$RSSI(d)_{dBm} = P_t - \left(10n \log_{10} (d/d_0) + PL(d_0) + L_{cable} \right)_{attenuation} + \left(G_t + G_r \right)_{optional} [dBm] \quad (D.1)$$

where P_t is the transmit power. Optional parameters such as G_t and G_r are the transmitter and receiver antenna gains (can be ignored for wired setup). n is the path loss exponent (defined by the channel model) and $PL(d_0)$ is the free space path loss at the distance or d_0 , and L_{cable} is the cable loss of the system particularly used for high frequency wired setup. The attenuation term can be replaced by the attenuator for wired setup.

Moreover, RSSI can be calculated by the OFDM symbol (within the measurement bandwidth over total resource blocks) received power carrying all sources such as co-channel non-serving and serving cells, adjacent channel interference and thermal noise [156].

CCA-ED LTE-U coexists fairly with Wi-Fi by using a clear channel assessment on Energy Detection (CCA-ED) threshold. If the interference level at the Wi-Fi device caused by the LTE-U channel is above the ED, the device must wait for a period of time called the backoff. The impact of ED threshold has been demonstrated in [157]. Power interference can be with the energy above ED threshold and moderate power interference could be below ED threshold

[158]. In addition, the average channel power based on RSSI at the receiver can be measured by the spectrum analyzer as received power in dBm per bandwidth and power spectral density measured as received power in dBm per Hz.

The average energy detection threshold of the received signal is a spectrum sensing method, given in [159, 160] and can be defined as,

$$T_{ED} = \frac{1}{KN} \sum_{k=1}^K \sum_{n=1}^N |r_{kn}|^2 \quad (D.2)$$

where N is the number of samples received within K observation times and r is the linear amplitude of the sample. If T_{ED} compares with predefined threshold t_{ed} (-62 dBm) and if $T_{ED} < t_{ed}$ then it decides Null Hypothesis (the channel is free) otherwise Hypothesis 1 (the channel is occupied or busy).

Wi-Fi uses ED thresholds to identify non Wi-Fi energy such as LTE-U signal on the current channel. This non Wi-Fi energy can be in the same frequency band or due to corrupted Wi-Fi transmission, which is not identified and unable to decode header defined in the PHY layer.

ED threshold usually set -62 dBm, which is 20 dB higher than the Wi-Fi carrier sense (CS) threshold (-82 dBm) as shown in Fig. D.8. If the channel is in the busy state (i.e. $T_{ED} > t_{ed}$), Wi-Fi station senses the channel every time slot to determine whether the energy still exists or not. During channel sharing moment between Wi-Fi and LTE-U, Wi-Fi access points or Wi-Fi stations have to follow this procedure more frequently before getting the channel access. Since the sensing time will increase when LTE-U interference is present, Wi-Fi performance significantly degrades [137, 161] which implies a necessity of fair coexistence mechanisms.

CCA-CS Carrier Sense (CS) threshold is the threshold to be able to detect preamble (the training signal depends on the bandwidth) used for 802.11 devices to avoid interference usually set at -82 dB shown in Fig. D.8.

Busy state identification by a Wi-Fi station :

- If PHY detects the energy level $> -82dBm$.
- If PPDU header successfully decoded.

RSRP Reference Signal Receive Power (RSRP) is the average power of Resource Elements (RE) over the considered bandwidth which carries reference signals without noise and interference. RSRP is not used for coexistence interference measurements, particularly used for cell reselection and handover decisions [162].

RSRQ Reference Signal Receive Quality (RSRQ) is the reference symbol power with interference from cells and neighboring systems. It determines the existence of interference, but it cannot identify the source of interference. It can be determined as $RSRQ = (N \times RSRP)/RSSI$, where N is the number of Resource Blocks (RB) of the OFDM symbols.

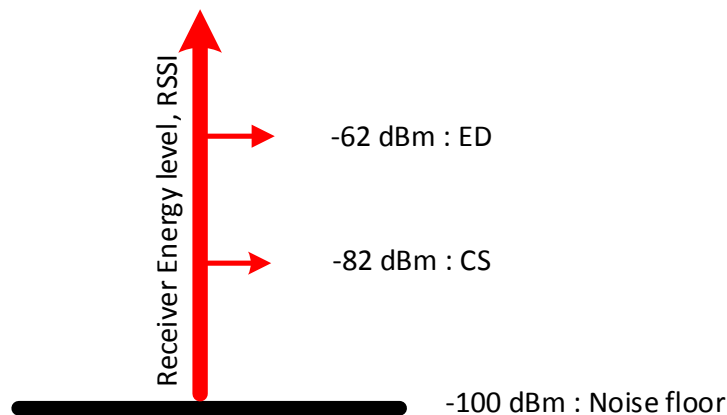


Figure D.8 Receiver energy levels.

CQI Channel Quality Indicator (CQI) indicates the RF link quality, including interference from a neighboring cell and coexistence. It cannot indicate also the interference sources (such as other base station's existence and coexistence) [162].

SNR Signal to noise ratio (SNR) is the ratio between the received signal and the noise energy, usually expect higher SNR (i.e, 30) value to have a maximum throughput at UE.

MCS Modulation and coding scheme (MCS) is chosen by the channel quality indicator (CQI).

HARQ Hybrid Automatic Repeat Request (HARQ) is a combination of high rate forward error correcting (FEC) coding and ARQ (Automatic Repeat Query) error control.

Duty cycle :

Duty cycle (DC) can be defined as a percentage of the ratio between the active ON time and total time described in Fig. D.9. DC can be formulated as $DC = \frac{O}{T} \times 100\%$, where DC is the duty cycle, O is the active ON time, and T is the total time or period. Thus, a 60% duty cycle means the signal is ON 60% and OFF 40%.

Carrier sense adaptive transmission (CSAT) :

CSAT is an algorithm to have a fair coexistence between Wi-Fi and LTE-U network developed by Ericsson and LTE-U forum [158]. Simulation results with CSAT show that LTE-U provides a proper fair sharing with the neighbour Wi-Fi channel. CSAT algorithm provides a fair Transmission opportunity based on the current channel RF conditions. The procedure follows once RBS (eNodeB) will sense the channel during the OFF period of time, if recorded samples are higher than -62 dBm, then decrease the ON period gradually and Infinite Impulse Response (IIR) filter is used

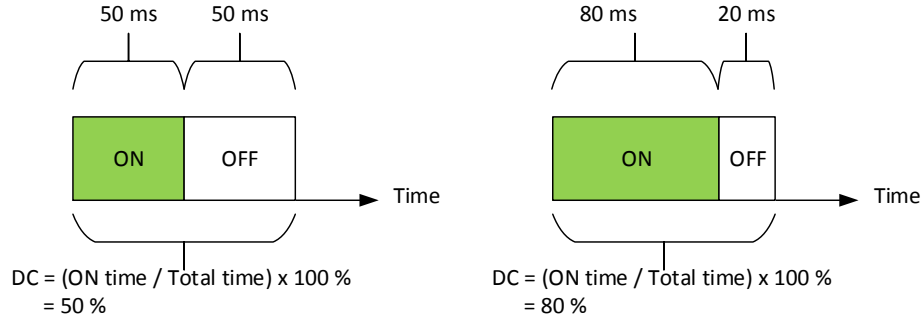


Figure D.9 An example of the duty cycle

for smooth operation (increment and decrement) and CSAT algorithm consequently gives an access period to Wi-Fi on the unlicensed channel.

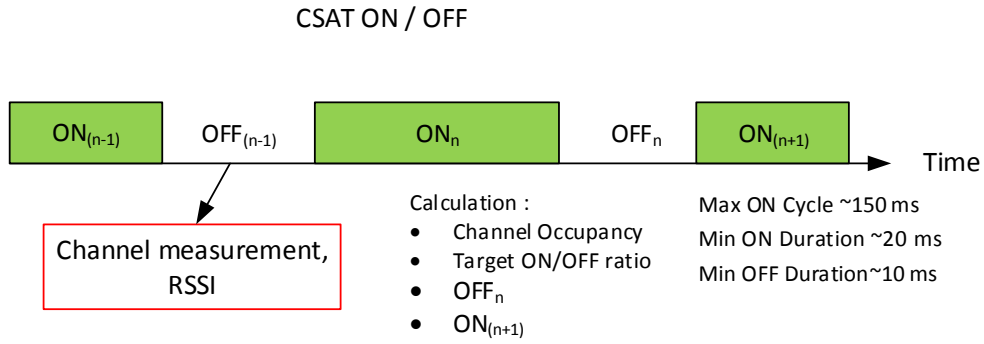


Figure D.10 Primary explanation of CSAT.

Fig. D.10 shows a primary CSAT mechanism for an unlicensed band which takes the channel measurements (RSSI) during the OFF time, and based on the channel condition, calculate the channel occupancy, target ON/OFF ratio, next ON and OFF time. Note that, the new CSAT specifications define (Max ON cycle = 20 ms, Min ON = 2 ms, Min OFF = 2 ms) the lower values of CSAT specification for better Wi-Fi coexistence.

Throughput calculation per radio channel :

The approximate calculation of the throughput within one OFDM subframe can be defined as $Throughput_{OFDM}$ and expressed as [163]

$$Throughput_{OFDM_{onesubframe}} = \left(\frac{A \times S \times OS \times RB \times TS \times MS}{SF_{time}} \right) \times 0.75 \quad (D.3)$$

where A is the number of antennas, S is the number of subcarriers, OS is the number of OFDM symbols, RB is the number of resource blocks, TS is the number of time slots, MS is the modulation scheme (i.e., QPSK, QAM etc.) and SF_{time} is the one subframe time duration. The resource elements (RE) are defined by the number $(S \times OS \times RB \times TS)$ of symbols where 75% of the bits are assumed as user data.

An example of the calculation of a RE with 20 MHz bandwidth is equal to 16800 symbols (12 subcarriers, 7 OFDM symbols, 100 resource blocks, 2 time slots). Hence, one RE carries one modulated OFDM symbol, if 64 QAM (6 bits/symbol) modulation is used in one symbol, and the subframe duration is 1 ms then throughput will be 100.8 Mbps. About 25% overhead of reference signals, sync signals, and coding etc can be estimated. The throughput will be $100.8 \text{ Mbps} \times 0.75 = 75.6 \text{ Mbps}$ with one antenna. With 2×2 (rank 2) MIMO antennas the throughput will be approximately 151.2 Mbps.

LTE-U and WiFi wired setup requirements :

In order to perform an LTE-U experiment in the laboratory, the following requirements are necessary to follow :

- Verify channel interference in the laboratory setup area (with the wire and wireless channel) by a spectrum analyzer.
- Use of shielding boxes to isolate all radioactive components.
- Use of cooling fans (two cooling fans for small cell RBS such as Pico 6402).
- Verify each frequency dependent RF components such as coupler, combiner, attenuator.
- Adjust attenuators (3, 6, 10, 20, 30 dB) on the Tx/Rx side to ensure the channel power measurements are less or higher than -62 dBm.
- E2E RF calibration (using two-port network analyzer).
- Verify frequency dependencies of RF cables.
- Commissioning of RDS and RBS radio parameters such as center frequency, bandwidth, cell power, cell ON/OFF etc. and ensure the CSAT is implemented in the software load.
- Familiar with QXDM, QCAT, QC UE, Moshell and installation of RBS software load.
- Familiar with input and output parts of the frequency converter.
- Verify necessary network IP configurations (UE, APs, STAs, RBS), iperf server/client.

LTE-U setup with RDS :

RDS setup was with a preliminary prototype software load and hardware. It has been investigated as a primary reference setup for the measurements that has been developed with the setup of Pico

6402 product (with latest software load and hardware) to have a co-existence test between LTE-U and Wi-Fi technologies.

As shown in the Fig. D.11, the wired setup contains a modified RDS and two Wi-Fi access points (backhaul connection). A Digital Unit (DU) and an Indoor Radio Unit (IRU) were connected with an optical fiber cable. DU performs the baseband (BB) processing and IRU performs radio signal processing, digital to analog converter (DAC), analog to digital converter (ADC), intermediate frequency (IF) conversion [164]. IRU is connected with RDS via LAN cable. Two power amplifiers were used to boost up the radio signals of the modified RDS at the 5 GHz band. The two output signals were connected through two bidirectional couplers (TAP). TAP outputs were connected via coax cable to two Wi-Fi access points. All radioactive components were in the shielding boxes. The center frequency and bandwidth of both Wi-Fi and RDS were same. Since the UE did not support 5 GHz band, a frequency converter was used to convert from 5 GHz to LTE bands.

Inside the UE shielding box, 2x2 MIMO channel configurations were conducted as shown in the Fig. D.11 by using four splitters/combiners. The secondary cells (S-cell) are then connected to UE via wires. The primary cells (P-cell) were connected to the UE from another base station. After the installation and configuration of the setup through corresponding network IPs, the iperf software, the UDP traffic was sent in two ways, one from the core network IP server to UE (300 Mbps ; P-cell and S-cell), another is from Wi-Fi AP to another Wi-Fi AP (150 Mbps). Since the RDS prototype and software load were a preliminary version, the primary co-existence test cases were investigated and followed in the PICO setup shown in Fig. 8.1. Fig. D.11 shows LTE-U setup with RDS.

LTE-U setup with Pico 6402 :

The setup is shown in Fig. 8.1. AP and STA were connected as backhaul connection. EPC (evolved packet core) network was connected to Pico 6402 radio base station. Pico 6402 contains 2x2 MIMO antennas for LTE, LTE-U (5 GHz) and Wi-Fi (2.4 GHz was not active) radios. LTE and LTE-U transmitter and receiver antennas were connected by a combiner/splitter in order to combine and split two radio signals. The primary LTE cell (P-cell) power were attenuated through attenuators and connected to UE. Two output signals of LTE-U radio were connected through two bidirectional couplers (TAP). Couplers output were connected via cables to Wi-Fi access point BelAir20E and Wi-Fi station TP link AC1200. All radioactive components were in the shielding boxes in order to avoid external interference. The center frequency and the bandwidth of 5 GHz signals of both LTE-U and Wi-Fi were same. Since the UE supports LTE-U band (5 GHz), the frequency converter was not used. Channel powers at locations 1, 2 and 3 in Fig. 8.1 were set above the energy detection threshold (ED) of -62 dBm by using the measurements with a spectrum analyzer. After installation and configuration of the setup by using network and laptop IPs, an iperf script was developed by

between LTE-U and Wi-Fi, and the combined throughput on the time line (shown in lower figure) presents an amount of time that has given to Wi-Fi to access the channel.



Figure D.12 Real time QXDM output.

Bandwidth Monitor output :

Fig. D.13 shows a real time fair 5 GHz channel sharing experimental results to explain the CSAT algorithm explicitly. Qualcomm LTE-U UE has 5 GHz operational functionalities which combine LTE and LTE-U bands throughput. The Bandwidth Monitor software was used to monitor real time throughput during channel sharing. The basic functionality of that the CSAT algorithm, that it starts sensing the channel with a numbered channel measurement sample during the OFF period of time and if the channel is above -62 dBm then adapt the next transmission ON and OFF times. PICO 6402 was configured with a duty cycle duration of 210 ms, detection threshold of -62 dBm, a maximum channel usage of 95 % and a minimum channel usage of 33 %. There are four time slots have been considered in order to verify the channel sharing. Firstly, for LTE-U ON of 60 s and Wi-Fi OFF of 60 s and channel usage 95 % of the duty cycle, The UE recorded around 278 Mbps since Wi-Fi channel is OFF. Secondly, once LTE-U and Wi-Fi both channels are ON, during sharing via CSAT, LTE-U channel starts decreasing the transmission opportunity (from 95 % to

33 % of the duty cycle) until around 30 seconds, and simultaneously Wi-Fi starts getting channel access from 5 % to 77 % of the duty cycle until the shared channel becomes stable. During the next 30 seconds (around) both LTE-U and Wi-Fi becomes stable and share the channel smoothly (33% and 77 % of the DC of LTE-U and Wi-Fi, respectively). Thirdly, once LTE-U is ON and Wi-Fi is OFF, LTE-U starts to sense the channel and increase the usage of the channel from 33 % to 95 % of the duty cycle and correspondingly throughput increases to around 278 Mbps during the first 30s and throughput becomes stable to 278 Mbps in next 30s. Finally, once LTE-U is OFF and Wi-Fi is ON, Wi-Fi gets the entire channel access since LTE-U is OFF and consequently Wi-Fi records around 128 Mbps by using a standalone channel.

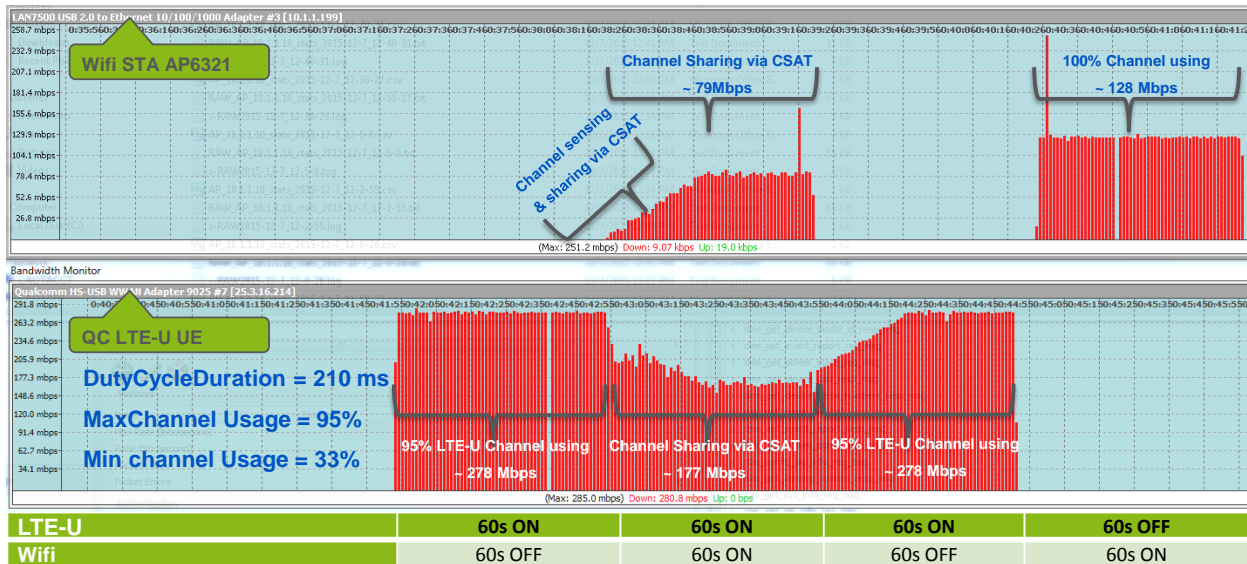
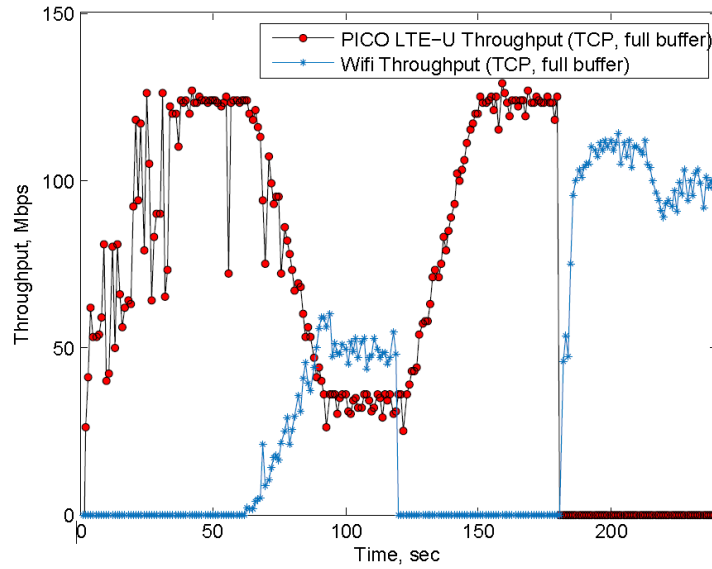


Figure D.13 Fair sharing output (Bandwidth monitor).

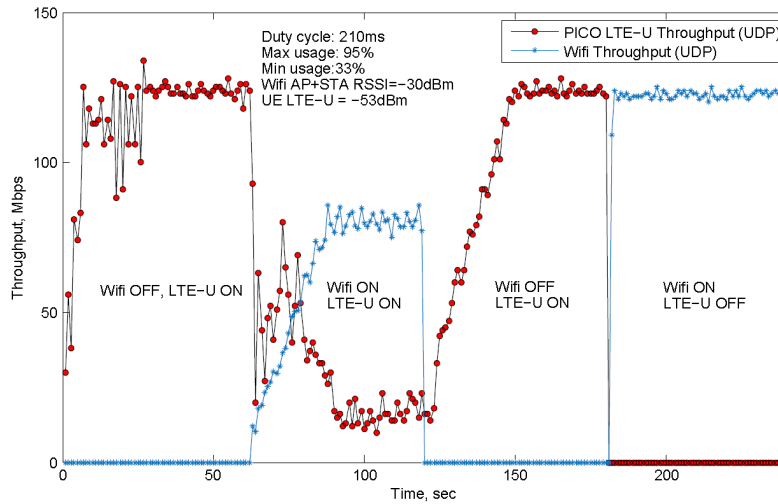
Results analysis :

Fig. D.14 shows a better illustration of the fair sharing mechanism with the corresponding recorded throughputs both at Wi-Fi STA and UE. It can be noted that during channel sensing at the initial state of CSAT at LTE-U channel, a degradation of the LTE-U throughputs were recorded from 60 s to 80 s. This issue has been solved by using an additional attenuation of 20 dB at the Wi-Fi access point antenna port, since a higher channel power was measured at the RBS pico transmitter/receiver. The results shown with TCP traffic in Fig. D.14a. It can also be noted that, a certain distance might be necessary to be maintained between RBS and Wi-Fi AP to achieve a fair sharing. Moreover, Wi-Fi AP and Wi-Fi STA noise floor values were also measured during the entire 240 seconds

measurement period in order to investigate the interference caused by LTE-U channel. Table D.1 and D.2 show the list of parameters and the channel sharing performance with UDP traffic where Fig. D.14b illustrates the results of the channel.



(a)



(b)

Figure D.14 Performance results. (a) and (b) are the fair sharing with TCP traffic and fair sharing output with UDP (post processed), respectively.

Table D.1 LTE-U setup parameters and performance results at LTE-U

LTE Technology	LTE-U (S-cell)
PICO model	6402
Frequency	5.745 GHz
Channel Number	149
Bandwidth	20 MHz
Throughput (calculated, 100%)	150 Mbps
Throughput (calculated, 95%)	142.5 Mbps
Throughput (measured, 95%)	113 Mbps
Duty cycle	210 ms
Max channel Usage	95%
Min channel usage	33%
Channel Sharing Calculated (33%)	49.5 Mbps
Channel Sharing Measured (33%)	Avg. 28 Mbps, Min 10 Mbps, Max 80 Mbps

Table D.2 Setup parameters and performance results with Wi-Fi (5 GHz) channel

Wi-Fi Technology	Wi-Fi 802.11n
Model	AP : Belair20E, STA : TP link AC1200
Frequency	5.745 GHz
Channel Number	149
Bandwidth	20 MHz
Throughput (calculated, 100%)	150 Mbps
Throughput (calculated, 100%)	122 Mbps
Channel Sharing Calculated (77%)	Avg. 115 Mbps
Channel Sharing Measured (5-77%)	Avg. 64 Mbps, Min 10 Mbps,Max 85 Mbps

Fig. D.15 shows the characteristics of the coexistence mechanism with different maximum channel usage times such as 85 %, 75 %, 65 %, 55 % of the duty cycle (i.e., 210 ms). Results show that, once the maximum channel usage of the LTE-U decreases, Wi-Fi is getting more time to access the channel and the transition period of both LTE-U and Wi-Fi decreases before going in a stable state. The performance results of the channel sharing using a full buffer (data always available to send)

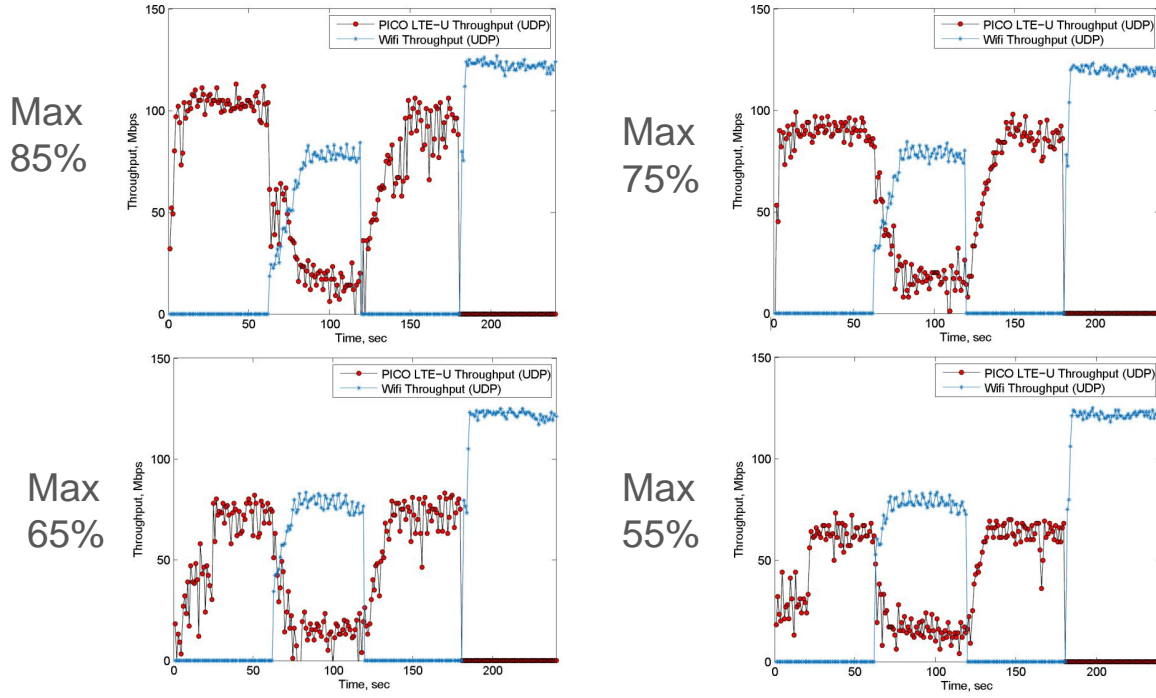


Figure D.15 Channel sharing with different percentage of duty cycle values.

condition with TCP traffic using the same setup parameters defined in the Tables D.1 and D.2. Full buffer condition can be calculated for both UDP and TCP as

$$RTT(80ms) \times data\ rate(150\ Mbps) = 1.5\ MB \quad (D.4)$$

where RTT is the round trip time between sender and receiver (80 ms from iperf server to UE) and set at 5 MB (TCP window size or UDP bandwidth on the iperf command). It has been shown that using the full buffer with the TCP packet transmission, a smooth fair sharing also exists since the channel condition is stable with wired connection though some fluctuations were observed.

The future work could be the characteristics of CSAT by using different Wi-Fi AP and Wi-Fi STA vendors such as Aruba, Cisco, Linksys, D-link, etc., by using multiple numbers of PICOs and Wi-Fi APs, by increasing the number of Wi-Fi STAs by serving one AP, to test how many STAs can share the same channel, VoIP test, by using below -62 dBm of the channel power. Moreover, the coexistence characterization by using the new LTE-U Forum specification requirements for CSAT could be the future work.

APPENDIX E LIST OF PUBLICATIONS

S. A. M. Tariq, C. Despins, S. Affes and C. Nerguizian, "Angular and Temporal Characteristics of an Underground Wireless Channel in a 60 GHz Band," Submitted to IEEE Transactions on Wireless Communications 2016 (Chapter 5, 6 and 7).

S. A. M. Tariq, C. Despins, S. Affes and C. Nerguizian, "Polarimetric Measurements and Characterization of Wireless Propagation at 60 GHz for Underground Applications," Submitted to IEEE Transactions on Communications (Chapter 3 and 5).

S. A. M. Tariq, C. Despins, S. Affes and C. Nerguizian, "Statistical Modeling of 60 GHz Wireless Channel in an Underground Mine Gallery," 2015 IEEE International Conference on Ubiquitous Wireless Broadband (ICUWB), Montreal, QC, 2015, pp. 1-5. (Chapter 7)

S. A. M. Tariq, C. Despins, S. Affes and C. Nerguizian, "Experimental Results of Rician K-Factor and Co-Polarization Ratio of 60 GHz Wireless Channel in an Underground Mine Gallery," 2015 IEEE International Conference on Ubiquitous Wireless Broadband (ICUWB), Montreal, QC, 2015, pp. 1-5. (Chapter 5)

S. A. M. Tariq, C. Despins, S. Affes and C. Nerguizian, "Scattering effect based on measurements of reflection coefficients at 60 GHz in an underground mine gallery," 2014 IEEE 25th Annual International Symposium on Personal, Indoor, and Mobile Radio Communication (PIMRC), Washington, DC, 2014, pp. 217-221. (Chapter 4)

M. El Khaled, P. Fortier, M. L. Ammari and S. Ahsanuzzaman Md Tariq, "Optimal power allocation for underground selective channel at 60 GHz," 2014 IEEE International Conference on Communications Workshops (ICC), Sydney, NSW, 2014, pp. 736-741. (A part of chapter 5)

S. Ahsanuzzaman Md Tariq, C. Despins, S. Affes and C. Nerguizian, "Rough surface scattering analysis at 60 GHz in an underground mine gallery," 2014 IEEE International Conference on Communications Workshops (ICC), Sydney, NSW, 2014, pp. 724-729. (Chapter 4)